UNIVERSITY OF CALIFORNIA
SANTA CRUZ

ATCAM: AUTOMATED TESTING AND CHARACTERIZATION OF ADDITIVE MANUFACTURING

A dissertation submitted in partial satisfaction of the
requirements for the degree of

DOCTOR OF PHILOSOPHY

in

COMPUTER ENGINEERING

by

Arash Alex Mazhari

September 2021

The Dissertation of Arash Alex Mazhari
is approved:

Dr. Mircea Teodorescu, Chair

Dr. Patrick Mantey

Dr. Sean Swei

Peter Biehl
Vice Provost and Dean of Graduate Studies

Table of Contents

List of Figures

List of Tables

Abstract

ATCAM: Automated Testing and Characterization of Additive Manufacturing

Arash Alex Mazhari

Additive manufacturing (AM) lends itself as a powerful tool which leverages the automated fabrication of digital product definitions through the computer numerical control of physical toolpaths. The process conventionally requires modification of these digital definitions for compatibility with the physics governing that fabrication process; this commonly leads to unoptimized solutions due to design-for-manufacturability constraints. I propose a process which empowers this manufacturability as a multi-functional constraint to the input design itself by sensing the performance of manufactured objects through the automated actuation and testing of components as a function of their fabrication. The sensitivity of AM to the variability of feedstock quality, machine calibration, and accuracy drives the need for frequent characterization of fabricated objects for a robust material process. The constant testing is fiscally and logistically intensive, often requiring coupons that are manufactured and tested in independent facilities. By modeling the expected performance of an object and comparing the differences from expected to physical observations of the object through multiple dimensions of sensing, one may start to infer, characterize, validate, and even potentially qualify and standardize a component's actual implemented realization. As a step towards integrating testing and characterization into the AM process while reducing cost, I demonstrate Automated Testing and Characterization of AM (ATCAM). ATCAM is configured for Fused Deposition Modeling (FDM) and introduces the concept of dynamic coupons to generate large quantities of basic AM samples. An in-situ actuator is printed on the build surface to deploy coupons through

impact, which is sensed by a load cell system utilizing machine learning (ML) to correlate AM data. We test ATCAM's ability to distinguish the quality of three PLA feedstock at differing price points by generating and comparing 3,000 dynamic coupons in 10 repetitions of 100 coupon cycles per material. ATCAM correlated the quality of each feedstock and visualized fatigue of in-situ actuators over each testing cycle. Three ML algorithms are then compared, with Gradient Boost regression demonstrating a 71% correlation of dynamic coupons to their parent feedstock and provided confidence for the quality of AM data ATCAM generates. Further, by employing ATCAM through the automated high-volume testing of derivated fabricated objects capable of flight, I use the basis of ATCAM to consider the aeronautical characterization and manufacturability of a design for its environment through an automated network of systems comparing and characterizing the performance of an aircraft they manufactured, deployed, and sensed cooperatively.

I dedicate this document to my loving parents and grandparents. This dissertation is a product of their collective belief that if I put enough effort into anything, I would be able to achieve it. My grandfather sat me down one day when I was a freshman in aerospace engineering and told me that if something was difficult to obtain, the intrinsic value of that thing would be reflected accordingly. I echo this sentiment in his memory, and will cherish the value of my education in tandem with the countless days spent inching along this journey.

Acknowledgments

The text of this dissertation includes reprints of the following previously published material:

A. A. Mazhari, A. Zhang, R. Ticknor, S. Swei, E. Hyde and M. Teodorescu, "Printing and Programming of In-Situ Actuators," 2020 IEEE/ASME International Conference on Advanced Intelligent Mechatronics (AIM), 2020, pp. 445-450. https://doi.org/10.1109/AIM43001.2020.9158926

Mazhari, A.A., Ticknor, R., Swei, S. et al. Automated Testing and Characterization of Additive Manufacturing (ATCAM). J. of Materi Eng and Perform (2021). https://doi.org/10.1007/s11665-021-06042-2

The co-authors listed in this publication directed and supervised the research which forms the basis for the dissertation.

I could write an entire chapter just to properly thank and acknowledge everyone who has helped me pave a brick in the figurative foundation that is a doctoral degree.

Family:

*Mom and dad, you are excellent role models. You both have contributed endlessly to providing me the skills to work hard and learn from my mistakes. Baba, the persistence and work rate I have learned from you has become my strongest attribute. Moman, your attention to even the smallest details has given me the mindset to pay attention to the little things, because to the right eye they can be the largest, most significant detail. Those skills in particular are so incredibly useful for the PhD, and consequently I'd like to thank you both for them among 1,000,000 other things.

*Sophia, you're an incredible life partner and I'm extremely grateful that you support me unconditionally. Be it staying in with me and keeping me company

because I need to work on a paper, or regularly asking me about research and progress on this document, your presence is synonymous to my success. I truly appreciate everything you do for me, and hope to continue to do the same for you in your pursuit for a Professional Engineering license. You'll get the PE, whatever it takes. Love you.

*Nima, I really appreciate who you are. Even when you occasionally get a good game in at FIFA (which, mind you, is extremely rare. Look at the records) or make a horrible pass when we play soccer, you're a fantastic brother, a genuinely kind person, and a solid engineer. You helped me get this degree in more ways that you'll realize, and for that I thank you.

*Uncle Mustafa and Aunt Christina Tunnah, "thank you very much!" for teaching me about up and coming collectible art, what an IPA was, and chanting old songs whenever I was just trying to study. They're quite endearing, so I'll share them with the general populous:

-Sa'at 3:30pm shod, as ab goosht khabari nist, magar masghare kardid?!

It's 3:30pm, and there's no sign of the stew. Do they think it's a joke?!

-To Karbala ab nabood, Pepsi Cola bood. Shishah sefid, khodesh siyah bood.

In Karbala there was no water, but there was Pepsi. The glass was white, and the drink was black.

*Wendt Family, I thank you all for welcoming me so warmly over the last eight years and apologize for having to miss countless family events to attend to the requirements of this degree. Your encouragement in my pursuit of a doctorate was and is extremely appreciated, and I am eager to finally attend a Wendt gathering without someone asking "So... when are you going to finish that PhD and plan a wedding?!"; love you all.

Mentors:

*Dr. Mircea Teodorescu, thank you for putting up with my crazy ideas and unconventional schedule. I was not your typical student, nor has my full-time working status been the best for your lab structure, but you provided me an opportunity and stuck through all of the highs and lows that come with mentoring a PhD student that's doing their own thing. I appreciate you being tough on me (I really do) and encouraging me to think outside of the box, because I learned quite a bit through the adversity. I am extremely proud to have graduated from your lab, and look forward to enjoying some scotch with you as a colleague now that I don't have to be terrified of you anymore.

*Dr. Sean Swei, I could not ask for a better mentor. The questions you have asked me along the way stick with me as I continue to digest them years later. From your courses back at SJSU, through jointly trying to figure out how to best represent the dynamics of an ISA for a paper at NASA, or just getting through the logistics of the PhD, I would not have been able to do this work without you and will be forever grateful for your guidance and contributions. Thank you.

*Dr. Pat Mantey, thank you for your encouragement, ideas, and for helping me through the logistics of the dissertation and the defense.

*Mr. Dean Giovannetti, I could not ask for a better supervisor. Working with you is the sole reason I have stayed with NASA, as you help me learn the skills I need to be a useful public servant while trusting me to make the right move when I'm presented with a difficult position. I look forward to continuously developing my leadership skills under your guidance and genuinely thank you for the endless support you have given me to seek, pursue, and execute the requirements of this tedious degree.

*Mr. Shawn Seader, your help was extremely crucial in helping me understand how to become a better student. The skills you taught me and the friendship you

gave me when you guided me in undergrad is a core reason I was able to obtain the doctorate all these years later. I'm still using the same tools, and for that, I thank you.

Friends and Colleagues:

*Guillermo "G10" Marmolejo, like Nima, you have helped me through this degree more than you'll know. Coming over the hill every Sunday to play soccer and regularly making a concentrated effort to chat and hang out when I could not was your way of keeping me sane and meeting me wherever our friendship's median was, primarily due to this degree. I dedicated as much time to this as was required, and often that stretched bro time to the limit. I look forward to compensating, and then some. You rock, G10.

*Rachel Ticknor, thank you for your continued friendship. The ability to bounce an idea off of you and know for a fact that the technical merit of your input was unquestionable has been extremely helpful in the pursuit of this dissertation. You're brilliant, as a friend and as a colleague.

*Dr. Daniel "Luccador" Cellucci, thank you for your awesome feedback on closed-loop manufacturing (mind the pun), and more importantly, thank you for being there when it was just us doing our thing in the shop. The incredible times we've had in DTSJ and SF paired with your advice developed our friendship into something I not only cherish, but respect. Thank you.

*Andres "Nesinho la Rana" DP and Eddie Uribe, you guys have heard me moan and groan about school more often than you deserved. I thank you for your patience and your understanding. You're both outstanding people and I'm proud to call you my close friends. No, you can't call me Dr. M. And no, Eddie, you can't teach Santi to call me Dr. M. I won't respond.

*Pat Pansodtee, you're a fantastic engineer, and a good friend. Thank you for

being a great roommate, helping me get through the crazy logistics of coursework, for "staying woke", and most importantly, thank you for being a wonderful dude. Our friendship may have started because we were in the same cohort, but it will carry through the next few decades for anything but that. I look forward to hanging out for many years to come, and truly want you to know that I respect you for who you are and will always be here whenever you need it.

*Erik Jung, Victoria Li, and DANSER Lab folks, thank you for your friendship over the Ph.D. You're my Santa Cruz fam, and although I wish I could have spent more time over the hill with you all, I appreciate your understanding in knowing that I had to attend to life and work on this side of it. Thank you for your help, every step of the way.

*Elizabeth Hyde, Jay Singh, thank you for your understanding whenever I was ghosting the group. My heart was there, but my head was elsewhere.

*Keven Gallegos, Jorge Enriquez, Marvin Jay, I appreciate that you guys have been there through thick and thin. I've been primarily absent keeping individual tabs with you guys through this degree, and hope that when you go through the document you'll take a peak at some of what was keeping me so busy the last few years. Cheers, boys.

*Daniel Likins and Jenny Wagner, thank you both for your understanding over the last three years. Your support during this degree was unparalleled and I appreciate that you let me do my thing. I look forward to making up for lost time.

*Mike Ho-Nguyen and Daisy Nguyen, thank you for your friendship and your contributions to keeping both Sophia and I sane during the pandemic. It made the hours spent working on this degree more sustainable.

*Arthur Deschamps, Hemil "PM" Modi, Roberto Carlino, Witold Koning, Arno

Rogg, Luke Idziak, Anh Nguyen, Dr. Chatterjee, and everyone else from the NASA crew, I am sincerely sorry for not being able to spend time with you all on countless occasions because of the work that makes this document. I've told you since I started back in 16' that as soon as I finished this degree in five years (which I kept my promise, I'm writing this in 21'), we'll make up for it. I look forward to doing that. Cheers to your friendship.

Chapter 1

Introduction

1.1 Motivation

There is currently a significant reliance on technical human labor to optimize and validate design parameters for not only manufacturability, but field performance. In many instances, these highly-nonlinear and interdependent considerations overlap and constrain the design space to globally-defined parameters which may not be optimal to individual applications.

By exploring the implementations of recent advances in localized sensing and self-contained fabrication, one may decouple the problem by observing the performance of objects fabricated in-situ and comparing expected outcomes to those physically realized. This would allow for digital manufacturing processes to characterize and autonomously program additional dimensions of environmental considerations into their toolpaths for optimized designs automatically localized to their exposed design spaces.

A novel realization of an inexpensive and adaptive manufacturing platform for adaptive robotics is the automated exploration of a design space. Through this rapid and iterative implementation of embodied intelligence, one may sense and

physically validate a vast number of environmental characteristics through testing. The work presented in this dissertation considers a wide range of automated design-space exploration. An example is the characterization of flight-related variables, such as inducing the variables driving lift and drag coefficients through testing a gradient of iterated components and their respective projectile paths. The platform even allows for the determination of that projectile's material properties from the subsequently resulting deployment(s).

If nothing more, automating and integrating the engineering processes of designing, fabricating, testing, iterating, optimizing, and validating objects in a closed-loop manner significantly reduces the cost and logistical requirements for tailoring individual components for their environment through the automated exploration of a design space. This significantly frees technical bandwidth for humans to focus on tasks of increased complexity.

1.2 Background & Setting

The ability to program dimensions of digital information into the manufacturing process has only been recently enabled through computer-numerically-controlled (CNC) machines. With the advent of 4D printing, additional dimensions of information can be embedded within in a system [Ge et al., 2016] [Tibbits, 2014] [Wehner et al., 2016]. The increased dimensions permit an increased span of solutions for a given set of parameters, as per [Bender, 1987] and [Wang et al., 2000]. The demonstration of physically actuating an object is an example of designing a component with programmed dynamics to specifically interact with and autonomously demonstrate kinematic performance characteristics through the manufacturing platform. This allows the components to interact with each-other while simultaneously automating the post-processing stage

of single-gantry additive manufacturing. The result is a process which allows for the possibility of a significantly larger span, or number of possible tests and manufacturable outcomes without the need for additional or modified hardware [Medina and Lawrence, 2008].

The applicability not only lies in the uniquely enabled autonomous physical validation of a digitally-designed system, but also in the proposed capability of characterizing the physics-embedded within a design through digital manufacturing and actuation. The proposed method for achieving these tasks is to design a process which would not only translate a component from a digital to physical medium, but autonomously activate and demonstrate the performance characteristics nested within the object's physical implementation.

A prime novelty of this work is the ability to retrofit existing systems for automated actuation digitally. This allows for the manufacturing process to be physically augmented through encoding, without the addition of independent robotic manipulators. To increase the applicability and adoptability of this technology, the toolpaths were generated with respect to the most common additive manufacturing methodology at the time of publication, Fused-Filament-Fabrication (FFF) [Griffey, 2014]. To further allow the ability to be adopted, the specific platform utilized was the most common FFF system, RepRap[Moilanen and Vadén, 2013]. The specific configuration of RepRap was the Prusa i3 MK3, as it provided a universal and reliable basis that contained features which increase the reliability of the FFF process, such as auto-leveling [Attaran, 2017].

By pairing this automated fabrication and deployment technique with sensing methods that track an object visually and determine their physical forces through impact, a strategy was developed to automatically detect the actual performance of a digital design. This integration of the manufacturing, deployment, and test-

ing process itself yields numerous novel realizations. We can further the utility by using this process as a platform for exploring the design space of an object by implementing an evolutionary algorithm which detects the performance of an object undergoing multivariable changes and defining local design optima. By closing the loop from digital design through manufacturing, deployment, testing, sensing, validation, and iteration over many generations of an object we can converge a design for an optimized realization for its environment with respect to the physical limitations of the manufacturing and deploying mechanisms utilized.

This process creates the analogous ability to define basic optimization criteria (such as desired velocity, coefficient of lift), or mission definition (reach a certain target, follow a trajectory, etc.), start the process with the press of a button, and leave the system overnight. The following morning, many generations of an object will have been created, physically validated, and converged to a design heuristically tailored for the performance or mission criteria with generated data defining the design space explored along the evolutionary cycle with the performance for each varied phenotype.

1.3 Identification of Problem

The open-loop nature of an object's design cycle is relatively inefficient and cost-intensive. The design, fabrication, integration, and testing of an object can take months for a single iteration as demonstrated by Ref.[Wong, 2012], [Harvey et al., 2005] and Ref. [Floreano, 2015]. It has been noted that one of the limiting factors in designing robotic systems is the logistical constraint of validating coupled multivariable design spaces through iterative protocols, as per Ref. [Arias-Montano et al., 2012a], [Yang et al., 2018], and [Vargas et al., 2014]. To further automate the cycle, the author proposes the integration of multiple

stages of an object's design: fabrication, deployment, validation, and iteration. By developing an analogous system which creates an object and tests the component it has created autonomously, we can demonstrate that humans can be removed from these stages of engineering an object and observe the design space it governs. An in-depth literature review has validated that the consolidation of these stages of design has never been previously demonstrated for the automated characterization of an object's design space. With a combination of in-situ fabrication, automated deployment, and autonomous sensing for validation with subsequent iteration for global optimization through converging local optima, one may realize the joint-considerations of these processes to employ a strategy for automated exploration through a design space by deploying evolving robotic systems.

1.4 Contributions of This Work

This document develops a method to automate the exploration of a design space by employing and automating digital object design, manufacturing, deployment, testing, sensing, and iterating protocols for evolutionary convergence to validated optimization. By integrating the considerations of each these fields into the computer-aided-manufacturing process, one may digitally embed, autonomously actuate and even validate dimensions of kinematic information into additively manufactured components as a function of the 3D-printing process.

The result also enables current systems to provide significantly-increased physical realizations through self-contained post-processing of digital manufacturing toolpaths. By embedding physical additive process-specific interactions into the manufacturing toolpath of a component, an object may be augmented with additional dimensions of information that provide the ability for a printed part to kine-

matically interact with its environment without human intervention on conventional Fused Filament Fabrication platforms. Additionally, multiple objects may be processed to simultaneously interact with both the manufacturing-environment and components fabricated on the same platform for an increased complexity of interactions and a significantly-expanded range of outcomes otherwise impossible from existing systems.

In this work a novel systematic algorithm is defined to program additively manufactured objects to autonomously actuate and displace as a function of toolpath modification. It then demonstrates the implementation through a physically validated example, and simulates the modeling of the observed behavior to characterize additive manufacturing-specific considerations. The work then defines an evolution of the platform, modified for implementation as an automated high-volume additive manufacturing and testing tool. The tool is then experimented and validated for the development of locally-optimized, autonomously actuated aircraft.

Additional discussion and overview of this document's deliverables are presented in Section 7, with relevant locations of each deliverable identified in Section 7.3.

1.5 Definition of Terms

- Additive Manufacturing - Additive Manufacturing (AM) is a convention to localize bulk material to create a physical object with respect to a product definition through a cumulative process. Also commonly referred to as 3D-Printing.

- Aerostructure - A pressure-regulating structure whose loading conditions

vary with respect to localized reynold's numbers accross the surface.

- ATCAM - Automated Testing and Characterization of AM. ATCAM is defined as the entire system, integrating sensing into the ISD process to automate the characterization of AM.

- Build Surface - Also referred to as the build-plate or build-tray, is the platform on which an AM machine conventionally processes material during fabrication.

- Deployable - The ability for an object to successfully be subjected to ISD from the AM build surface.

- Digital Product Definition - An AS9100-derived terminology for the digital information describing an object. Typically, this information is embedded within a computer-aided draft (CAD) existing in two or three dimensions. The finalized definition is commonly formatted as a reference to be later used for manufacturing purposes.

- Dynamic Coupon - A standardized AM object fabricated and subjected to ISD. ATCAM senses properties from large quantities (1000+) of dynamic coupons to generate a material database which can be used to characterize the AM process.

- FFF/FDM - Fused Filament Fabrication (FFF), or Fused Deposition Modeling (FDM), is a form of additive manufacturing localizing thermoplastic filaments in a quasi-fusion process. The resulting components are mechanically quasi-isotropic.

- gCode - Also referred to as the toolpath, gantry code (gCode) is a machine

language which provides instructions for the AM process. ATCAM manipulates gCode files to retrofit and execute ISD.

- ISA - An In-Situ Actuator (ISA) is a discrete retrofitted mechanism fabricated onto a build-surface. An ISA can be used to store and impart mechanical energy onto an in-situ deployment (ISD) object.

- ISD - In-Situ Deployment (ISD) is the process in which an ISA or ISLS is referenced to eject an object from the AM build surface. ISD is the method this document uses to automate the AM process and eject dynamic coupons.

- ISLS - An In-Situ Linear Spring (ISLS) is a self-contained object capable of ISD. ISLS are distinguished from other ISD objects because they have an integrated deployment mechanism (a linear spring) built onto the bottom of the deployable object.

- Reynold's Number - Commonly referred to as the quantitative dynamic interaction, or 'stickiness', of an object translating with respect to a fluid in a control volume.

- Slicing - The process of converting a volumetric digital product definition into a cumulative series of lower-dimensional layers. The output of this process is commonly referred to as a toolpath, and is a necessary component for computer-numerically-controlled manufacturing.

- Tool Head - The subsystem on an FFF/FDM machine which contains the extrusion nozzle. The tool head is used by ATCAM to deflect ISA and ISLS through the ISD process. Also commonly referred to as the build head.

Chapter 2

Literature Review

2.1 Introducing the Literature

To develop a method for automating the characterization of an aeronautical design space through additive manufacturing, it was crucial to investigate and understand a wide-scope of relevant fundamentals within the fields of digital design, computer numerical control of toolpaths, aerostructures, high-volume testing, and the automated sensing of performance criteria. This highly broad set of fields defines a multi-variable problem, where locally optimal solutions can easily maintain globally-sensitive coupled implications.

This diverse and theory-heavy section consequently overviews a variety of processes realizing multi-functional dimensions and provides context to the necessary considerations of their respective applications. A review of aerospace design-for-manufacturing is implemented to help uncover the requisites and concerns regulating flight. Numerous fabrication methodologies and their respective toolpathing strategies are investigated to characterize their relevancy to regulating the design of an aerospace system, where applicable. Autonomous systems enabled through novel prototyping methods are discussed, with their strategies and

methods for solving functional design issues bottle-necked through manufacturing. An overview is conducted of existing high-volume testing systems, followed by a discussion on the state of automated sensing and current applications.

The section navigates through the necessity of a system capable of automating the convergence of highly-correlated multi-variable designs by finishing with a review of how scientists and engineers have been trying to solve this problem by mimicking nature's solution through evolution.

2.2 Digital Fabrication

2.2.1 Additive Toolpathing Algorithms of Digital Definitions

The additive manufacturing process conventionally relies on the cumulative processing of lower-dimensional layers or blocks of information as a function of localizing bulk data [Steuben et al., 2016, Jin et al., 2014]. For Fused Filament Fabrication, three-dimensional components are commonly sliced into stacks of two-dimensional layers for fabrication [Jin et al., 2013]. Geometric and structural data is typically lost along the toolpathed build-axis direction as a function of the mechanically-bounded layering process [Liu et al., 2014, Tymrak et al., 2014].

The geometric inaccuracies of this process compile through errors accumulated through the layered-toolpath following an additive manufacturing process [Lensgraf and Mettu, 2016]. Systematic issues, such as quasi-isotropic mechanical properties can arise with these compiled volumetric discrepancies. The asymmetric properties can be primarily associated with the chronology of fabrication, with errors introduced via varying environmental conditions, material properties, algorithmic inaccuracies and gantry-based mechanical issues along the

z-axis [Zou et al., 2016a] . Consequently, there exists a defined discretization within three-dimensional components in regards to these two-dimensional layers, confirming implicit directionality as a function of the manufacturing process [Shaikh et al., 2016, Tymrak et al., 2014, Lee and Huang, 2013]. This rendering directly relates the macroscopic orientation of digital coordinates to physical, mechanical properties which may be tailored for directionally-complaint structures [Garcia et al., 2012, Montero et al., 2001].

2.2.2 Multi-stage Manufacturing

Many conventional definitions of multi-process manufacturing systems utilize independent robotic manipulators to progress an object through multiple stages of fabrication [Mehrabi et al., 2000]. The Keck Center of the University of Texas, El Paso has implemented this concept through a multifunctional component toolpathed on numerous machines, pending applicability of each desired feature or attribute [Olivas et al., 2010]. There has been work conducted at Lockheed Martin Corporation to create an autonomous storefront where an object's digital model is uploaded by an engineer through a graphical user interface, with a multi-physics engine computing the most relevant manufacturing processes to manufacture the object. A signal is then sent to a machine which controls a traversing belt, which in turn localizes and translates a starting build-plate through a series of machines, serially [Xu and He, 2004]. This ecosystem allows for the embedding of discrete systems; a common example is the integration of electronics into a structure, allowing for uni-body components no longer requiring assembly [Macdonald et al., 2014] [Espalin et al., 2014].

A prime factor for driving the development of this technology is the appealing reduction of relative cost and manufacturing time, primarily through the as-

pect of significantly-reduced labor requirements for a given system. Alternatively, Ref. [Kwas et al., 2014] suggests such platforms can be implemented to serve a wide-range of applications, including but not limited to the ability to create fully-functional weapon systems, in-situ. A common issue facing these platforms are power and infrastructural requirements [Holshouser et al., 2013]. Both the 'Factory of the Future' concepts from the Keck Center and Lockheed Martin require dedicated and specialized facilities to be dedicated for the successful implementation [Holshouser et al., 2013]. These logistical requirements are due to the requisite for traversing platforms, and discrete robotic manipulators to localize and move the object being fabricated [Quaid and Hollis, 1996]. Resulting in part to these requirements, the driving factors for fast-paced innovation within the field of digitally-enabled manufacturing seem to show no sign of decreasing [Huang et al., 2015].

2.2.3 4D Printing

There has been an increasing number of investigations regarding the manufacturing of components containing information programmed to autonomously interact with its environment, either during or after its fabrication[Momeni et al., 2017] [Kokkinis et al., 2015] [Wehner et al., 2016]. This field, also commonly referred to as 4D Printing [Tibbits, 2014], heavily revolves around the concept of shape-deformation as a function of time [Gladman et al., 2016]. A specific consideration of this design methodology is the single state encoding the functions these objects serve[Felton et al., 2014] [Dickey, 2016]. A limiting factor of this constraint is that they reach their programmed state with permanence, limiting the reprogramming potential.

Additive curing processes, such as the derivative stereolithographic process

referred to as polyjet printing, rely on time as a function of the polymerization process with respect to exposure to ultraviolet wavelengths [Singh, 2011] [Barclift and Williams, 2012]. Various shape memory polymers have been developed as a method of tailoring to the unique capabilities of the polyjet process, embedding additional object dimensionality for increased component functionality with respect to time [Ge et al., 2016]. Research has been conducted note only to selectively cure the resin from the polyjet process, but to intentionally retain a portion of the resin in its fluidic form by housing it within cured material [MacCurdy et al., 2016]. A functioning hydraulic actuator was created with a modified Objet 260 polyjet machine. These actuators were implemented as the thrust-generating medium for a walking robot, which is noted as one of the few examples currently developed through additively manufactured components containing the embedded dimensionality of repeatable kinematic actuations. Work has also been completed within the field of pairing rigid materials with uncured resins as a function of designed compliance through additive manufacturing [Meisel et al., 2013] [Meisel et al., 2015] [Stiltner et al., 2011]. These methods, although extremely novel, required heavily on human labor for controlled postprocessing techniques. It also required human-in-the-loop assembly for integration of the energy-delivering variables which could allow it to demonstrate repeated automated motion. Various machines have come to market enabling an off-the-shelf integration of previously independent systems. The Voxel 8 additive manufacturing platform cleverly utilizes lithography to embed electronics into polymers by selectively depositing photo-sensitive resins where the user requires rigidity, and conductive ink for circuitry [Silverbrook, 2010]. The novelty of this platform lies in the ability to embed electrically-regulated dimensions of functionality into a structure without human intervention. Unfortunately, this platform still re-

quires post-processing to actuate the information due to its photo-sensitive nature [Dizon et al., 2018] [Vanek et al., 2014].

Even as the number of lithographic 4d printing applications have continued to increase over time with maturation of the technology [Kuang et al., 2019], thermoplastic fusing processes continue to demonstrate their utility in shape-morphing applications [Rajkumar and Shanmugam, 2018]. The ability to selectively deposit material that diminishes thermal energy to reach a solid-state within a fraction of a second allows for novel applications regulating internal stresses as a function of time [Ly and Kim, 2017]. By regulating these forces over defined dimensions, one may program numerous dimensions of performance objectives as a function of lower-order dimensions [Hu et al., 2017] [Bodaghi et al., 2018]. Although the majority of 4D thermoplastic applications contain the ability to deform their own geometry for functionality, the applicability of their structures are severly limited to low-energy applications, or those with limited repeatability [Pei, 2014]. Efforts have been made to increase the longevity of these functions by utilizing composites [Dudek, 2013] and polymers demonstrating elastomeric properties [Baker et al., 2019]. However, it is clear that the applications of repeatable, fatigue-resistant 4D printing of thermoplastics are highly limited and not well-demonstrated [Kuang et al., 2019]. The field of programming the sequential fabrication of repeatably ejected, semi-compliant thermoplastics as a function of additive manufacturing is relatively under-investigated.

2.3 Manufacturability Considerations for Aerospace Applications

2.3.1 Aerospace Loading Conditions

The manner in which expected loads traverse throughout a structure are typically amongst the first considerations engineers take when designing a pressure-regulating component [Tumer and Stone, 2003a]. Conventionally, aerospace vehicles and their freestream-facing components must be able to withstand relatively large pressure differentials within a span of millimeters of material-thickness. By integrating streamers, forces can be diverged throughout load-bearing structural members without increasing the thickness of an entire structure, allowing for significant savings in weight and consequently gliding efficiency. Optimal load displacement is especially critical for wing structures, as their compliance is finely tuned to several parameters which can differ greatly across various portions of flight. A common example is the tuned dihedral angle for an aircraft, as a function of speed and altitude. As an aircraft is stationary, aircraft wings require relative compliance with respect to ground-clearance to mitigate physical damage. As the freestream surrounding a wing increases in relative velocity, the lift generated and consequent applied load increases at a disproportional rate. Considering a common elliptical lift distribution seen in steady, level flight is applied along a wing, the structure must be able to deform with regards to the aerodynamically optimal dihedral angle at that given velocity. An analogous aerostructure following similarly multi-variable design parameters are turbine blades.

2.3.2 Designing for Directionality

Isotropic structures can have wide-ranging implications and resulting considerations for aerospace applications [Harris et al., 2002] [Hueber et al., 2016]. Common relevant applications for digital fabrication include the manufacturing of complex geometries pertaining to pressure-regulating components, as per [Williams and Starke Jr, 2003]. Such aeronautical systems typically pertain propellers, fans, and wings [Murr, 2016] [Brans, 2013]. Astronautical applications include nozzles, fairings, and pumps [Leach, 2014] [Joshi and Sheikh, 2015]. These components have historically been fabricated in either subtractive methodologies from raw material stock or cast from fabricated molds and conjoined into assemblies [Shen and Furrer, 2000] [Liu, 1995]. Due to the relatively homogeneous aspect of stock materials conventionally used for subtractive manufacturing, structural considerations have traditionally been taken as mechanically isotropic [Cheng et al., 2006] [Totaro and Gürdal, 2009]. Pressure-regulating surfaces such as wings typically have highly-directional loading patterns and are structurally-validated with respect to mechanical testing of the expected loads, iterating accordingly [Kimberlin, 2003]. Due to these design variables, specific considerations must be integrated into the components composing these systems for developing predictable structures and controlled manufacturing processes to help alleviate uncertainties that can be perpetuated through layer-based manufacturing techniques [Kassapoglou, 2013] [Murr, 2016]. Because of the highly-cyclic loading patterns experienced with pressure-regulating structures [Greenhalgh and Hiley, 2003], mechanical tolerances [Vogelesang and Vlot, 2000] for aerospace implementations must be defined and well-characterized.

2.3.3 Failure Modes and Manufacturing Considerations of Aerostructures

Investigating the various failure modes commonly applicable to pressure regulating structures provides correlations of mechanical performance to input design parameters [Frangopol and Maute, 2003]. Most aerostructures are reinforced with beams and bars specifically designed to compress under sufficient loading. Streamers are integrated into the design to transfer loads. These considerations require additional weight with respect to unibody configurations. Manufacturability has typically limited the implementation of low-weight unibody aerostructures. The current state of the art is implemented through carbon-composite laminate technology [Shanyi, 2007]. The manufacturability and load predictability of these systems are of upmost concern, as these structures are highly quasi-isotropic. Although the current state of the art for the additive manufacturing of aerostructures allows for unibody implementations of conjoined and integrated systems that reduce weight, they must still be highly proof tested, like their composite counterparts. NASA currently considers additive manufacturing for aerospace applications to be point-design, requiring uniquely developed inspection and evaluation criteria for additive part qualification. The agency is currently working on further-standardizing the process [Russell and Hall, 2008].

2.4 Bio-Inspired Robotic Systems

2.4.1 Platforms for Automated Evolution

The field of automated evolution has a rich spectrum of applications, varying from the self-optimization of an antenna for its environment, to adaptively tailoring the metaheuristic features exhibited by robots. Humans have increasingly

adopted nature's method of converging to complex yet functional designs through semi-controlled deformations, and are dedicating increasing resources to automate and apply the method to otherwise labor-intensive applications. [Bongard, 2011] defines a necessary strategic thrust within evolutionary robotics as self-contained development through automated design, manufacturing, and deployment. Various semi-automated deployments of robotic assemblies are demonstrated in Figure 2.1. It is noted that all of the physical implementations required human interaction for deployment, post-fabrication.

[Eiben and Smith, 2015] suggests that the method to realize automated considerations could come through the development of rapid prototyping, and in particular, 3D-Printing. They discuss the unique progression of digital evolution to physical evolutionary systems. Evolutionary robotics is specifically challenging due to noisy correlations between intended functionality and environmentally-conditioned convergence [Watson et al., 2002]. The paper concludes by describing the differences between various protocols for evolution, distinguishing between artificial and natural derivatives.

[Borenstein and Moraglio, 2014] applies the utility of evolutionary algorithms to address multi-functional issues with novel solutions, particularly as a function of naturally-occurring problem solving. The work describes this bio-inspired optimization as a function of exhausting numerous parameters, rendering through trial-and-error. The work conducted by [Eiben et al., 1999] provides the fundamental strategy by noting the inefficiencies of conducting highly-iterative approaches with evolutionary computation. It addresses the basis for choosing a decision while simultaneously computing and realizing a solution.

[Brest et al., 2006] furthers the discussion through a numerical benchmark narrative for self-adapting parameter control in differential evolution. The focus of

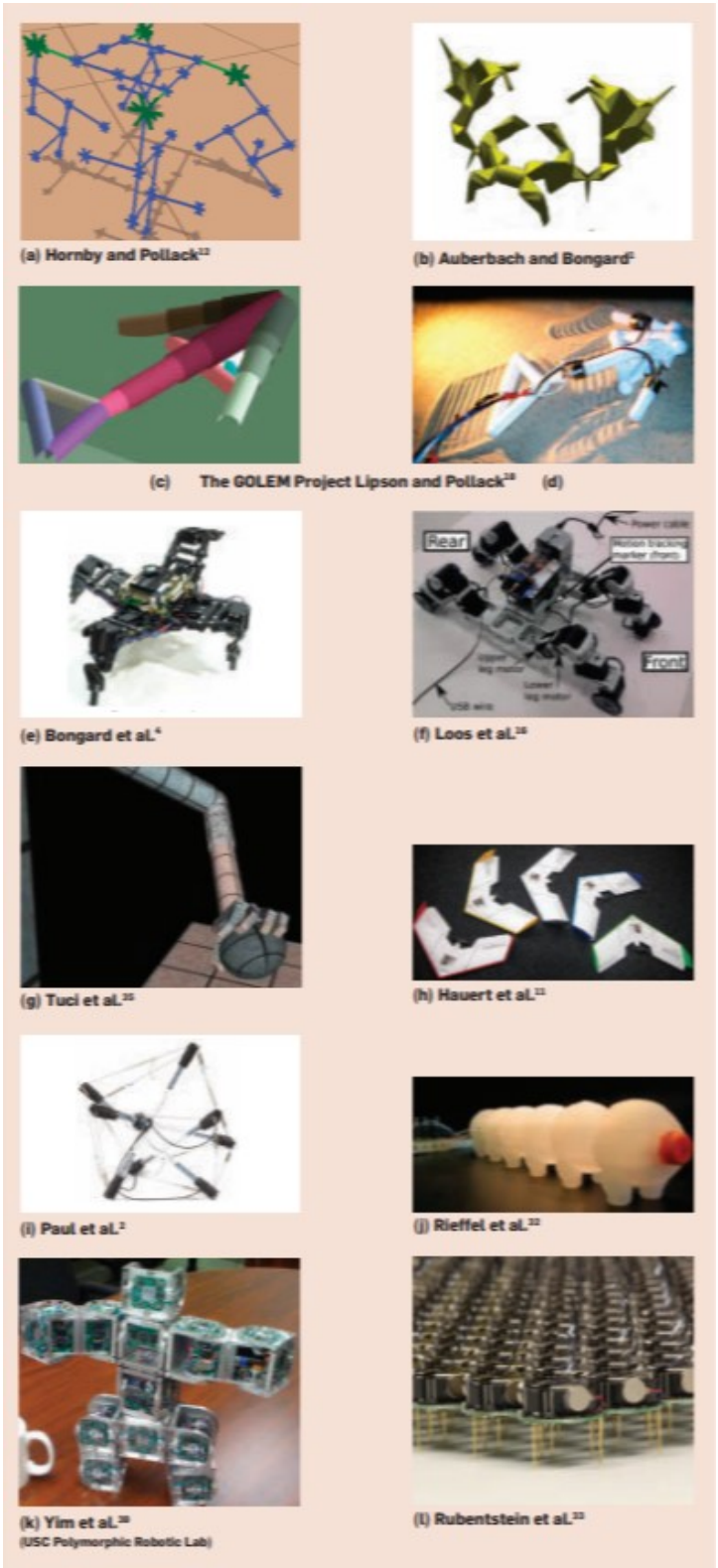

Figure 2.1: Various examples of semi-automated deployments of robots developed through evolutionary algorithms [Bongard, 2011]

decision making operations through individual iterations and mutations is described through the lens of mutation rates and the permutation representations within genetic algorithms by [Serpell and Smith, 2010] [Bredeche et al., 2012] and [Watson et al., 2002]. These works explore a property that is demonstrated in nature, describing mutations as not relevant to a single globally-optimal parameter, but a dynamically-shifting one which changes per iteration. This conclusion is also supported by the machine learning approach provided within [Filipic et al., 1999]. Serpell discusses a novel realization regarding the interwoven aspects of self-adaptation, considering mutations as an intrinsic process within evolution. A benefit of this characterization is the removal of specific mutating aspects from necessitating user-input, resulting in a reduction in computational intensity for each generation of mutation. Trends within parameter control are summarized by [Karafotias et al., 2014], presenting the topic by describing trends and their optimal use-cases. The investigation outlines the difficulty of proper parameter control within evolutionary computing through a comparison of computational intensity with respect to accuracy and time. The framework hierarchy of parameter tuning is demonstrated in Figure 2.2.

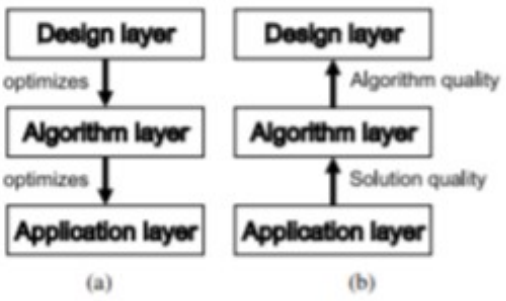

Figure 2.2: A definition of parameter tuning hierarchy through (a) control flow, and information flow (b). [Karafotias et al., 2014]

Highly influential work was conducted within the field of multi-objective optimization through specific considerations of increased complexity within parameter

mutation through evolution. By considering parameters with four or more objectives, many-objective optimization criteria could be defined for a system requiring multi-functional tailoring through an evolutionary algorithm [Deb and Jain, 2013]. The term evolutionary multi-objective optimization (EMO) was defined in this work, permitting widely increased applicability of evolutionary algorithms for complex, real-world problems [Deb, 2014]. EMO has served as a platform for complex applications ranging from railway networks [Fang et al., 2015], load demand testing for smart grids [Raza and Khosravi, 2015], to Kalman filters, and bee colonies [Luo et al., 2017] [Chugh et al., 2016]. Although none of these platforms fed data through design space sensing for automated, physical iteration through manufacturing, the work still serves as a premise for our document's own highly diverse multi-opmitizaion design strategy. EMO provides a basis for employing evolutionary algorithms with specifically-defined mutations to alter higher-order traits and characteristics through integrated iteration. Further bio-inspired context for evolutionary algorithms are provided through [Schmidt and Lipson, 2009]. Schmidt and Lipson discuss the barriers to automating evolution and provide support for the nontrivial aspects of characterizing these complex systems. They propose an algorithm which can define underlying dynamics through observed results, an example of which is demonstrated in Figure 2.3.

Decision-tree inductions of evolutionary algorithms are proposed as an alternative to computationally-intensive divide-and-conquer approaches. Barros' method compares the state of criteria for varied heuristic metrics with respect to partitioning technique [Barros et al., 2011]. The work then compares strategies for initializing populations, and defines fitness protocols over a wide variety of work. A conclusion of the findings are that when attempting to find global optimizations, evolutionary algorithms aid in avoiding convergence to local optima. They also

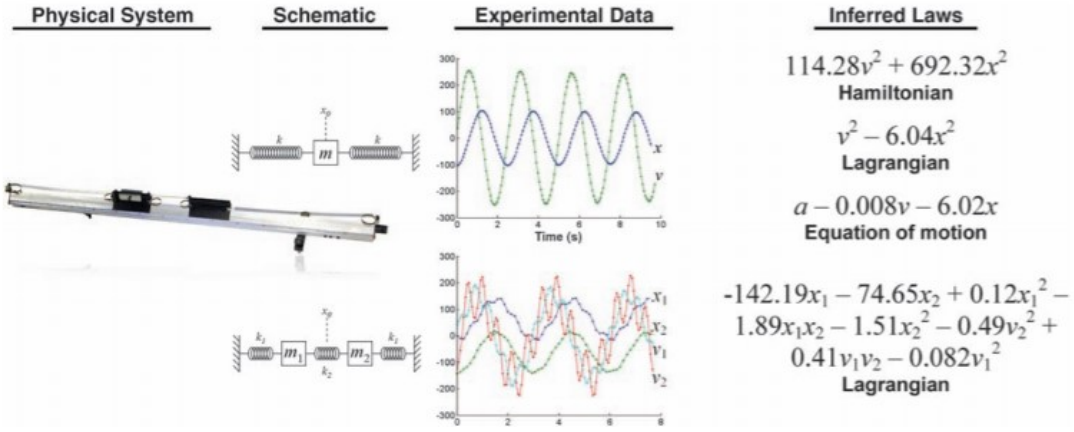

Figure 2.3: Inferred laws from experimental data generated by physical systems [Schmidt and Lipson, 2009]

find that induction trees can bias the search in potential solutions through EMO [Kalles and Papagelis, 2010] [Secretan et al., 2011]. Concluding remarks are made reaffirming that although novel solutions can be found through evolutionary algorithms, they are highly resource-intensive. It is suggested that parallel computation for characterization of members speed evolution, and are proposed as the most common method to support this method of heuristics [Cantú-Paz, 2001] [Van Veldhuizen et al., 2003]. Applicability of EMO's for aerospace applications are outlined by [Arias-Montano et al., 2012b]. Arias discusses the current necessity to validate EMOs within the fields of aeronautics and astronautics due to aerospace design redundancy. Driven by necessary factors of safety, the work urges that while EMOs are highly useful for the multi-objective optimizations present in many aerospace applications, progress must be made for proving that solutions are optimal and improved. This urges the current requirement and opportunity for a platform demonstrating the fitness of specimens [Yao, 1999] undergoing multi-objective evolution through physical validation within the field of aerospace [Wang et al., 2002] [Arias-Montano et al., 2012a].

2.4.2 Automated Testing

The increasing automation of testing protocols for both digital and physical implementations has been historically driven from a cost-saving perspective for detecting defects and managing logistics [Hoffman, 1999] [Albus et al., 1983]. As per [Thummalapenta et al., 2012], the automation of testing promises to disrupt the rate at which correlative insights are made through data generated through automated testing.

By allowing observations through conducted tests to drive the method in which tests are themselves implemented, the applicability of AI-driven validation will evolve into roles otherwise impractical to implement [Endres et al., 1998, Vogel-Heuser et al., 2015]. As per [Mao et al., 2017], much of the development of automated testing has been conducted within the fields of software development for optimized deployment within development protocols [Kehoe et al., 2015, Iqbal et al., 2015].

Strategies for deploying these methodologies within cyberphysical systems has recently increased in importance as hardware deployment and localized computing capabilities increase in performance [Winkler and Biffl, 2012] [Garcia et al., 2018] [Vogel-Heuser et al., 2015]. The shifting requisites for industrial automation applications are contingent on the development of strategies for overcoming complexities caused by hardware errors introduced by software [Hametner et al., 2011]. Hametner suggest implementing semi-autonomous systems for automated derivations of tests. Winkler suggests that a protocol for implementing automated multi-variable quality assurance lies within the hierarchy of testing. Figure 2.4 demonstrates that by regulating the levels and output flow of observations, one may test across multiple variables and integrate tests as a function of technical system design [Winkler and Biffl, 2012].

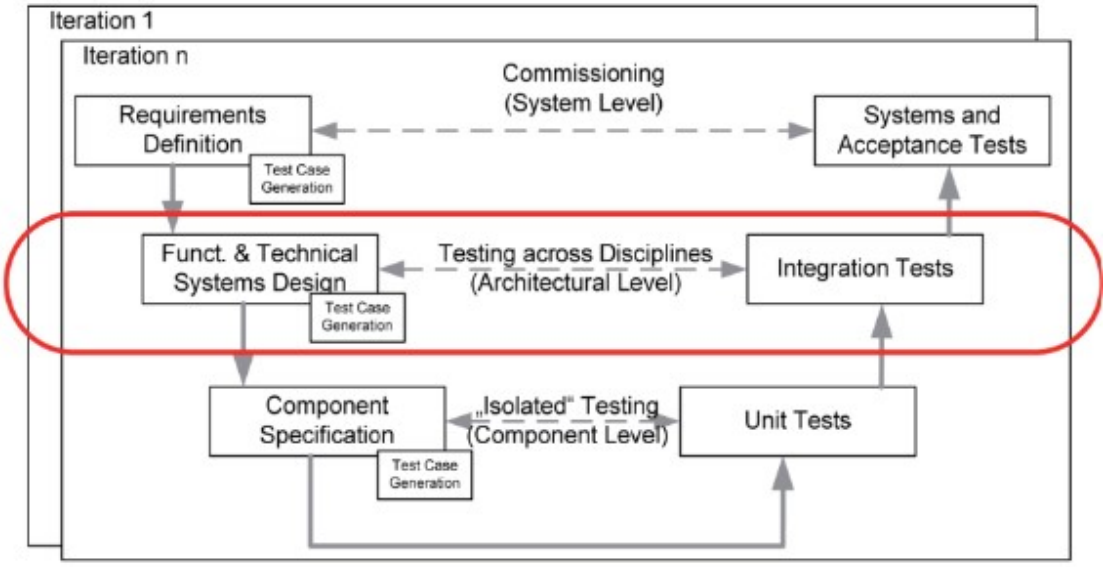

Figure 2.4: Automation of Testing Across Disciplines As a Function of Hierarchy [Winkler and Biffl, 2012]

Increasing research is being conducted within the fields supporting industrial automation [Grau et al., 2017] by adopting capabilities such as automated sensing [Wollschlaeger et al., 2017], assembly [Tellaeche et al., 2015], point-to-point mobilization [Wu et al., 2015], and machining [Prestes et al., 2016].

As seen in Figure 2.5, the number of active robots utilized within industrial applications has and is forecasted to continue increasing non-linearly as adoption of automated systems continues. Optimizing robots for the the design spaces they will serve has remained to be addressed, and argues for the necessity of a platform automating that process.

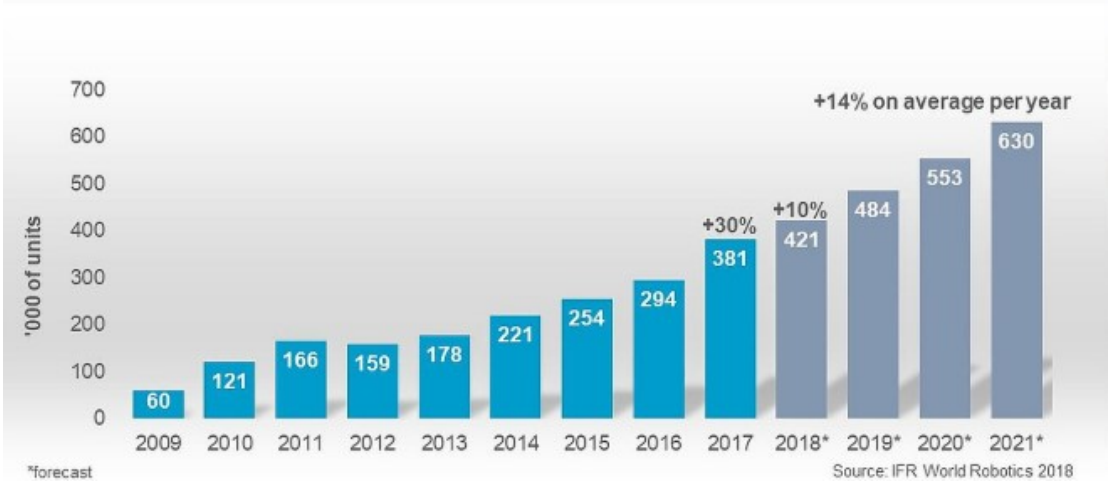

Figure 2.5: Number of deployed robots working in industrial applications [Heer, 2018]

Chapter 3

Augmenting the Additive Manufacturing Process to Enable Automation

Literature review sections 2.1 through 2.4 describe both the state-of-the-art and conventional techniques implemented in the fields of automated design, autonomous robots, aerostructures, adaptive manufacturing, performance sensing through computer vision, 4D printing, and high-volume testing.

This chapter will lay the foundation for the work that has been done over the past four years to develop ATCAM. The basis this section builds (1) The modeling and design of digital springs, (2) Automated programming and actuation of kinematic dimensions as a function of toolpathing by converging on the concepts of ISLS and ISA, and (3) The development of a repeatable, high-volume additive testing platform through ISA. The latter sections of this dissertation reference ISA as the method for ISD to create ATCAM and autonomous aircraft that fly off of the machine that built them. The specific deliverables can be described as

(4) The development of performance sensing and validation techniques for additive components manufactured and deployed in-situ, and (5) Characterization of autonomous aircraft capable of flying off of the build-platform.

As previously stated, the open-loop nature of an object's design cycle is relatively inefficient and cost-intensive. To further automate the cycle, I propose and demonstrate the integration of two important stages of an object's design cycle, fabrication and testing[Wong, 2012]. By developing an analogous system which creates an object and tests the component it has created autonomously, we can demonstrate that humans can be removed from these two stages of component engineering, reducing expenditures of human energy and other costs. An in-depth literature review has validated that the integration of these two stages of design have never been previously demonstrated with an additive manufacturing platform at the time of this document's writing.

Acknowledgements

The research and findings that are presented in this chapter were developed, consulted, and/or published with the following colleagues: Rachel Ticknor, Stanley Krzesniak, Sean Swei, Mircea Teodorescu, Daniel Cellucci, Alan Zhang, and Elizabeth Hyde. Additionally, portions of the content in this chapter were published and presented in IEEE/ASME's *Advanced Intelligent Mechatronics Conference 2020*. [Mazhari et al., 2020a]

3.1 Introduction

To develop an additively manufactured component that after fabrication would be automated to launch off of the machine that made it, I investigated various

methods to translate energy through fabricated components on the build-platform. From taking advantage of gravity by elevating the build platform, to storing internal stresses through varying the layer-by-layer geometry of the components fabricated, it was eventually determined that the most sustainable method to translate the electrical energy drawn from an additive machine into mechanical potential would be through the interaction of the physically-moving components within the manufacturing process.

3.1.1 Physical Realizations of Digital Kinematic Dimensions

In designing the mechanical interactions as an embedded dimensionality of the fabricated components themselves, one can remove the need for hardware modifications to translate mechanical potential for physical actuation. A novelty of this discovery is the ability to remove the necessity of introducing other processing stages by manufacturing the desired physical capabilities, in-situ.

In determining the necessary interactions required to transform electrical energy into mechanical potential, and subsequently into the thrust required for a projectile, the clearly non-linear translation can be broken into a series of linear systems for an investigation of given input variables for the observed output. This process was done partially to characterize the physical requirements necessary to actuate an object, and consequently define the additive platforms and materials required to demonstrate and validate the concept. A comparison of the hardware configurations of conventional additive manufacturing processes is demonstrated in Table 3.1.

Name	Additive Process	Materials (Ordered By Commonality)	Typical Moving Components
Fused Deposition Modeling	Thermoplastic	Polymers	Extrusion Head, Build Platform
Stereolithography,	Photosensitive Thermoset	Polymers, Ceramics	Laser, Build Platform, Resurfacing Tool
CLIP, Direct Light Projection	Photosensitive Thermoset	Polymers, Ceramics	Build Platform, Resurfacing Tool
Polyjet	Photosensitive Thermoset	Polymers	Jetting Head, Build Platform
Selective Laser Sintering / Melting, Electron Beam Melting, Laser Powderbed Fusion	Sintering / Melting	Metals, Polymers, Ceramics	Laser / Electron Beam, Leveling Roller, Powder Platform, Build Platform
Colorjet / Binderjetting	Adhesive Binding	Gypsum, Ceramics, Metals,	Jetting Head, Leveling Roller, Powder Platform, Build Platform

Table 3.1: A comparison of dynamic components over additive processes.

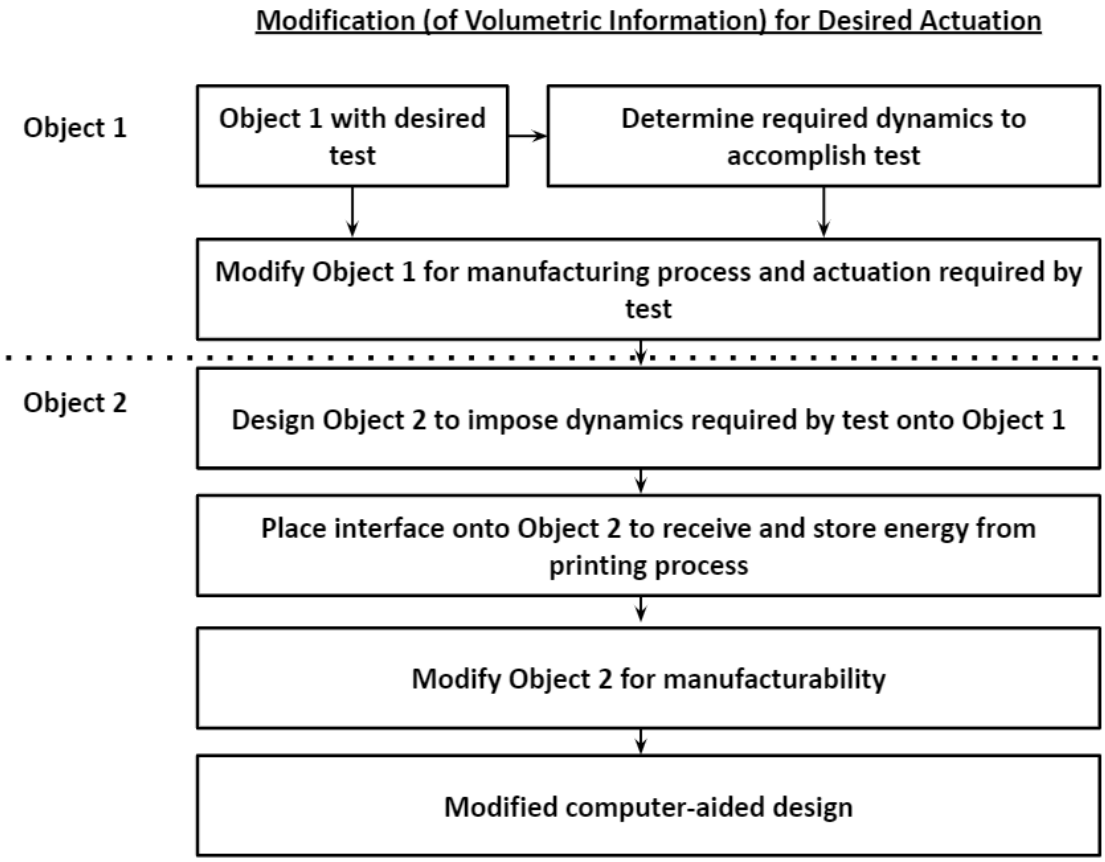

Figure 3.1: A Strategy for Modification of Volumetric Information for Desired Actuation. Object 1 and 2 reference the projectile and paddle, respectively.

3.1.2 Programming A Toolpath For Kinematic Interactions

To characterize and validate the physics embedded within fabricated components, a manufacturing process was utilized which utilized digitally-generated information within a build-file. This information would later be physically-relevant (with regards to its environment) within a serially-defined line of code within the same file. This programming is commonly referred to as '4D-Printing', with the fourth-dimension being a single external-to-manufacturing-process variable (such as time, temperature, humidity, etc.). Our process takes this a step further,

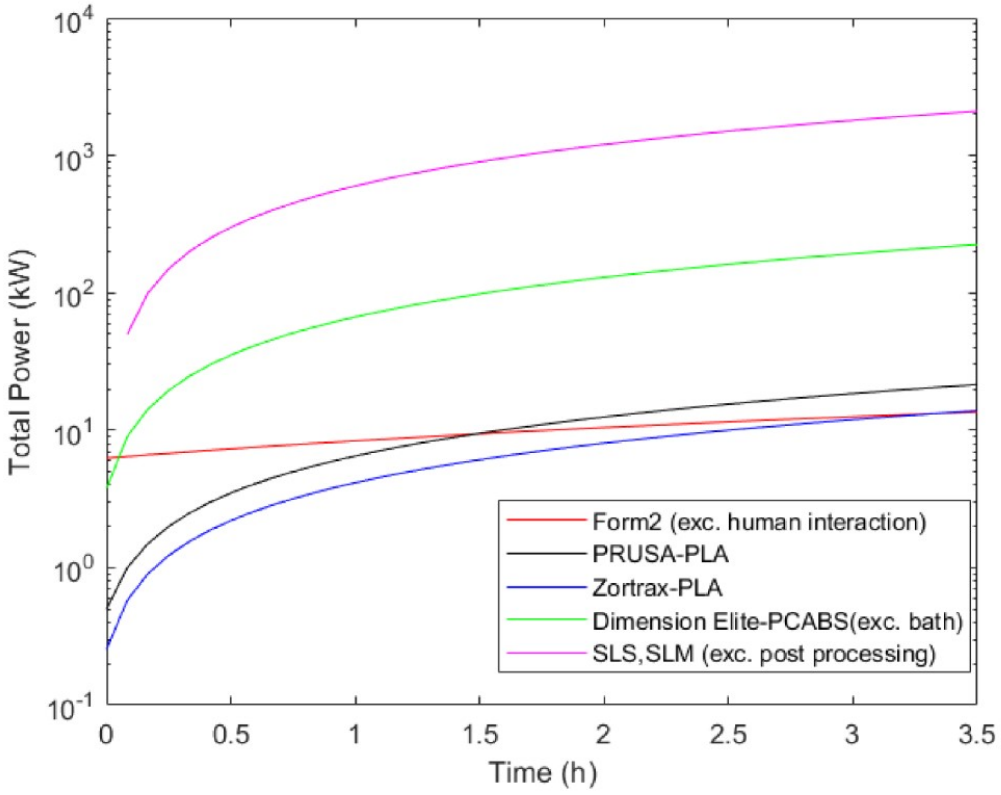

Figure 3.2: A comparison of additive processes with respect to total power consumption over print time

by embedding physical information that would autonomously enable kinematics and object validation through physical testing. By designing to-be-printed components with respect to material and manufacturing-specific variables such as specific-stiffness and Young's modulus, and cleverly utilizing the building process to enable physically-embedded information, the system is able to excite objects into new modes autonomously.

To change the mode of a fabricated object, physical mechanisms were embedded in the layer-design to be physically-actuated at a later point of the manufacturing process. We printed a sphere, with the intention of autonomously launching it off of the platform as part of the manufacturing process, without

human-intervention.

An investigation was conducted regarding the transfer of energy from an additive manufacturing gantry nozzle into an object the platform has fabricated by exciting a linear spring it creates and displaces. The spring's actuation transfers elastic energy into a simultaneously fabricated sphere via projectile motion, which are described and analyzed through Finite Elemental Analysis (FEA) and confirmed through numerical analysis with linearized equations of motion.

A catapulting linear spring was designed to be printed simultaneous to the sphere. This spring was intended to be physically excited via cantilever elasticity. The end of this spring would be pushed by the FDM machine's material-extruding tip, novelly translating a xyz g-code vector coordinate into elastic bending of the printed gate. This process transfers kinetic energy from the FDM machine's moving nozzle into potential energy stored elastically by the spring. The lever on which the FDM nozzle pushes upon was specifically tapered to actuate at a certain deflection angle for the spring. At this angle, the object would detach itself from the FDM nozzle, generating a pendulum which would physically contact the printed sphere with the purpose of transferring momentum. The fabricated ball is launched with respect to programmed collision-based physics, whose difference to calculated values allow the characterization of a design through automated manufacturing and testing.

The spring was iterated numerous times as we converged to a system that would detach from its static manufacturing mode, while still storing sufficient energy to launch an independent yet simultaneously fabricated object. We may characterize the theoretical elastic strain energy of our spring as a function of a point load provided by the FDM nozzle onto the cantilevered beam.

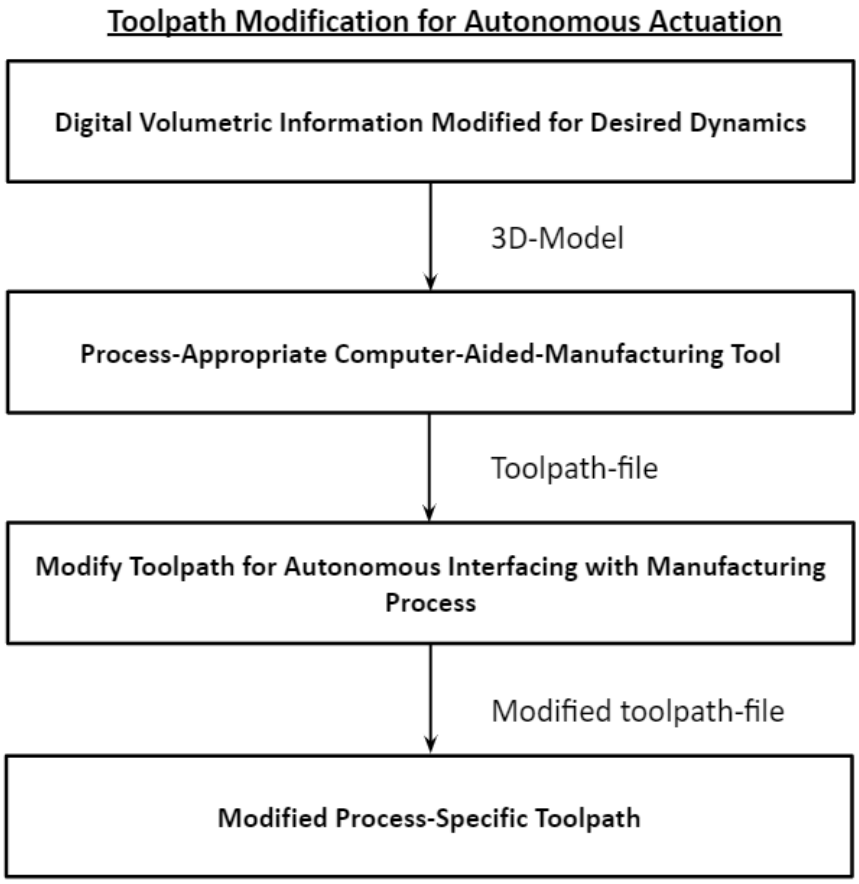

Figure 3.3: A Method to Modify the Toolpath of a Manufactured Object For Autonomous Actuation

3.1.3 Designing a Model

I proposed, converged, and compared the response of two representative models for an investigation of the design space through numerical methods.

The first representation was built upon the linearized spring-mass system derived above, tracing constraints from manufacturing-specific considerations with projectile equations of motion. The latter was conducted by isolating the relevant physics into two sub-models that would interact with one another. The first model consequently defines the interaction of the fabrication nozzle with the fabricated spring to embed potential mechanical energy into the system. The second model

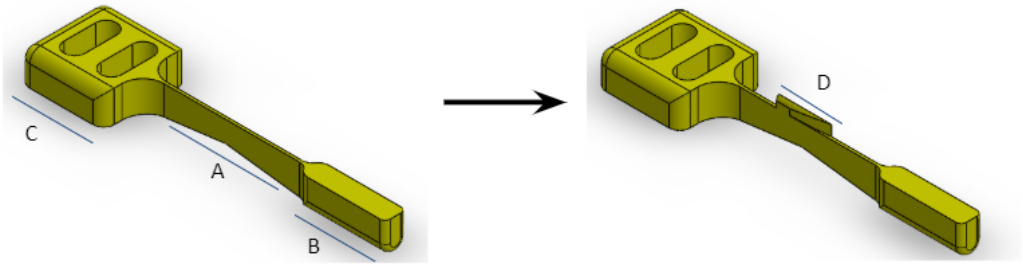

Example of Embedded Information

Description of referenced features:
Feature A stores elastic potential energy through a linear spring. B provides a contact area with to impose force onto Object 1 through conservation of momentum. C allows for the manufacturability of Object 2 by providing a large surface area to transfer the angular momentum caused through features A & B.

Example of Embedded Automation

Description of referenced features:
Feature D provides an interface between Object 2 and the 3D printer. This lever allows for the 3D printer's nozzle to pull on the lever, storing potential energy. The taper causes slip, novelly releasing the spring at a predetermined angle.

Figure 3.4: Examples of embedded information within deployer

demonstrates the kinematics of the spring contacting and catapulting the sphere manufactured within its proximity.

The second representation of the system is also divided into two separate interactions for the same reasons mentioned above. The differences are with respect to the method in which potential energy is embedded into the objects on the build-platform, and the considerations and assumptions characterizing the system. The first interaction represents a deforming cantilever beam driven by manufacturing variables and constraints, transferring strain energy to a sphere through an impulsed contact. The sphere's flight is characterized by a mixture of manufacturing-specific variables, such as normalized build-plate adhesion forces and a ballistic coefficient driven by the manufacturability of a sphere through FFF.

Nozzle-Spring Model

The interaction of the nozzle and spring can be considered as implicitly nonlinear, with [Armero and Romero, 2001] describing elasticity related to the bending of the spring. The order of this system can be reduced by assuming the spring to be a beam with an applied torque [Phillips and Costello, 1972]. One may further simplify this model by considering the torque as a point force applied on a mass connected to a linear spring, as demonstrated in Figure 3.5.

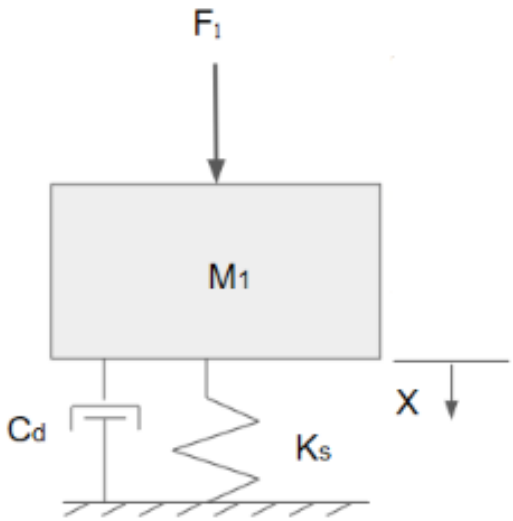

Figure 3.5: Free Body Diagram of Linearized Spring

In our model, the point-force F_1 is analogous to the nozzle pulling the mass M_1 connected to the spring K_S a distance of X with a damping coefficient of C_d. We take the assumptions that normalized friction forces are linear, and that aerodynamic drag and adhesion forces are consolidated into the damping coefficient of the spring.

To reduce the order of the system for insights to the underlying physics, we can investigate the state space:

$$\begin{bmatrix} M & 0 & 0 & 0 & \dots & 0 \\ 0 & M & 0 & 0 & \dots & 0 \\ 0 & 0 & M & 0 & \dots & 0 \\ \vdots & \vdots & \vdots & \vdots & \ddots & \vdots \\ 0 & 0 & 0 & 0 & \dots & M \end{bmatrix} \begin{bmatrix} \ddot{x_1} \\ \ddot{x_2} \\ \ddot{x_3} \\ \vdots \\ \ddots x_m \end{bmatrix} + \begin{bmatrix} -2c & c & 0 & 0 & \dots & 0 \\ c & -2c & c & 0 & \dots & 0 \\ 0 & c & -2c & c & \dots & 0 \\ \vdots & \vdots & \vdots & \vdots & \ddots & \vdots \\ 0 & 0 & 0 & 0 & \dots & c \end{bmatrix} \begin{bmatrix} \dot{x_1} \\ \dot{x_2} \\ \dot{x_3} \\ \vdots \\ \dots x_m \end{bmatrix} + \begin{bmatrix} -2k & k & 0 & 0 & \dots & 0 \\ k & -2k & k & 0 & \dots & 0 \\ 0 & k & -2k & k & \dots & 0 \\ \vdots & \vdots & \vdots & \vdots & \ddots & \vdots \\ 0 & 0 & 0 & 0 & \dots & k \end{bmatrix} \begin{bmatrix} x_1 \\ x_2 \\ x_3 \\ \vdots \\ x_m \end{bmatrix} = \begin{bmatrix} u_1 \\ u_2 \\ u_3 \\ \vdots \\ u_m \end{bmatrix} \tag{3.1}$$

This results in the system of equations

$$\begin{aligned} \dot{x} &= Ax + Bu \\ y &= Hx \end{aligned} \tag{3.2}$$

As we previously inferred,

$$A = \begin{bmatrix} 0 & I \\ -M^{-1}K & -M^{-1}C \end{bmatrix}, B = \begin{bmatrix} 0 \\ M^{-1} \end{bmatrix}, H = I \tag{3.3}$$

The resulting motion can be described by the second-order ordinary differential equation (ODE) in Equation 3.4:

$$M_1\ddot{x} + C_d\dot{x} + K_s x = F_1 \tag{3.4}$$

We may subsequently linearize this kinematic equation by reducing the order of

the ODE through substitution of the state variable, as demonstrated in Equation 3.5:

$$\dot{x_1} = x_2(t) \tag{3.5}$$

Leaving a reduced-order ODE for the state mass-damper system in Equation 3.6:

$$M_1\dot{x_2} + C_d x_2 + K_s x_1 = F_1 \tag{3.6}$$

Taking manufacturability with respect to FDM provided insight to optimized values that would allows for the overlap between generated thrust, contact mechanics, minimum feature sizes for specific layer-requisites, manufacturing time, and the quantitative surface area requirements.

3.1.4 Manufacturing for Mechanical Potential

From analyzing and weighing the various additive processes in Table 1 against one another, methods of translating energy were investigated with respect to the moving components of each manufacturing process. The rationale behind this bounding factor is to limit the translation of mechanical potential purely through physical movement. This allows for the relatively simple spatial actuation of the fabricated components through non-chemical, non-thermal processes. Although processed thermosets intrinsically allow for the thermal and photo-manipulation of fabricated objects post-cure, the postprocessing required to attain a state of physical conformance was deemed to be not self-contained or easily designed-for.

The ability to actuate a fabricated component purely through a physical toolpath allows for the implementation of well-defined translating mechanical features, such as springs and levers. Removing the additive processes that have

limited capacity for spatial interactions on their build platform directly after fabrication refines the list to just FDM. As a process whose post-processing stages are driven by the detaching of any generated (gravity-relevant) support structure and physical removal of the component from its build tray, FDM was deemed as the most favorable process at the time of this publication for automated translation of mechanical energy through an additive build-volume. Additionally, the physical necessity for component support structure was removed from the process purely through design-for-manufacturing methodology, as demonstrated in [Thrimurthulu et al., 2004] and [Attaran, 2017].

3.1.5 System Development and Characterization

The problem of integrating fabrication and testing is the highly-nonlinear aspect of the multiple forms of physics required to do such a process. This complexity can be illustrated by observing the transfer of the electrical energy from a high-voltage source, into a series of motors which convert the energy for fabrication and subsequent physical interaction for testing. By developing relevant models of each stage and solving them through numerical methods, we can relate the behavior of kinematic models to physical observations. The differences of values obtained by these methods can provide insight into the validity of the implied system characterization and methods utilized.

3.1.6 Defining the Analogous System

As defined above, the driving constraint was to fabricate the ability to launch an object off of the manufacturing build-platform. For increased simplicity and the ability to more-easily relate the kinematics with respect to well-defined projectile motion, it was determined that the launched projectile would be spherical. By

placing this constraint, the sizing consideration was consequently conducted with respect to the amount of thrust required to propel a sphere off of the build-platform after its fabrication. Although the manufacturability of a sphere through FDM is conventionally well-defined, the complexity of the problem became evident when I considered that the component would need to be static during the manufacturing process, but be easily launched afterwards. As a control, the sphere was designed to have a one-inch diameter.

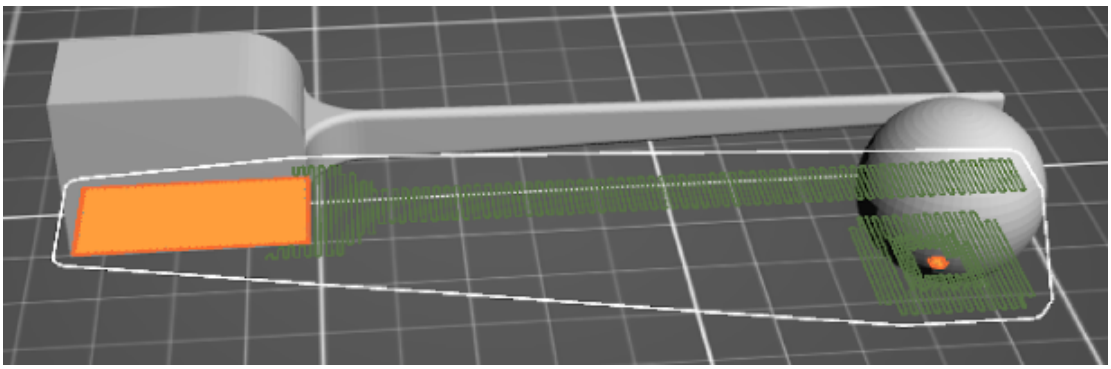

Figure 3.6: Proposed System Configuration

To integrate the mentioned stages, I proposed the analysis of two objects fabricated onto the same stage. The first object would be a test-specimen, intended to characterize the fabricated system by providing insights through exposure of kinematic physics and aerodynamics. This component would be catapulted by a simultaneously manufactured second object. The second object would translate energy from the manufacturing system into potential energy required to actuate the second object. The proposed system configuration is demonstrated in Figure 3.6.

The two objects can be classified as a torsional cantilever spring and a sphere, respectively. Realizing this configuration relies on the convention of FFF, leveraging the printing process which deposits layers of thermoplastic through a heated nozzle via a stepper motor mounted on a gantry [Ahn et al., 2002]. In our imple-

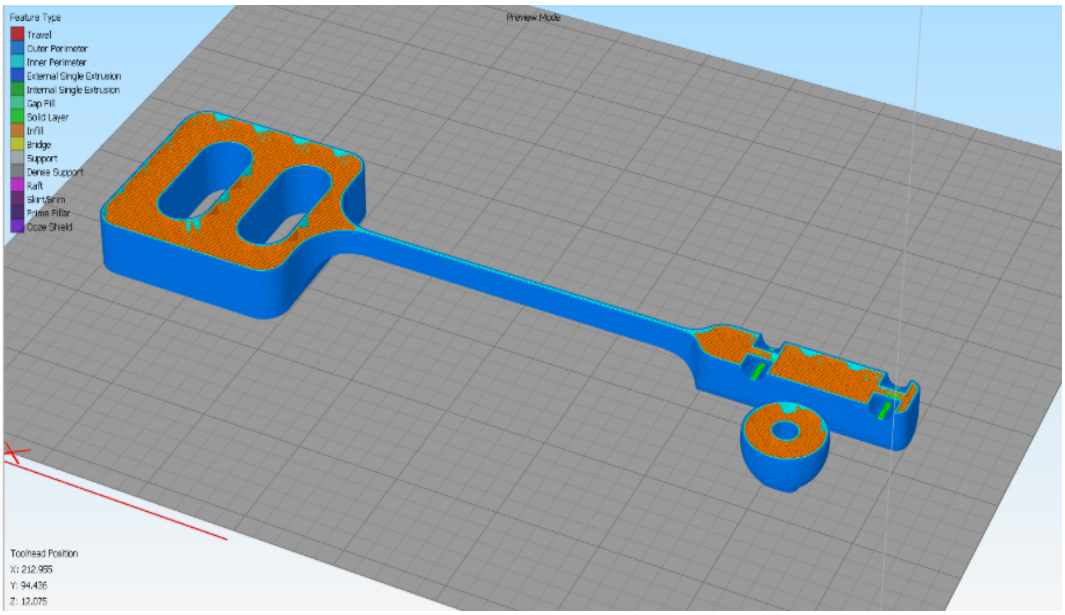

(a) Demonstration of process-specific deployer toolpathing methodology implemented for FFF

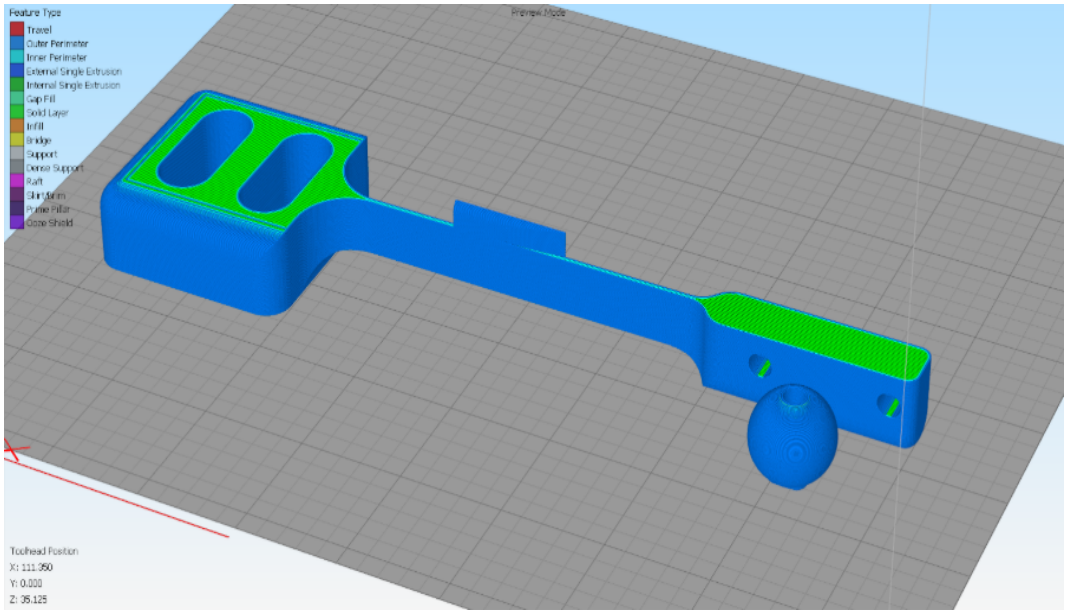

(b) Completion of toolpath resulting in nozzle placement at deployer lever

Figure 3.7: Bridging Technique for Deployer

mentation, the nozzle would build the spring and sphere simultaneously. Once the objects are fully fabricated, the nozzle would traverse towards the spring, pulling

a lever designed to deflect the spring.

At a prescribed angle, the nozzle would release from the spring. This release simultaneously allows the embedded elastic potential energy to head towards equilibrium, contacting the sphere in front of the object. The conservation of momentum from the spring would then theoretically launch the sphere off of the build-platform, allowing for the object to provide useful aerodynamic data to complement the system characterization and implied physics of the component through projectile motion. This portion of the system is demonstrated in Figure 3.8, with the the arrows demonstrating the dynamic trajectory of motion.

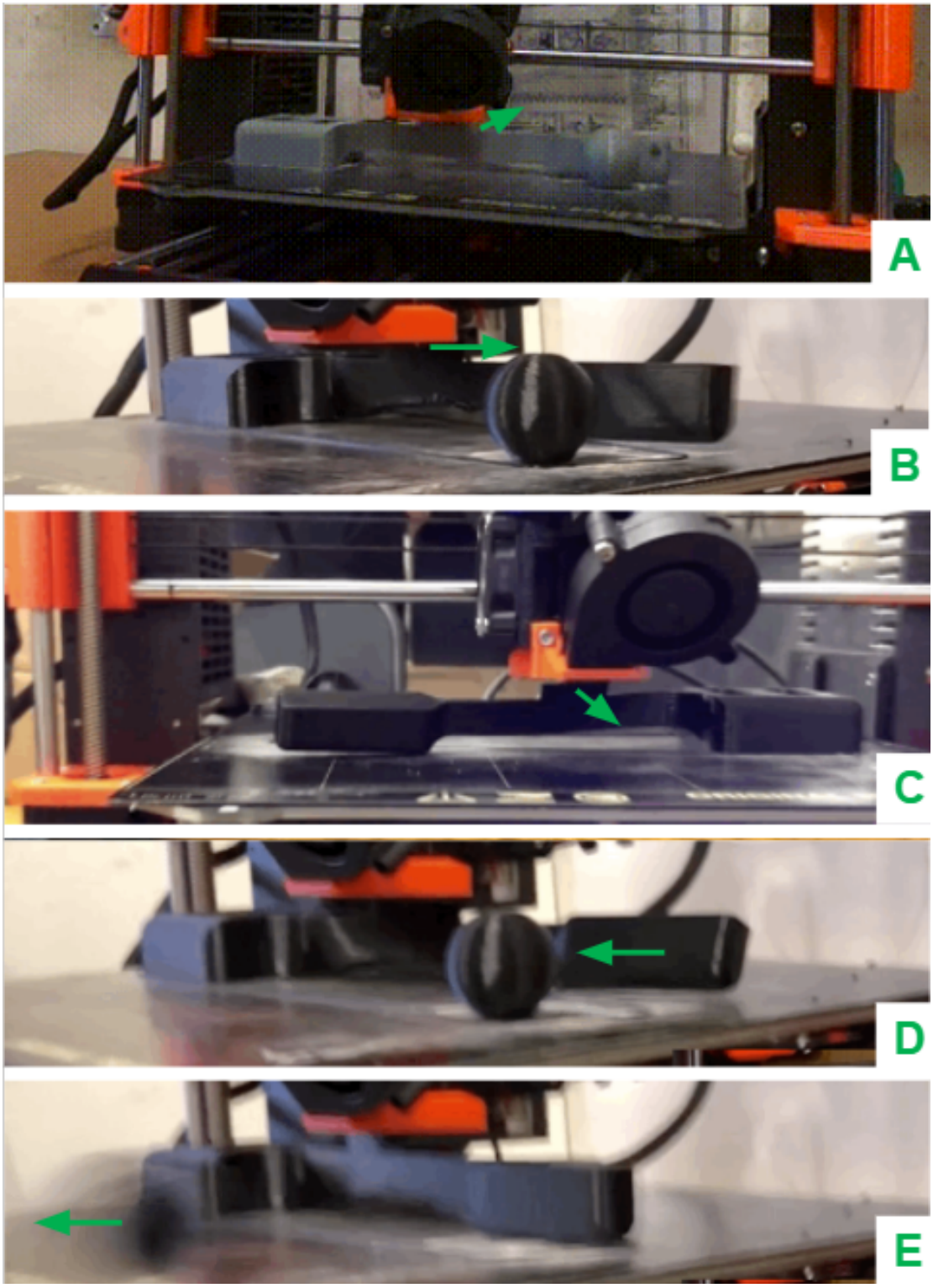

Figure 3.8: Spring-Ball Interaction, Visualizing the Projectile Motion Chronologically

3.1.7 Prototyping to Investigate the Design Space

For increased simplicity and the ability to define the kinematics through observations related with projectile motion, it was determined that the target projectile would be spherical. To constrain the spring's variables, sizing considerations were primarily conducted with respect to the amount of thrust required to consistently propel a sphere off of the build-platform. The manufacturability of a sphere through FFF is conventionally well-defined, however the complexity of the problem became evident when I considered that component would need to be static during the manufacturing process, but be easily launched afterwards. As a control, the sphere was designed to have a one-inch diameter.

Iterating the sphere for both optimized contact area with the build-plate and logistical manufacturing efficiency provided a ball with medium-density rectangular fill at 5.1 grams of weight. To constrain the problem, a desired velocity of 10 meters / second at an acceleration of 1 meters / square second was defined. This drove the thrust requirements for the object to be roughly .005 Newtons. It was determined that the thrust would be physically imposed onto the object through conservation of momentum from a separate object.

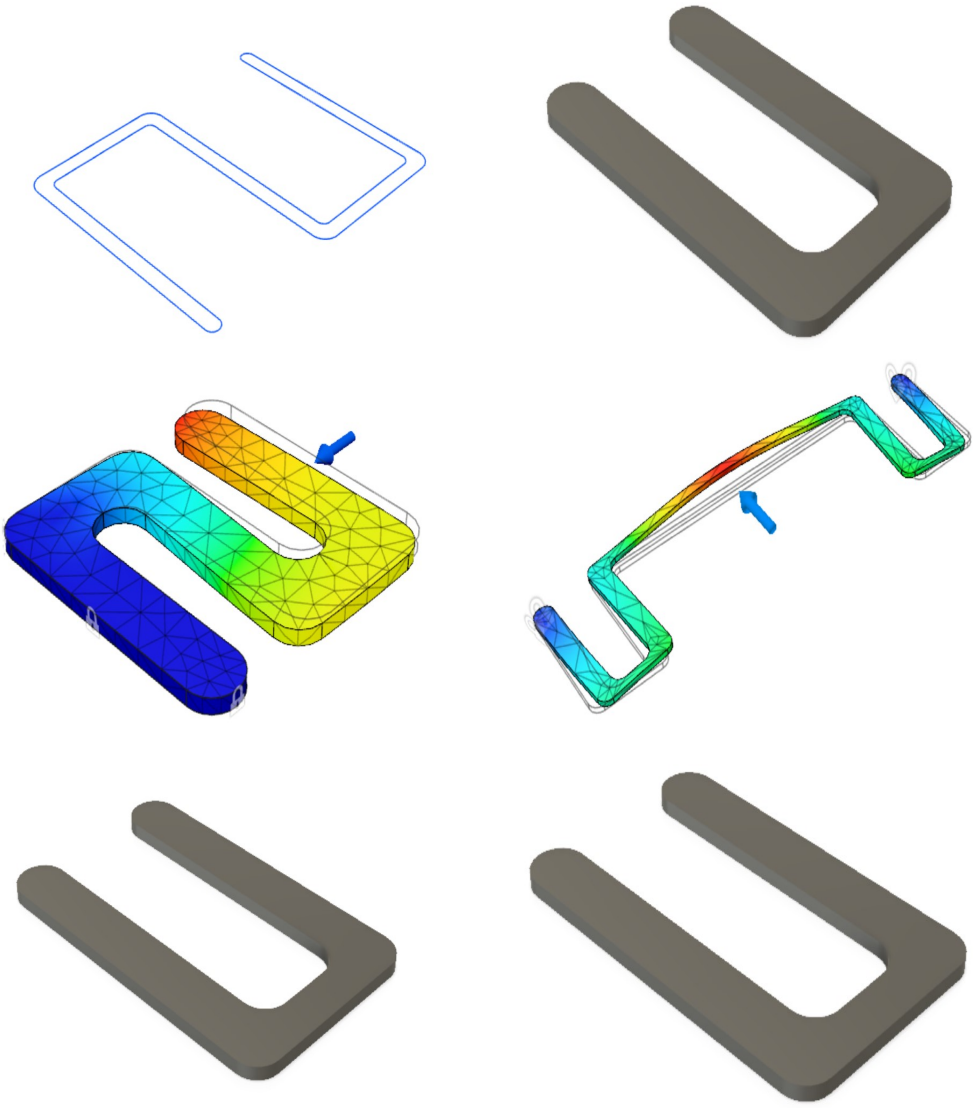

Figure 3.9: Investigation of spring functionality

3.2 A Solution for Repeatable, High-Volume Testing

3.2.1 Introduction

An investigation was conducted on various methods for in-situ mechanical actuation with respect to manufacturability. To store potential energy mechanically, I bound the design space to a system which could physically compress to elastically store energy. By designing a spring system specifically tailored for interaction with and compression from the manufacturing process which made it, one can fabricate and enable the novel ability for a machine to store different forms of mechanical potential without hardware modifications. To sustainably manufacture an elastic spring which could maintain one end of its position on the build-platform, while having the ability to partially deform meant carefully-tailored design-for-manufacturing considerations. Literature reviews for linear elastic gates provided a fundamental basis for an initial approach to solving this problem. As the material considerations were defined by the intrinsically-defined manufacturing constraints, Finite-Elemental-Analysis (FEA) was able to be utilized for quickly iterating a vast array of designs. Through the rapid iteration of 3D models with respect to conducted Von-Mises stress calculations, and observed deformations and deflections, I proposed and converged on a tailored spring-mass system. A novelty of this solution is the ability to characterize the state-space with the well-defined spring-mass-damper system. Furthermore, the sizing of a spring-mass-damper could be conducted through numerical methods, allowing for a design study between required and realizable-through-manufacturing deflection and physically-observed damping. Although such a design approach is typically highly error-prone due to the effects quasi-isotropic additive manufacturing has

on physical objects, the ability to rapidly iterate and physically validate designs allows for the tuning of the system's state-space for manufacturing.

3.2.2 Designing The Repeatable Transfer of Mechanical Energy Through Manufacturing

The feasibility of both generating and manufacturing a spring that exhibits desired mechanical characteristics additively proved to be a complex challenge. The theoretical equations were linearized for correlative insights to specific manufacturing variability within the design space. This unconventional methodology allowed for explicit correlations that a review of current literature suggests is relatively uncharted research. Through linearization, the spring mass damper system was described by its underlying principles. This principle defined the mass of the spring as a function of the tool-path the additive process follows through layer-based fusion.

An observation I noted was the validation of the connection between infill patterning and wall-thickness layering techniques to modified and highly-tuned spring rates, damping ratios, and stiffness through the quantity of and center of the spring's mass. By creating a linear, torsional spring whose center of mass was tailored to be located at its free-end, the spring's moment of inertia was desirably increased. Tuned to deflect four inches from equilibrium, the spring was observed to generate roughly .01 Newtons of force at four inches of deflection. To cancel the angular momentum, a base was generated which would provide a counter-moment to absorb the energy generated by the spring. The design consideration taken into the base was for manufacturing efficiency through reduced mass, while maintaining enough stability for the FDM process to be successful. The early evolution of this deploying mechanism is demonstrated in Figure 3.10.

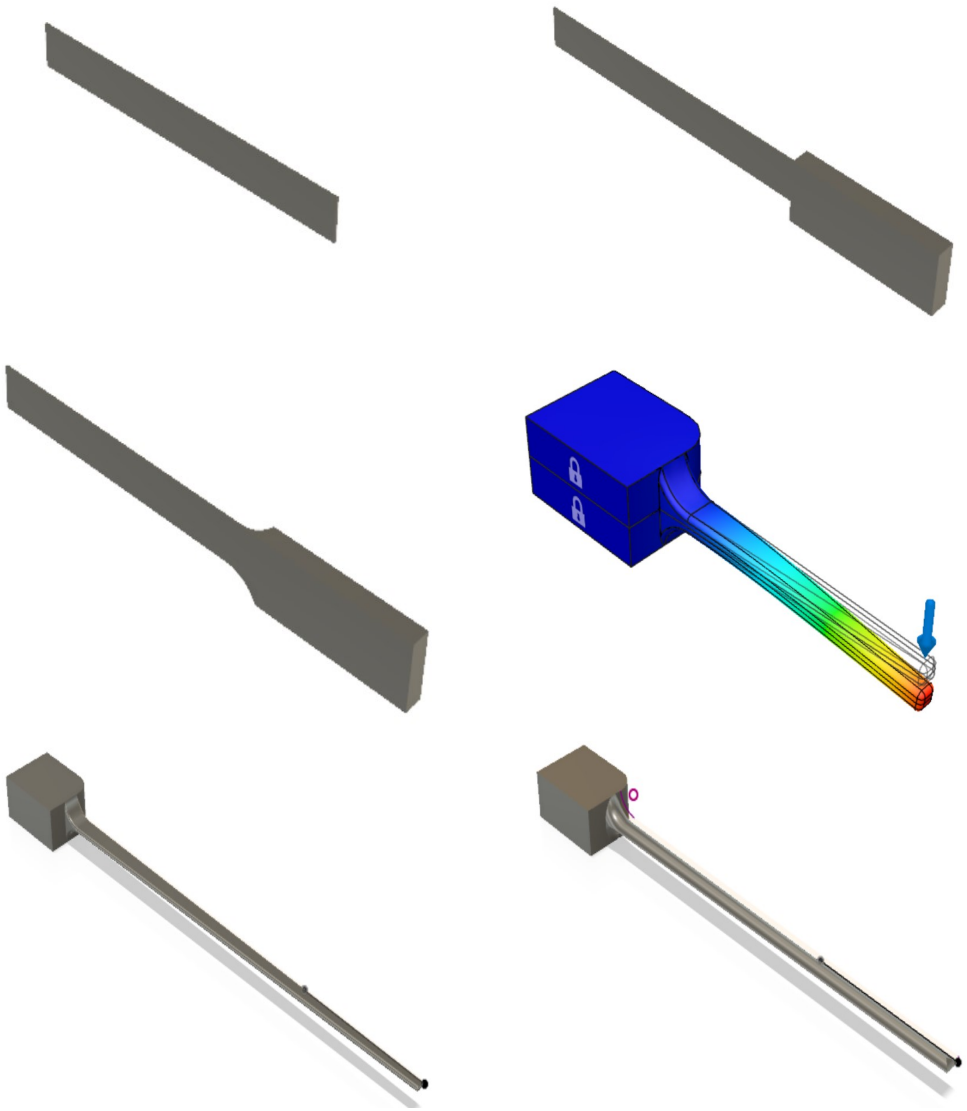

Figure 3.10: Early evolution of deployer, Gen: 1 - 6

Specific manufacturability considerations were taken with respect to the tool-pathing requirement of support structures [Fernandez-Vicente et al., 2015]. The slicer's automatic support-structure generating settings were not used; tailored design was leveraged for overhangs. Taking the .4mm FDM nozzle at a .2mm layer thickness, the theoretical maximum overhang angle threshold is 45 degrees

with respect to the conventional build-plane [Lensgraf and Mettu, 2016]. To generate the spring design observed in Figure 3.16, a toolpathing technique was utilized to aggressively cool material as the build-gantry quickly accelerates parallel to the build-plane. This process is commonly referred to as bridging, and serves as a relatively advanced design-for-additive technique [Dumas et al., 2014] [Volpato et al., 2014]

The base of the spring and the high moment of inertia through the pendulum design cleverly allow tapered starting and ending coordinates for the bridging, controlling the process through geometry. By radiusing the inner sections observed in Figure 3.16, the toolpath accelerates the bottom-most layer of the spring linearly, allowing for the solidification of the material between the two bases. The resulting effect generates a few layers of geometrical error, however this section proves stiff enough to fight gravity and support its own weight. After initially printing on air, the first few layers of the spring act as in-situ support structure, fighting gravity and allowing for the subsequent layers of the FDM process to sustainably take place with minimal error.

A comparative study was done to observe the effects of the bridging technique versus conventional support structure with respect to their effect on the realized spring constant. It was concluded that the effect on spring constant is negligible (due to the error-induced layers only consisting of a fraction of a single-digit percentage of the overall spring volume), and thus was a sustainable method for additively fabricating a linear torsional spring.

To allow the weighted-end of the spring to detach from the build-plate, a mixture of the model's tapering and radiusing was conducted near the initial base-layers of the print.

By implementing a high-aspect ratio torsional spring, the amount of surface

area in contact with the build-plate was minimal when compared to square or spherical compression springs. This design consideration proved highly advantageous, as it provided the ability to further reduce the contact area with the build plate through applying a variably filleted gradient.

It was found that on a conventional TPU build-tray, $.8mm^2$ of PLA contact area provided desirable build characteristics as a platform for maintaining stability of its subsequently fabricated layers, while releasing from the build-plate with minimal force when physically contacted. The resulting configuration served as the base for all surfaces which were required to be released when actuated by the printer.

To automate the actuation of the spring such that it would transfer energy to its neighboring component, a variety of methods were implemented. By designing a lever to be fabricated as a function of the spring, we attained the fundamental ability to interact with the FDM printing head. This head is easily controllable through g-code, and as such could be used to actuate and deflect the torsional spring. By placing the lever on top of the spring, physical contact would generate a moment which could detach the base of the weighted spring through the generated moment arm.

3.2.3 Design of Test Sphere

The sphere was designed employing many of the same conventions applied to the paddle. The primary considerations of the sphere were FFF manufacturability and optimization for collision with the paddle as a function of the toolpath. It was designed to be manufactured serially, after the fabrication of the paddle. This meant that the sphere needed to be fully additively fabricated without being impacted by its proximity to the paddle, but still be within its radius of motion

once actuated. Rapid prototyping methodology proved crucial to the iterative optimization of these constraints. After dozens of iterations, it arrived at the configuration demonstrated in Figure 3.18

3.2.4 Automating Object Deployment

Once a design was converged for the sphere with respect to the normal force acting on the object from the build-plate, the toolpathing considerations of FFF, and the deployer's kinematics, efforts were taken to standardize the process that was undertaken to optimize the design for deployment. The results are visualized in the algorithm demonstrated in Figure 3.3. By writing a script which replaces the base of an object with a geometry compatible for deploying off of the build-platform, the applicability of launching numerous objects was realizable.

The first approach for implementing this process was to demonstrate that a standardized base could be applied to the bottom of any object without removing any of the geometry existing within that object's volume. This is visualized in Figure 3.19. This concept is analogous to the generation of a tee platform used to maintain and elevate golf balls for contact with the club. Alteration was required due to the nature of FFF requiring a 45 degree overhang threshold for sustainable fabrication without toolpath acceleration and retraction requirements. The second iteration tapered the geometry with the deployable base for manufacturability, while keeping a second deployable base on the platform to be detached from the manufacturing platform, and the deployed object through momentum. The implementation for the deployed object is visualized in Figure 3.21.

Although the design was functional, the base was not reliably serving the function of maintaining stability for the object supports, deploying with the supported object, and detaching from the deployed object without interfering with

its dynamics once contacted.

While this iteration provided interesting and novel functionality for a manufacturing platform (a machine creating a sacrificial platform for launching an object off of itself), it was shelved due to variability caused in object deployment. The platform was too inconsistent for repeatable high-volume testing. Considerations were taken to alter the geometry of the deployed object itself by replacing a standardized section of layers off of the volume through a script which would input toolpathed layers as an automated digital post-processing technique for a given gantry code. By defining the design criteria for a deployed object to be within a certain range, we can create a range of automated deployments to maintain the repeatable aspect of the process. A visualization of this toolpathing process is demonstrated in Figure 3.19.

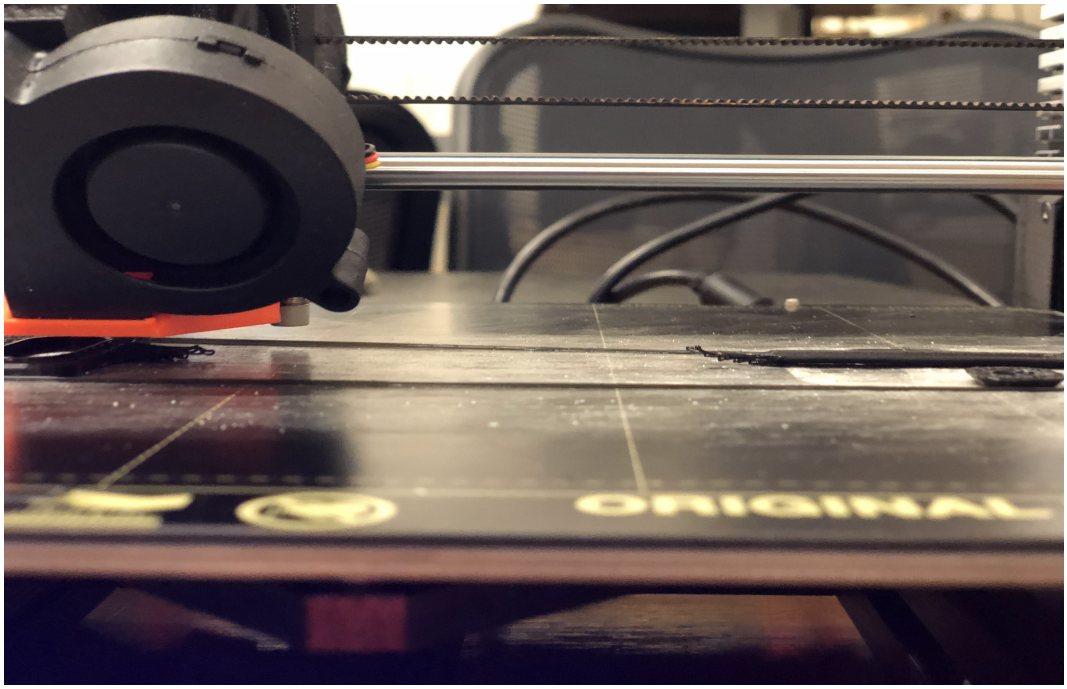

(a) Initial layers of thermoplastic solidification between base and paddle, removing the need for support structure generation

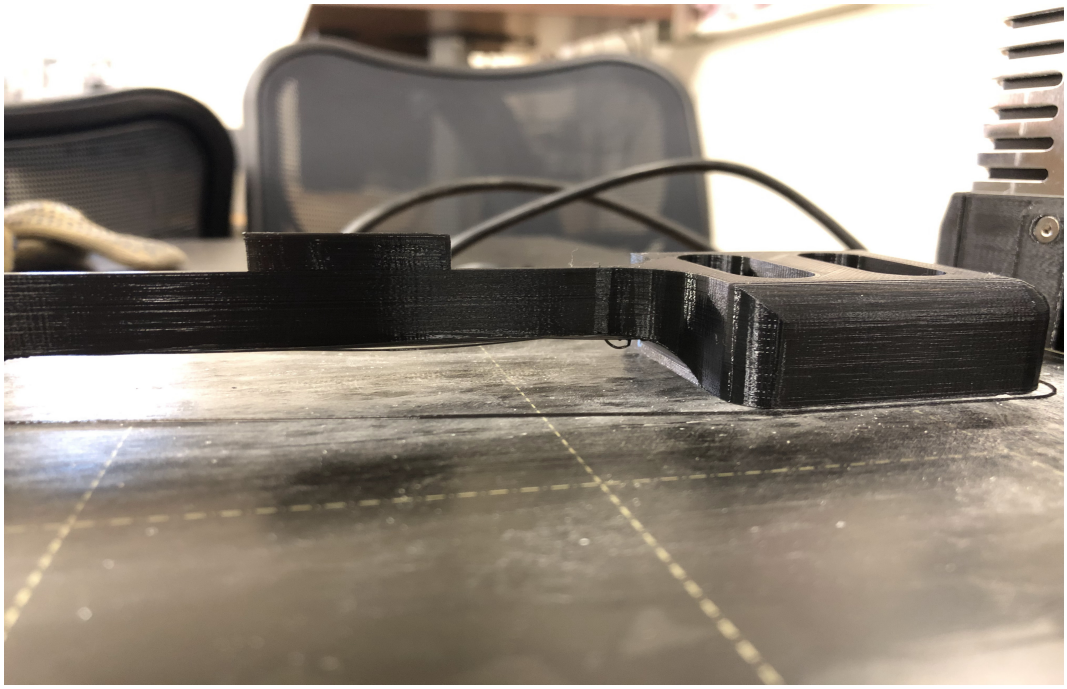

(b) Bridged layers, demonstrating only minor associated geometric errors arising from the lack of support structure.

Figure 3.11: Bridging Technique for Deployer

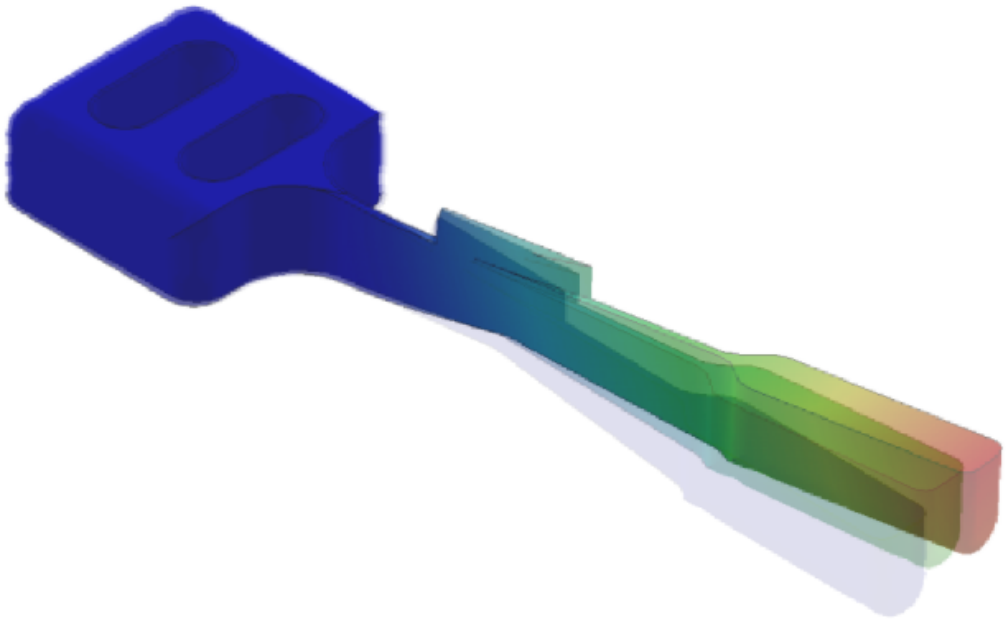

Figure 3.12: Visualization of Deployer Deflection Functionality

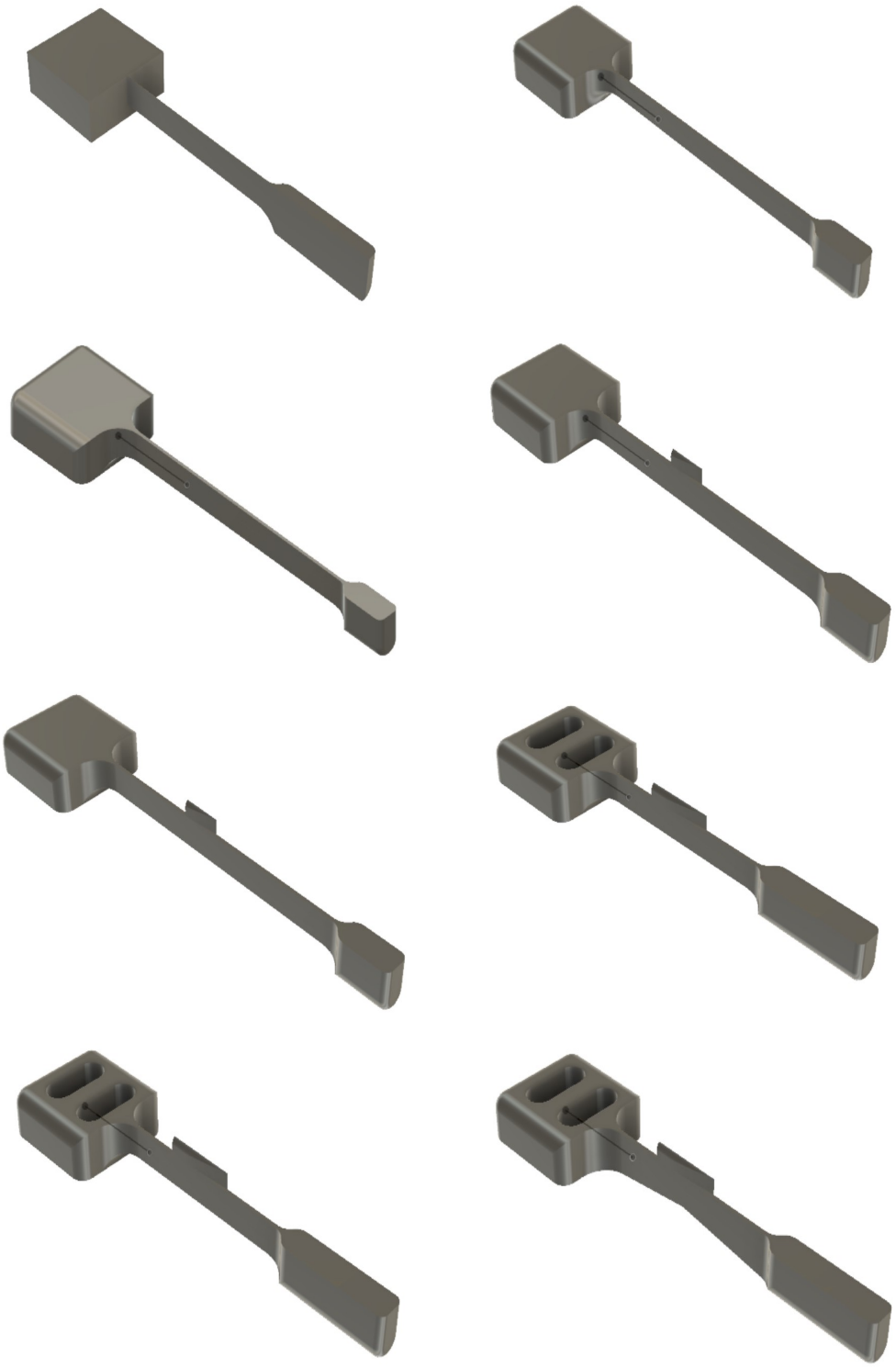

Figure 3.13: Evolution of Deployer, Gen: 7 - 14

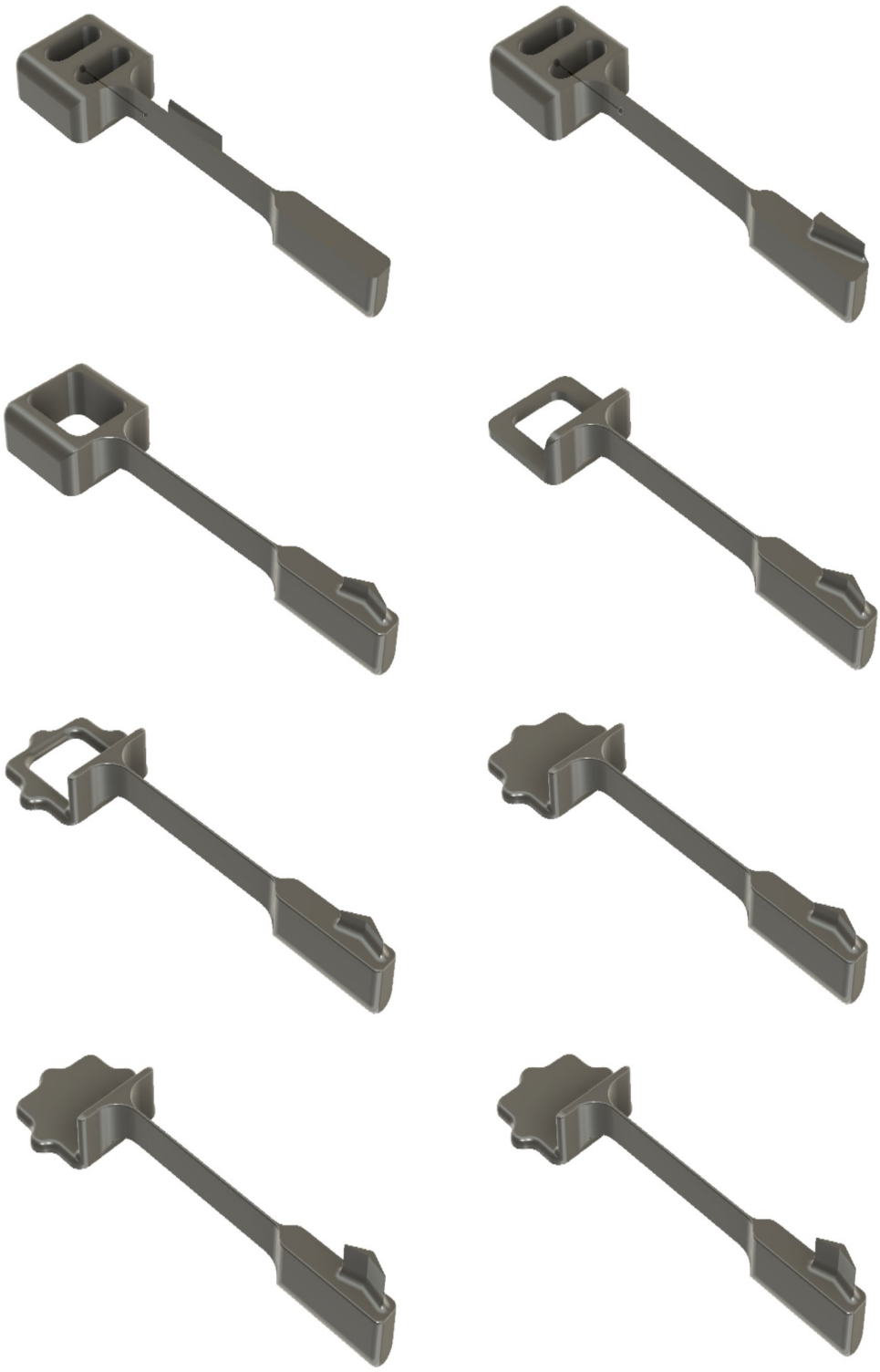

Figure 3.14: Evolution of Deployer, Gen: 15 - 22

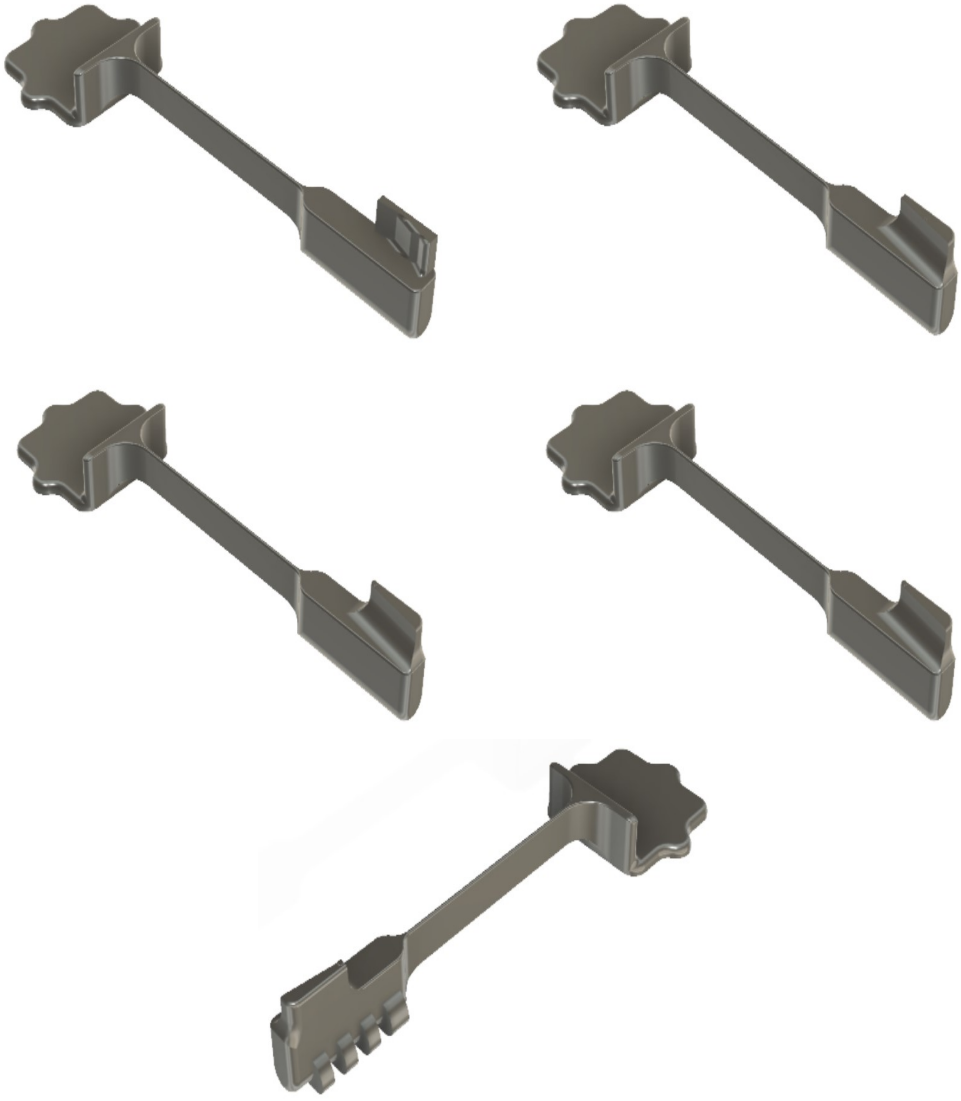

Figure 3.15: Evolution of Deployer, Gen: 23 - 27

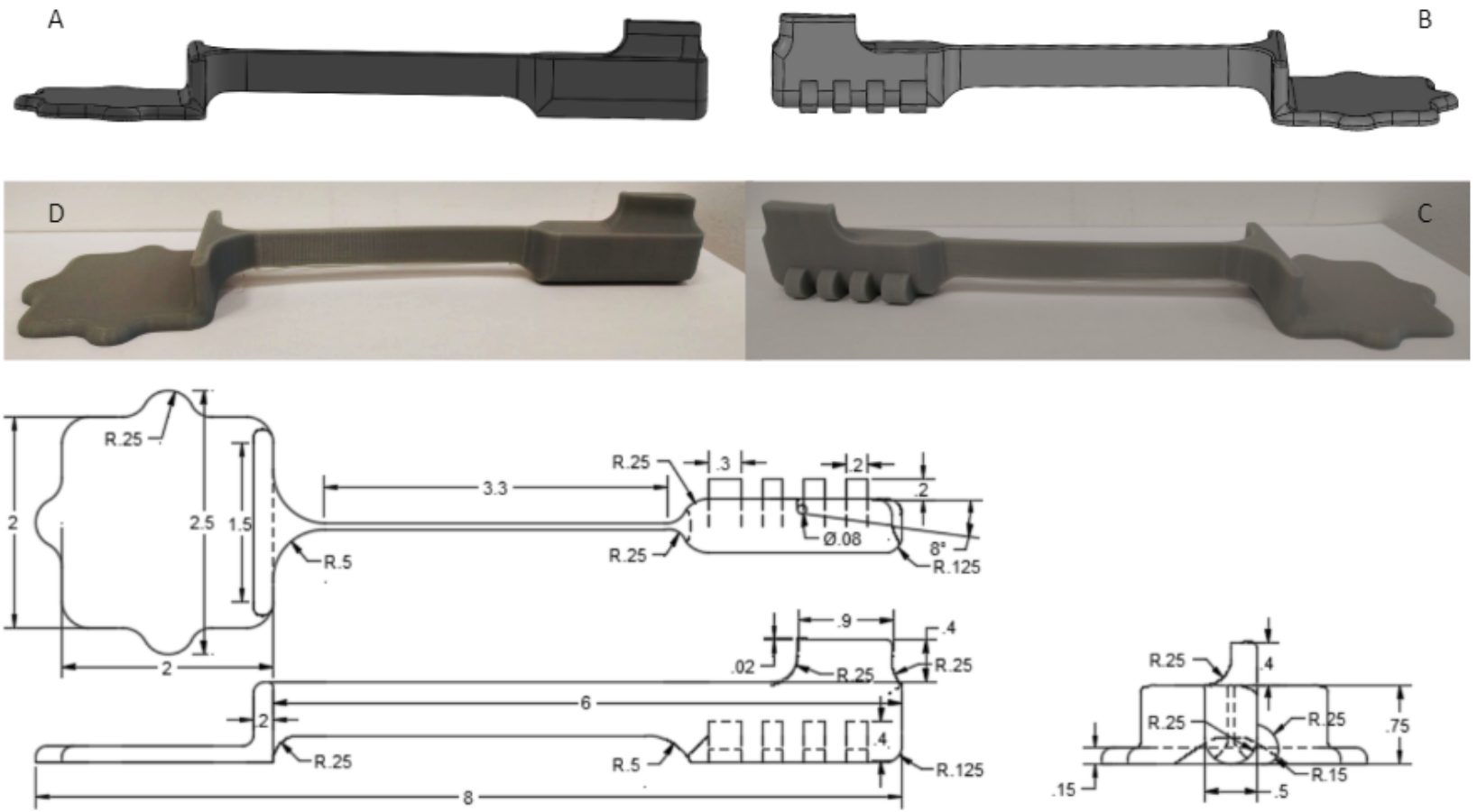

Figure 3.16: Dimensional description of paddle drawing in ASME Standard; all units are in inches.

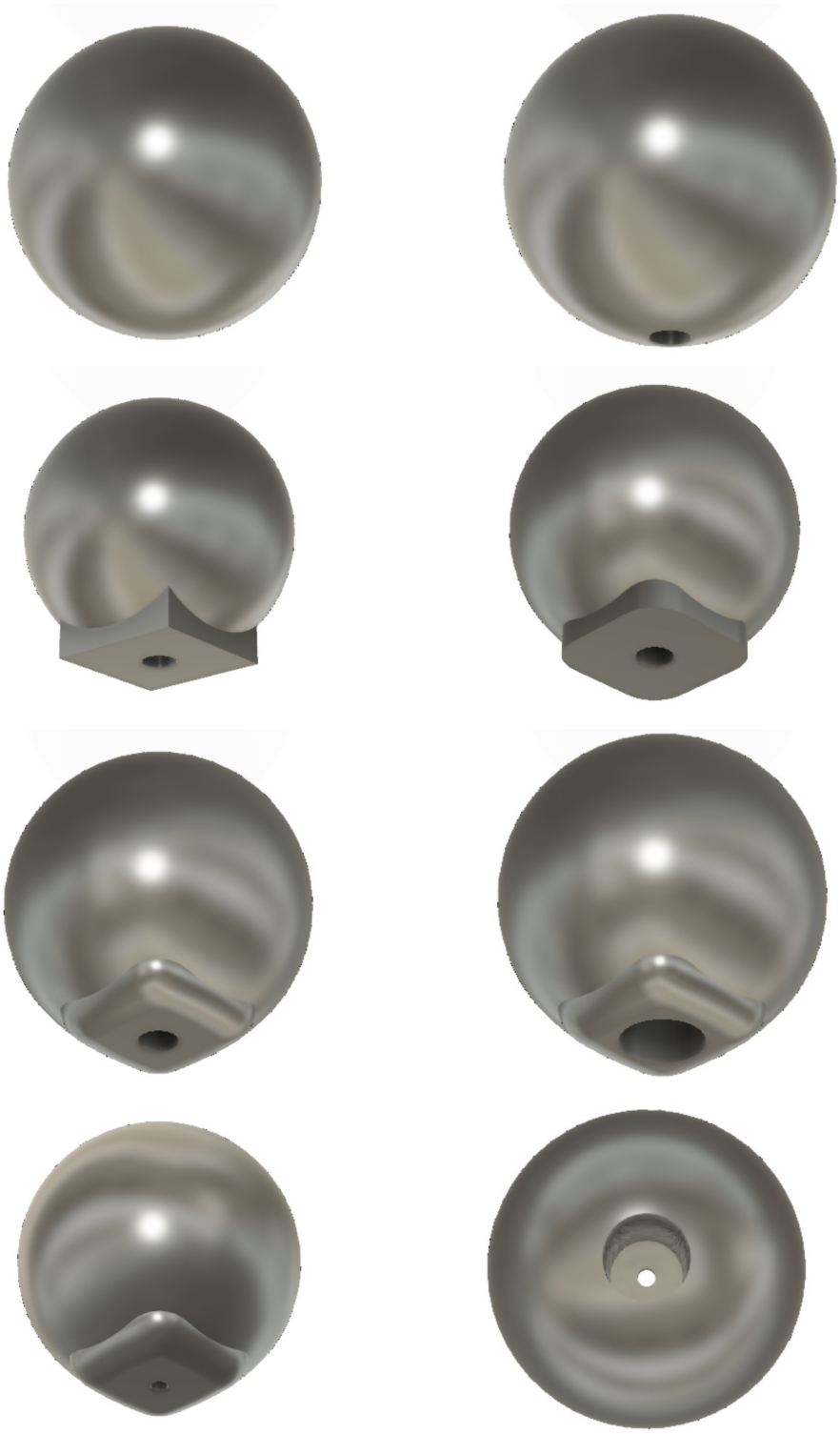

Figure 3.17: Evolution of Sphere, Gen: 1 - 8

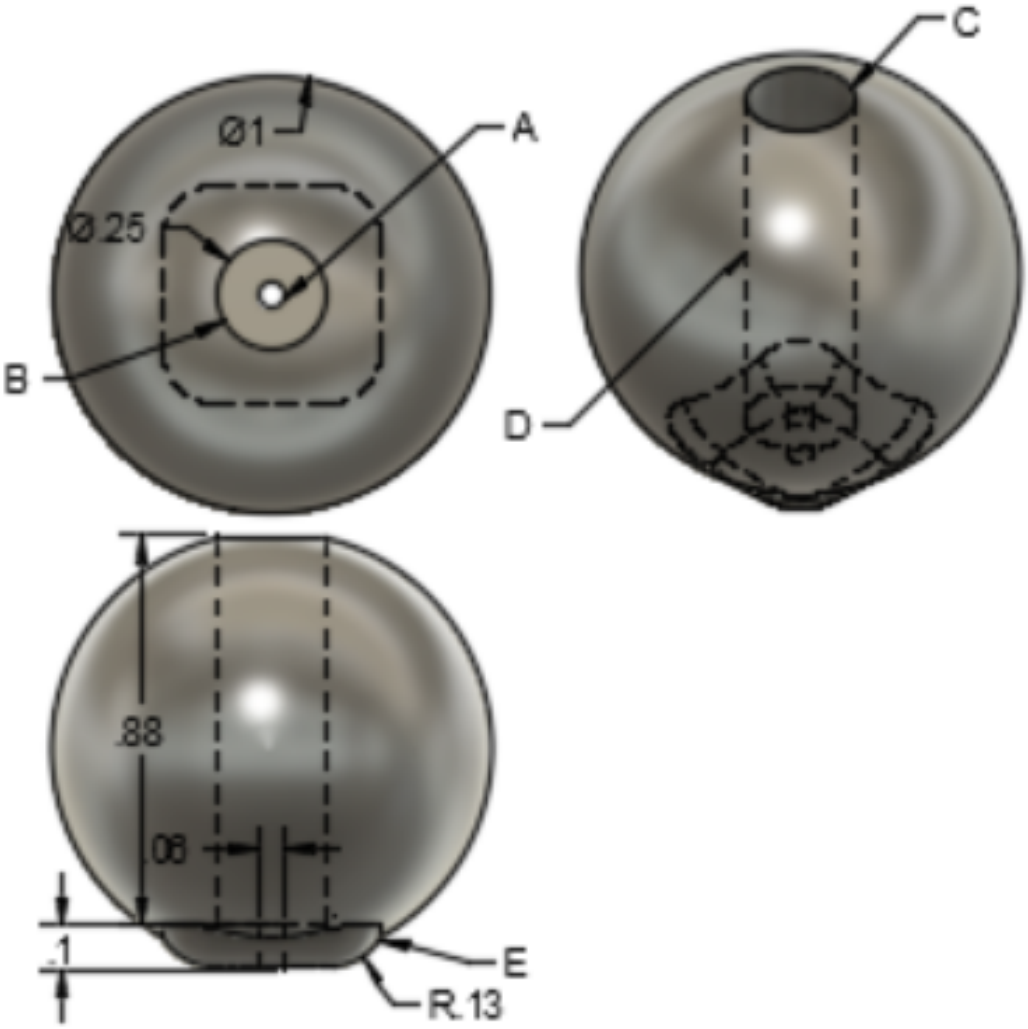

Figure 3.18: Technical Drawing of Test Sphere in ASME Standard; all units are in inches.

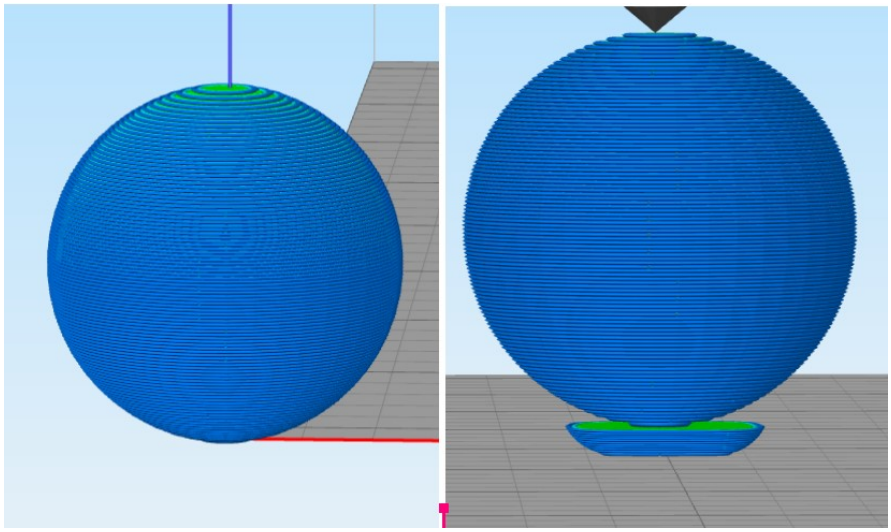

Figure 3.19: Visualization of the toolpath processing script used to implement a repeatable deployment platform

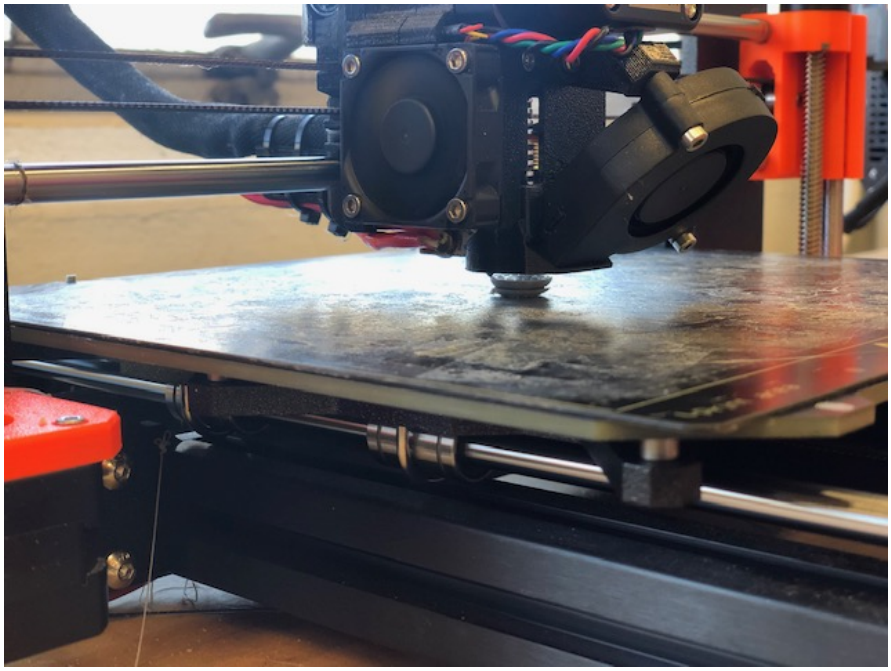

Figure 3.20: Printing of the sphere demonstrating the results of the toolpath processing script necessary for integrating a base to elevate the height of the object for deployment

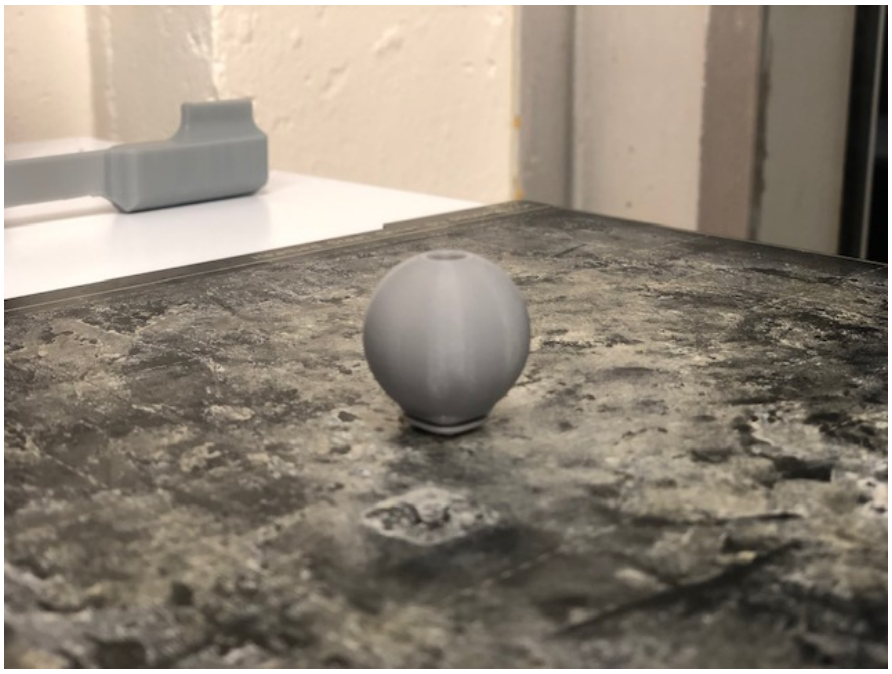

Figure 3.21: Printed sphere demonstrating the results of the toolpath processing script necessary for integrating a base to elevate the height of the object for deployment

3.3 Automated Platform

3.3.1 Spring-Sphere Model

The forces applied to the sphere are resultant forces from the nozzle acting on the spring in section 3.1.3.

The force F_2 in Figure 3.22 can be described through the conservation of momentum through the kinetic energy transferred by the spring. Through conservation of energy, we have the elastic potential PE_e related to kinetic energy KE by

$$1/2mv^2 + 1/2kx^2 = Constant \tag{3.7}$$

This energy can be translated into aerodynamic forces that describe the trajectory of the ball with respect to axial forces, as seen in Equation 3.8.

$$\begin{aligned} h &= v_0 t_h \sin(\theta) - \frac{1}{2} g t_h^2 \\ y &= v_0 t \sin(\theta) - \frac{1}{2} g t^2 \end{aligned} \tag{3.8}$$

Assuming simple pendulum oscillation, we can linearize the problem and show that $v = L\omega$, and $k = mh/L$, with $x = L\theta$. Taking our spring at equilibrium

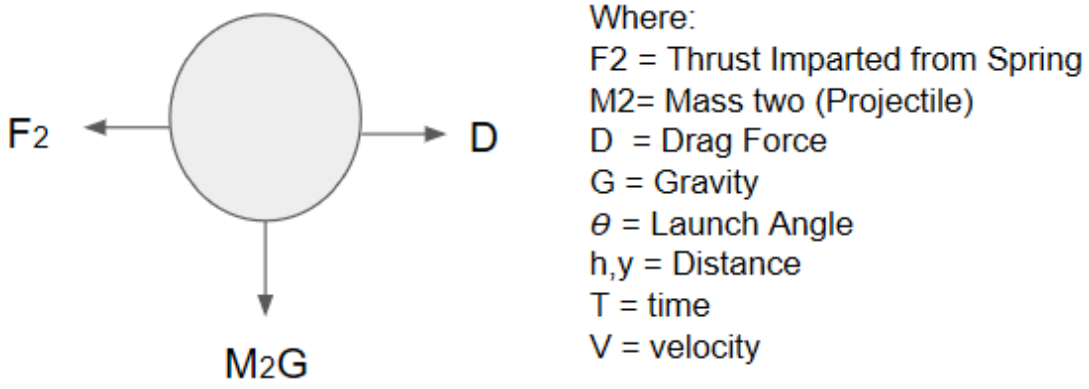

Figure 3.22: Simplified Free Body Diagram of Sphere

and applying the maximum displacement allowed through x, we can simplify the problem into the form of

$$v_m = \sqrt{k/m}(x) \tag{3.9}$$

Using this equation to calculate a maximum velocity for the sphere, we can implement the velocity into a projectile motion of equation to calculate the drag force, D.

$$D = 1/2(C_d)\rho V^2 A \tag{3.10}$$

C_d is the geometrically-dependent coefficient of drag, ρ is density, V is velocity, and A is reference area area. We can linearize this system by taking the root-mean-square of the only higher-order term (V^2) into V_{rms}. [Sohankar et al., 1998].

$$D = 1/2(C_d)\rho V_{rms} A \tag{3.11}$$

Taking the equations of motion described in 3.1.3, we develop the linearized state-space equations.

3.3.2 Linearized State-Space Representation of Model

We linearized the equations of motion representing the ODE's referenced in 3.1.3. To implement numerical methods, we require the equations in state space format. These equations can be described by the following matrices:

$$\begin{bmatrix} \dot{x_1} \\ \dot{x_2} \end{bmatrix} = \begin{bmatrix} 0 & 1 \\ -k/m & -c/m \end{bmatrix} \begin{bmatrix} x_1 \\ x_2 \end{bmatrix} + \begin{bmatrix} 0 \\ 1/m \end{bmatrix} F_l \tag{3.12}$$

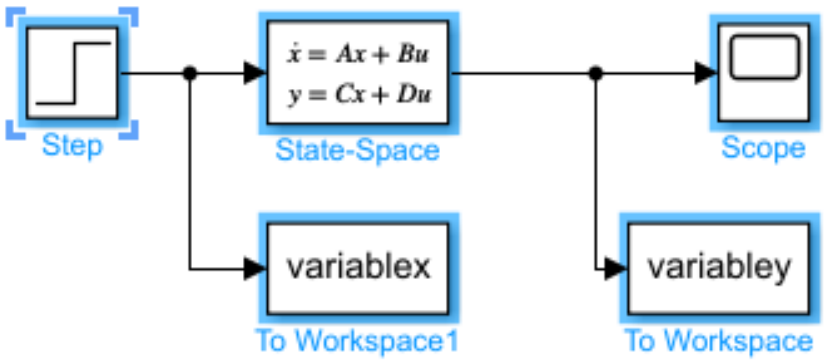

Figure 3.23: Simulink Representation of Linearized Spring Mass Damper Model

$$y = \begin{bmatrix} 1 & 0 \end{bmatrix} \begin{bmatrix} x_1 \\ x_2 \end{bmatrix} \tag{3.13}$$

Equation 3.12 represents the linearized dynamical mass damper system, and Equation 3.13 is the state space output.

3.3.3 Numerical Methods and Simulation

The equations in Section 3.3.2 provided the fundamentals for the implementation of numerical methods. The chosen solver was Matlab, utilizing Simulink for a nodal representation of the system, as seen in Figure 3.23

Simulating this model provided insight regarding the spring's bounding parameterization. Taking the spring as having a mass of 10 grams and a spring constant of 0.5, we observe the range of possible dampened motions in Figure 3.24a.

The color-scale represents a range of damping ratios to help tune the system,

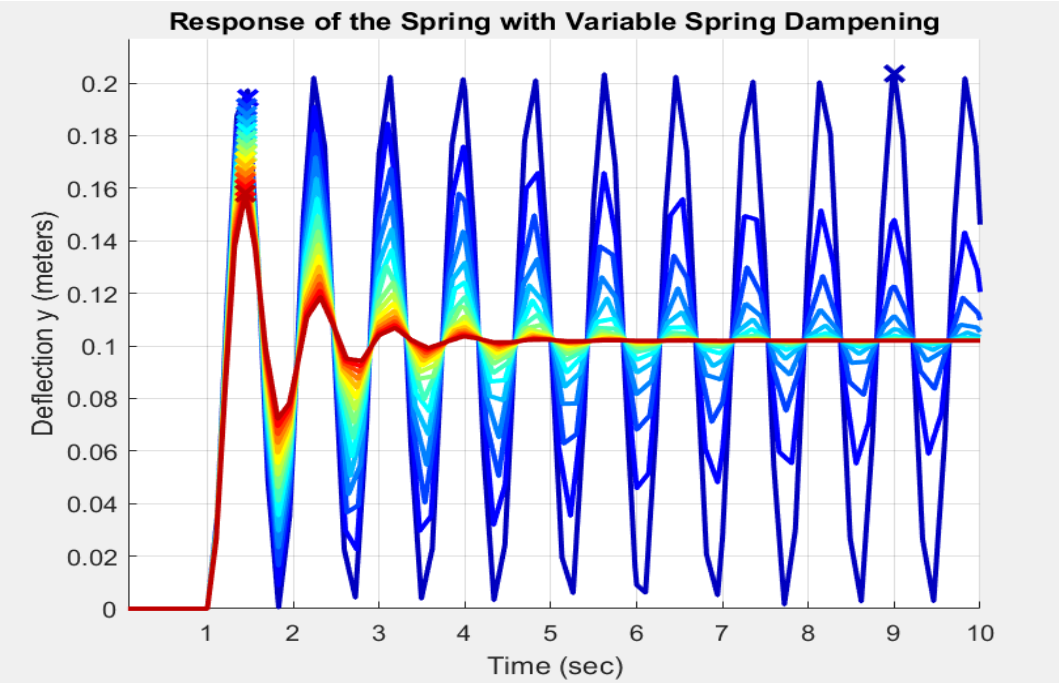

(a) Spring Displacement and Response over Varied Damping Ratios

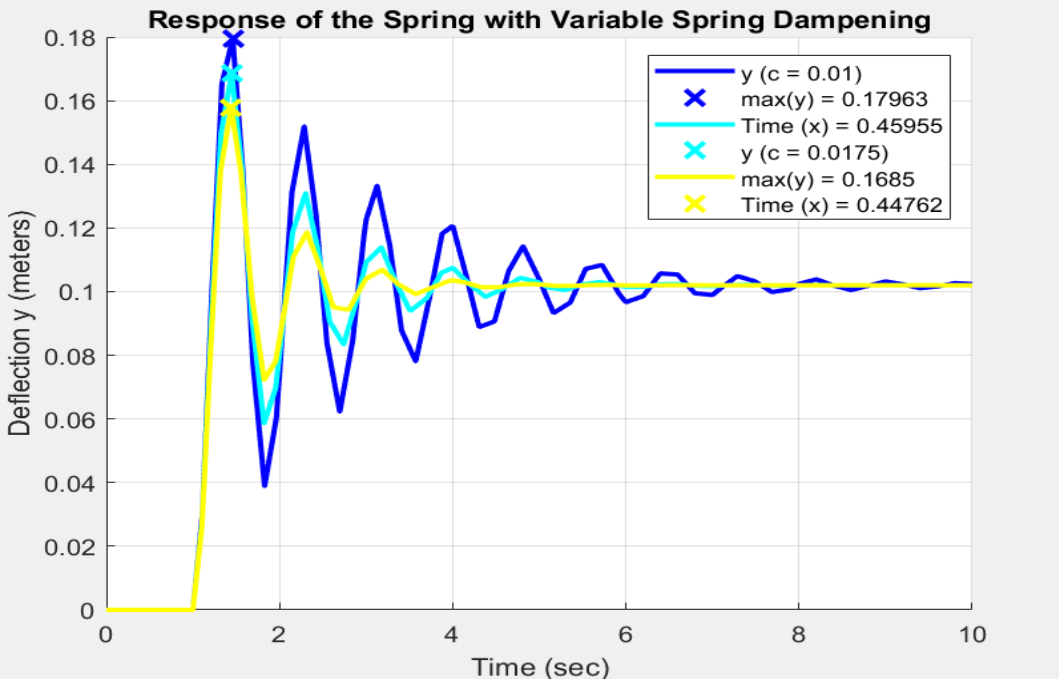

(b) Spring Displacement and Response over Tuned Damping Ratios

Figure 3.24: Bridging Technique for Deployer

with blue representing small C, and red large C, respectively. After investigating the system further, three damping ratios reflecting physically-observed values were chosen to parameterize and tune the model. These three ratios are visualized in Figure 3.24b.

This figure is extremely helpful for determining the visually-observed response of the actual system. The maximum deflection for each response was calculated numerically in Matlab, with the relevant time to reach maximum deflection integrated into acceleration. Utilizing this acceleration with respect to mass, force was calculated through $F = ma$.

Although the error of simulated acceleration was found to be within single digit percentage of observed spring acceleration ($.878m/s^2$ versus $.881m/s^2$), this is likely due to bias of the linearizing assumption that the drag acting on the spring into the damping coefficient. I further investigated the simulated versus observed values by characterizing the interaction of the spring-sphere system.

3.3.4 Spring-Sphere Calculations

Taking the linearized drag in equation 3.11 at standard temperature and pressure, we plug in the observed and calculated values from above. As a function of a geometry's fluid-viscosity interaction with respect to velocity, the unitless coefficient of drag for a sphere at our range of velocities can be assumed to be .5. This assumption was validated by Abraham's work on sphere-drag observations over various Reynold's numbers [Abraham, 1970]. Standard temperature and pressure assumptions provide the density ρ as 1.2 $kg/(m^3)$. The V_{rms} is calculated at $0.421m/s$, and reference area A simplified to πr^2.

To determine the collision reaction force, we utilized an inelastic impulse-based contact model defining friction through Coulomb's Model [Lötstedt, 1981]

[Stewart and Trinkle, 1996]. The collision between the paddle and sphere was recorded with a 960hz camera and found to have an impulse of approximately 300hz, transferring the energy from the paddle to the ball within .003 seconds. At a radius of $1in$, we have $A = 3.14in^2$. This provides us with a D of $.0006N$. Taking the F_2 through idealized conservation of momentum of the spring, we obtain $F_2 = .0081N$. The residual force from our model is consequently taken as $F_2 - D$, giving us $.0075N$.

The projectile's path was calculated through the equations of motion in Section 3.2, and is visualized in Figure 6.1.

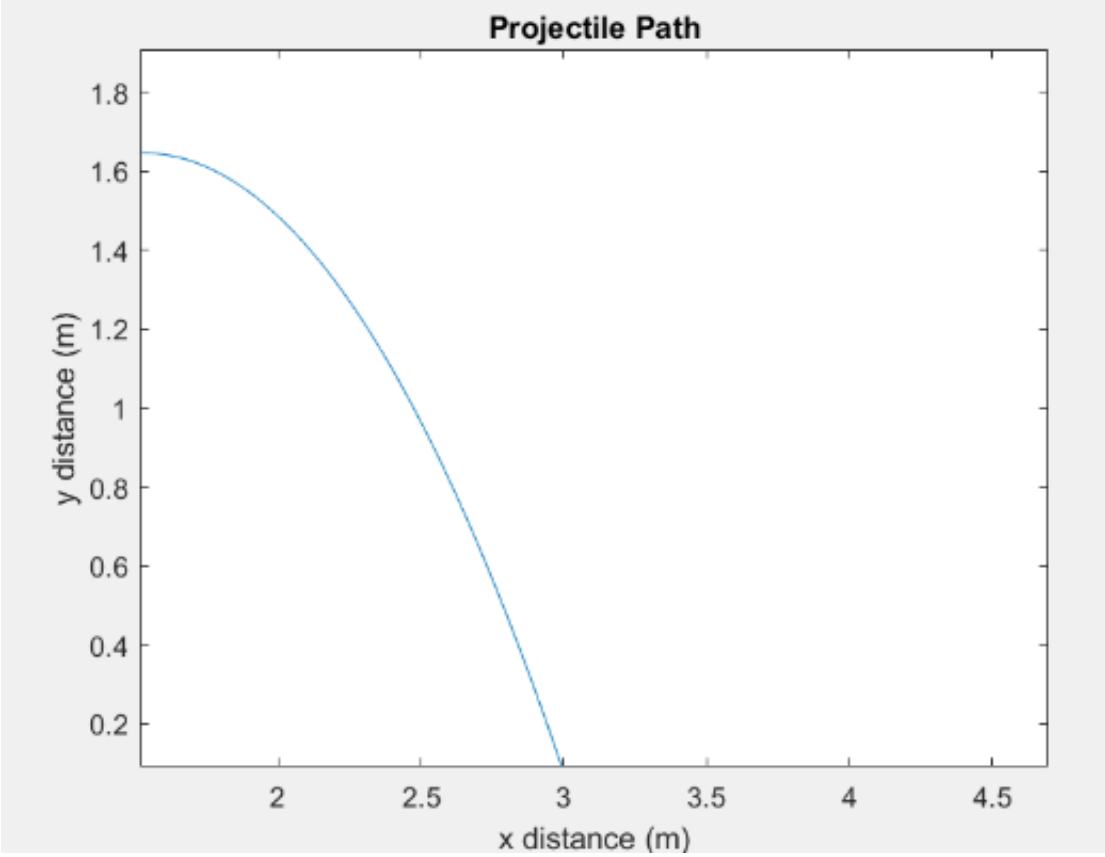

Figure 3.25: Projectile Path of the Ball As Per Linearized Spring Mass Damper Model

3.4 Printing and Programming In-Situ Actuators (ISA)

3.4.1 Introduction

The research presented in this section enables novel kinematic interactions on the additive build platform through the fabrication of hardware which is selectively designed to deflect elastically and deploy, while maintaining stability on the build plate for repeated usage. The in-situ actuator demonstrated in this paper provides a method for storing mechanical potential energy on the build platform in the deflection of a linear spring printed onto the platform by programming the additive manufacturing gantry to pull the spring using the print head nozzle. A novelty of this approach is the ability to repeatably pull and deploy the actuator without the need for a separate robotic manipulator, as the process is fully contained within a common off-the-shelf additive platform. This method provides a basis for unique interactions on the build platform. A proof of concept is provided using a Prusa MK3S 3D printer, demonstrating the deflection and release of an in-situ actuator to interact with a simultaneously-fabricated object within the actuator's proximity.

Section 3.4.2 describes the proposed modeling and design approach. Section 3.4.3 shows the integrated methods and physical results and Section 3.4.4 concludes the work on printing and programming ISA's.

3.4.2 Modeling and Design

Design of Actuators for Additive Manufacturing

On a fundamental level, a mechanical actuator must have an energy source and a control signal (input) in order to produce a mechanical motion (output). The work in Ref. [Gomis-Bellmunt and Flavio Campanile, 2010] was considered for the implementation of an actuator for an additive manufacturing platform. Ref. [Huber et al., 1997] further assisted in distinguishing the design criteria as follows:

- The physical properties (e.g. geometry, material, weight) and range of motion are known;
- The actuator positions (translational and rotational degrees of freedom) are known and controllable at all times;
- The functional mapping, from inputs to outputs, is well-characterized and robust to external factors;
- The actuator meets its specifications (e.g. required speed, force, expected life cycle, etc.);
- The actuator retrofits into the system without major design change;
- The actuator is safe for human operations.

Design of In-Situ Actuators for Additive Manufacturing

This section proposes that by designing mechanical interactions as an embedded dimensionality of the fabricated components themselves, one could remove the need for hardware modifications to extend the functionality of the platform

to include physical actuation and deployment. A novelty of this concept is the ability to remove other processing stages by manufacturing the desired physical capabilities in-situ, such that they would not require removal from the build plate to provide functional utility. This work concurrently demonstrates a manufacturing platform, programmed for fabrication and subsequent actuation by virtue of programming interactions within the build platform. To demonstrate these objectives through the general mechanical actuator design framework, specialized criteria for additively manufactured in-situ actuators are defined:

- The actuator stores mechanical energy from the moving components of the additive manufacturing platform (in the form of a functional spring);
- The actuator is able to transfer energy into objects fabricated within its proximity;
- The actuator is fabricated directly by its parent machine and functions without further processing.

The first and second design criteria are proposed as the simplest method to transfer the electrical energy of the machine into mechanical potential energy for the actuator. The third design criteria imposes limits on the actuator geometry and material selection and also enables automated deployment. For the Prusa printer, the following parameters bound the above design criteria:

- Build Volume: $(25 \times 21 \times 21$ cm) ;
- Minimum feature size: 0.4 mm diameter nozzle, 0.05 mm layer height;
- Material: Ultimaker PLA;
- Desired force generated by spring: 2.5 N;

- Degrees of freedom: Three translational degrees of freedom (two in the conventional xy-plane of the build platform, and one along the vertical z-axis of the nozzle).

Note that energy can only be transferred to the actuator through nozzle motion in the xy-plane or a downwards push of the nozzle in the negative z-direction; the nozzle design scheme was tailored to provide minimal non-axial loading on any fabricated components. The printing-specific conditions are summarized in Table 3.2.

Material	Nozzle Temperature (℃)	Nozzle Diameter (mm)	Printing Density (%)	Average Printing Speed (mm/s)	Layer Height (mm)	Raster Pattern	Support Structure
PLA	210	.4	20	30	.2	Stars	None

Table 3.2: Additive manufacturing printing conditions.

To mechanically store potential energy, the in-situ actuator was designed such that it could be physically compressed. This would enable it to store energy in elastic deformation from interactions with the 3D printer itself. By designing a spring system with properties specifically tailored for interaction with compression from the same manufacturing process that made it (Fig. 1), one can enable the novel ability for a machine to store different forms of mechanical potential energy without hardware modifications. Early iterations and implementations of these in-situ actuators are demonstrated in the following section.

Printing for In-Situ Actuation

To implement the physics embedded within the fabricated components, a manufacturing scheme was utilized which references digitally generated information

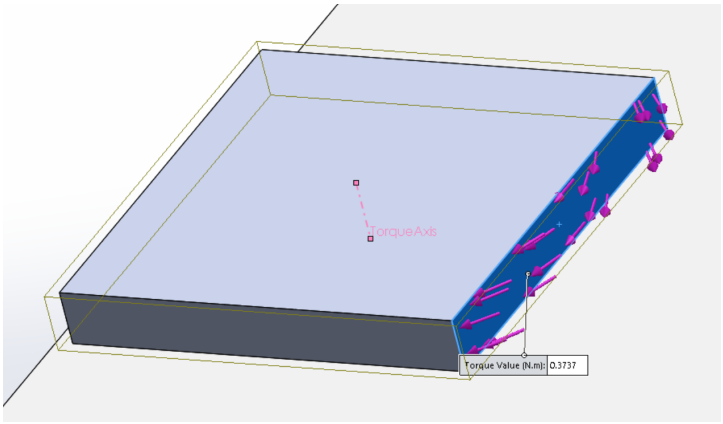

(a) Loading condition visualization on FEA model of actuator base

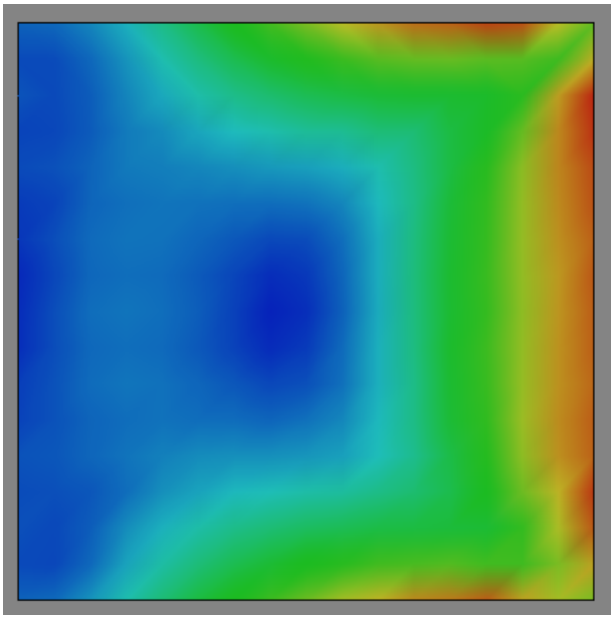

(b) Simulation of base undergoing resultant torsional force from actuator deployment. Red signifies concentrations of Von-Mises, with blue accounting for the lack-of stress.

Figure 3.26: FEA conducted to confirm design space for actuator stability and force concentrations on the build-plate

within a build file. This information would later be physically relevant (with regards to its environment) within a serially defined line of code within the same file. This process redefines the scope of what would be typically defined as 4D Printing [Khoo et al., 2015] by embedding physical information that would enable kinematics as a functional extension of the manufacturing platform. By design-

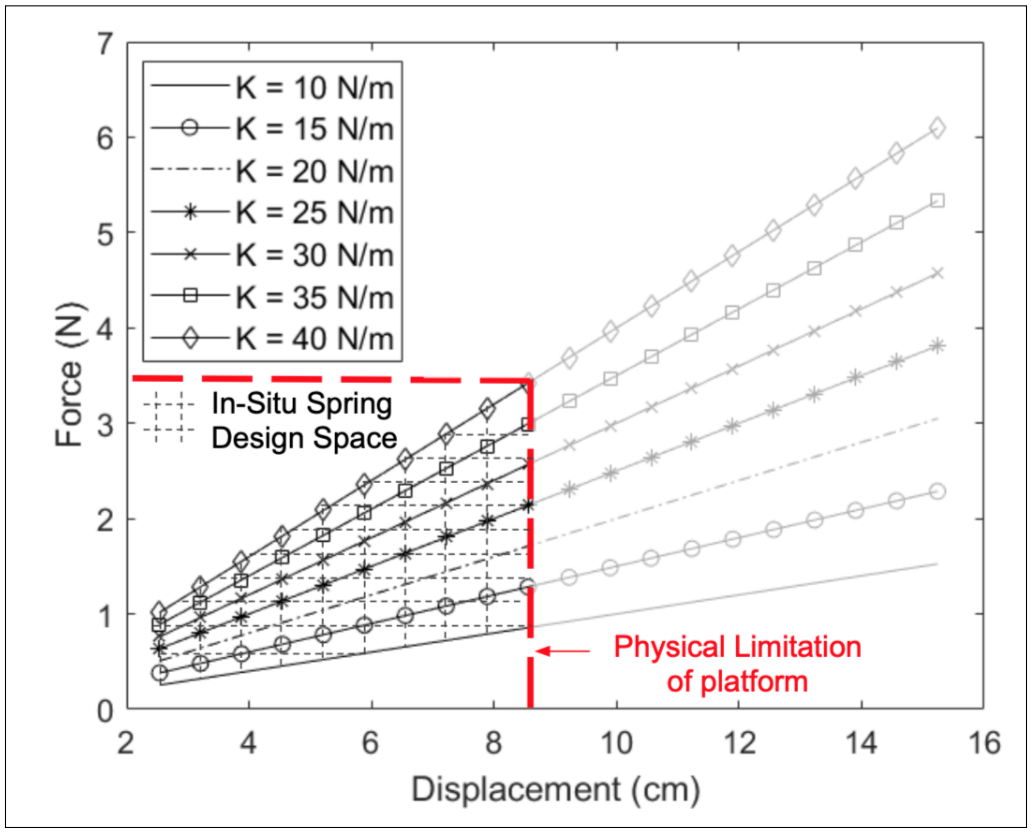

Figure 3.27: A comparison of spring force output with respect to displacement length over a range of spring constants, K ranging from 10 to 40 Newtons per meter. The graph demonstrates the necessary spring constants to generate the desired force with respect to distance.

ing to-be-printed components with respect to material and manufacturing-specific variables and uniquely utilizing the building process to enable physically embedded information and interaction, the system is able to excite objects into new modes autonomously.

To change the mode of a fabricated object, physical mechanisms were embedded in the layer-design to be actuated at a later point of the manufacturing process. By utilizing the gantry on the additive manufacturing platform to deflect the spring mechanism after its fabrication, one may actuate and deploy an extra dimension of functionality, in-situ. A tap-lever was placed onto the spring that allowed for the extruder nozzle on the FFF platform to pull the spring through an insertion of gantry code which synchronized the nozzle with the lever's location on the build-platform.

As FFF requires human involvement to remove any support structure generated through the additive process, novel toolpathing techniques that allow for conditional compliance of the spring were utilized. Generation 6 - 7 in Fig. 3.28 demonstrate an evolution that enabled the removal of support structure from the manufacturing process. By placing mass on the end of the cantilever spring, the actuator was able to both generate larger angular momentum through the additional mass and overcome the requirement of support structure by bridging the mass to the base of the spring in a series of profiled layers. A visual of this process is demonstrated in Fig. 3.29.

3.4.3 Implementation and Results

Rapid Prototyping to Evolve Design

Repeatable manufacturing of an actuator in which one end of the system maintains stability on the build platform while the rest of the system has the

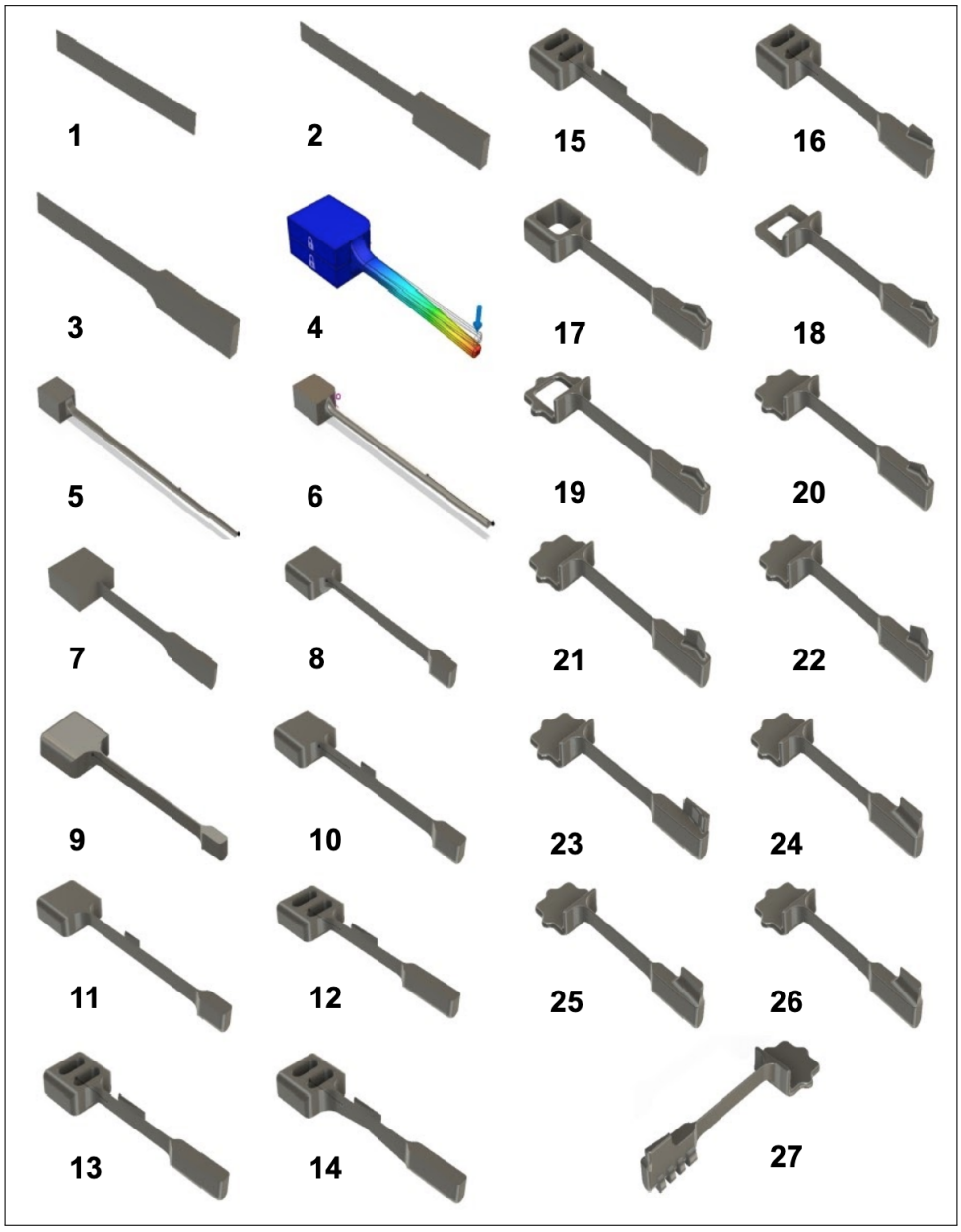

Figure 3.28: Consolidated Evolution of In-Situ Actuator, Generation 1 - 27

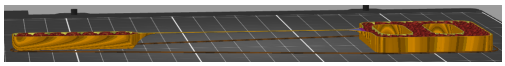

(a) Toolpath visualization of the first bridged layer

(b) Physical demonstration of bridging 10 layers

Figure 3.29: Bridging technique utilized to remove the necessity of support structure for in-situ deployment. The bridge was designed to act as a cantilever spring between the mass and base.

ability to partially deform and actuate drove the necessity for tailored design-for-manufacturing considerations. The design space presented in sections 3.4.2 and 3.4.2 guided criteria for developing the in-situ actuators. As the material considerations were defined by the intrinsic geometric constraints, Finite Element Analysis (FEA) was utilized to iterate an array of designs. An example of the conditions utilized for the FEA are demonstrated for the simulation within in-situ actuator generation 27, in Table 3.3 and and further visualized in Fig. 3.31.

FEA Type	Solver	Material	Nodes	Mesh	Load (N)	Constraints	Deflection (cm)
Nonlinear Static Stress	NASTRAN with Autodesk GUI	Orthotropic FFF PLA	841	Adaptive to Curvature	2.5	Fixed at base	5.4

Table 3.3: FEA conditions utilized for generation 27 in-situ actuator deflection simulation

An evolutionary milestone from generation 12 - 15 significantly reduced the error of the bridging process demonstrated in generation 7 - 11. The design in generations 12 - 15 converged the concept of connecting a free-ended mass to a base through a linear spring. This design is visualized in Fig.3.30a. By tuning this design as a function of length, thickness, and starting layer to introduce the spring, the physically-observed geometric error associated with the first layer of

the spring from generation 15-onward proved negligible.

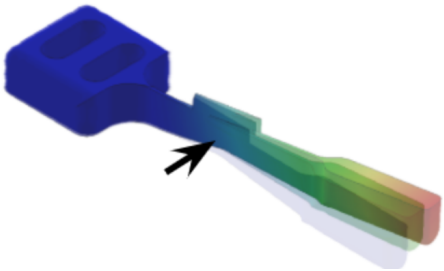

(a) Simulation of generation 14 emulating loading from nozzle, deploying the actuator

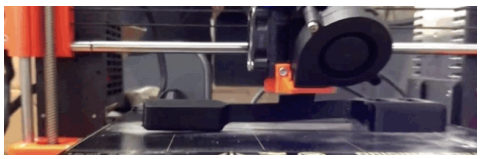

(b) Physical demonstration of generation 14 undergoing actuation

Figure 3.30: Simulation and physical demonstration of generation 14 actuation.

The physically-validated actuation in Fig. 3.30b also demonstrates the utility of an introduced lever, enabling the printer's nozzle to control the deployment of the actuator. The design choice placed the lever mid-spring to deflect large angles with relatively small physical movement, for more efficient spring deflection. This process simultaneously led to an additional coupling moment along the lever from the center of mass, and proved unreliable, ultimately leading to the shear of the lever during actuation of the spring by the nozzle. In response, the lever was thickened and extended to occupy a longer portion of the spring.

The primary manufacturability considerations were taken with respect to the toolpathing requirement of support structures [Fernandez-Vicente et al., 2015]. The 3D model's toolpath was modified to remove support structure and enable the bridged-spring design. Taking the 0.4mm FFF nozzle printing at a 0.05mm layer thickness, the theoretical maximum overhang angle threshold is 45 degrees with respect to the conventional build-plane. To generate the spring design observed in

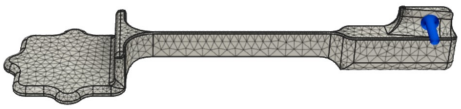

(a) Simulation of final configuration emulating loading from nozzle actuating lever

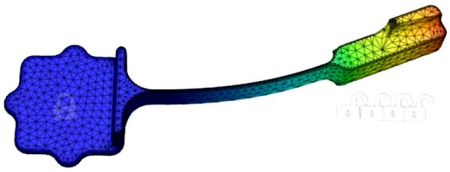

(b) Simulation of final configuration at maximum deflection

Figure 3.31: Simulation of the final iteration of the actuator demonstrating elastic deflection through loading emulating the gantry nozzle pulling the deployment lever.

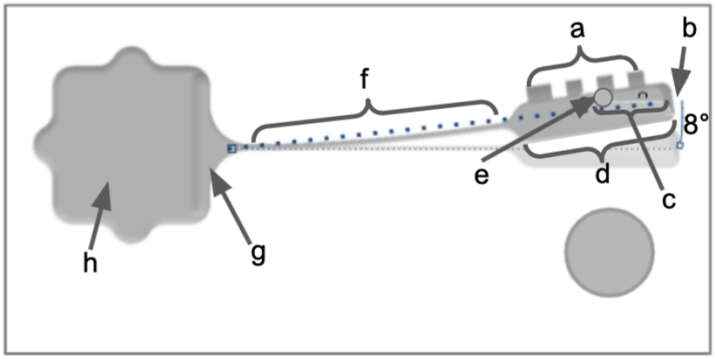

Figure 3.32: Functionality of In-Situ Actuator

Fig. 3.32, a toolpathing technique was utilized to aggressively cool material as the build gantry quickly accelerates parallel to the build plane (commonly referred to as bridging) [Lensgraf and Mettu, 2016].

Through geometry, the base of the spring and the high moment of inertia through the pendulum design cleverly allow tapered starting and ending coordinates for the bridging. By radiusing the inner sections observed in Fig. 3.32f and Fig. 3.29, the toolpath accelerates the bottom-most layer of the spring linearly, allowing for the solidification of the material between the two bases. The resulting

effect generates a few layers of geometrical error; however, this section proves stiff enough to support its own weight. After initially printing on air, the first few layers of the spring act as in-situ support structure, resisting gravity and allowing for the subsequent layers of the FFF process to repeatably occur with minimal error.

To allow the weighted end of the spring to detach from the build plate, a mixture of the model's tapering and radiusing was conducted near the initial base layers of the print, and is demonstrated in Fig. 3.32b and g. By implementing a high aspect ratio cantilever spring, the amount of surface area in contact with the build plate was minimal when compared to square or spherical compression springs. This design consideration proved highly advantageous, as it provided the ability to further reduce the contact area with the build-plate through applying a variably filleted gradient.

Referencing the previously defined additive adhesive forces necessary to develop a base to absorb the rotational force of the actuator, it was found that on a conventional polyethermide build-tray, $0.8mm^2$ of PLA contact area provided desirable build characteristics as a platform for the features in Fig. 3.32a,b,d, and f for maintaining stability of its subsequently fabricated layers, and demonstrated the necessity for the nozzle's interaction with the lever to generate enough force to release the actuator's free end from the build plate when contacted. The resulting configuration served as the premise for all surfaces that were required to be released when actuated by the printer.

Programming The Actuator

A variety of methods were implemented to automate the deployment of the actuator such that it could be programmed to store and release energy through

machine code. By designing a lever to be fabricated as a function of the spring, e.g. Fig. 3.32c, the actuator attained the fundamental ability to interact with the FFF printing head. This actuator is easily controllable through G-code, and as such could be used to store and deploy energy through deflecting the bridged spring without human interaction, satisfying the previously defined design requirement for autonomous deployment. By placing the lever on top of the spring, physical contact would generate a moment which could detach the base of the weighted spring through the generated moment arm. To synchronize the nozzle's location with the correct starting point for pulling on the lever through its actuation scheme, a geometry of the minimum feature size was placed at the desired origin to have the toolpath always finish the object and place the nozzle at a specific location. This design feature is visualized in Fig. 3.32e.

To provide a proof of concept for the actuator's ability to deploy an object, a 2.54cm (1in) diameter sphere was printed simultaneous to the actuator. The toolpath contained information to synchronize the nozzle with the actuator's lever, deflect the spring by 5.4cm from its equilibrium position, and subsequently deliver enough force to successfully deploy the sphere. This physical validation is demonstrated in Fig. 3.33.

Observations from In-Situ Actuators

The feasibility of both generating and additively manufacturing a spring mechanism that exhibits desired mechanical characteristics proved to be a complex and challenging task.

Observations between common additive-specific FFF considerations and the physical performance of in-situ actuators are discussed below. The correlations are as follows:

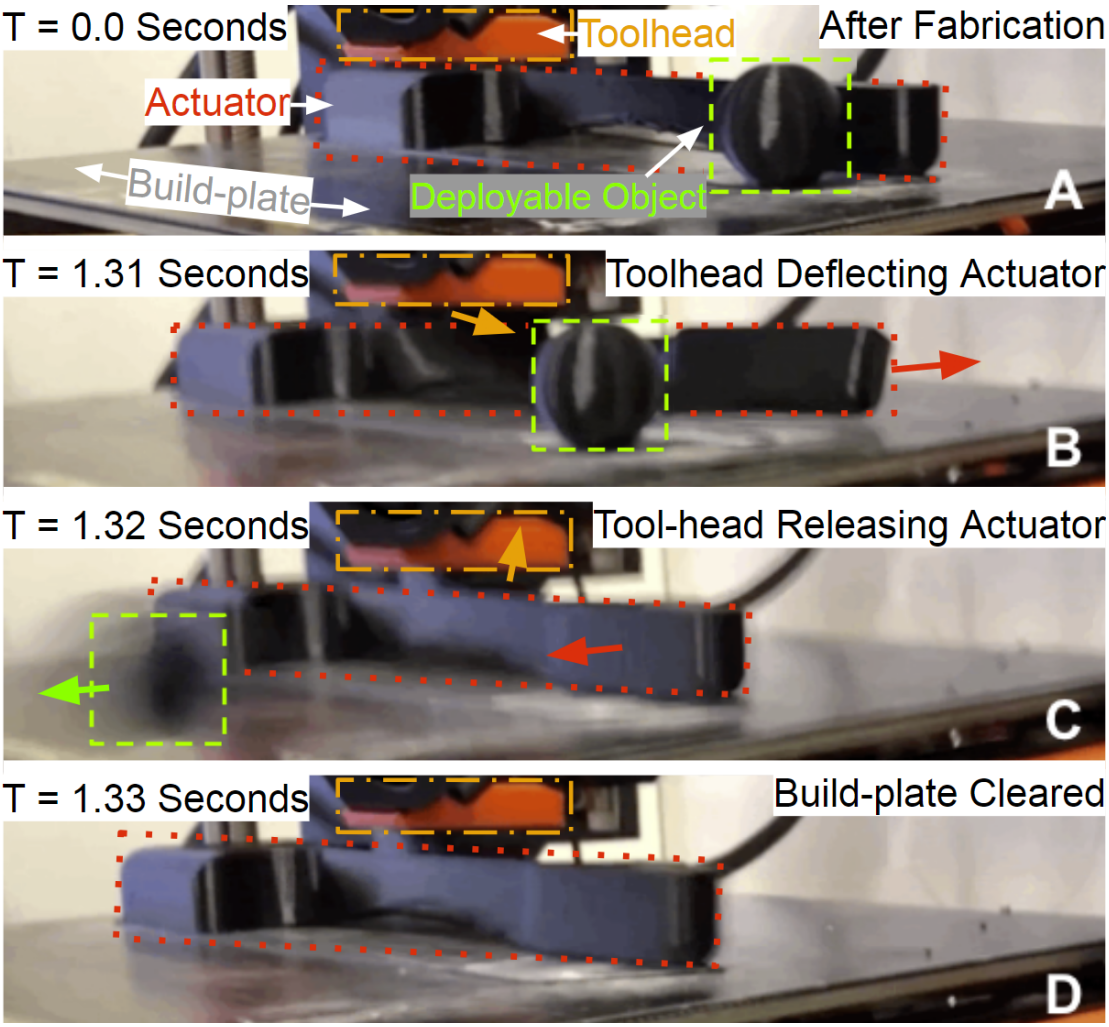

Figure 3.33: Demonstration of In-Situ Actuation of Sphere. Fig. 3.33A demonstrates the steady-state of the platform, post-fabrication (taken at the end of fabrication for both the in-situ actuator and the sphere). Fig. 3.33B demonstrates the nozzle pulling on the actuator's lever, releasing the cantilever end from the build-tray, with Fig. 3.33C and 3.33D validating the sphere's deployment and a return of the actuator to its undeployed position

- Variations with infill patterning techniques (e.g. rectangular, hexagonal, etc.) do not have a measurable effect on actuator performance;
- There must be at least 20% infill density for consistent fabrication of perimeters. This includes springs;
- The nozzle must travel at least 30mm/s for 1.75mm filament to successfully bridge the spring for the perimeters outlined in this paper;
- The correlation of layer height with spring constant was negligible from 0.05mm (minimum tested) through 0.2mm. Layer heights of 0.3mm - 0.4mm (maximum tested) provided errors within the fusion process and subsequent delamination upon actuation;
- The nearest perimeter of the weighted end of the actuator must not be greater than 120mm away from the edge of the base. This effectively dictates the maximum spring length as a function of bridging capability;
- There must be at least 10 sacrificial layers of bridging to accommodate for the lack of support structure between the base and the weighted end of the actuator. This is visualized in Fig. 3.32f.

To counter the rotational moment generated about the spring-axis by the nozzle pulling the lever, feature in Fig. 3.32a was implemented, which was the final iterative consideration from generation 25 to 27 in Fig. 3.28. This design feature allowed the actuator to rotate only along the xy axis, satisfying the last required feature defined in Section 3.4.2.

The scored results of individual generations with respect to desired actuator functionality is demonstrated in Figure 3.34

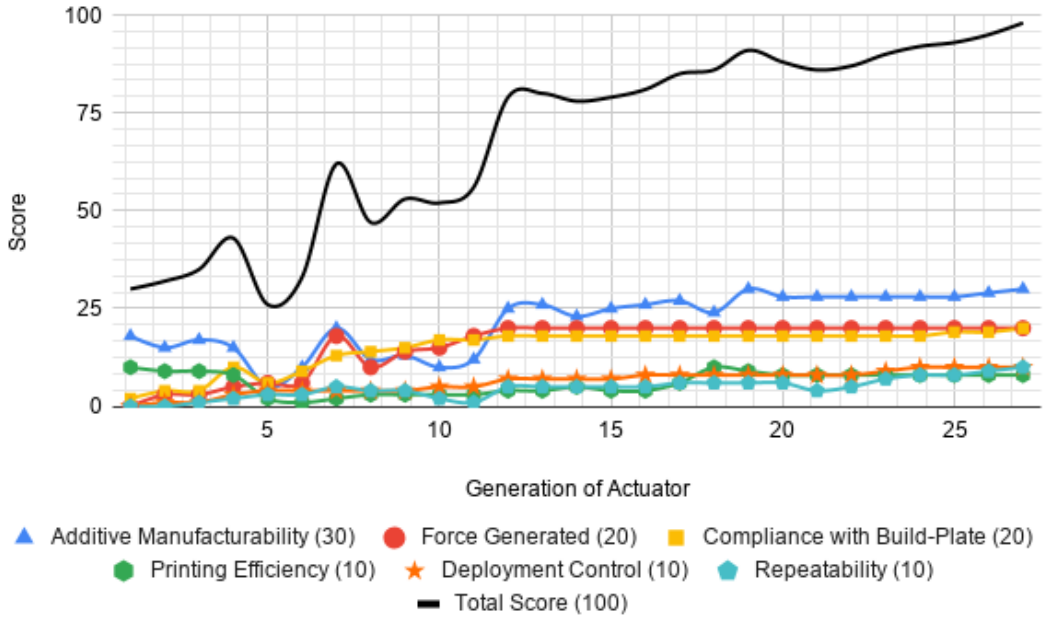

Figure 3.34: Score of Desired Functionality Per Generation of Actuator

3.4.4 Conclusion

This section presented the physical implementation of an in-situ actuator retrofitted onto an additive manufacturing platform. By programming a tool-path to create and subsequently deploy the actuator in-situ, the functionality and consequently number of physical realizations of an object is extended as a function of manufacturing. By achieving this without the need for modified or additional physical hardware, one may deploy this retrofit purely through software, enabling the extension of additive manufacturing platforms to incorporate in-situ actuators digitally. The concept was successfully demonstrated through iterative rapid prototyping, referencing simulations with respect to physically-validated designs of over 27 generations of actuators. The final generation of the actuator allows for synchronization from the 3D printer's nozzle to deploy the actuator, storing energy in a cantilever spring without the necessity of human interaction. By pro-

gramming the nozzle to deflect the lever on the actuator to store and subsequently release energy through machine code, one may introduce a low-cost and unique kinematic functionality into the additive manufacturing platform. The actuator may also be utilized to program the deployment of subsequently manufactured objects through nozzle-actuator interactions. This concept provides the potential for automated high-throughput additive manufacturing that no longer involves human interaction to clear the build plate post-fabrication.

Chapter 4

Automating Sequential Additive Manufacturing

4.1 Introduction

As academia and industry continue to respectively develop and adopt additive manufacturing (AM) processes [Ramola et al., 2019, Delic et al., 2019], novel methods to increase the functionality [Shakor et al., 2019, Urhal et al., 2019] and utility of the AM process by virtue of toolpathing methods are continuously being proposed [Niaki et al., 2019, Wiberg, 2019, Heikkinen et al., 2020]. A specific request is a method to the reduce the labor cost for polymeric AM, as demonstrated by Ref. [Baumers et al., 2016] and Ref. [Thomas and Gilbert, 2014]. Ref. [Najmon et al., 2019] supports that despite significant technological advances and mainstream industrial usage [Li et al., 2019], the economical sustainability of the AM process has yet to be adequately addressed [del Mar Espinosa et al., 2019, Jiménez et al., 2019] due to the need for manual labor [Meng et al., 2019]. As a result, the throughput of AM technologies for a sequential [Macdonald et al., 2014],

repeated object fabrication is severely limited, as demonstrated by [Tibbits, 2014]. This limitation is exacerbated when the number of serial fabrications becomes large [Hicks et al., 2019, Zadeh et al., 2019], due to the need to constantly remove fabricated objects from their build volumes by hand [Bhushan and Caspers, 2017, Götzelmann et al., 2017]. When discrete mechanical systems are incorporated into the AM process to remove fabricated objects [Nelaturi et al., 2019], the theoretical maximum throughput [Dilberoglu et al., 2017] of the process is limited due to the need for a human-in-the-loop to monitor and control the process [Attaran, 2017]. Some AM processes are limited in throughput due to the need for additional post-processing [Prendergast and Burdick, 2019], such as the removal of support structures [Serrano et al., 2019] and cleaning or treatment of a build-surface [Brockmeier, 2000]. Furthermore, sequential fabrication within the same build process requires fabricated parts to have sufficiently small volume, such that they do not interfere with the motion of the printer's toolhead and subsequent objects occupying volume on the same build-surface [Aroca et al., 2017, Jiang et al., 2018a, Jiang et al., 2018b].

The current state-of-the-art AM automation addresses the sequential throughput bottleneck through two common protocols [Whitten et al., 2020] which are provided in Table 4.1. The most common method utilizes a wide revolving belt [Günther et al., 2014], as the build surface to translate components off of a fabrication area [Schurmann, 2020, Brown, 2020, n.a., 2020b, Pax et al., 2012, Wu, 2020], acting as a precision conveyor belt. When a part finishes, it is transported to the end, detaches physically, and falls off. Although the process was patented in 2012 [Pax et al., 2012], it has not yet achieved commercial scales of production [n.a., 2020b]. Utilizing a flexible, translatable build surface is not ideal; it is both difficult to maintain at a desired temperature and difficult to maintain

consistent adhesion across different thermoplastics [O'Connell, 2020]. The other common method uses a robotic arm to carry the fabricated component off of the build surface, such as in [Aroca et al., 2017, n.a, 2020, n.a., 2020a]. Though this method can in theory be inexpensive, precision robotic arm positioning is difficult without active control systems; the cost of such a system increases exponentially due to R&D costs. Consequently, these configurations are out of reach for the majority of AM users [Rylands et al., 2016, Steenhuis et al., 2020, Woodson et al., 2019].

Widely accessible improvements in software-defined automation have allowed retrofitting of in-situ deployment (ISD) into common and open-source fused filament fabrication (FFF) platforms. This has the potential to provide significant cost reductions in sequentially fabricated parts by increasing AM throughput. As the proposed methods are entirely software based, the applicability of the proposed ISD concept offers low risk testing across a diverse set of research fields that are reliant on high throughput iteration. The following design specifications provide guidelines for assessing successful implementation of the automation retrofits:

- AM process shall be free of human involvement;
- Fabricated object shall deploy from its build-surface;
- Fabricated object shall not collide with printer throughout deployment process;
- The printer toolhead shall act as a robotic manipulator;
- AM process shall not require additional hardware or hardware modifications;
- AM process shall have no support structures;

- A fabricated object shall be greater than the minimum feature size, bounded by nozzle diameter and layer height.

We investigated ISD methods to address these requirements and developed a preliminary method that matures to a second method. Section 2 describes this first method, referred to as an in-situ leaf spring (ISLS), which utilizes the concept of self-deployment through elastic deformation. The method leverages the gantry code (G-code) to allow an FFF toolhead to be used as an in-situ robotic manipulator [Attaran, 2017, Nycz et al., 2018, Wimpenny et al., 2017]. This method was previously demonstrated by Ref. [Katakura et al., 2019], however it relied on physical modifications that were not purely software-based, such as with an ISLS. We modified this technique by fabricating and immediately deploying the leaf spring using the printing toolhead as a manipulator. The printer's toolhead was lowered onto the printed leaf spring, deflected to a certain degree, and traversed off to release the ISLS from the print volume and allow a trajectory away from the build surface. This automated deployment would enable a new component to be fabricated without human intervention. Based on the ISLS concept, the method matured into a separate, in-situ leaf spring actuator (ISA), which was fabricated onto a designated location on the build surface. After printing an object along the path of the ISA, the toolhead was lowered onto the actuator and translated to elastically deflect it along a predefined G-code trajectory. The toolhead was raised to release the leaf spring actuator, which allowed it to impart its spring potential energy onto the fabricated object, deploying the object from the build surface. The concepts were mathematically modeled, printed, tested, and iterated upon to improve the concept's maturity. In particular, in order to demonstrate the applicability of the proposed autonomous deployment solutions, the open-source based Prusa i3 [Bowyer, 2020] FFF plat-

form was utilized with polylactic acid (PLA), one of the most ubiquitous materials in AM [Cotteleer and Joyce, 2014, Ishengoma and Mtaho, 2014, Evans, 2012, Wohlers, 2019]. As per Ref. [Kuznetsov et al., 2018], the combined configuration has heritage and is widely adopted by industry and academia [Wong, 2012].

The ISLS was able to partially meet the design specifications, but was limited in scalability due to the large overhang angle from the build-plate, however it served as a successful initial proof of concept. The ISA evolved from the ISLS and through testing demonstrated that it met the design specifications and demonstrated a greater than 99% reliability, deploying over 4,500 AM objects. This design was standardized into high-level algorithms to summarize the ISD process and increase the portability of the concept for other machines, as described in Section 4.4. The empirical results from the ISA testing were modeled for demonstrated cost and throughput. These results were compared to non-retrofitted platforms which accounted for labor-in-the-loop. This analysis demonstrates the utility of the retrofit as more than just a proof of concept, showing realized cost savings and increased throughput over non-retrofitted platforms. This chapter subsequently provides discussion regarding the novel implications of this technology, in addition to current limitations of the system configuration and future work.

Acknowledgements

The research and findings that are presented in this chapter were developed, consulted, and/or referenced with the following colleagues: Rachel Ticknor, Stanley Kryzsniak, Sean Swei, Mircea Teodorescu.

Printer	Company Location	Process	Price (USD)
Rep-Rap FFF	Open Source	In-Situ Leaf Spring	<1 for retrofit. <1k for printer.
Rep-Rap FFF	Open Source	In-Situ Actuator	<1 for retrofit. <1k for printer.
Rep-Rap FFF [Aroca et al., 2017]	Open Source	Robotic Arm	1-5k
Figure 4 [n.a, 2020]	Somerville, MA USA	Robotic Arm	25-50k
Form Cell [n.a., 2020a]	Rock Hill, SC USA	Robotic Arm	25-50k
CR-30 PrintMill [Wu, 2020]	Shenzhen, China	Revolving Belt	1k (est)
White Knight [Brown, 2020]	Open Source	Revolving Belt	1-5k
BlackBelt [Schurmann, 2020]	Belfeld, Netherlands	Revolving Belt	10-25k
Continuous Build 3D Printer [n.a., 2020b]	Eden Prairie, MN USA	Revolving Belt	Not For Sale.
Cincinnati SAAM, SAAM HT [n.a., 2020]	Harrison, OH USA	Scraper	10-25k
Tiertime X5 [n.a., 2020c]	Beijing, China	Build-Surface Swap	1-5k

Table 4.1: Comparison of various systems with automated sequential AM.

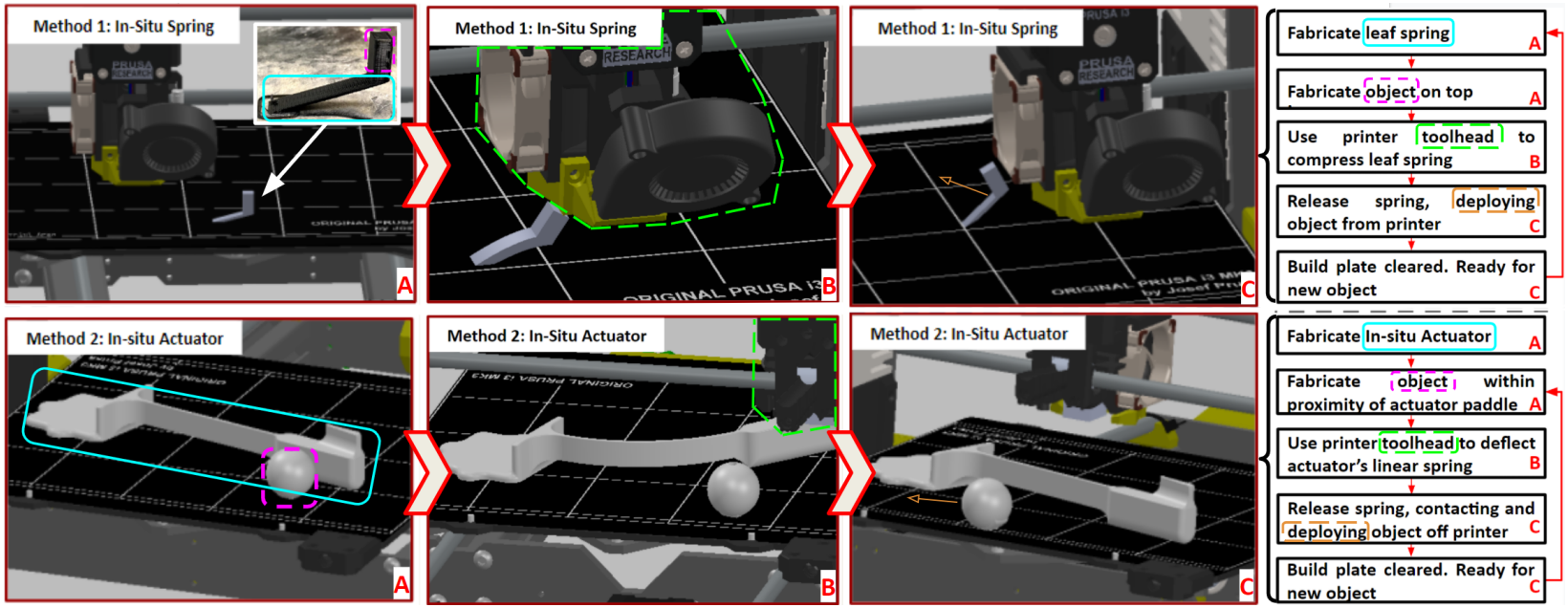

Figure 4.1: Demonstration of the novel methods to automate sequential AM through ISD. The top row demonstrates an ISLS deployment. The bottom row provides deployment with ISA. The automated deployment process flow of each ISD method is visualized on the right column of each row.

4.2 Retrofitting In-Situ Leaf Springs

The ISLS refers to an additively manufactured object that exists as a detachable actuator from a fabricated object, or a fabricated object bounded by the power delivery capabilities of the gantry stepper motors and the maximum allowable elastic deformation of PLA.

4.2.1 Modeling of In-Situ Leaf Springs

To develop a model for this configuration, the ISLS was treated as a flat leaf spring with a weighted end [Wielandt, 1982]. Given that the potential energy stored in the cantilever spring was highly dependent on the material selection, extruded PLA characterized the theoretical design space of an AM ISLS [Shokrieh and Rezaei, 2003]. The build geometry of the FFF ISLS had a direct correlation to stored energy; consequently, unique AM properties such as layer thickness and infill were defined as fixed parameters as shown in Table 4.3. This reduced the dimension of the design space, allowing for exploration of the utility of an ISLS [Kessentini et al., 2019, Garanger et al., 2018].

To find the stored potential energy of the ISLS, u, a cantilever beam structure was assumed, and hence could be found using the process shown in Fig. 4.2. In this visualization, p is the force applied by the toolhead, E is the spring's modulus of elasticity, I the spring's moment of inertia, L the spring length, and leaf spring deflection is taken as Δ [Wielandt, 1982, Shokrieh and Rezaei, 2003].

As part of the trade-off study, the parameters for the final iteration of the ISLS were provided as $E_{PLA} = 2$ GPa, $I = a^4/12$, and $a = 1.34$ mm. This particular design point is Generation 5 as shown in Figure 4.4.

Given the stored potential energy, the jump height h can be modeled by using

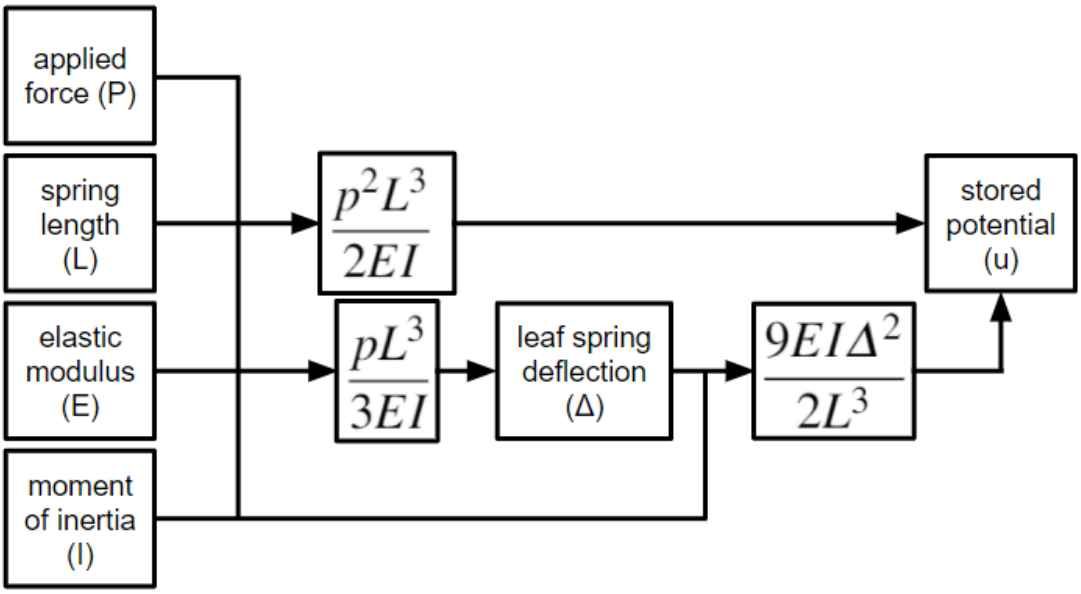

Figure 4.2: Flow diagram for calculating the stored spring energy of ISLS.

the equation for gravitational potential [Anderson and Pandy, 1993], i.e.

$$h = \alpha \frac{u}{mg} \tag{4.1}$$

where m is the spring mass, and α denotes the mechanical efficiency of the spring [Wegst and Ashby, 2004]. This represents the effective stiffness, strength, and elasticity of the material, which is a function of manufacturability. To gauge this efficiency, the theoretical jump height of the spring configuration is compared with the empirical data and estimated at $\alpha \approx 0.6$ [Kessentini et al., 2019]. Given this jump height, kinematics may be used to find the initial jump velocity V_0 [Samozino et al., 2008] as

$$V_0 = \sqrt{2gh}\,. \tag{4.2}$$

The initial acceleration a_0 can then be determined by observing the time t_r, nec-

essary for the leaf spring to release from the build surface, given by

$$a_0 = V_0/t_r \tag{4.3}$$

Note that t_r is experimentally determined through analyzing still images taken at 960 hz of the physical object deployment, as shown in Figure 4.5. The initial jump force, F_j, can then be given by

$$F_j = ma_0 \tag{4.4}$$

As demonstrated in Figure 4.4, at a given spring length, increased tip displacement is proportional to an increased jump height. Additionally, for a given tip displacement, a shorter spring would store more energy and thus greater jump height bounded by elastic deformation limits [Besnea et al., 2018]. These visualizations provide insights into sizing of the spring and its design space, and whether it meets the automated sequential AM specifications.

4.2.2 Simulating In-Situ Leaf Springs

Due to the high overhang angle between the build-surface and the leaf spring, the adhesion between these two contact surfaces would inherently generate torque [Sanatgar et al., 2017, Pan et al., 2016] over the extremely small footprint of the spring. Therefore, understanding the characteristics of this adhesion force becomes critical. After physical design space exploration and consideration of the maximum overhang angles possible with FFF, as per [Gaynor and Guest, 2016] and Ref. [Fernandez-Vicente et al., 2015], a nonlinear FEA was performed using NASTRAN's solver wrapped in Autodesk's user interface on the ISLS to gauge the compressive forces generated at the base of the leaf spring. The final design is

denoted as Generation 11 and is shown in Figure 4.4. The FEA's structure meshing utilized an adaptive-to-curvature methodology, which provided reliable results while maintaining an efficient, convergent computation [Zhang and Zhao, 2007]. A grid independent study was conducted by running the mesh with an order of magnitude higher - approximately 8,400 nodes - with the output of the maximum and the minimum differs only by approximately 3%. This meshing method is popular for non-linear FEA, and provides adequate fidelity given the number of nodes required for a high-level overview of the forces on the base of the spring [Centin and Signoroni, 2018]. A 0.2 cm deflection along the Z-axis was applied at the tip of the spring to emulate the physical deflection required for deployment from the theory, with the constraint being a fixture at the base to configure the spring's as-built surface area constrained on the build-surface. The material selected for the FEA is orthotropic FFF PLA, and its mechanical properties were taken from samples made from similar print settings in [Rajpurohit, 2018]. In summary, the parameter settings for FEA can be found in Table 4.2.

As shown in Figure 4.3, it was assumed that the entire leaf spring base was in contact with the build-surface, then the compressive force is mostly concentrated along the right-hand side of the spring base at the minimum force indicator, while the opposing adhesive tensile force is distributed over the central portion of the leaf spring base. This spatial force difference generates a torque, enabling automated removal of the leaf spring upon releasing of its potential energy. This particular leaf spring can theoretically generate a stored energy of 69.3 mJ.

In retrospect, this is a telltale sign of a design flaw: the overall force distribution throughout the build-surface contact area. Because the tensile force is concentrated near the center area of the base, this means that either a design iteration to spread the tensile force throughout the contact area could have been

made or a design iteration to reduce the contact area to the concentrated tensile force could have been made. A benefit of the former would allow the centroid of tensile force to be moved further from the centroid of compressive force, resulting in a larger moment arm. The latter iteration would have kept the centroids of tensile and compressive forces the same, but a reduced contact area by cutting off part of the left-hand side would potentially result in a smaller obstruction for the spring to jump forward.

As discussed in the following section, these solutions would have at least partly addressed some of the shortcomings of this in-situ deployment method. However, iterations on this aspect would have substantially increased the dimensions of the design space, which was not desirable.

FEA	Solver	Material	Deflection	Constraint	Nodes	Mesh
Nonlinear Static Stress	NASTRAN, Autodesk GUI	Orthotropic FFF PLA	.2 cm	Fixed at Base	841	Adaptive to Curvature

Table 4.2: Parameters used in FEA design iterations as in Figure 4.3.

4.2.3 Iterating In-Situ Leaf Spring Design

As highlighted previously, it is important to relate an object's contact area on the build platform to its adhesive force, and the subsequent amount of force required to displace the object from its as-manufactured position. The configuration settings were held consistent throughout the AM process in order to maintain a controlled toolpathing environment. These settings are given in Table 4.3.

Material	Nozzle Temp.	Nozzle Diameter	Bed Temp.	Infill Density	Infill Pattern	Print Speed	Layer Height
PLA	215 ℃	.4 mm	60 ℃	20%	Rectilinear	45 mm/s	.2 mm

Table 4.3: AM print settings used to generate ISLS.

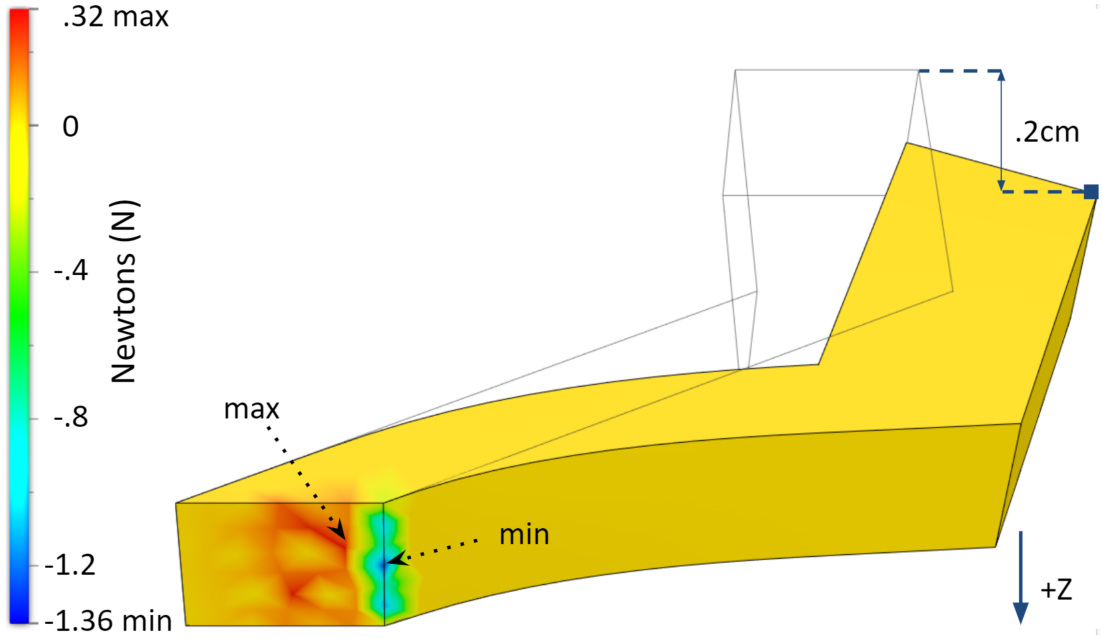

Figure 4.3: FEA modeling of the ISLS, visualizing reaction force in z-axis after applying 0.2cm deflection.

The physical prototypes displayed an elastic deflection mode, but required iterations to embed manufacturability considerations, such as overhang angle, thickness of the spring, build-surface contact area, and amount of mass placed atop the actuator. Various configurations of ISLS are visualized in Figure 4.4, with a successful deployment of Generation 5 shown in Figure 4.5. This experiment is conducted by applying a 2.0 mm deflection onto the spring. Upon release, enough angular momentum to overcome the opposing torque induced by build-surface adhesion force is generated, deploying the object.

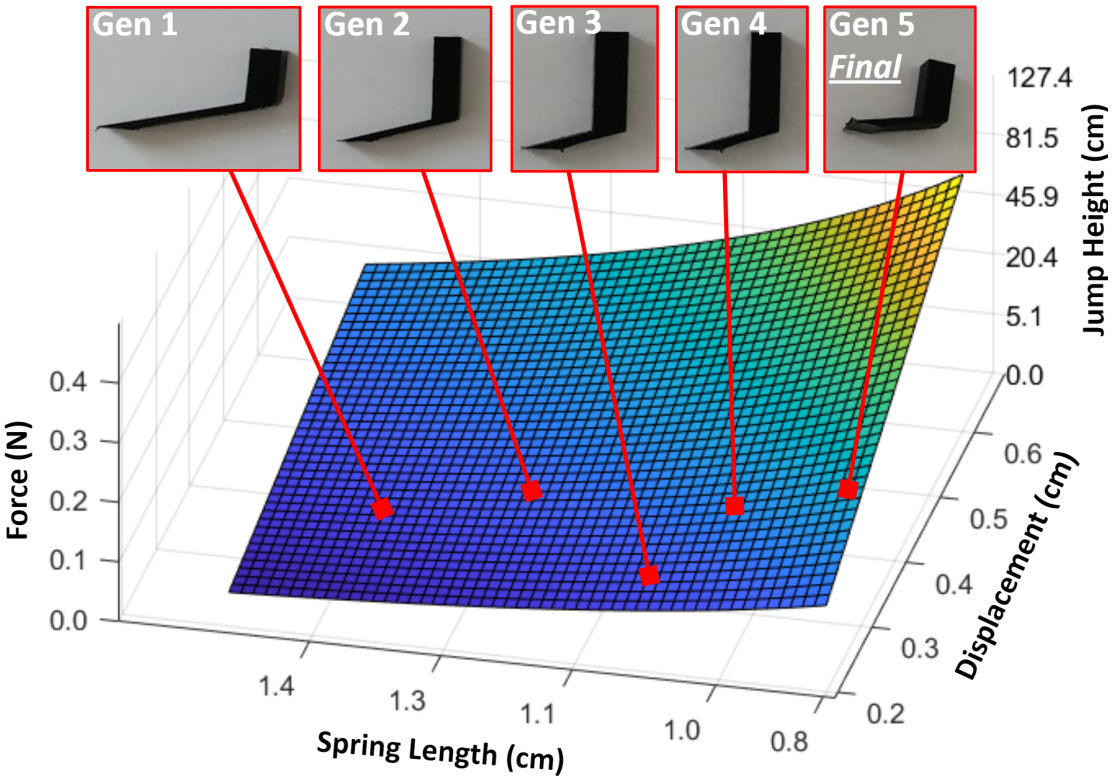

Figure 4.4: Design space simulated for ISLS. The indicated point shows the performance of milestone design configurations.

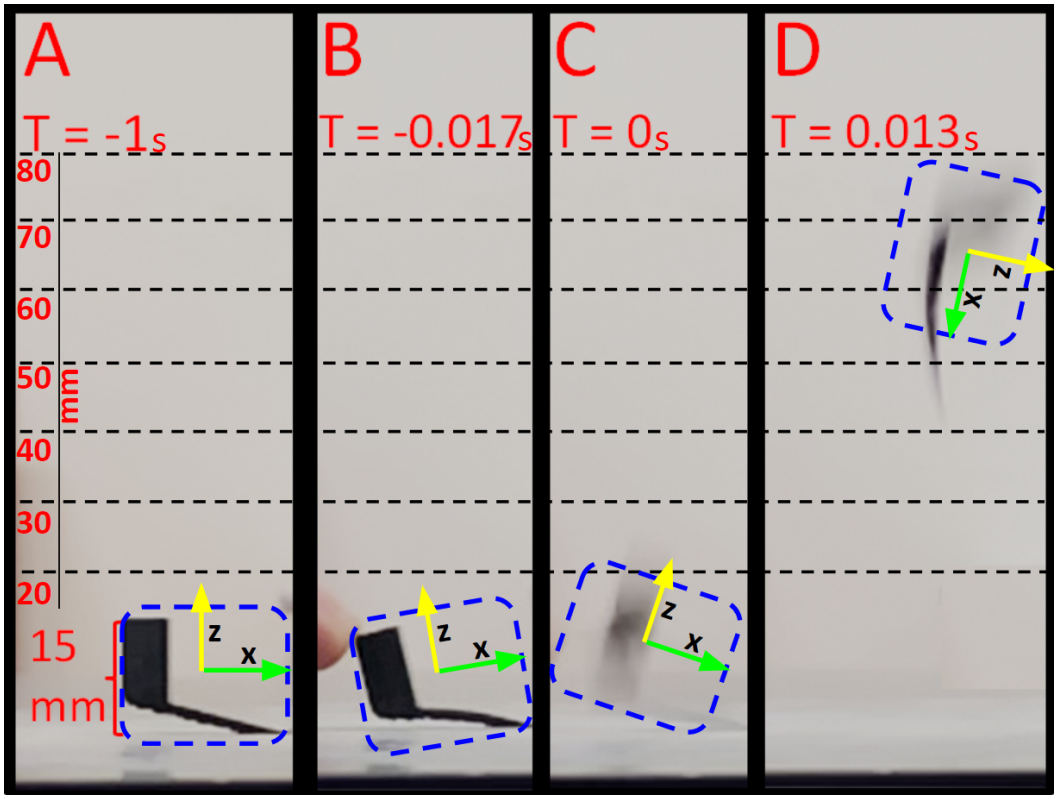

Figure 4.5: Example of a manual deployment sequence of the final generation ISLS taken from high speed video. A) ISLS at rest. B) ISLS loaded four frames before release. C) ISLS at instant of release. D) 0.0125 seconds (three frames) after release, ISLS is rotated clockwise 90 degrees and translated to the right.

4.3 Retrofitting In-situ Actuators

Based on the ISLS design, this section documents a novel object deployment concept. This additively manufactured ISA is completely decoupled from the fabricated object and is used to impart kinetic energy onto the object on a build platform to deploy it, enabling sequential AM process. Similar to the ISLS in Section 4.2, the extruder toolhead deflects the leaf spring upon completing a print. On release of the leaf spring, impact with the object deploys it off the build surface as illustrated in Figure 4.6.

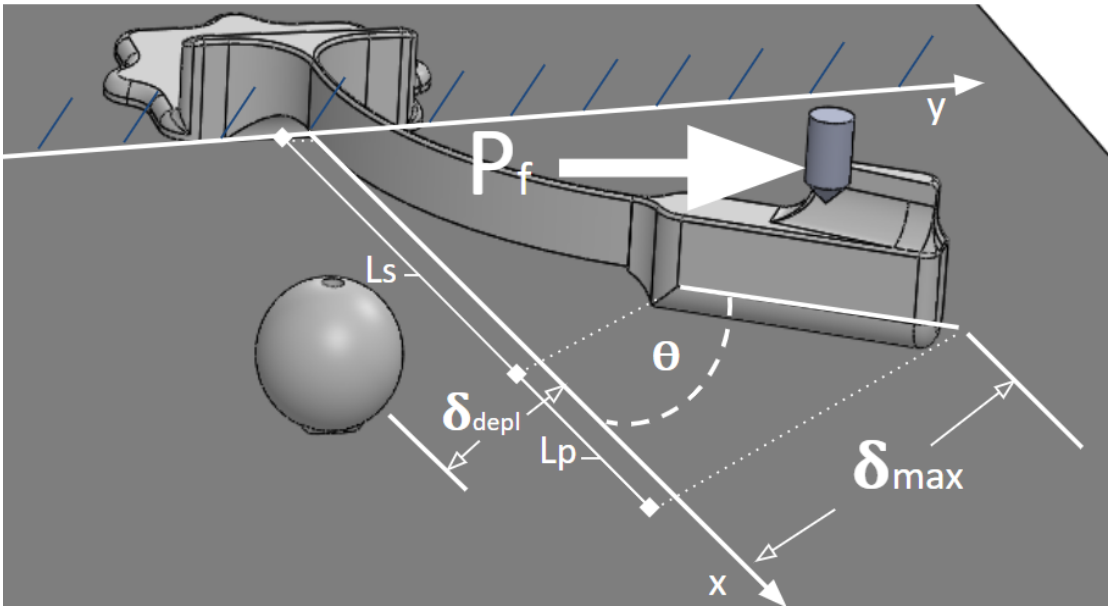

Figure 4.6: Visualization of deflected ISA with relevant parameters in mathematical model.

4.3.1 Modeling of in-situ actuator

As a cantilever spring, the theoretical performance of the ISA was modeled using beam energy methods [Chen, 2010, Ou et al., 2010, Chung and Yoo, 2002]. Figure 4.6 visualizes the parameters regulating the following equations. To calcu-

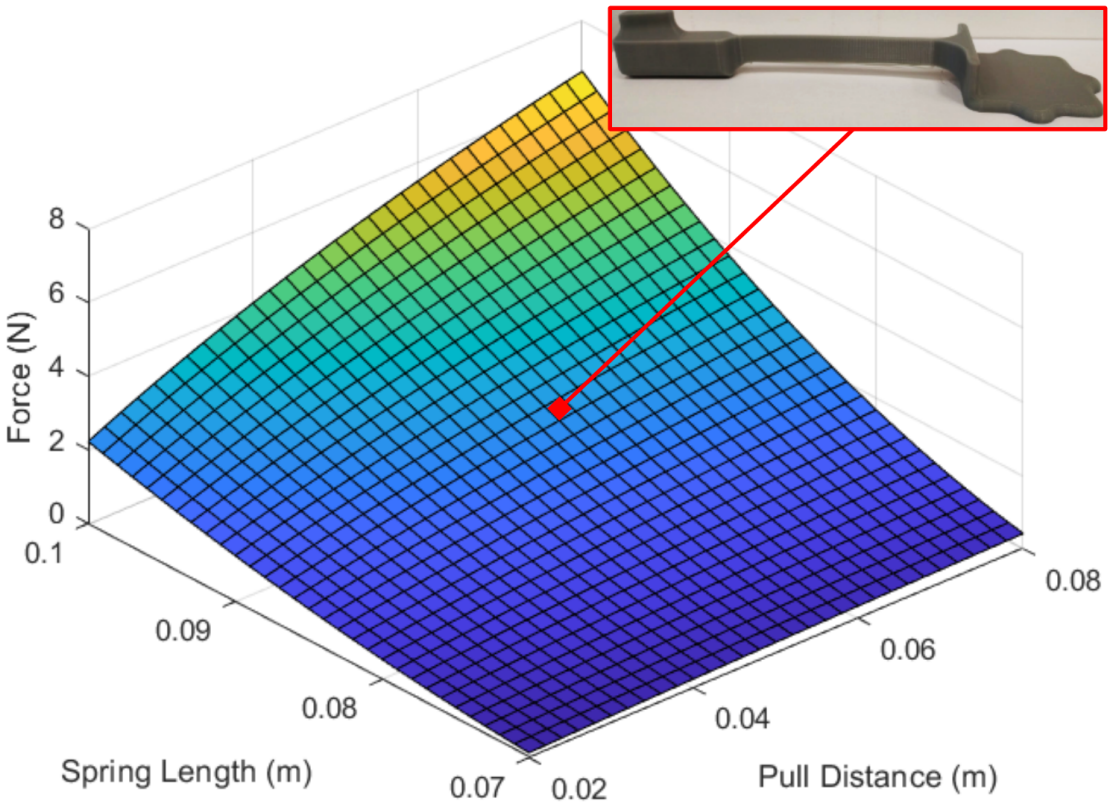

Figure 4.7: Design space demonstrated for ISA on the PRUSA FFF platform. The actuator designed for this investigation was chosen to allow for a large build volume and a modest pull distance, so as to not excessively plastically deform the spring after each actuation, allowing for higher endurance.

late the strain energy of the actuator (U_a), the bending inertia (I_b) must first be taken as a function of the spring's geometry:

$$I_b = \frac{width^3 \times height}{12} \tag{4.5}$$

This, and the actuator's linear deflection distance in Equation 4.6b, is substituted into Equation 4.7 with respect to the printer interface tab (S_p in Equation 4.6c), the pull force by the printer on the actuator's tab ((P_f) in Equation 4.6a),

and the modulus of elasticity (E).

$$P_f = \frac{3EI_b\delta_{max}}{S_p^3} \tag{4.6a}$$

$$\delta_{max} = \frac{P_f(L_s+L_p)^3}{3EI_b}(2L_s+3L_p) \tag{4.6b}$$

$$S_p = \sqrt[3]{2L_s^3+7L_s^2L_p+8L_sL_p^2+3L_p^3} \tag{4.6c}$$

$$U_a = \frac{P_f^2\ S_p^3}{6EI_b} \tag{4.7}$$

The rotational inertia (I_r) of the spring was determined as

$$I_r = \frac{m_sL_s^3}{3} + \frac{m_p\left(W_p^2+L_p^2\right)}{12} + m_P\left(L_s+\frac{L_p}{2}\right)^2 \tag{4.8}$$

L_s is the length of the spring, m_s is the mass of the spring, L_p is the length of the paddle, W_p is the width of the paddle, and m_p is the mass of the paddle section. The cantilever spring was assumed to be an ideal rod, and the paddle section was assumed to be a rectangular prism [Lee, 1995].

With rotational inertia known, the angular velocity of the actuator can be found, expressed as

$$U_{\mathrm{a}} = \alpha U_{depl} + \frac{I_r\omega_{depl}^2}{2} \tag{4.9}$$

Equation 6.40 can be used to find the angular velocity of the actuator (ω_{imp}) on impact with the printed object. The energy at the impact point, U_{depl}, was found using Eq. 4.7, with δ_{depl} taken as the distance to the object impact location as opposed to δ_{max} in Eq. 4.6a.

The angular velocity at impact is used to find the velocity of the paddle during deployment, where r_{depl} is the radius to the impact point. When paired with the mass of the deployable object (m_{depl}), Eq. 6.41 was used to find the deployable object's kinetic energy (D_{KE}) the moment after deployment [Kane et al., 1987].

$$D_{KE} = \frac{1}{2} m_{depl} (\omega_{depl} r_{depl})^2 \tag{4.10}$$

The initial velocity of the deployable object could then be found. Velocity loss from overcoming the adhesive force was modeled using Equation 6.42,

$$V_{loss} = \frac{A_{depl} \mu D_b}{m_{depl}} \tag{4.11}$$

where A_{depl} is the contact surface area of the deployable object on the build-surface, an adhesion coefficient μ [Sanatgar et al., 2017, Pan et al., 2016], and D_b is the break time. The normal frictional force at the manufacturable, deployable scale of objects for sequential FFF is significantly smaller in total force contribution than the adhesive forces and was consequently neglected as an assumption [Arakawa, 2017, Coogan and Kazmer, 2017, Spoerk et al., 2018].

Work energy equations can then be used to find the force on the deployable object. This distance was taken to be equivalent to the radius of the object due to its spherical geometry. Eq. 4.12 gives the impact force and Eq. 4.13 gives the equivalent impact force if losses are taken into account.

$$F_{impact} = \frac{D_{KE}}{r_{depl}} \tag{4.12}$$

$$F_{resultant,equivalent} = \frac{m_{depl} \left(\sqrt{\frac{2 D_{KE}}{m_{depl}}} - V_{loss} \right)^2}{2 r_{depl}} \tag{4.13}$$

The design space of the ISA modeled through the equations above is visualized in Fig. 4.7.

4.3.2 Configuration and Operations for Automated Deployment

The deployment configuration of the ISA is visualized in Figure 4.8. Figure 4.8A describes the ISA with major features and dimensions. The ISA automatically deploys an object in Figure 4.8B. The object - a sphere with a flat base - is created as a representative object meeting the criteria in Equation 4.14, and to create as simple of an object as possible to reduce print time. The max pull back distance (δ_{max}), occurring at the point labeled 2 in Figure 4.8C, corresponds to a normal distance of 5.0 cm and an angle (θ) of 60 degrees along the arc. While a larger pull back would provide more energy and thus be more desirable, it was a compromise providing a reliable release from the printer toolhead and was more controllable and repeatable through G-code. Figure 4.8D demonstrated the release of the ISA by the printer toolhead, visualizing the trajectory of both the actuator after toolhead release and the demonstration object [Laplume et al., 2016].

Several assumptions influenced the design of deployable objects for use with ISAs. Concerning the build surface, the parameters presented to the demonstration object are applicable for smooth polycarbonate (PC) with a thin (approx 0.1 - 0.2 mm) layer of polyvinyl alcohol (PVA) adhesive applied on the build surface to ensure repeatable adhesion - these materials are very common for FFF platforms [Laplume et al., 2016]. It is also assumed that the density of the object is low enough that the normal-frictional force is negligible with respect to the adhesive force holding the object to the build surface. To fit the actuator in its current configuration, it is assumed that 25 cm by 20 cm is available on the build surface

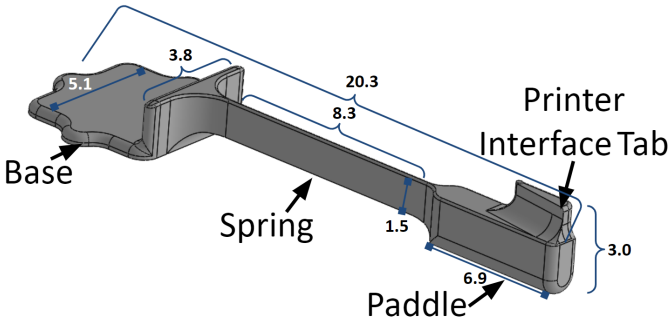

A. ISA design. All units are in cm.

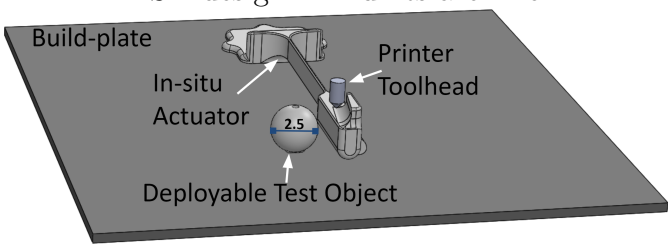

B. Example set-up for automated deployment, utilizing ISA to eject the deployable test object. Features are individually labeled, and units are in cm.

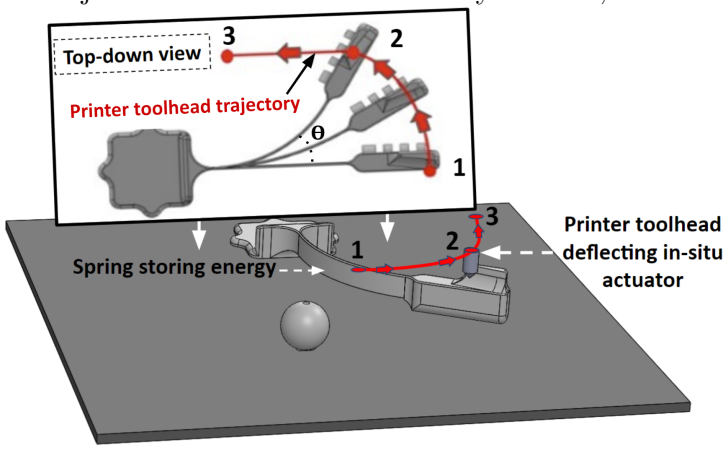

C. Visualization of the toolhead's toolpath to deflect the ISA, storing energy utilized for deployment.

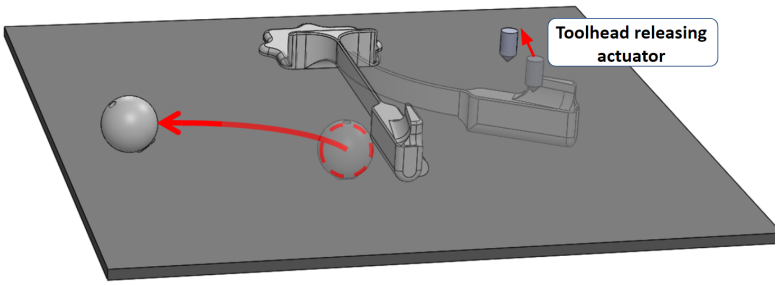

D. Toolhead releases actuator at specified point, deploying the fabricated object by impacting, detaching, and consequently ejecting it from the build-surface.

Figure 4.8: Concept of operations for the ISA deploying the demonstration object.

for the test to be performed successfully.

Deployable objects are primarily limited by geometric constraints. The deployable object must have a striking surface configured such that the force of the paddle can be directed through the objects' center of gravity to maximize the efficiency of energy transfer. The object must also be no taller than the top of the tab of the actuator. This is due to physical interference by the print head assembly on the adjacent deployable object. For example, the actuator used in this section imposes a maximum object height of 2.5 cm. Another limitation is that the build surface contact area with the deployable object needs to be small enough such that the resulting force in Equation 4.12 is positive. Rearranging this equation for a given impact force gives the maximum contact area as Equation 4.14. If the conventional contact area is too large, standoffs may be inserted into the object design to reduce the contact surface area to comply with the following design rule:

$$A_{contact} \leq \frac{F_{impact}}{\mu} \tag{4.14}$$

Additional limitations for deployable objects are driven by the location of the object on the build surface, as demonstrated in Figure 4.9. The entirety of the object must be located within the object range. This ensures that fabrication of the object does not interfere with the actuator. The center of gravity of the object must also be within the center of gravity (CG) range indicated by Figure 4.9. This area is normal to the motion of the actuator's paddle, and enables the energy stored in the actuator to be transferred through momentum. The homing and actuator ranges indicate zones that must not be occupied by the deployable object as they are used by i3 FFF printers for both homing and calibrating, and the actuator's necessary surface area during the energy storage stage for deployment.

Any rotation, mirror symmetry, or translation on a larger build surface can be easily utilized so long as the toolhead calibration path lies within the homing range or outside of any of the highlighted regions. A 2.5-cm sphere was utilized as a geometric basis for the sequential deployment test object. This was due to the relatively simple and well-defined mechanical dynamics and aerodynamics associated with a sphere [Cross, 1999]. The test object's deployment sequence is demonstrated in Figure 4.10.

The actuator was designed to impart 2N force onto the test object, while the test object was designed to release at 1N force to provide a reliable deployment which accounted for error. A flat standoff with appropriate contact surface area was used to achieve both of these design goals, and was accomplished by tailoring the surface area of the sphere in contact with the build-surface per [Mazhari et al., 2020b]. Rapid prototyping methodology proved crucial to the iterative optimization of these constraints [Zhou et al., 2015, Kokkinis et al., 2015]. The resulting toolpath test configuration and physically prototyped implementation is provided in Figure 4.11.

4.3.3 Digital Modifications to Synchronize the Platform for Deployment

The synchronization protocol for pairing a toolhead to the ISA's printer interface tab involved inserting a G-code subroutine into the actuator and demo object routine. Pairing the toolhead with the interface tab was conducted by first localizing the FFF nozzle after actuator manufacturing had been completed. By inserting G-code commands to create a cylindrical extrusion of the machine's minimum feature size on the last layer of fabrication, the toolhead always finished at the same coordinate location. This is crucial as the following process amounts

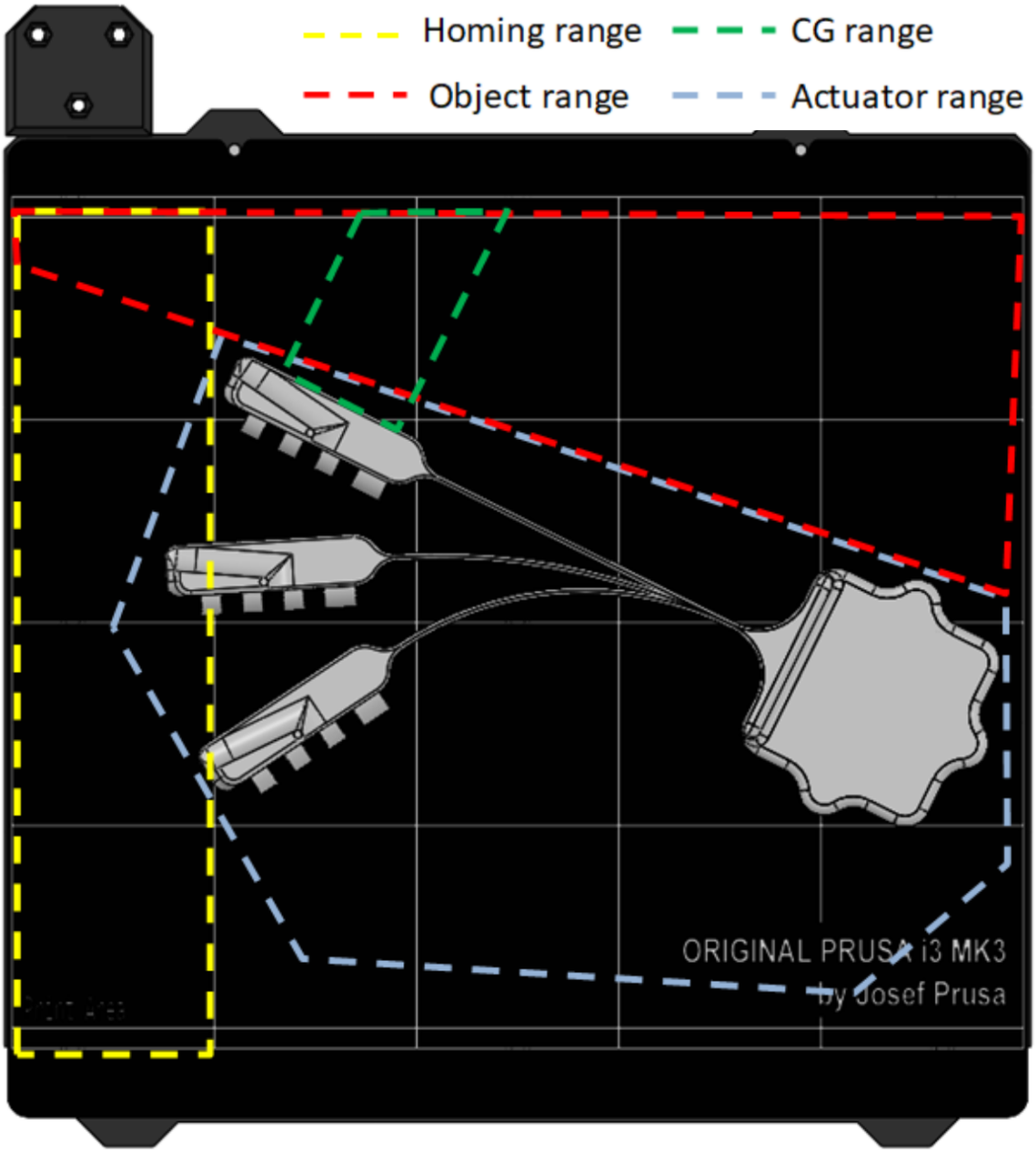

Figure 4.9: Visualization of regions on the build surface for an ISA. The test configuration utilizes a Prusa i3 FFF printer build surface. The red region provides the surface area a deployable object can occupy, so long as its center of gravity lies within the the green region for ensured contact with the ISA and deployment from the build surface. The yellow region is the homing range and is required by the printer to recalibrate its axes, and must be clear of any objects. The blue region indicates the surface area covered by the ISA and toolhead during deployment stage, which also must be clear of objects.

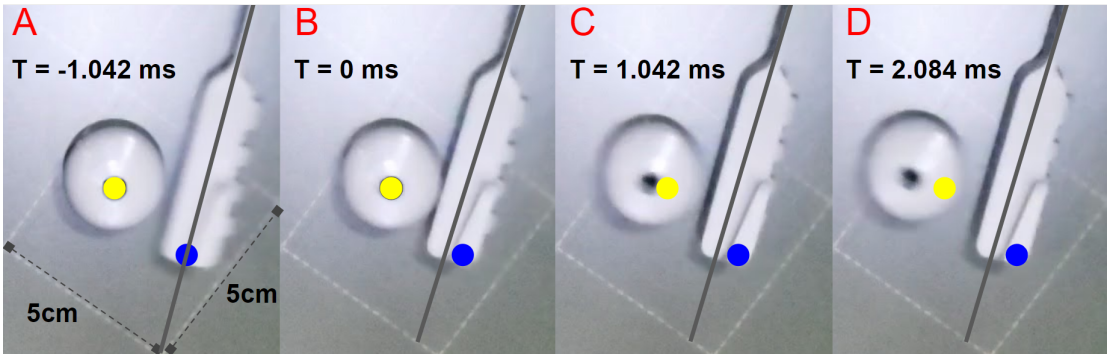

Figure 4.10: Deployment sequence of ISA taken at 960 frames per second. The yellow and blue dots indicate the original positions of the deployed object and ISA, respectively. The line along the ISA demonstrates the movement of the paddle during deployment. The figures are sequentially presented as follows: A) actuator released, B) actuator impacting fabricated object, C) one frame after impact, and D) fabricated object deploying from platform.

to dead reckoning. From there, the toolhead translated to the interface tab, where a trial and error process to develop the arc of movement along the actuator deflection path followed, which was then inserted as a series of commands to make as smooth of an arc as possible. These commands deflected the actuator up until the predetermined θ. The head was then programmed to slide parallel along the interface tab, releasing the actuator and dislodging the demo object.

4.3.4 Digitally Automating Sequential AM

To repeat the fabrication and deployment of an object and to standardize the modifications such that any object could be repeatably automated for deployment, MATLAB scripts were written which modified an object's toolpath to retrofit the capabilities. The script takes a user's toolpathed object and inserts a subroutine to manufacture an actuator, rotated and positioned to deploy the object off the

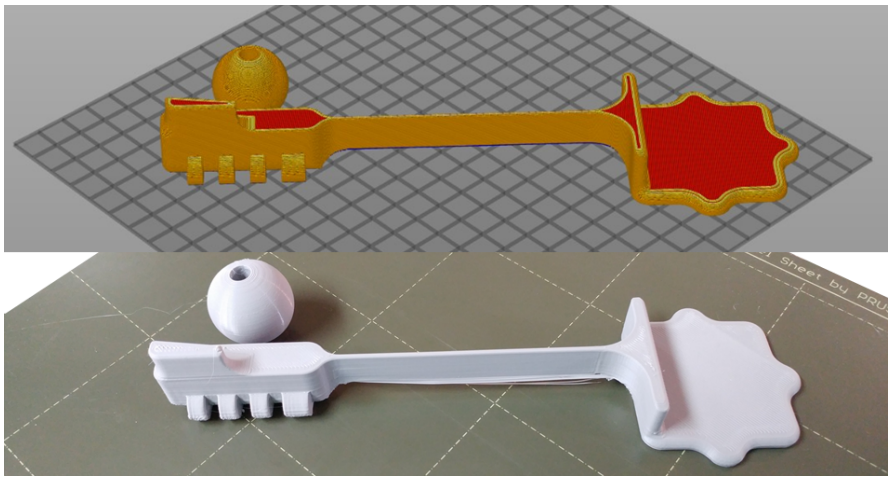

Figure 4.11: (Top) Toolpathed configuration of the ISA and deployable test object. (Bottom) Manufactured result from toolpathed geometry.

platform. The script then inserts commands to synchronize the deposition head, deflect the spring after fabricating both objects, and deploy the deployable object off of the build platform, as seen in Algorithm 1. The script interacts with the user by inquiring for the number of desired copies of an object.

The scripts can either be programmed to directly begin manufacturing the sequential objects after printing of an actuator, or reprogrammed into the platform after a deployment by toolpathing and sending new G-code to the printer. This allows the user the ability to either preprogram the repeatable, automated sequential fabrication and deployment of a certain set of desired components, or wait for the command to start a new object after each deployment. The latter configuration introduces the possibility of automated iterative testing configurations, fabricating a set of differing prototypes manufactured sequentially. This process is demonstrated in Algorithm 2.

Algorithm 1: Retrofitting In-Situ Deployment

Input: Object geometry file to be deployed
Output: G-code file to deploy object
Use slicing program to get G-code file of object located at coordinate system origin
if *Add ejection base to object* **then**
    Translate object z coordinates up
    Add ejection base to G-code file
else
    Replace bottom of object with ejection base G-code
end
Translate coordinates in G-code file
if *Add actuator* **then**
    if *Default actuator orientation doesn't fit on print bed* **then**
        Translate and rotate leaf spring or actuator as needed
    end
    Add ejection actuator to G-code file
end
Add ejection pull to G-code file
if *Add repeats* **then**
    Append number of copies of object to G-code file
end

Algorithm 2: Fabrication Workflow and Deployment Execution

Input: G-code file to deploy object
Output: Deployed object(s)
Upload G-code file to printer and start print
if *Multiple objects to be printed* **then**
    Set up receptacle
end
Printer prints actuator and first object
Printer deploys object
while *Multiple objects left to be printed* **do**
    Printer prints subsequent object
    Toolhead deflects actuator
    Printer deploys object
end

4.4 Testing Retrofitted Deployment for Automated Sequential AM

Reliability becomes a challenge when addressing automation of ISD methods. The systems need to be robust enough to remove humans from the loop without posing negligent harm to the machine, as per Ref. [Parasuraman et al., 1993] and Ref. [Parasuraman and Riley, 1997]. To test this, an experiment was conducted to measure the repeatability and reliability of the deployment methods. The design of this experiment consisted of executing each method and observing whether the printer was able to deploy the object from the platform successfully and clear the build surface. To determine the life cycle of an ISA, thirty tests were conducted with the same configuration of sequentially deploying the sphere. This demonstrated a maximum of 200 sequential fabricated components. The criteria for a successful sequential object was similar to the reliability experiment; the objects were collected in a bin shown in Figure 4.12 and counted at the end of the test. In Figure 4.13, we provided the results of the 30 ISAs, each allowed to sequentially fabricate and deploy objects until they failed. We limited each actuator to 200 deployed objects to conserve PLA feedstock.

As noted in Table 4.4, the leaf springs were not reliable and unable to be automated. They consequently received a 0% reliability mark. The manual hand deployment proof of concept described in Section 4.2.3 provided an average of only 2 per 100 leaf springs fabricated manually deploying off of the platform through the process. As the utility for sequential AM comes as a virtue of automation, precisely actuating the leaf spring 0.2 cm reliably proved to be difficult. Approximately one in three of the failures that occurred required human intervention to continue operation without damaging the machine. This failed the basic automa-

	In-Situ Leaf Spring	In-Situ Actuator
Max Force	0.29 N	2.00 N
Print Time (0.2mm layers)	7 min, per	82 min, per 100
Material Usage	0.50 g	21.90 g, per 100
Cost (PLA @ $30/Kg)	$0.02	$.66, per 100
Volume	0.54 cm^3	30.54 cm^3, per 100
Print Surface Area	1.33 cm^2	139.44 cm^2, per 100
Life Cycle	1	100+
Reliability	Automated, 0% | By hand, 2%	99%

Table 4.4: Comparison of design metrics of the two deployment techniques, with preferable results for sequential AM outlined in red. Results are provided with respect to requirements per object deployed, unless stated otherwise.

tion criteria, resulting in the development of the ISA.

4.4.1 Modeling the Cost and Throughput of In-Situ Deployment

The cost of producing batches of retrofitted automated deployment of sequential parts is provided from an economic and logistical perspective below. We note that these equations do not account for initial machine cost, as retrofitted deployment enables software defined sequential AM and adds no additional cost aside from feedstock material. Benefits of such automation are provided with respect to machines that are already procured by a user, are not covered already in Table 4.1, do not have automated capability and can be expressed as the following:

$$C_a = N_a C_o \tag{4.15}$$

$$C_m = N_m(C_o + C_l) \tag{4.16}$$

where C_a is the cost using the retrofitted automation, N_a is the number of

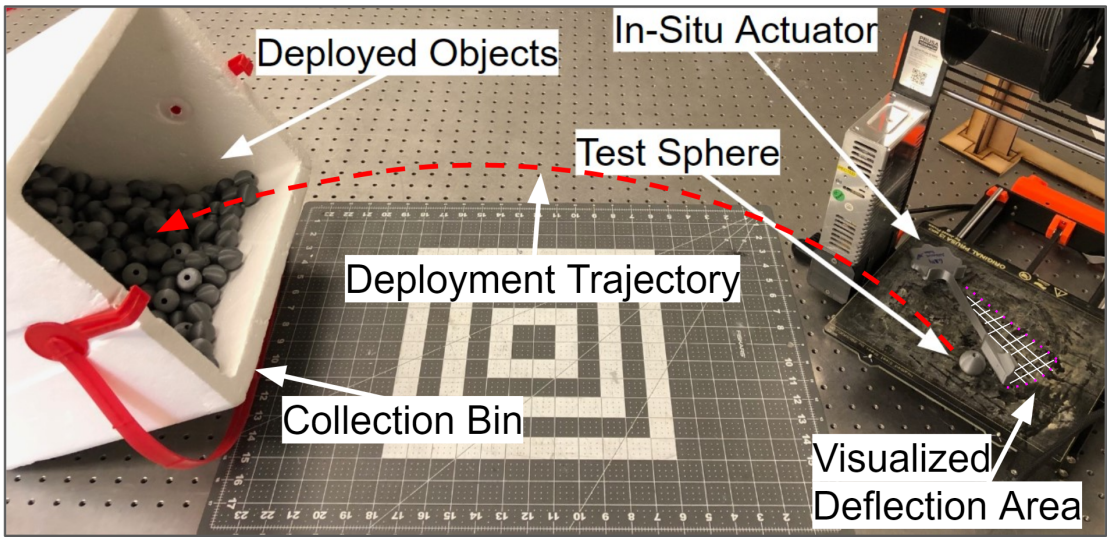

Figure 4.12: Experimental setup retrofitting deployment. The ISA and example of the test sphere is on the right, with the deflection area visualized. The test sphere's typical trajectory into the collection bin is also displayed, demonstrating the method to collect the deployed objects.

objects made with the automated system, C_o is the cost of the objects, C_m is the cost using a manual (non-automated) system, N_m is the number of objects made with the manual system, and C_l is the effective cost of labor per object.

Similarly the volume of parts manufactured per unit time can be obtained using the following:

$$Y_{auto} = \frac{W_a R_v T_o}{T_o + T_{c,auto}} \tag{4.17}$$

$$Y_{manual} = \frac{W_m R_v T_o}{T_o + T_{c,manual}} \tag{4.18}$$

where Y_{auto} is the throughput of the automated method in a sample window (e.g. 24 hours), W_a is the time within the sample window where the automated method is running, R_v is the volumetric print rate of the printer, T_o is the time to print an object, $T_{c,auto}$ is the time to cycle to the sequential object with an automated system, Y_{manual} is the throughput of the manual method in a sample

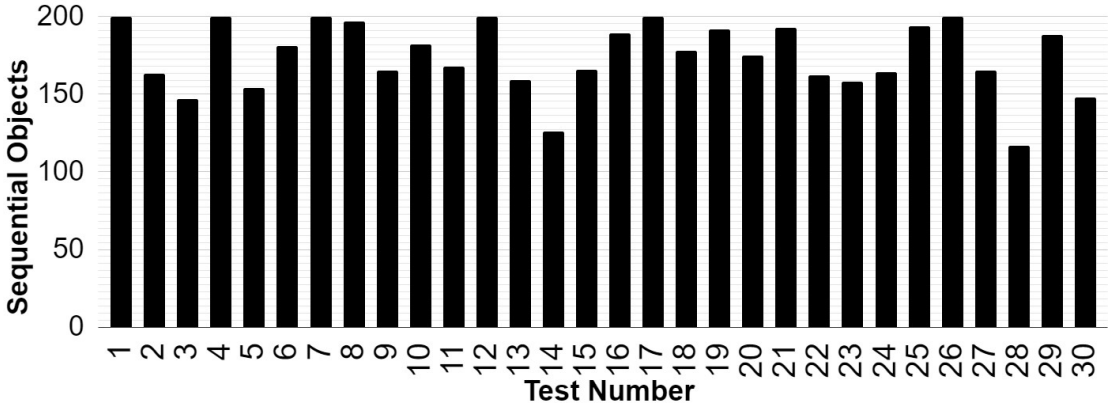

Figure 4.13: Results of life cycle testing of retrofitted automated sequential manufacturing with the ISA test configuration.

window, W_m is the time within the sample window where the manual method is running, and $T_{c,manual}$ is the time to cycle to the sequential object in a manual system. Additionally, the number of objects capable of being fabricated over time by the system is modeled below. A human in the loop system is provided for comparison to gauge the effectiveness of the automation method. To numerically illustrate this, the following equations describe sequential deployment of the demonstration object:

$$T_a = \sum_{i=1}^{ISA_i} (T_{ISA} i + \sum_{n=1}^{N_a} T_{N_a} n) \tag{4.19a}$$

$$T_a = \sum_{i=1}^{ISA_i} (82.5i + \sum_{n=1}^{100} 30.15n) \tag{4.19b}$$

$$T_m = \sum_{n=1}^{N_m} T_{N_m} n = \sum_{n=1}^{N_m} 35n \tag{4.20}$$

T_m is the time to make N_m number of objects with manual removal, and T_a is the time to make N_a number of objects with automated removal and T_{a_i} initial

set-up time. The actuator required 82 minutes of fabrication time, accounting for the time required to heat the extender's hot end and a 30 second interval to re-calibrate the platform. The demo object required 29 minutes for each fabrication, and a 30 second interval to cool down the hot end prior to deflecting the actuator. The printer was then programmed for another 24 second calibration interval and continued with fabrication of the next copy. The time required to fabricate and deploy a certain number of objects for this configuration becomes Equation 4.19, with conventional AM utilizing manual labor to remove the demo objects in Equation 4.20.

It is observed that the shorter the cycling time, the higher the throughput of the system will be. For the manual system, it is assumed that the time to remove the object and prepare the print environment takes exactly the same amount of time, which is only a best-case scenario. With an automated system, the delays are highly uniform and efficient. For a time window that exceeds a standard work day or other similar environment where a technician cannot be at a printer during completion (e.g. multiple printers or very fast print cycles), it may not be practical or financially viable to have enough technicians on hand to quickly attend to each object. These considerations are illustrated over a work week in Figure 4.14 to evaluate the logistical performance and benefits of the automated system with respect to manual removal. After extensive experimental observation, it was determined that the average time for a technician to prepare an AM system for a new job was approximately 5 minutes. This was used to provide a comparison of a manual versus retrofitted automation for printing the test sphere on both methods over a Monday through Sunday, 9am - 5pm full work week, rotational shifts providing manual labor for the entirety of the week (168 hours), and the automated AM system described.

From the figure, we can see that the benefits of the automation method become superior at 10 objects or greater. This is because the retrofitted printer must fabricate an actuator for the first 82 minutes. Each demo object takes 30.15 minutes each, which results in a throughput of 45 completed objects per day, a significant increase due to the increased window for serial fabrication due to the automated process.

Similarly, the throughput of the systems is provided in Figure 4.15 as a function of volume deposited with respect to cost. The cost of labor is taken conservatively, at $USD\$20$ per hour in addition to material cost of $USD\$30$ per kilogram, as outlined in Table 4.4. Each demo object requires $23.95cm^3$ of PLA, regardless of automated or manual methods. As the retrofitted automated AM platform is able to clear the build surface and continuously fabricate components without labor costs, Figure 4.15 shows that it has a higher throughput for the same cost than non-retrofitted methods. The cost savings for the automated method continue to grow as the required volume increases. It should be noted that these figures represent sequential fabrication of the demo object configuration. These figures jointly support that cost and time savings for automated sequential AM is proportional to increased build-cycling frequency and the quantity of objects fabricated sequentially. The demo part provides a baseline metric, and consequently objects requiring less time to fabricate would result in greater cost savings through automated removal. Similarly, fabricating an increased number of objects sequentially increases cost-savings as well versus manual removal by virtue of reliable automation.

It must be noted that the primary drawbacks from in-situ methods are the necessity for embedding deployability onto the sequentially fabricated objects, limiting the design space as defined in Sec. 4.3.2. As visualized in Fig. 4.9 the

actuator requires quite a large occupied space for full utilization and consequently constrains the usable deployable object range further. Additionally, the durability of the ISA limits automation to no more than 200 cycles until it must be removed by hand and re-retrofitted. Although the in-situ leaf spring method provided a favorable force-to-mass ratio, it could not scale past the designs provided and was not controllable by the printer; this method was only demonstrated by hand as a proof of concept. The ISA's reliability and ability to provide enough force demonstrates why the embedded leaf-spring method is not suitable for automated sequential AM.

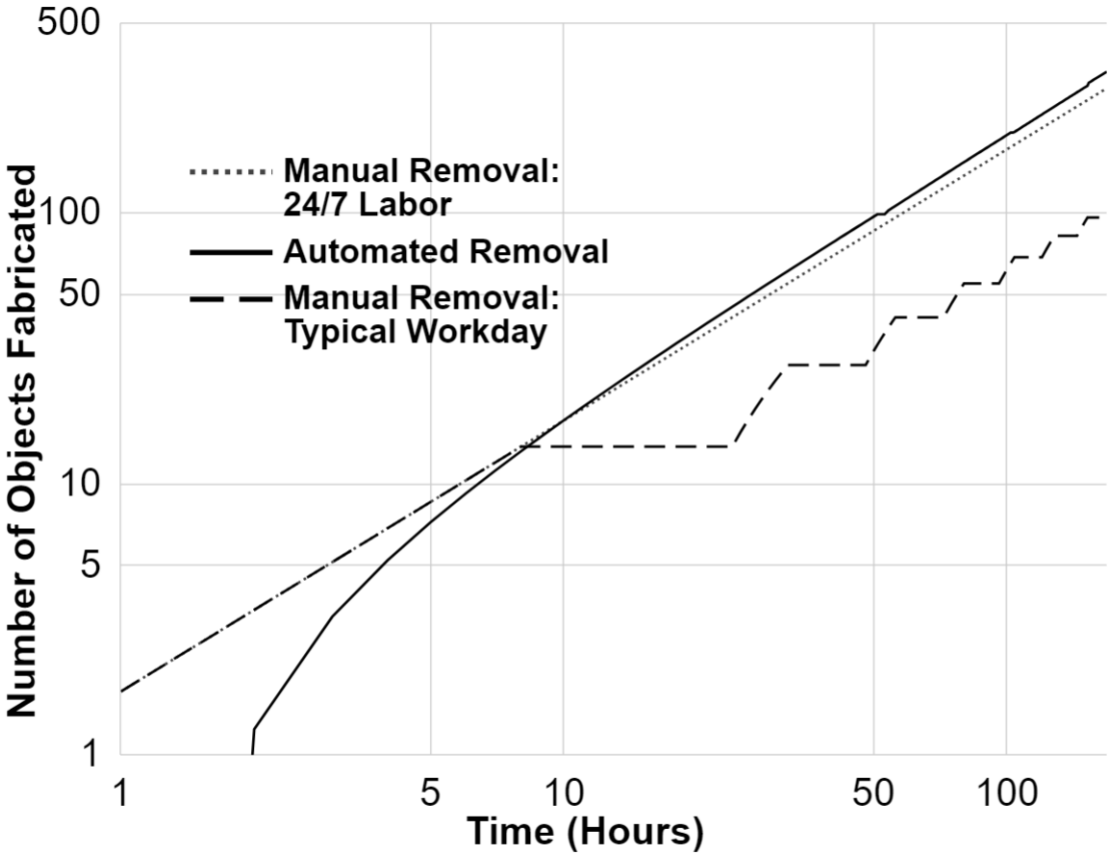

Figure 4.14: Comparison of sequential additive manufacturing throughput over seven days, under three paradigms. The solid line represents the number of sequential objects fabricated over a week in the testing configuration with automated removal through the ISA, with the two dotted lines representing two manual configurations. The first represents if labor was scheduled to continuously remove objects over 24-hour periods, and the other shows with labor present during typical 8-hour workdays, including weekend shifts. Due to the reliability demonstrated by the ISA, labor was only required to remove the ISA after 100 objects in the test configuration.

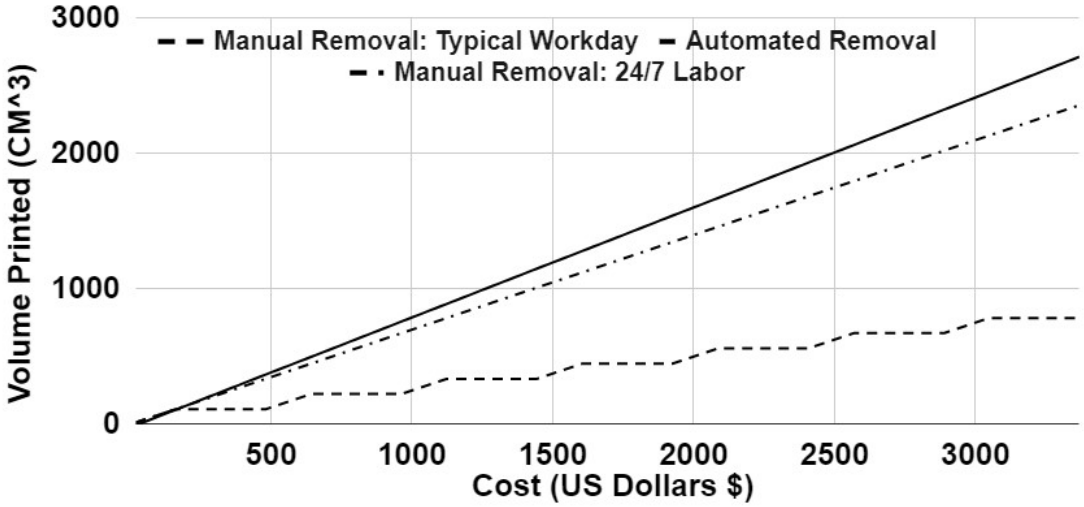

Figure 4.15: Comparison of additive manufacturing throughput of PLA on an i3 FFF platform versus cost under three paradigms. The solid line represents the volume fabricated over a week with retrofitted automated removal, with the two dotted lines representing labor present to remove objects over 24-hour periods and another with labor present during typical 8-hour workdays, including weekend shifts.

4.5 Conclusion

This section has presented designs, demonstrated prototypes, and compared novel and low cost methods for retrofitting ISD to enable sequential AM on FFF platforms. By printing two different configurations of springs onto the build surface and utilizing the printer toolhead as a software-defined robotic manipulator for deflection, ISD can be implemented onto common open source platforms. With this concept, a printed object on an FFF printer required minimal human interaction in order for it to be removed from a build surface for high-throughput sequential AM. The first method utilized ISLS, and integrated leaf springs onto to objects which would deploy through deflection. While bringing the benefit of a relatively small deployment footprint, the modeling and subsequent prototyping for this method provided an initial a proof of concept which partially met the required design specifications. The ISLS method was evolved into the ISA as it was limited in scalability and unreliable within its design envelope due to the small and precise deflection required by the toolhead.

The second ISD method was the ISA, which was also modeled and tested in an experimental setup. The ISA evolved from the ISLS, but met all of the design specifications and successfully demonstrated over 4,500 PLA test spheres fabricated, deployed, and collected in cycles of up to 200 objects per batch without human intervention. This removal of labor from the manufacturing process enables a high throughput platform which costs less than $USD\$1$ and roughly 82 minutes to implement, while providing up to 99% reliability when limited to 100 automated objects. I predict that this ISD platform may be easily adopted due to the portability of the digital ISA retrofit. The implemented design framework allows for one of the most common additive platforms to deploy objects off of the build platform purely through toolpath modification, as no physical hardware is

modified on the machine. We successfully demonstrated that external hardware is not required to enable automated removal or deployment. The drawbacks of the ISA stem primarily from the footprint it requires for ISD, constraining the surface area available to deployable objects. Additionally, ISA's have a limited lifespan for each actuator and can reliably deploy 100 sequential objects prior to requiring a human to cycle the ISA and repeat the process.

Because of the robust nature of the second method, the experimental performance of the ISA were investigated further, modeled, and compared to manual labor schemes which required a technician present to otherwise remove the objects off every cycle of the non-retrofitted platforms. It was found that the ISA's retrofitted automation enabled a more reliable cycling of the build surface. This allowed for more objects to be fabricated than otherwise possible from a non-retrofitted system with a human-in-the-loop paradigm. In addition to increasing the throughput of sequential AM, these results significantly reduce the cost of object removal and automate the cycling of FFF platforms. Future work includes evolving the platform to allow for the automatic removal of the ISA at its end-of-life, which would further decrease the need for a human in the loop to increase throughput to the maximum capability of an FFF system printing sequential components.

Chapter 5

Automated Testing and Characterization of Additive Manufacturing

5.1 Introduction

This section demonstrates the techniques utilized to investigate methods for characterizing individual iterations of an object's deployed performance. The ability to automate the sensing of objects allows for rapid and successive iterations of each variation in an object's evolution. By leveraging different sensing protocols, one may increase the fidelity of performance-altering phenotypes for a given criteria. By physically deploying objects, translating momentum through the deployment spring, this section describes the methodology for sensing the performance of the objects once they have become airborne and detached from their build-plate.

Acknowledgements

The research and findings that are presented in this chapter were developed, consulted, and/or referenced alongside the following colleagues: Rachel Ticknor, Stanley Krzesniak, Sean Swei, and Mircea Teodorescu. Additionally, the content was published in Springer's *Journal of Material's Engineering and Performance* in the *Special Issue on Additive Manufacturing.* [Mazhari et al., 2021]

5.1.1 Sensing physical loads

To sense physical force, a single ended sheared loading cell was placed onto the build-tray to characterize kinetic energy through the ISA impact force through contact. Initially, the loading cell was used to provide a platform for detecting the ISA forces through repeated impact over thirty different paddles, each actuated 100 times. These insights allowed for not only characterization of the average deployment force from the paddle, but the deployer's fatigue through inspecting

the useful duty cycles.

To conduct this experiment, the paddle was pulled to its deployment deflection angle of 45 degrees, and released for a spring deflection of 2.75 inches. The loading cell was located two degrees from the origin, with the centroid of the loading cell, aligned with a complimentary two degree paddle centroid offset. This process was repeated for 100 cycles per paddle to provide insights to the life-cycle and force variability of each paddle in characterizing the error due to manufacturing.

It was found that after 100 cycles of deployment, the amount of force generated by each paddle was reduced linearly over the number of the cycle. This provides insight to the internal stresses compiling micro-fractures within the micro-structure of the thermoplastic PLA over the cycles. This testing was repeated for thirty paddles, identical in geometry, but varying in the batch of raw material used in their fabrication. The thirty paddles were composed of ten batches of thermoplastic PLA, with three paddles from each set of filament.

The strategy allows for investigating the conformance of error across multiple copies of the same component. This simultaneously allows for identification of error not only due to the precision of reproducing the geometry over the entirety of the paddle's life cycle, but also for insights to the variability of material lots. To characterize the variance of material lots, lot certification certificates were obtained from different vendors, tracing the PLA back to their original resin lots.

The resulting data demonstrated the invariability regarding the precision of making the paddle from the same batch of material provided a linear regression within two grams of force for a 98 percent confidence interval. The range between the different batches of the PLA was within 10 percent. The range of grams force generated by the lowest-performance paddle and highest from different material lots was under 25 percent. This maximum variance over the life cycle of the

paddles was surprisingly low, given the well-documented mechanical differences arising from thermoplastic filaments [Dudek, 2013]. A similar test was repeated for detecting the grams force of the deployed objects, utilizing a loading cell to detect force through impact. As seen in Figure 5.1, the load cell was relatively small, and a solution was required to ensure that the deployed objects would reliably and repeatably be registered by the cell's internal strain gauge.

Subsets of the results from this work inspired a higher fidelity directed study on automated characterization, whose results are provided in the ATCAM section.

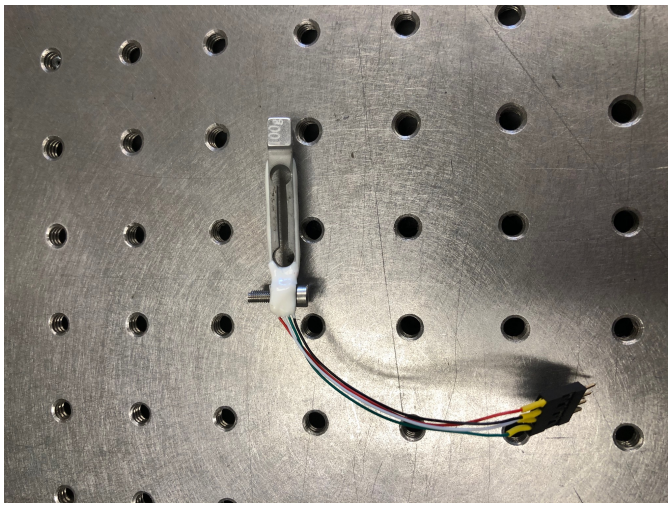

Figure 5.1: Example of 100g single ended shear beam loading cell utilized for physical sensing

To aid this process, the surface area sensed by the load cell was increased by laser-cutting a plate and attaching it to the load cell. This system is demonstrated in Figure 5.3. The subsequent error due to the induced moment and plate's dampening effects was characterized over a series of tests, spanning the range of the plate and a correction factor was accounted for. The modified loading cell was placed within the deployment trajectory.

A script was written with respective hardware implemented to automate the data capture of the loading cell. In the original configuration of this recording

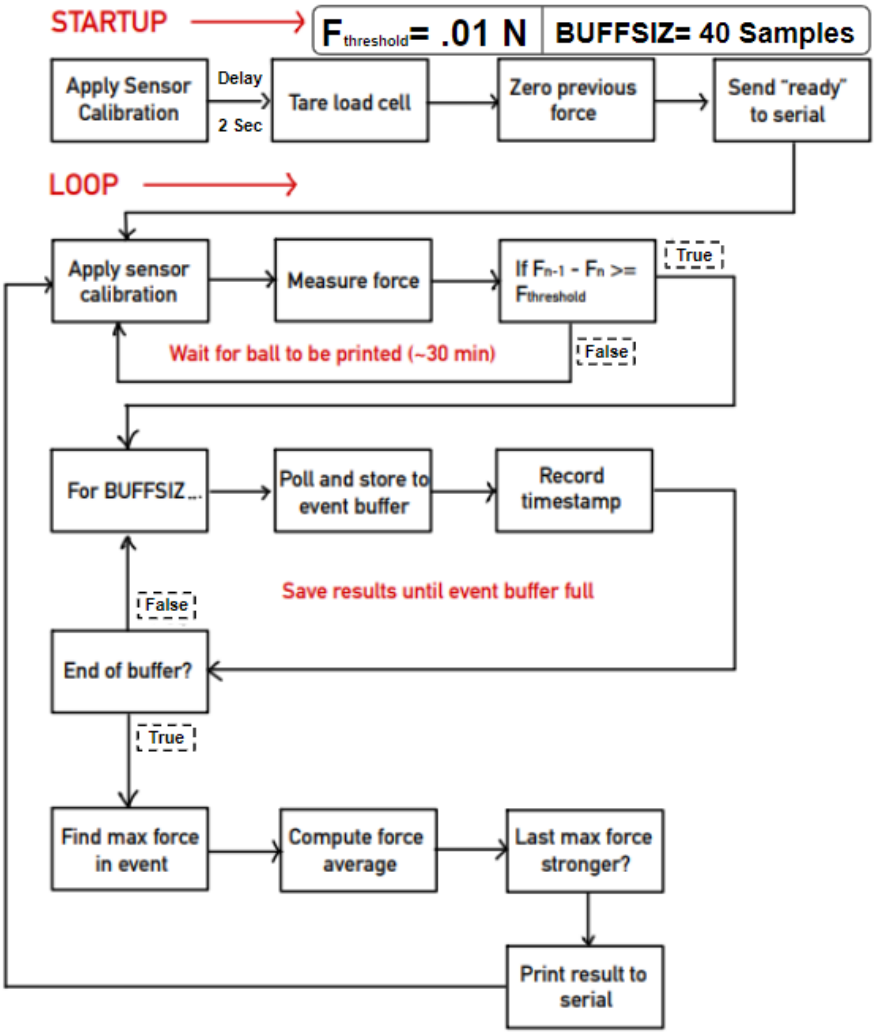

Figure 5.2: Sensor flow decision tree for data logging process

strategy, a microcontroller was actuated at the beginning of the automated manufacturing and deployment cycle. Through physical testing, the frequency of the data sampling rate was converged to 10hz, taken as the minimum threshold to capture the data correctly without generating redundant noise. The selection of 10hz was also a hardware limitation, serving as the blend of data fidelity and polling rate of analog-to-digital conversion. To store this data, code was generated to output the signal received from the loading cell to an independent file placed on the microcontroller's storage.

As the manufacturing and deployment intervals were well-defined, an investigation was done on methods to turn off the sampling during manufacturing slots, and turn it back on to capture the data as the platform was ready to deploy. Various methods were compared in regards to the necessary autonomy of the platform and the hardware the Prusa contained. In observing the manufacturing process of the printer, it was characterized that the machine's firmware regulated a command which would follow a homing sequence after a print and subsequently inform the printer's user of successful fabrication process completion with an audible alarm.

To attain that signal as the indicator for initiating the sensing microcontroller's signal capture, the platform was disassembled and the alarm's signal line was traced to its origin. It was determined that due to the electrical considerations taken into the alarm at that point of the circuit board, it would be impractical to utilize the alarm trace as the regulator of initiating physical sensing.

Ideally, a digital command from the toolpath would be the initiator of such sensing. Due to the complexity of controlling a separate machine as a function of a toolpath on-board a non-networked system, a workaround was found in wiring a physical switch which would allow for a user to press the button once the printer's audible alarm was heard to start the sensing. This would be automated by employing a microphone as an audible sensor for initiating the physical sensing subsequent to the print in preparation for a deployment.

A major issue with this configuration was with respect to the audible threshold for starting the data capture, which provided a source of error from false signals due to background noise. Although the necessary amplitude of initiating signals was increased, the false signals due to even conversations taking place around the machine proved to dictate a more sustainable solution. This issue was addressed by developing and integrating a method to connect the printer through a network

regulating multiple digital platforms.

After investigating existing solutions to network 3D printers in regulating and monitoring toolpaths, Octopi was utilized. This open-source software serves as a networking interface between multiple 3d printers and the sources which control them. The platform was developed to serve for remote fabrication monitoring, and as such its interface, APIs, and functionalities are tailored and limited to receiving information from the manufacturing process more-so than transmitting and actuating it.

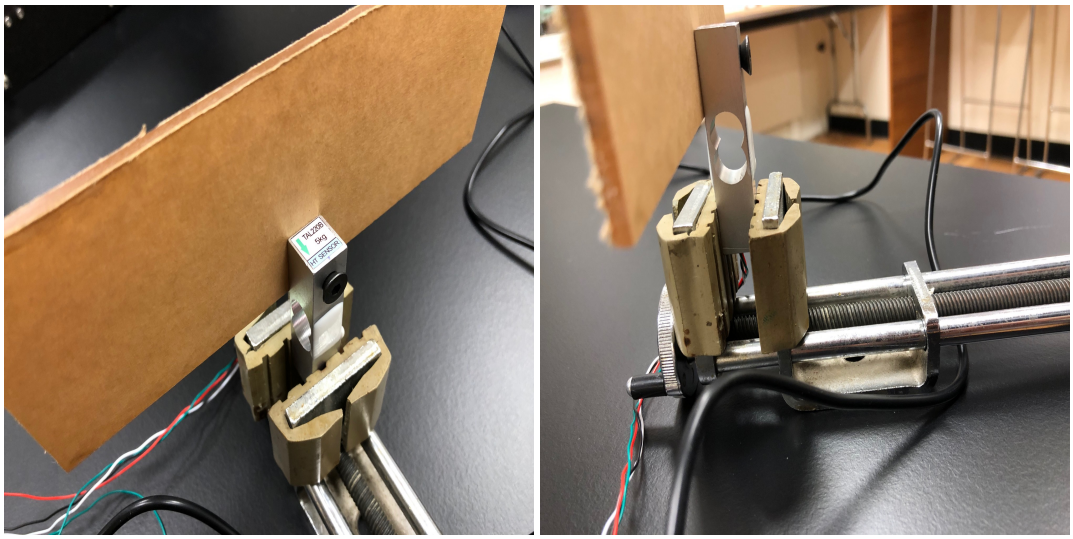

(a) System view of modified physical sensing platform

(b) Side view demonstrating attachment mechanism for the loading cell modification

Figure 5.3: Modifying the physical sensing of deployed objects by increasing the applicable surface area in contact with the loading cell.

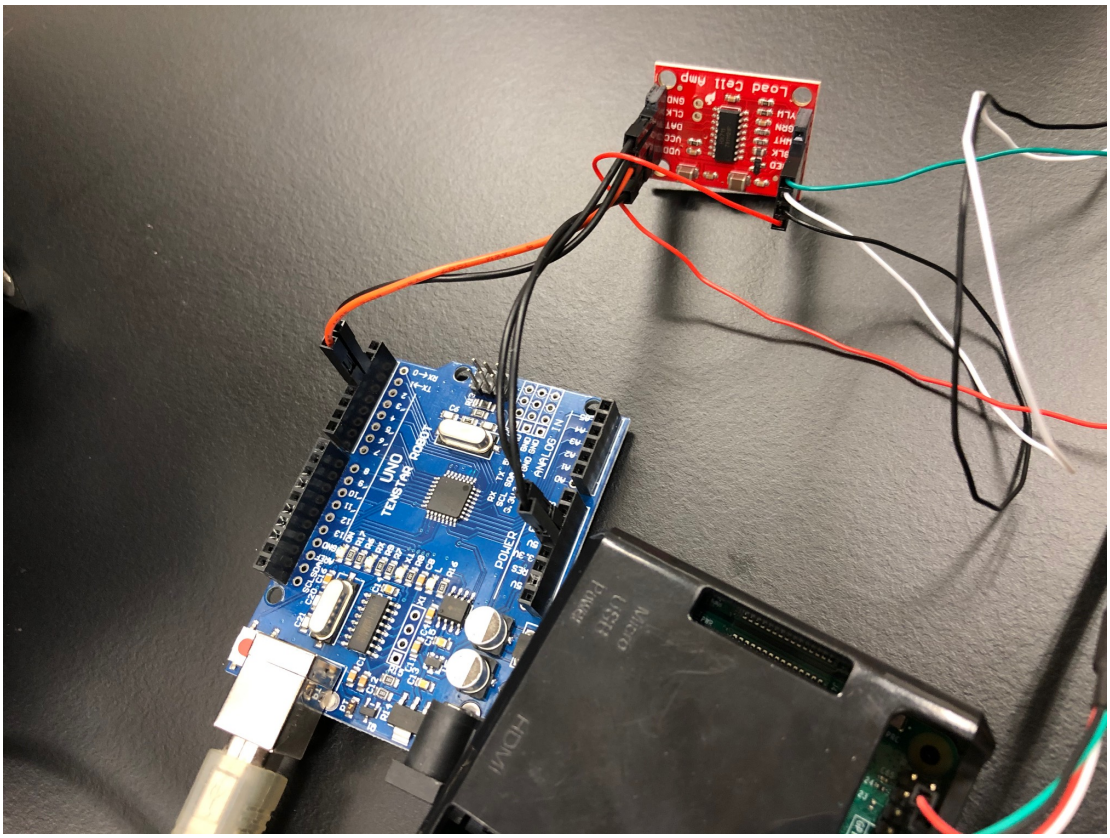

Figure 5.4: Microcontroller for sensing physical force of deployed object

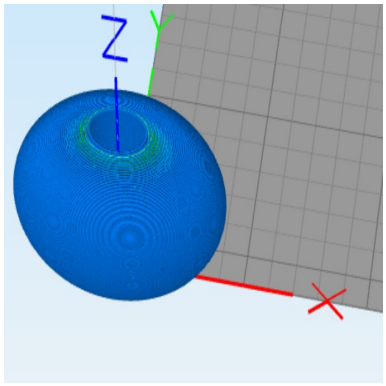

(a) Example of scripted toolpathing of a varied phenotype. The object defaults to the xyz origin.

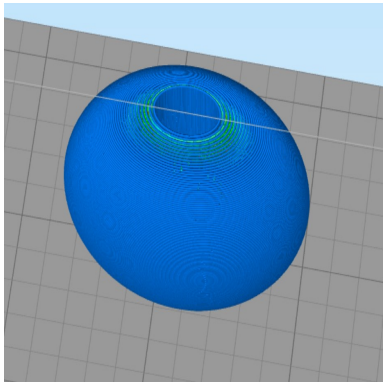

(b) Example of toolpathing a varied phenotype, automatically shifted for deployment.

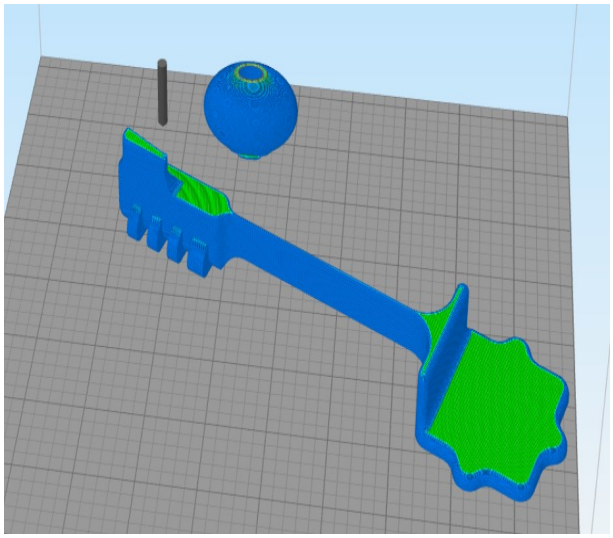

(c) Example of toolpathing a varied object phenotype, automatically shifted for deployment.

Figure 5.5: Visualization of toolpathing scripts varying phenotypes and shifting object for deployment, respectively.

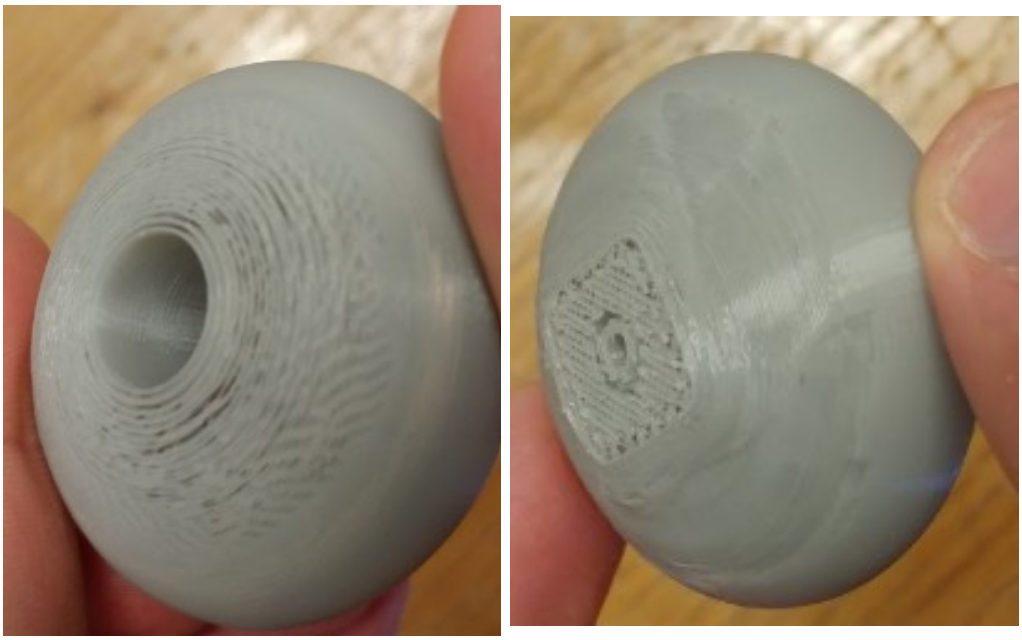

(a) Top of object, demonstrating slight under-extrusion as a function of layering effects.

(b) Bottom of object, demonstrating success of deployment platform and toolpathing strategy

Figure 5.6: Visualization of toolpathing scripts varying phenotypes and shifting object for deployment, respectively.

5.2 ATCAM

As an emerging material process, additive manufacturing (AM) continues to increase in industry adoption due to its versatility to realize novel geometries, provide highly tailorable object performance, and reduce costs by virtue of digital dependencies and automation [Bourell et al., 2014, Tofail et al., 2018, Babu et al., 2015]. These realizations are not only highly dependent on precision within the manufacturing process parameters, but require tight control of the AM feedstock material as well [Hassen and Kirka, 2018, Lu and Wong, 2018]. It has been well-documented that low-quality AM feedstock can reduce predictability within the fabrication process [Yang et al., 2018, Vargas et al., 2014] and account for a large contribution to the inertial error that engineers account for within the design-for-manufacturing process [Tofail et al., 2018, Chua et al., 2017, Arias-Montano et al., 2012a]. This has the knock-on effect of frequently burdening AM designs with redundancies [Wood et al., 2012, Sanatgar et al., 2017, Hadley and McCarthy, 2011], numerous iterations [Wong, 2012, Floreano, 2015, Harvey et al., 2005], and proof testing [Hilton et al., 2015, Coccia et al., 2015] to accommodate the lack of engineering authority as per Ref. [Miller et al., 2016] and Ref. [Demoly et al., 2011]. Consistently generating and testing material coupons is critical to characterizing [Chua et al., 2017, Forster, 2015] and maintaining [Kim et al., 2018, Seifi et al., 2016] the AM process; however, this itself is both cost and time inefficient due to the relatively slow and laborious nature of fabricating materials and testing them on other platforms [Costabile et al., 2017, Koester et al., 2016]. Sensing platforms have been integrated into AM as a method to control the processing parameters in-situ, such as by Ref. [Trapp et al., 2017, Wang et al., 2017] and [Anderegg et al., 2019]; Ref. [Everton et al., 2016] notes that these methods have difficulty maintaining the tractability of errors within

the material process. Ref. [Cotteleer and Joyce, 2014] and [Kennedy et al., 2019] specifically note the difficulty of correlating AM directly to material qualities and reference the need for more research in this area.

This section presents a method that assists AM characterization by leveraging automation and machine learning to quickly generate and test large sets of data for Automated Testing and Characterization of Additive Manufacturing (ATCAM). The development of the method required the ability to generate and sense large amounts of empirical AM data. To attain this, the concept of a dynamic coupon and in-situ actuator [Mazhari et al., 2020b] are demonstrated, which allow AM material to be automatically fabricated and ejected sequentially for a high-throughput FDM process. Ejected coupons impact a load cell to generate a data point. Logging and repeating the process automatically allows for the rapid accumulation of a database, enabling many automated applications. This includes systematically identifying a feedstock's quality control, standardizing the calibration of a machine's processing parameters, understanding the sensitivities of an AM material under various conditions, recognizing a machine that is drifting from its intended material process, determining if a material is from a specific vendor or origin, embedding and detecting counterfeiting protocols, potentially adapting a design for its environment through repeated iteration and exploration of design space, among many others.

To test ATCAM's utility, three polylactic acid (PLA) feedstocks at differing price-points and effective quality were utilized to generate, deploy, and capture data from 3,000 dynamic coupons in batches of 1,000 coupons per feedstock, conducted with 100 coupons per in-situ actuator. The machine utilized was an open-source and widely available Prusa MK3S. Coupon impact force was logged through a load cell connected to an analog-to-digital converter attached to a mi-

crocontroller. The data was analyzed, correlated, and compared through three machine learning algorithms (deep learning, support vector machine, and boost gradient) supported by cloud computing with the DisplayR platform. At the time of writing, the entirety of this AM material testing setup costs less than USD $1,000. This made the test widely adoptable, portable, low risk, and highly cost-effective. Section 2 provides the methods utilized for creating ATCAM, with Section 3 presenting the data generated by the system and the machine learning correlations. Section 4 provides an analysis of the results, potential sources of error within the data, and discusses ATCAM's main findings. This work aids Section 5 by demonstrating the novel processes ATCAM introduces to AM testing and characterization within the limitations of the current configuration and provides potential next steps to improve the system.

5.2.1 ATCAM's Framework, Method for Implementation, and Testing Procedure

The concept of ATCAM was developed to integrate AM fabrication and testing into a single consolidated process. Fig. 5.7 provides an overview of the system's components, configuration, and process flow to automate the translation of AM feedstock into characterized data. In the following section, we present the system's framework and components in detail by their subsystem, describe how the platform functions, discuss the data output and provide the testing procedure used to analyze ATCAM's performance.

5.2.2 AM Platform

The additive manufacturing process utilized to develop ATCAM was FDM. This decision was primarily to increase the applicability of the platform, as FDM

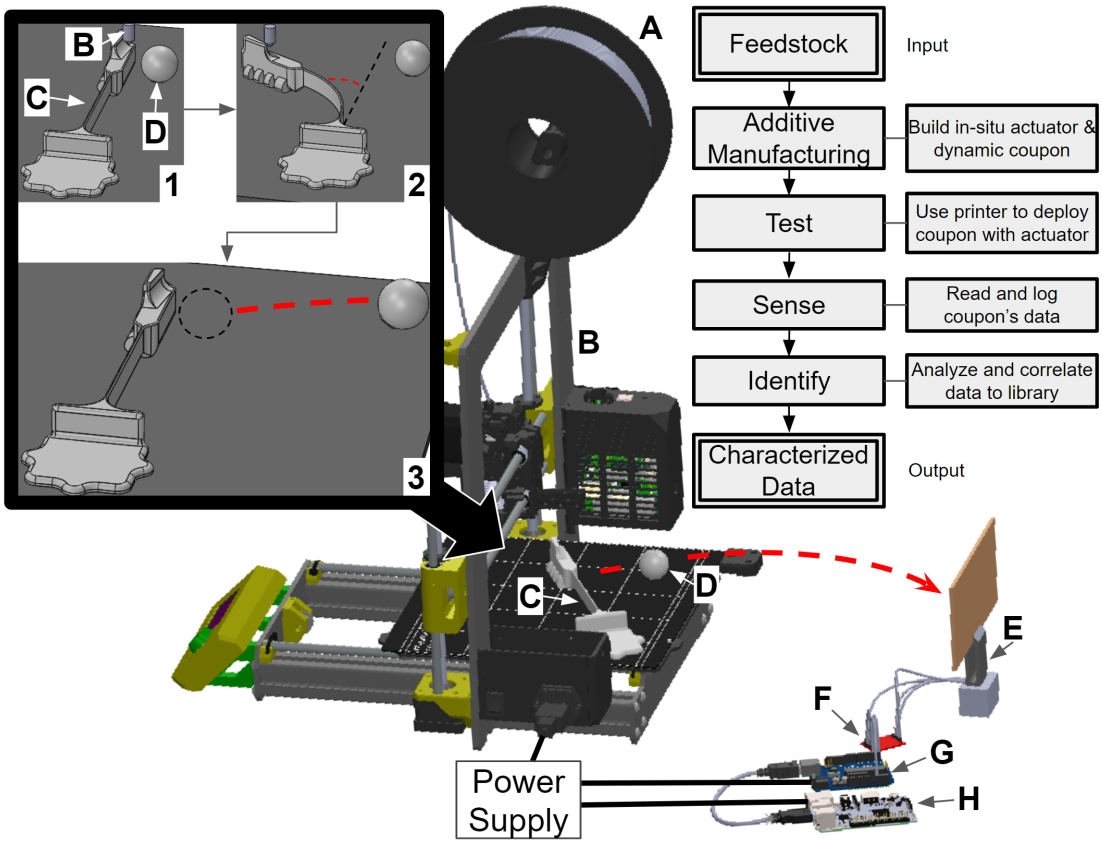

Figure 5.7: Rendering of ATCAM setup, including process framework. (A) is the feedstock material, (B) is the 3D printer, (C) is the in-situ actuator after deploying the dynamic coupon (visualized in (1 - 3) chronologically in the top left), (D) is a dynamic coupon under deployment following the black trajectory to impact the load cell, (E) is the load cell unit for physical load sensing of the impact of the dynamic coupon, (F) is a Wheatstone bridge equipped with a 24-bit analog-to-digital converter, (G) is an Arduino Uno to read and log the Wheatstone bridge data, (H) is a Raspberry Pi 3B to analyze and correlate the data.

is a widely accessible [Sells et al., 2010, Inoma et al., 2020] and relatively mature AM process [Jones et al., 2011, Galantucci et al., 2019, Nazir et al., 2020]. Additional consideration for selecting FDM was the wide variety of vendors available to source feedstock materials as demonstrated by [Stansbury and Idacavage, 2016], the relative low cost of the platform [Costabile et al., 2017], and the flexible nature of both the machine language (G-code) [Bowyer, 2020] and its firmware [Popescu and Amza, 2017, Sells et al., 2010, Jones et al., 2011]. Due to the open-market nature of FDM [Steenhuis and Pretorius, 2015], a wide variety of materials are available for the process [Sa'ude et al., 2018, Mazzanti et al., 2019]. The quality control of these materials typically varies significantly with price point and origin [Hassen and Kirka, 2018], making characterization of FDM materials a highly relevant challenge [Chua et al., 2017, Seifi et al., 2016]. Of the FDM machines available on the market, the Prusa MK3S [Prusa, 2020] was selected due to the robustness of the machine [Sierra et al., 2020], portability, cost [Brus and Barvíř, 2015], and ease of reconfiguration [Nasirov, 2019].

5.2.3 Dynamic Coupons and In-Situ Actuation

Developing a method to automate a high throughput characterization of coupons was not trivial; it proved to be the most difficult task in creating AT-CAM. This was primarily due to the lack of reference, as a literature review concluded that there is no practical integrated solution to fully automate the creation and testing of AM coupons. The association of mechanical properties with AM processing parameters has been documented in reviews by [Mandache, 2019] and [Rodríguez-Panes et al., 2018]. Works by Ref. [Lu and Wong, 2018] and Ref. [Chua et al., 2017] provide the critical need for consistent AM coupon testing to control mechanical properties and process quality, with Ref. [Honarvar, 2020] pro-

viding a novel strategy to use ultrasound for AM control. Ref. [Smith et al., 2018] discusses a method to integrate printed circuitry into structures for AM part health monitoring and crack detection, however this method of testing was not demonstrated as directly applicable for determining the quality of AM materials or processes and is highly object-specific. These works demonstrate that although constant testing is crucial for increased industry adoption of AM, there currently exists a testing throughput limitation for AM characterization due to lack of automation.

The premise of automation by in-situ actuation has been previously demonstrated through programmed interactions between AM platforms and printed parts, such as by [Aroca et al., 2017] and [Katakura and Watanabe, 2018]. In both examples, the modifications to the printers are not purely software-based, as physical modifications are made to machines to provide new capabilities. Our method allows for the retrofits to be printed and manipulated entirely in-situ through programmed revisions. We removed the need for physical modifications that were ex-situ to reduce the inertial error which can accumulate into the system. This is especially important for deducing the origination of an error source. Additionally, extensive physical modifications limit the adoption and portability of the system. [Besnea et al., 2018] provided insights into functional AM leaf springs, including associations regarding their deflections and energy storage. The springs in the results were not automated, nor were they deflected on the AM platform themselves, but they were referenced as a validated method for printed energy storage.

We developed dynamic coupons to address the technological gap between these different fields, allowing a large quantity of AM objects to be printed and tested entirely in-situ. The process works by printing an in-situ actuator (ISA) onto

the build surface [Mazhari et al., 2020b]. This allows for the printer to print and pull back the ISA on the build platform to eject objects and clear the surface for further parts. ATCAM leverages this by printing a 25.4mm (1-inch) sphere onto the build surface, utilizing the tool head and ISA to transfer energy to the coupons through high-force impact. This ejects and transports them to a load cell which detects the force of the coupon's impact. The cleared build surface is then used to print a subsequent dynamic coupon, and the ejection process is repeated. This process is repeated 100 times per ISA before manual removal, which was the experimentally determined non-destructive lifespan [Mazhari et al., 2020b]. One cycle of this process is visualized in the top-left (1-3) of Fig. 5.7.

The dynamic coupon was designed as a sphere for compatibility with the ISA to achieve reliable deployment within the 2N of force generated. A base was implemented on the bottom of the coupon to provide a tailored surface for deployment. This base also increased the coupon's manufacturability, as the surface area of the sphere's base was too small for the printer's configuration. The base's edges were integrated onto the dynamic coupon through a radius to decrease the overhang angle and increase manufacturability. An infill density of 20% was used in a rectangular configuration to increase the platform's throughput and minimize thermal issues occurring from dense raster patterns. This resulted in the coupon having a designed mass of 4 grams. A diagram of the dynamic coupon is provided in Fig. 5.8.

5.2.4 Physical Sensing and Data Logging

An aluminum 1kgf-rated single-ended shear loading cell was utilized to collect dynamic coupon impact force through contact. The load cell was calibrated against the manufacturer datasheet, providing measurement linearity of +/-0.5%.

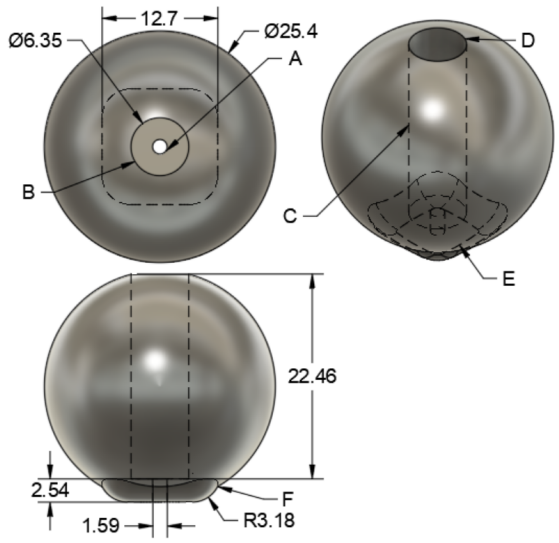

Figure 5.8: Technical drawing of the dynamic coupon. All dimensions given are in millimeters. Note A is a cavity in the base to reduce the surface area in contact with the build plate and ISA force required for deployment. Features B, C, and D describe a channel embedded within the dynamic coupon to reduce the material consumption and printing time per coupon. Feature B is the interface between the base and the channel in Feature C. Feature D is a cut that removes the need for the support structure which would be required if the channel was enclosed within the coupon. Feature E is the base on the bottom of the coupon which creates a tailored surface area and aids object deployment. Feature F demonstrates the base's external geometry, notably an incorporated radius to reduce the overhang angle from the base to the rest of the coupon to increase manufacturability.

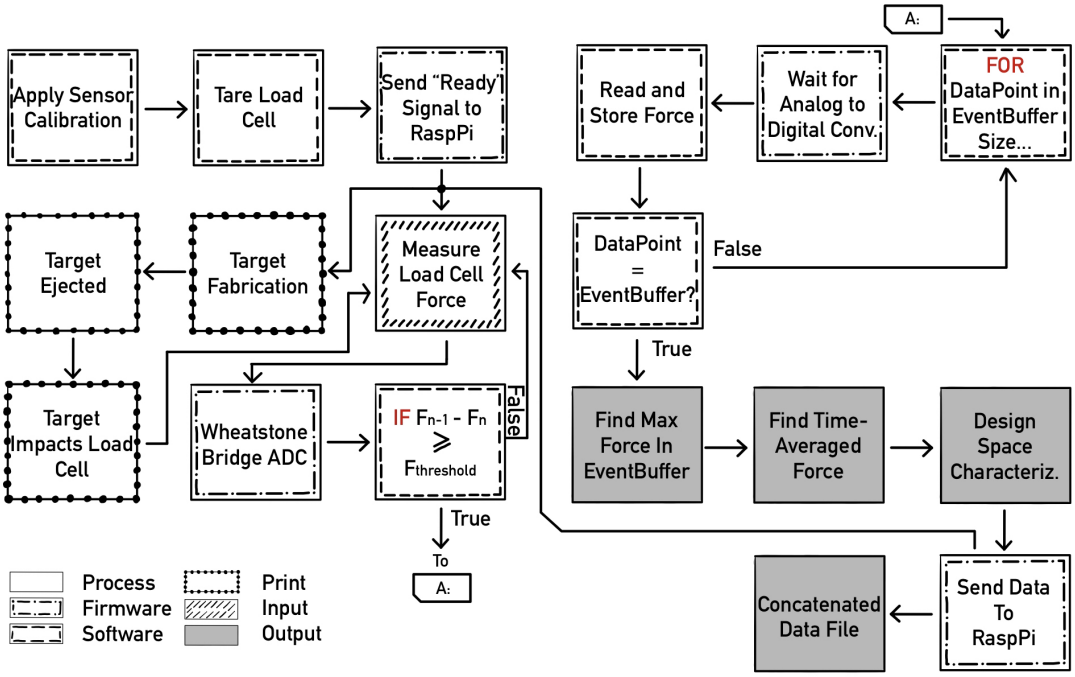

Figure 5.9: Process flow diagram of ATCAM's physical sensing capability. The data file generated from this process contains the load cell readings and time stamps of each impact, enabling force readouts. Temporal and force resolution are dependent on hardware.

The process flow for data logging is shown in Fig. 5.9. After a coupon is ejected, it impacts the load cell. This is registered as strain; the change in resistance is fed into a Wheatstone bridge and is digitized by a 24-bit analog-to-digital converter. This digital data is then read by an Arduino Uno microcontroller. The Arduino saves the value to a text file, formatting the coupon's data as a force within a row of comma-separated variables including the timestamp and the number within the test cycle. After logging these values, the microcontroller then waits for the next data point. Fig. 5.9 demonstrates that a minimum force threshold is imposed onto the load cell's reading to reduce the likelihood of erroneous data occurring from ATCAM's environment; a minimum of 1N force was required to log a data point as a dynamic coupon.

As seen in Fig. 5.7, the load cell is relatively small at 80.0mm x 12.7mm x 12.7mm (3.15"x0.50"x0.50"), so a solution was required to ensure that the dynamic coupons would reliably and repeatably be registered. The surface area sensed by the load cell was increased by affixing an acrylic plate. This provided a highly reliable target for the dynamic coupons. The modified load cell was placed within the average deployment trajectory, shown in Fig. 5.7.

5.2.5 Machine Learning and Cloud Computing to Analyze Dynamic Coupon Data

To analyze the information from the deployments at the end of a testing cycle, the dynamic coupon data logged by the Arduino Uno is captured by a Raspberry Pi 3B due to its networking and processing capabilities. Data is converted from comma-spaced variables accumulated by the text document into columns of data sets associating dynamic coupon forces and uniquely identifiable information by their deployment number from their testing cycle. This information is formatted in association with each feedstock OEM, vendor name (where applicable), and batch number (e.g., feedstock material, vendor 1, batch 1). The consolidation of these identifiers serves as ATCAM's database, which allows for dynamic coupons to be correlated with feedstock information.

Analysis of ATCAM's database relies on machine learning (ML) algorithms to systematically associate intrinsic material information with extrinsic parameters. This process allows for larger sets of data with altered parameters to be paired to differences within the intrinsic data, as per Ref. [Myers and Myers, 1990] and Ref. [Poole and O'Farrell, 1971]. These correlations generally benefit from analysis through statistical regression [Preacher et al., 2006, Regulski et al., 2019], and are consequently adequate methods for analyzing [Qi et al., 2019] and correlat-

ing otherwise complex multi-variable properties from lower-dimensional values. An example of this form of analysis is the printed electronics characterization demonstrated by [Mubarik et al., 2020]. They compared multiple ML algorithms such as decision trees, support vector machine, and logistical regression for appropriateness to their low dimensional AM and electronics data. The work in [Goh et al., 2020]'s overview of the status of ML for AM specifically notes the emerging need for automated data handling and libraries for in-situ processes, such as the method by [Delli and Chang, 2018]. Additionally, Goh references ML's utility for AM material characterization [Goh et al., 2020]. ML's usage in AM extends into toolpathing considerations within the work of [Conev et al., 2020], where optimized orientations for fabricating scaffolding is considered. Similarly, [Elbadawi et al., 2020] investigates the applicability of ML in the loop for optimized AM of medicines. These papers discuss the ML link between AM characteristics and the final object's performance; however, both processes have a relatively small data library to pull from compared to ATCAM and consequently do not fully leverage the capabilities of linear ML models.

5.2.6 ATCAM Testing Procedure

An initial test of ATCAM is provided to gauge the automated platform's AM characterization performance and identify potential error sources for improvement. Three 1.75mm PLA feedstocks from different manufacturers were tested by the system in 10 batches of 100 dynamic coupons per feedstock. PLA dictated a standard 215 C 0.4 mm extruder and 60 Cuild surface temperature. The toolpath was configured for 0.2 mm layer height with 20% rectangular infill due to the thermal considerations previously noted. The resulting settings provided an average volumetric flow rate of $5mm^3/s$ at $2mm/s$ feedstock extrusion speed. This created

a dynamic coupon that required an average of 4.5g of material and took approximately 30 minutes to fabricate. The initial cycle with the ISA generated a toolpath which required 82.5 minutes for the first test cycle and a subsequent cycling frequency of about 2 dynamic coupons tested per hour, which made the testing regime require a little over two days of automated fabrication and testing per 100 coupons generated. The three feedstocks were selected by their price points, USD$60/kg, USD$30/kg, and USD$20/kg, identified as Feedstock 1, 2, and 3. To gain a basic understanding of the generic quality control parameters taken by the feedstock OEM's, the feedstocks were each measured for filament diameter consistency at 30 points taken at random along the spool during the AM process with a Mitutoyo 500-464 dial caliper of 5-micron tolerance. Weight was measured per each 1kg quoted spool of filament with an OHAUS V31XH2 bench scale, which had 0.1-gram readability. These two parameters were utilized due to their importance in the FDM process; filament diameter consistency creates variability of mass flow rate in the extrusion process [Cardona et al., 2016, Gilmer et al., 2018].

The considerations of these filament issues are consolidated and outlined in Table 5.1. The weight was measured and taken for the average filament diameter to understand the material density to provide an indicator of the material's moisture content. This parameter is one of the leading sources of print variance in FDM [Kakanuru and Pochiraju, 2020], as water vapor cavities are formed in the FDM tool head, causing sputtering, the variability of mass flow rate, and inconsistent print results [Minh and Tuyet, 2020, Leite et al., 2018, Kim et al., 2016]. To provide an additional metric for material performance, the surface roughness of three dynamic coupons fabricated from each feedstock were measured with a digital profilometer, the Sunnen SP-211. As per [Townsend et al., 2016]'s review of surface texture metrology, conducting this profile topography with a contact

Type	Issue	Effect
Filament diameter	Variation of diameter below expected mean	Diameters below the expected value lead to under-extrusion. This produces low-density regions within the bulk material [Cardona et al., 2016, Gilmer et al., 2018]
Filament density	Variation of weight due to feedstock moisture absorption	When wet filament is utilized for FDM it flash steams and creates cavities in the print. This leads to geometric errors, increases surface roughness, and reduces the overall strength [Kakanuru and Pochiraju, 2020, Minh and Tuyet, 2020, Leite et al., 2018, Kim et al., 2016]

Table 5.1: Various filament issues and their potential correlations to the dynamic coupon data spread.

stylus provides a measurement that is both widely accepted and utilized in both industry and academia. The testing scheme followed along the top of the coupon and recorded the roughness every 5mm of the height for a total of five data points per test. Each test was repeated 10 times, generating 150 data points per feedstock. These results are provided in Table 5.2. Basic mechanical properties of the three feedstock were derived by conducting a three-point bending test to the ISO 178:2019 standard for the determination of flexural properties of thermoplastics. Three 80mm x 10mm x 4mm coupons for each feedstock were fabricated to the standard in a planar orientation, with the longest axis printed parallel to the build-plate. The printing parameters were taken as the same as the dynamic coupons. The bending test was conducted on a Chatillon TCM 201, fitted with a 2.22KN Interface 1110AF-500 strain gauge. The loading rate was set to .3175 millimeters per minute. The fixturing was fitted with 6.35mm diameter pins, with

the base set to 25.44 mm apart to follow a conventional 16:1 ratio for the length of the tooling to the specimen's thickness, respectively. The tests' results were taken from a customized lab-view interface to gather physical load, time, and displacement. These measurements were used to calculate properties for each feedstock, with the results consolidated in Table 5.2.

Feedstock	Cost (USD/kg)	Flexural Strength (MPa)	Modulus of Elasticity (GPa)	Surface Roughness (RMS Microns)	Diameter Tolerance (Microns)	Density Tolerance (g/cm^3)
1	60	48.21	2.35	.37	14	.023
2	30	44.96	2.12	.42	18	.036
3	20	39.79	1.86	.49	41	.062

Table 5.2: Measured feedstock properties.

Force measurements from the 3,000 dynamic coupons were collected through the deployment and sensing process described above and processed through three different machine learning algorithms for comparative purposes. Deep Learning, Support Vector regression, and Gradient Boost regression were selected to provide a diverse assessment of the data. Due to the computationally intensive nature of Deep Learning, we decided to process the data through cloud computing. The Raspberry Pi leveraged the DisplayR cloud platform through an internet connection due to its simplicity, accessibility, and visualization capabilities. This process allowed for the intensive ML computations to be performed in DisplayR's servers. Deep Learning was processed under multiple parameters until the accuracy proved consistent and independent of training errors from the data set. This converged to 1,000 epochs with predictors normalized and 1 hidden layer to prevent overfitting. To gauge ATCAM's ability to generate correlating data between dynamic coupons and feedstock, 100 randomly selected data points were obtained and

removed from each feedstock's 1,000 coupon database to be processed through each algorithm and observe whether they could be correlated back towards the data. Success would demonstrate ATCAM's ability to generate uniquely identifying coupons that could be automatically characterized and originated back to their feedstock source, paving the path for further correlations. The output of these tests was visualized by prediction-accuracy tables comparing the predicted force values 100 data points would theoretically have from the previous 900 data points to the 100 observed values. An additional ML test was conducted using simple linear regression to determine if 100 data points from a random feedstock could be compared to 2,700 data points (100 removed from each to provide the same library for each feedstock) and utilized to identify the parent feedstock. Diagnostic plots were created to analyze the constant variance of the input data and gauge the ML data's sensitivity to external variables. Histograms demonstrating frequency distribution of force by the number of occurrences were also generated over the 1,000 coupons per feedstock, with a complimenting scatter plot of the cumulative dynamic coupon data to provide an additional perspective of correlating information.

5.3 Results

The results of ATCAM's testing configuration are provided in this section. The flexural properties and qualitative metrics of coupons from each feedstock are provided in Table 5.2. The histogram depicting the frequency distribution of the dynamic coupon force measurements is visualized in Fig. 5.11. To present the dynamic coupon readings over the index of each testing cycle, Fig. 5.10 demonstrates results by feedstock. Trendlines and 5% error bars are provided of each feedstock's average force reading per respective index point to display the

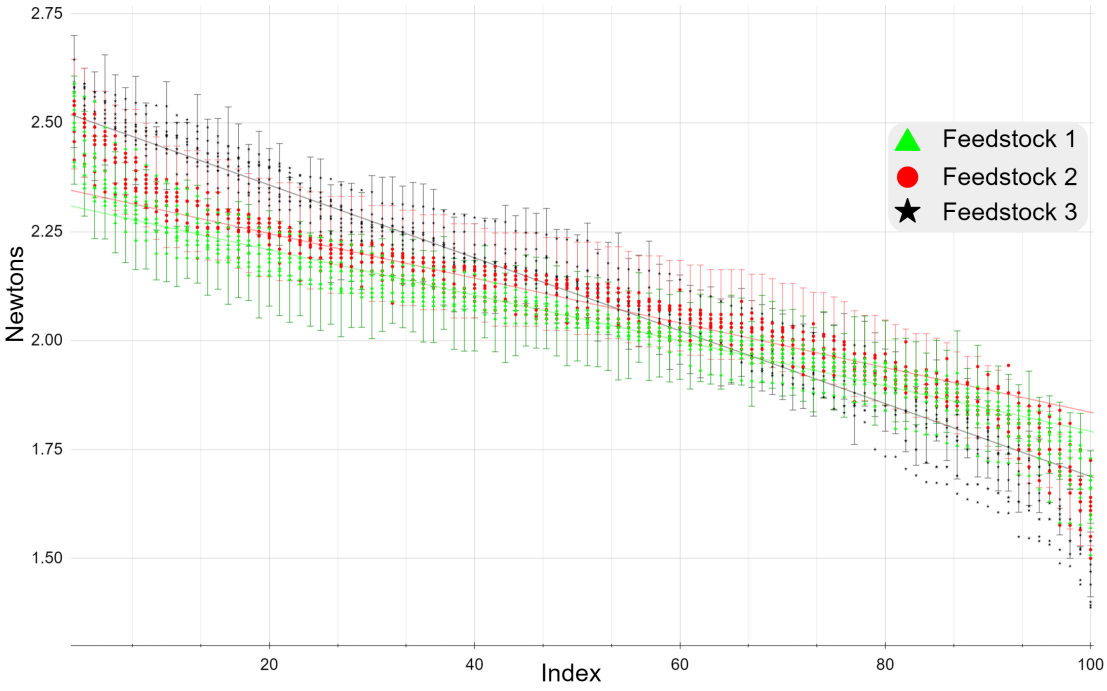

Figure 5.10: Scatter plot demonstrating ATCAM's fatigue distribution of dynamic coupons within each feedstock. The data is presented with a trendline and error bars correlating to each feedstock's average force over the index.

resulted grouping.

A comparison of the three algorithms on Feedstock 2 is presented in Fig. 5.12. This comparison is presented for Feedstock 2 as a concise indicator for the accuracy and applicability of ATCAM for material characterization due to this AM material providing the preliminary average between cost and quality control as per the frequency distribution demonstrated histogram in Fig. 5.11.

The diagnostic plots in Fig. 5.13 and 5.14 of the simple regression model are provided. These are used for determining whether a randomized collection of dynamic coupons could be correlated back to their parent feedstock. It gauges whether the data's dimensionality is correct or if there existed external influences (such as temperature differences for dynamic coupon numbers), which could alter the data. The sensitivity of these plots correlates to the linearity of the trend

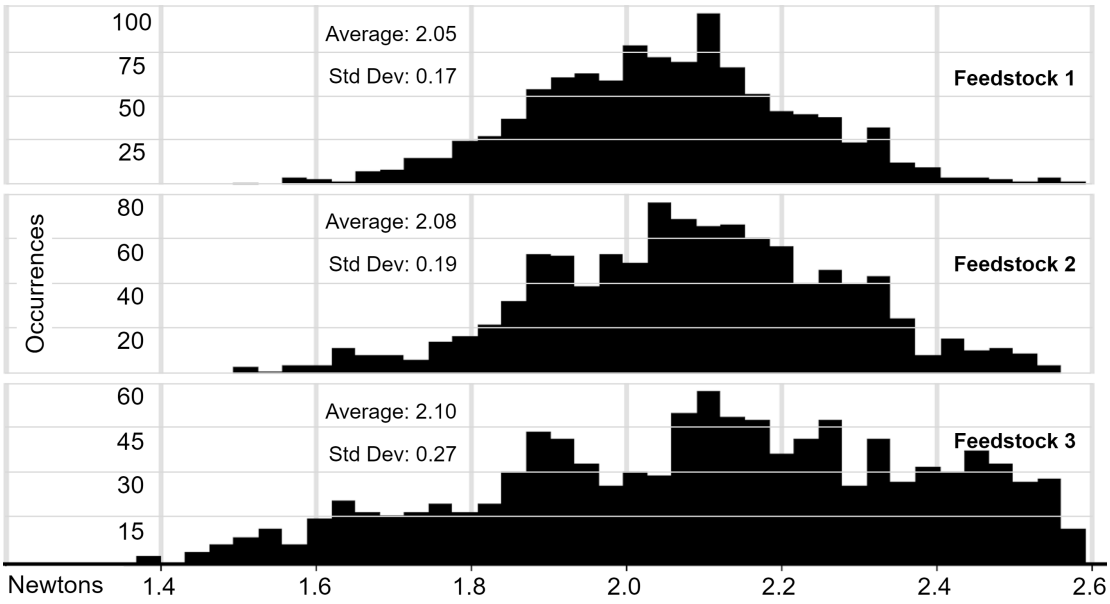

Figure 5.11: Histogram demonstrating ATCAM's frequency distribution over 1000 dynamic coupons within each feedstock. The average force and standard deviation of force ATCAM generated from each feedstock are provided.

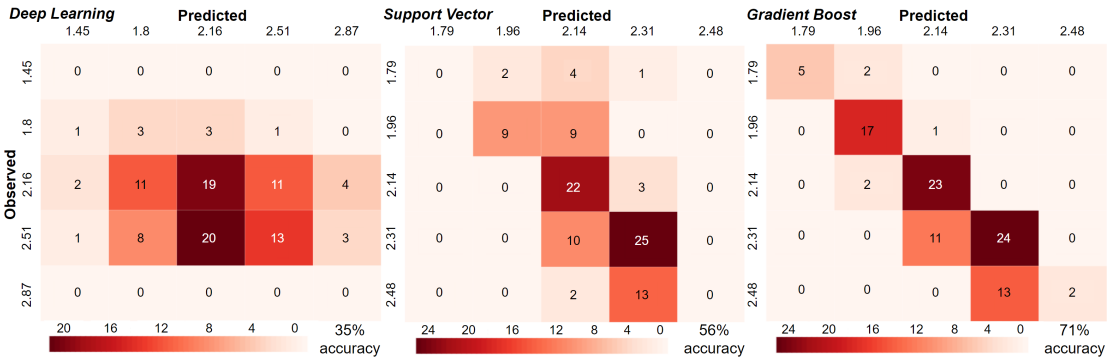

Figure 5.12: The prediction-accuracy tables are presented comparing various machine learning results correlating feedstock 2's automated dynamic coupon data to its database. The tables present a heat map to visualize the frequency in which a predicted measurement was observed and correlated successfully within the data. The accuracy is provided below each table to demonstrate the precision of the respected method for correlating 100 dynamic coupons to its raw feedstock allowing for automated characterization.

lines. Polynomial relationships indicate the model's sensitivity to lack of variability within the data, a condition that reduces the accuracy of the results.

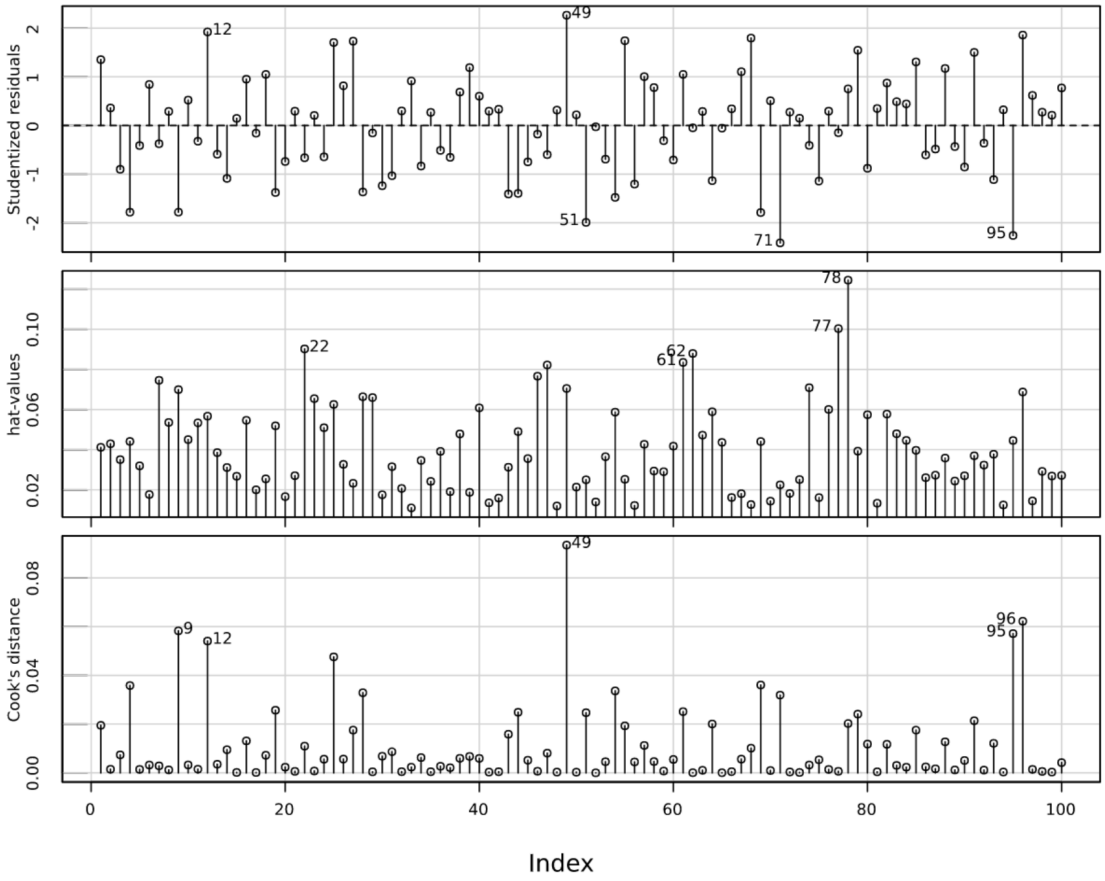

Figure 5.13: Diagnostics of the machine learning regression model characterizing AM feedstock. The data presents the correlation between Feedstock 2's developed material library and 100 dynamic coupons. The top figure distributes the studentized residuals over the coupon cycle index, while the middle figure demonstrates the hat-values, and the bottom visualizes the sensitivity associated with Cook's distance.

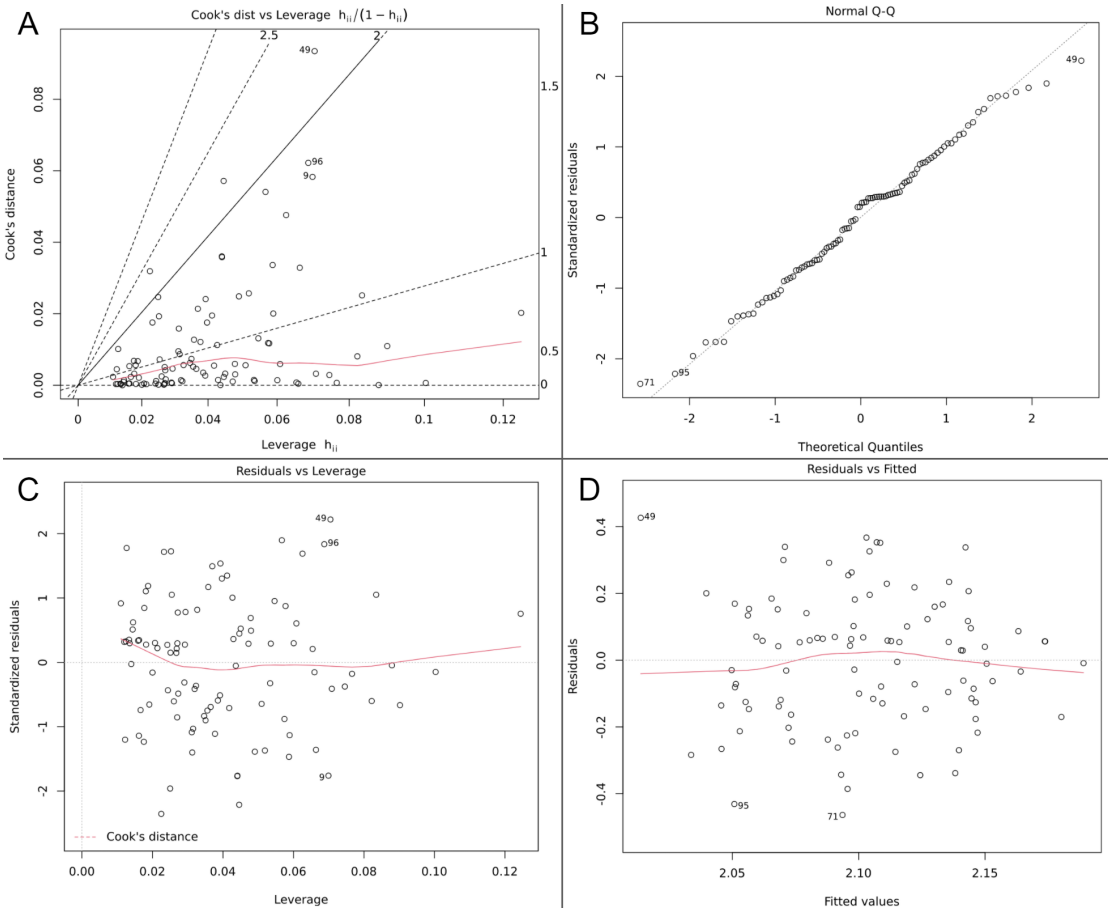

Figure 5.14: Sensitivity of the machine learning model characterizing AM feedstock. The data presents the correlation between Feedstock 2's developed material library and 100 dynamic coupons. Subfigure A provides Cook's distance with respect to the leverage each of the 100 data points have on correlating to the feedstock material. Subfigure B demonstrates a quantile-quantile plot of the data which indicates whether there are independent errors, or whether the errors are normally distributed and have constant variance within the relationship between the x-and y-axis. Subfigure C is plotted with the standardized residuals being compared to the data's leverage over the model prediction, while Subfigure D compares the residuals against fitted values to analyze potential external correlations or bias introduced into the model.

5.4 Discussion

The results from ATCAM's testing configuration provide highly relevant insight into the novel capabilities associated with relatively large amounts of AM coupons. Although the coupons only generated one data point at a time, cumulative data indicated the inherent quality of the feedstock. Fig. 5.11 provides a high-level perspective of a feedstock's apparent manufacturing tolerances, as the spread of the distribution was lower compared to a material's price point. The standard deviation of force distribution of Feedstock 1, 2, and 3 were 0.17N, 0.19N, 0.27N, respectively. The average deviation of each feedstock from its mean was 0.14N, 0.15N, and 0.22N, respectively. The various filament quality-related issues that can cause variability with the impact force were outlined in Table 5.1, and section 5.2.6. When paired to these generic empirical filament quality indicators, Feedstock 1 provided an average filament tolerance of +/- 14 micron, Feedstock 2 had a tolerance of +/- 18 micron, and Feedstock 3 was +/- 41 micron. When filament mass was compared, the average density tolerance of Feedstock 1 was consequently +/-0.023g/cm^3, Feedstock 2 had +/-0.036g/cm^3, with Feedstock 3 at 0.062g/cm^3. Table 5.2 provides additional metrics for analyzing the quality of the feedstock. Feedstock 1 demonstrated the highest flexural strength, modulus of elasticity, filament diameter tolerance, density tolerance, and smallest surface roughness. These results demonstrate a highly controlled manufacturing process as the deviations of the material's characteristics were the smallest. The respectively high flexural properties indicate that the printer had minimal underextrusion and moisture content. Feedstock 2 provided results that demonstrate lower tolerance than Feedstock 1, but higher than Feedstock 3. The flexural strength, modulus, surface roughness, diameter tolerance, and density tolerance were consistently impressive given the material's pricepoint. Feedstock 3 demonstrated

the lowest mechanical properties, and the least control over the density and feedstock diameter. This material also demonstrated the highest surface roughness, agreeing with the loose diameter tolerance and indicating geometric errors within the manufacturing process. As the flexural strength and modulus of elasticity of FDM PLA under the described configurations for Feedstocks 1 and 2 were within the range of the expected values [Ahmed et al., , Travieso-Rodriguez et al., 2019], but lower than those from Feedstock 1, it is considered that the lower mechanical properties and tolerancing of Feedstock 2 and Feedstock 3 are primarily an indicator of their comparative quality.

The average force generated by Feedstock 1 was comparatively lower than Feedstock 2 and 3. We speculate that this is due to the reduced dampening of the ISA generated by Feedstock 2 and 3, increasing the force generated upon its release. Another causation that would increase the force of lower quality feedstock is the reduced adhesion to the build plate from lack of an initial uniform layer. The underextrusion and resulting cavities would effectively reduce the dynamic coupon's surface area in contact with the build plate, subsequently reducing the force required for deployment. The deviation of ATCAM's detected forces followed the trend observed regarding the quality of the feedstock materials, implying that the average mechanical properties can not be independently referenced as a direct indicator of the average expected force through this experiment alone. However, it is noted that the deviations of these forces are correlated to the measured flexural properties, with higher quality feedstock generating smaller force deviations sensed through ATCAM, and better mechanical properties through testing. The agreement of the measured quality controls of the feedstock fabrication with ATCAM's independent data demonstrates an initial utility for automatically indicating the grade of a feedstock.

These results agree with those displayed for the testing cycle in Fig. 5.10. Feedstock 1's data grouping was the tightest with respect to both an R^2 trendline correlation of its average data per index point of 0.961, with Feedstock 2 providing an r^2 of 0.943 and Feedstock 3 at 0.910. Visually, the data point and error bar grouping cumulatively indicate a higher quality process for Feedstocks 1 and 2 than 3. Interestingly, Fig. 5.10 also clearly demonstrates that ATCAM can register material fatigue, identifying differences for effective performance degradation that occurs throughout ISA use. This result indicates an additional utility of ATCAM provided by gauging the life cycle of a test setup, catching when a machine is falling out of calibration, or at a minimum providing an extra dimension of data. The observed decay in Fig. 5.10 is relatively consistent between multiple ISA operating of the same feedstock, meaning that there are likely no significant variations within the batches of feedstock. The Prusa MK3 printing platform is configured to re-home its axes between the testing of each coupon and to fully self-calibrate between actuators. This allows for it to impart very consistent actuation, making it unlikely to be the source of the drift. The drift in the impact force of the ATCAM system over the testing-life of a particular actuator is predominantly due to the drifting of the experimental setup due to the mechanical wear fatiguing the ISA's spring. As the actuator is taken to full deflection and released, there will be residual plastic deformation that causes a reduction in overall elasticity and maximum energy the spring section can store. This slight decrease over each of the actuations causes the decaying drift of the impact force. We consider that because ATCAM can detect the drifting of its own experimental setup, characterizing and filtering the drifting factor from the test results would allow for increased sensitivity and potential insights into the drifting of the AM process itself. Future work for ATCAM would leverage this filtering to vary both

printer processing parameters and materials intentionally and gauge the effectiveness of potential correlations. The figure also shows a low-fidelity measurement of the inertial manufacturing errors introduced by each feedstock undergoing the same material process under the same parameters.

Fig. 5.12 gauges the relevancy of three machine learning algorithms to correlate 100 dynamic coupons from Feedstock 2 to its database, scaling their accuracy in the bottom right when the predicted data paired with the observed data. The diagonal heat-map in Gradient Boost regression displays a 71% accuracy at predicting the dynamic coupon to a deviation of tolerance of force over 100 data points, with Support Vector dialing at 56%, and Deep Learning measuring at 35%. These results concur with Deep Learning's general requirements for larger data sets to be effective correlating tools at describing phenomena. Consequently, the Deep Learning results do not provide initial confidence in their relevance for correlating the dynamic coupon data in its current configuration. The Support Vector data provided better results than Deep Learning but tended to overshoot the results. Utilizing Gradient Boost regression exhibits promising preliminary results to serve as ATCAM's primary correlation method.

In observing the sensitivity of the machine learning results to potential external factors driving the variability in the outcome, Fig. 5.13 provides valuable insights. The studentized residuals of the dynamic coupon results demonstrate the desirable constant variance required by regression over the coupons' index [Hosmer et al., 1997, Jarque and Bera, 1987]. For example, coupon 9's residual lies at a magnitude of -2N, while 12's residual lies at a magnitude of +2N. This magnitude of outlying error is displayed at random intervals throughout the index and is demonstrated by coupons 51, 71, and 95 all having nearly equal adjacency to opposite residuals. There does not exist a trend of increasing magnitude in

the hat-values or Cook's distance over the span of the index, providing confidence over numerous perspectives of the validity of the machine learning results for a constant variance [Stevens, 1984, Brown et al., 1975].

Due to the intrinsic reliance of regression on the quality of the data, Fig. 5.14 provides an additional diagnostic analysis of the output and is required to identify any potential dependence or patterns within the predictions and observations [Williams et al., 2013, Hocking, 2013]. Comparing the Cook's distance from the leverage each data point provides on the model displays potential issues individual results can imply [Stevens, 1984, Kannan and Manoj, 2015]. Subfigure A displays that the grouping of the data is near the trend, and visualizes that the model is not overly sensitive to any specific data-point altering the characterization. Subfigure B's quantile-quantile plot comparing the standardized residuals to the theoretical quantiles designates desirable linearity and packing of individual data points to the trendline [Williams et al., 2013]. Subfigure C and D compare standardized and regular residual to leverage and fitted values, respectively. The data from both subfigures indicates a primarily flat trendline that seems to overshoot when standardized and undershoot when not. The random spread of the residuals and the seeming inverse correlation over the two subfigures is a good sign that the values are not overly influenced by external variables, systematically bias, or indicate signs of heteroscedasticity, in which the variance of the data is time-dependent [Poole and O'Farrell, 1971]. Consequently, the results in Fig. 5.13 and Fig. 5.14 cumulatively indicate that there is minimal unexplained phenomena with high leverage within the data and regression serves as a statistically appropriate method to analyze this data and draw conclusions from its correlations.

It is crucial to note that ATCAM's results are a virtue of not only the error associated with the manufacturing process and quality control of AM feedstock

but significant limitations from the test setup and configuration as well. The accuracy of the generated data has multiple points of introduced ambiguity, including but not limited to the inherent control of the FDM process on a desktop machine, the in-situ actuator's tolerance, the cleanliness of the build-surface potentially altering the friction imposed on a deployed dynamic coupon, the dynamic coupon's susceptibility to the variability of the contact from the in-situ actuator, the dampening and induced moment from the physical load cell extension board, algorithmic computational errors associating the AM process to coupon performance results, and even variability of an unenclosed platform such as changes in temperature, humidity, and UV from sunlight over the number of days of the testing cycle of 3,000 dynamic coupons. Given these limitations, the quality of the results associated with ATCAM's automated testing of the three feedstocks is still statistically distinguishable, with data able to be traced and associated with its parent feedstock with the assistance of machine learning and sheer quantities of coupons to train and reference from.

5.5 Conclusion

Given the discussed limitations, the results automatically generated, tested, and characterized by ATCAM's dynamic coupons provided statistically relevant information that can identify and correlate data output by the AM process. The results presented are confined to automatically implying the quality of FDM feedstock, demonstrating drifting of the AM process and visualizing the life cycle of a part retrofitted onto the build-surface, fingerprinting the material process systematically through a single dimension of data, and demonstrating the initial applicability of Gradient Boost regression as an ML correlation tool for large quantities of AM data with low dimensionality. The significance of these initial results demon-

strates promise for ATCAM's continued testing and development as a low-cost test-bed for characterizing the AM process. The output from ATCAM's current experimental configuration are not inherently compatible with current testing industry standards, as the results do not imply a comparable value or metric that is currently used in industry. The results do, however, provide an additional novel metric that consolidate manufacturability as an empirical metric which is implied over the characterized grouping of thousands of coupons. Additionally, the ability of the algorithms to identify a strong correlation of a set of dynamic coupons to their feedstock source imply that new uses for cybersecurity and traceability are capable of being generated by ATCAM. In its current FDM-specific configuration, ATCAM's future tests can be conceptualized as maintaining a consistent feedstock material and intentionally altering process-parameters to identify sensitivities of the material process potentially identifiable through large quantities of controlled coupons. This consideration requires the characterization and filtering of the experimental drift referenced in the discussions to increase the sensitivity of the testing configuration to controlled variables. Another test that is of interest is to vary the feedstock's material (such as printing ABS, Nylon, etc.) and observing the quality of the generated data. Additionally, leveraging the portable in-situ methods and low-cost sensing platform can allow the current ATCAM testing procedure to be automatically conducted in intervals of production printing to catch if a machine's calibration is potentially drifting from its optimal parameters. Although this would limit the build-volume to the space unoccupied by the in-situ actuator, this result would be an extremely low-cost method for ensuring an FDM machine is performing to specification. Conversely, by controlling the calibration and material process, the dynamics introduced by the retrofitted in-situ actuator may be exploited for testing large quantities of iterated geometries to potentially

allow for automated design space exploration by AM. Improvements to increase the precision of ATCAM are to add additional dimensions of systematic testing to complement the physical sensors, retrofit an enclosure for the printer and the sensing setup, develop a robust automated method to remove an ISA at the end of its life cycle, develop a larger database for improvement in regression performance, and conceptualize the ATCAM process for non-FDM platforms.

Chapter 6

Autonomous Aircraft Which Fly off of the Machine that Made Them

6.1 Introduction

With the validation and characterization of autonomously-deployed objects undergoing projectile motion, drag-induced considerations were characterized and paired to manufacturing-related variables. To further the investigation of autonomous design-space exploration, I developed a protocol to autonomously pair and optimize the computer numerical control of lift-generating surfaces. Through a novel implementation of bio-mimicry, an auto-rotating lift-generating vehicle was autonomously deployed by imparting momentum onto a manufactured Samara seed. By leveraging the design knowledge previously gained from creating, deploying, and characterizing spherical objects undergoing ballistic motion, we refine the existing models for increased applicability in aerodynamical design space. Due to the increased complexity of the physics regulating lift-generating vehicles, a model with higher-fidelity theoretical characterization to tune physical observations was required with respect to those defined in earlier sections.

I start by pairing digital product definitions to toolpath-derived variables for automated deployment, then develop a lift-regulating aerodynamics model taking into account for asymmetrical volumetric considerations. To tune this model, a mixture of sensing protocols were utilized including automated loading-cells detecting impact forces from the spring and their deployed objects. Computer vision was implemented through embedded systems to observe physical trajectory-based object-fluid interactions. Integrating the joint-observations of both physical-loading and visually observed trajectories allowing for multi-physical insights to the sensitivity of theoretical laws defining an object's motion. By automating the process of sensing a design's performance and integrating the data as a basis for optimizing an object's deployed implementation in-situ, one is provided the powerful ability to automate the exploration of a robot's design space.

Acknowledgements

The research and findings that are presented in this chapter were developed, consulted, and/or referenced alongside the following colleagues: Rachel Ticknor, Stanley Krzesniak, Sean Swei, Mircea Teodorescu, and Dean Giovannetti.

6.2 Modeling ISD of Aircraft

6.2.1 Cantilever Strain Energy Model for ISD

This model defines the in-situ deployment kinematics of aircraft as a contribution of energy through physical contact. The moment of inertia capable of generation from the linear spring is calculated through the elastostatics of a rectangular beam and translated to the internal energy strain of a cantilever beam undergoing deflection:

$$I = \int_{-a}^{a} dx \int_{-b}^{b} y^2 dy = \frac{4}{3} ab^3 \tag{6.1}$$

This moment of inertia allows us to calculate the axial stress over the direction of moment and simultaneously allows us to affirm the design choice of bending the linear gate about it's longest axis.

$$\frac{U}{V} = u = \frac{(\sigma_x^2)}{(2E)} \tag{6.2}$$

Taking

$$U = \int_0^L \frac{(\sigma_x)^2}{2E} dV \tag{6.3}$$

with

$$\sigma_x = \frac{M_y}{I} \tag{6.4}$$

Simplifies to

$$U = \int_0^L \frac{M^2}{2EI} dx \tag{6.5}$$

Taking the integral provides us with

$$\frac{(P^2)(L^3)}{6EI} \tag{6.6}$$

Given that

$$W_E = \frac{1}{2} P\Delta \tag{6.7}$$

We get

$$W_E = U_I = \Delta = \frac{P(L^3)}{3EI} \tag{6.8}$$

At this point, we reference the previously defined geometry of the deployer through an alternative perspective accounting for the spring and its paddle independently to account for strain-energy and computer-regulated geometric variables.

Defining the mass of the aircraft as a function of its geometry through the printed density:

$$M_a = W_a * L_a * H_a * \rho_a \tag{6.9}$$

and the deployer similarly with spring and paddle considerations regarding printed density:

$$M_p = W_p * L_p * H_p * \rho_p \tag{6.10}$$

$$M_s = W_s * L_s * H_s * \rho_s \tag{6.11}$$

With the moment of inertia for the spring's cross section as:

$$I_{s_{cs}} = \frac{(W_s^3 * H_s)}{12} \tag{6.12}$$

For the spring's end:

$$I_s = \frac{M_s L_s^3}{3} \tag{6.13}$$

Considering the contact is through the center of the paddle:

$$I_{p_c} = \frac{M_p(W_p^2 + L_p^2)}{12} \tag{6.14}$$

The force being calculated through:

$$F = \frac{3EI_{s_{cs}}D_s}{Loc_n^3} \tag{6.15}$$

Providing the assembly's moment of inertia:

$$I_a = I_s + I_c + M_p(L_s + .5L_p)^2 \tag{6.16}$$

Allowing us to calculate the relevant angular frequency:

$$\omega = \sqrt{\frac{2U}{I_a}} \tag{6.17}$$

Leading to an impact velocity at the aircraft's impact origin through

$$V_{imp} = \omega O_{air} \tag{6.18}$$

and a consequent kinetic energy:

$$(KE)_{air} = \frac{1}{2} V_{imp}^2 M_p E_t \tag{6.19}$$

for a subsequent theoretically-defined aircraft deployment velocity by:

$$V_a = \sqrt{2 \frac{(KE)_a}{M_a}} \tag{6.20}$$

6.2.2 Requisites of Lift-generated Flight

As a process which takes advantage of pressure differentials generated through a finite volume of fluid, gliding conventionally translates potential energy into controlled flight. A form of non-powered aeronautics, gliding relies on geometry specifically tailored to maintain attached flow along the majority of a body (typically referred to as a wing) traveling through a surrounding fluid at a specific range of Reynold's numbers:

$$Re = \frac{\rho v c}{\mu} \tag{6.21}$$

Lift generated over the cross section of a surface can be calculated by taking into account for C_l the amount of pressure differential a geometry can conditionally produce), the relative velocity the geometry is traveling through fluid at, the density of the surround fluid, and the surface area of the cross section.

$$L = C_l \cdot \frac{v^2 \cdot \rho}{2} \cdot A \tag{6.22}$$

Similarly, we find the corresponding and penalizing drag force along the same cross section, acting perpendicular to the lift generated above, in steady, level

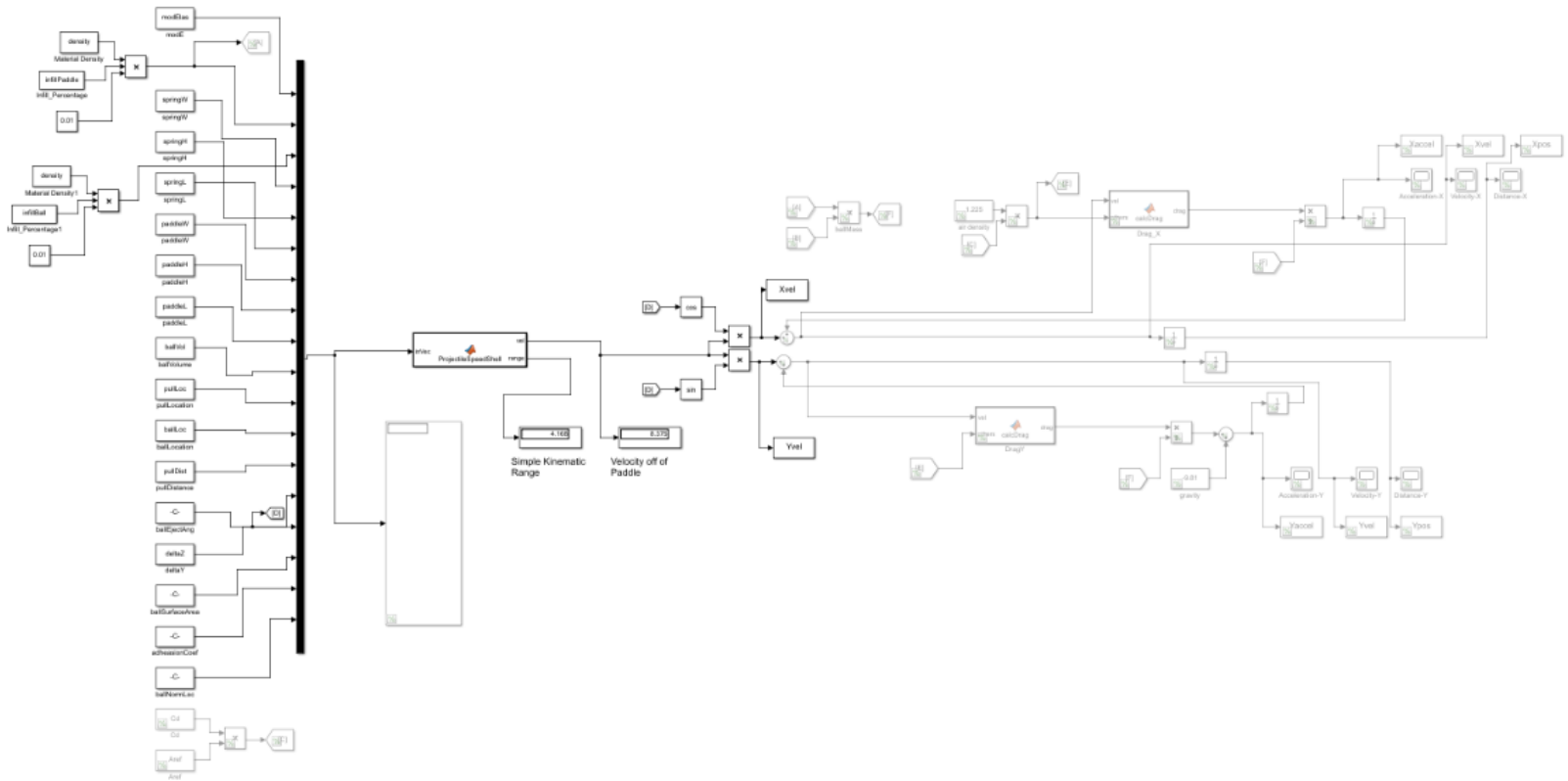

Figure 6.1: Simulink Model of Paddle with Cantilever Strain Calculations

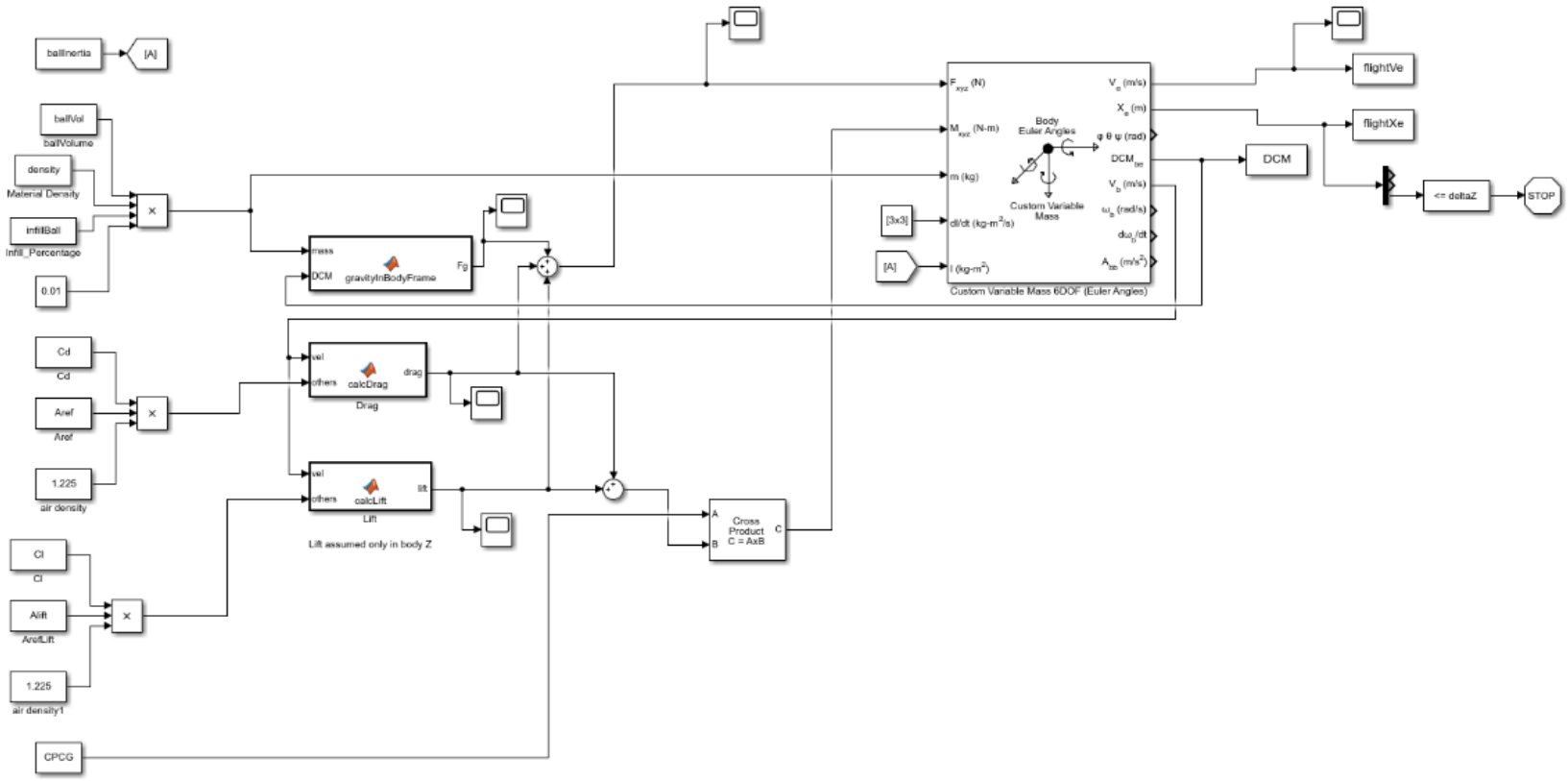

Figure 6.2: Simulink Model of an Actuated Ballistic Object

flight:

$$D = C_d \cdot \frac{v^2 \cdot \rho}{2} \cdot A \tag{6.23}$$

Unpowered thrust generation is typically nonexistent in steady, level flight. The equivalent translational force counteracting the induced drag imposed by lift on a gliding body is provided by the glideslope of the system. The corresponding angle is proportional to the incidence of the wing relative to the surrounding freestream of fluid. The downward angle rotates the lift vector, providing it with an axial component that thrusts the body forward.

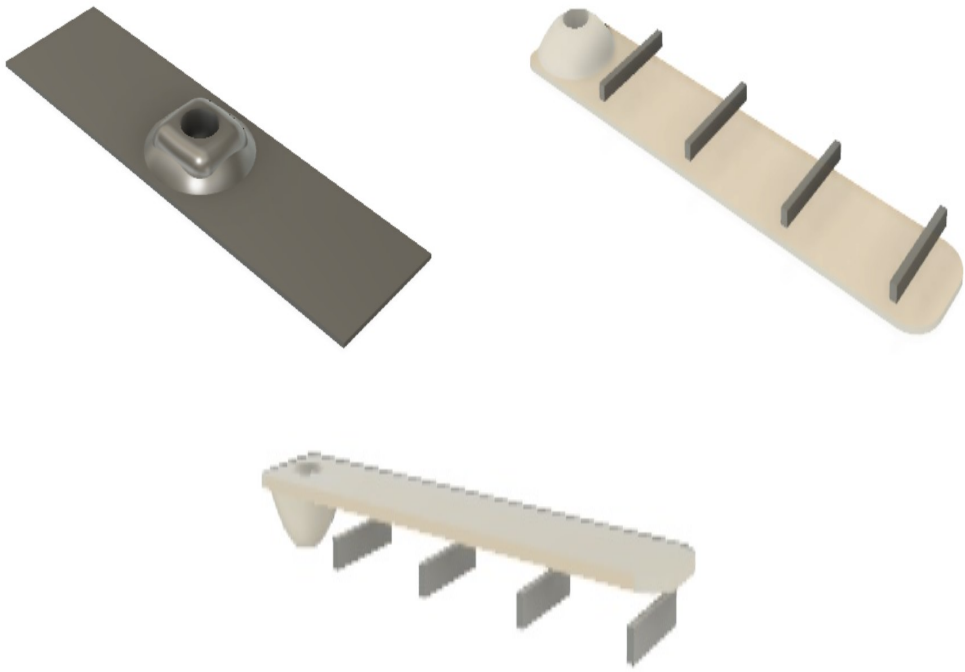

Figure 6.3: Investigating Lift-generating Spheres

Increasing the C_l by varying the relative angle of attack to generate a geometry and Reynold's number-specific C_lmax allows conventional airborne objects to land predictably and repeatedly. This angle of attack is typically generated by means of a pitching moment generated by varying geometry. Altering the camber along the lifting body will move the center of pressure, and alter the differential pressure imparted on the surrounding fluid. The resultant forces are increased lift and drag imparted over the body. Naturally occurring structures (such as maple-seeds) follow this process to decrease their glideslope for a gentle landing through a cambered wing, shifting the center of gravity, and increasing the otherwise angle of attack to near C_lmax through a permanent, induced angle. The aerostructure in this document follows a mixture of the same convention, but without the benefits of the favorable weight/drag ratio and variable elasticity encountered in its biological format.

6.2.3 Rapid Prototyping of ISD Airacraft

The considerations from the modeling of lift-generating sphere above were taken to iterate through numerous generations of ISD aircraft. As the primary objective for this airplane was ISD, the lift-to-weight ratio was as important as the friction and deployment mechanics described in earlier sections for the printing and programming of ISA's and ATCAM. Translating the ISA's defined force into aerodynamic variables and sizing to generate sufficient lift provided baseline configurations that are visualized in Figure 6.4. The aircraft in this figure represent modifications for manufacturability and compatibility with the ISD process more-so than for optimal aerodynamics. Further generations of these aircraft were tailored with respect to span-wise wing-loading and static stability after referencing plenty of literature. The final generation of the aircraft was selected due to

locally optimal performance, as characterized by its ISD trajectory and velocity through the CV system. The parameters of this aircraft are referenced to characterize the aerodynamics of the aircraft in the next section for the purpose of generating a model and comparing physically sensed values to simulated values.

6.2.4 Implementing the Aerodynamics

Although the effective airfoil altered through the various milestone iterations of the mapleseeds, an airfoil capable of generating the required C_{lmax} of 1.7 at the impending α and Reynold's number calculated above was selected as a desirable design. As seen in Figure 6.6, the AG38 was taken as the baseline and modified for a more-favorable mean aerodynamic camber line. The resulting airfoil is analyzed later in this paper via a computational fluid dynamics simulation.

To size the surfaces intended to generate auto-rotated lift, the intended scope of the aircraft was revisited. As the primary mission of this aircraft is to reach a destination through autonomous deployment, the bounding characteristics of an otherwise indeterminate series of equations were defined. The lift generated by an aerosurface needed to overcome the gravitational burden of its own manufactured weight, and induced drag as a function of lift is calculated below. The second bounding variable was cubic wingloading, as it is a metric that correlates an aircraft's performance characteristics without a relatively high fidelity of volumetric considerations required [Jameson et al., 2007]. A cubic wingloading of roughly 1 oz/ft^3 was desired to achieve a desirable stalling speed, permitting sustainable flight with a low Reynold's number regime.

Desired Cubic Wingloading:

$$(\frac{W}{S})^{1.5} \tag{6.24}$$

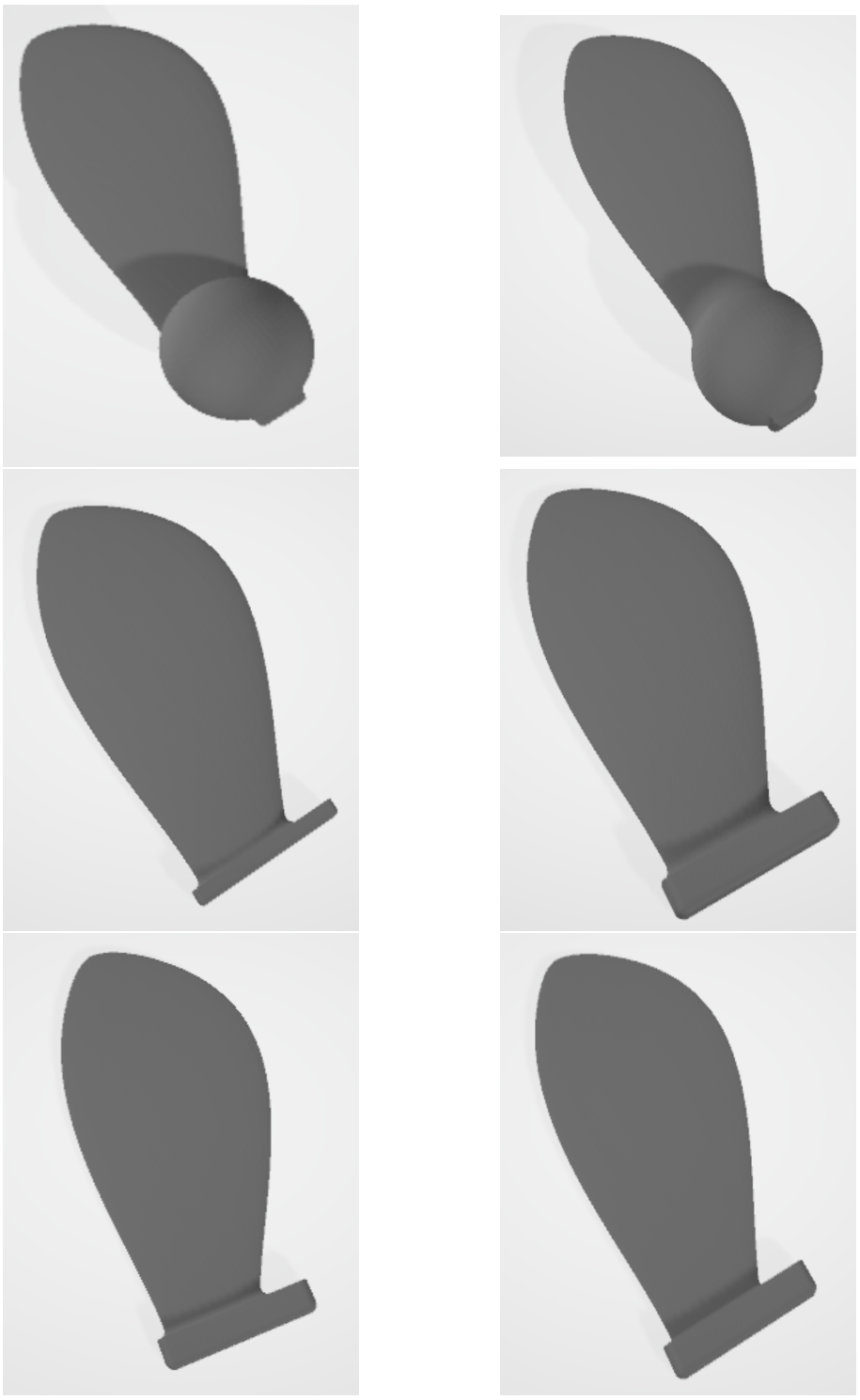

Figure 6.4: Evolution of Autorotating Aircraft Gen: 1 - 6

$$\approx 1oz/ft^3$$

From the cubic wingloading, a span of 3 inches and chord of .75 inches was selected to maintain the reynolds numbers within the scope of a slow-flying, lightly-loaded aircraft capable of generating lift through a gentle (as defined above) landing. At a C_lmax of 1.7, the stall velocity can then be defined in m/s by:

$$V_{stall} = \sqrt{\frac{2W}{1.23C_lmaxS}} \tag{6.25}$$

Resulting in a V_{stall} of $.2m/s$, and a consequent Reynold's number of $\approx 6,000$. The following investigation refers to the calculation of the appropriate glidespeed and respective glideslope for various lift-to-drag ratios. The equations and processes are universal amongst aerodynamicists, however the Matlab Aerospace Toolbox was utilized to perform calculations.

Taking $W = .05lbf$; $S = .02ft^2$, the aspect ratio as $AR = 4$, cofficient of drag at $C_{D0} = 0.04$, and an Oswald's efficiency of $e = 0.72$ provide a true airspeed of:

$$TAS_{gliding} = \sqrt{\frac{2W}{\rho S}} \times [\frac{1}{4{C_{D_0}}^2 + C_{D_0}\pi eA\cos^2\phi}]^{\frac{1}{4}} \tag{6.26}$$
$$\approx 1.6f/s$$

Converting velocity from f/s to kts results in $.948kts$. To confirm the angle at which we will have the highest lift-to-drag ratio, we can use:

$$\sin\gamma_{gliding} = -\sqrt{\frac{4C_{D_0}}{\pi eA\cos^2\phi + 4C_{D_0}}} \tag{6.27}$$

Solving Eq. 6.27 results in an idealized glideslope of $-1.8\,\text{deg}$. The consequent minimum drag can be calculated as:

$$D_{min} = D_{gliding} = \frac{1}{2}\rho(TAS^2_{gliding})S(2C_{D_0}) = -W\sin\gamma_{gliding} \tag{6.28}$$

At .012 lbf. Lift, concurrently provides:

$$L_{gliding} = L_{max} = W\cos\gamma_{gliding} = \sqrt{W^2 - D^2_{gliding}} \tag{6.29}$$

Solving Eq. 6.29 results in .011lbf, or 5g for confirmation of glideslope.

After taking into account for dynamic pressure ($\bar{q} \approx .08\frac{lb_f}{(ft)^2}$), the coefficients of lift and drag are solved, respectively:

$$C_{L_{gliding}} = \frac{L_{gliding}}{\bar{q}S} \tag{6.30}$$

$$C_{D_{bg}} = \frac{D_{bg}}{\bar{q}S} \tag{6.31}$$

With these figures we can now calculate the encountered drag, consisting of parasitic drag (D_p):

$$D_p = \frac{1}{2}\rho S C_{D_0}(TAS^2) \tag{6.32}$$

and induced drag (D_i):

$$D_i = \frac{2W^2}{\rho S\pi eA}\frac{1}{(TAS^2)} \tag{6.33}$$

The sum of which is referred to as total drag (D):

$$D = D_p + D_i \tag{6.34}$$

Taking the reconfigured lift coefficient as a factor of weight (with $L = W$) gives us

$$C_L = 2\pi\alpha \tag{6.35}$$

Simulating the results of this configuration provides us with the theoretical flight envelope the aircraft should perform in. The difference between the aircraft's physical performance and this theoretical performance can then start to be characterized and influence factors can be identified.

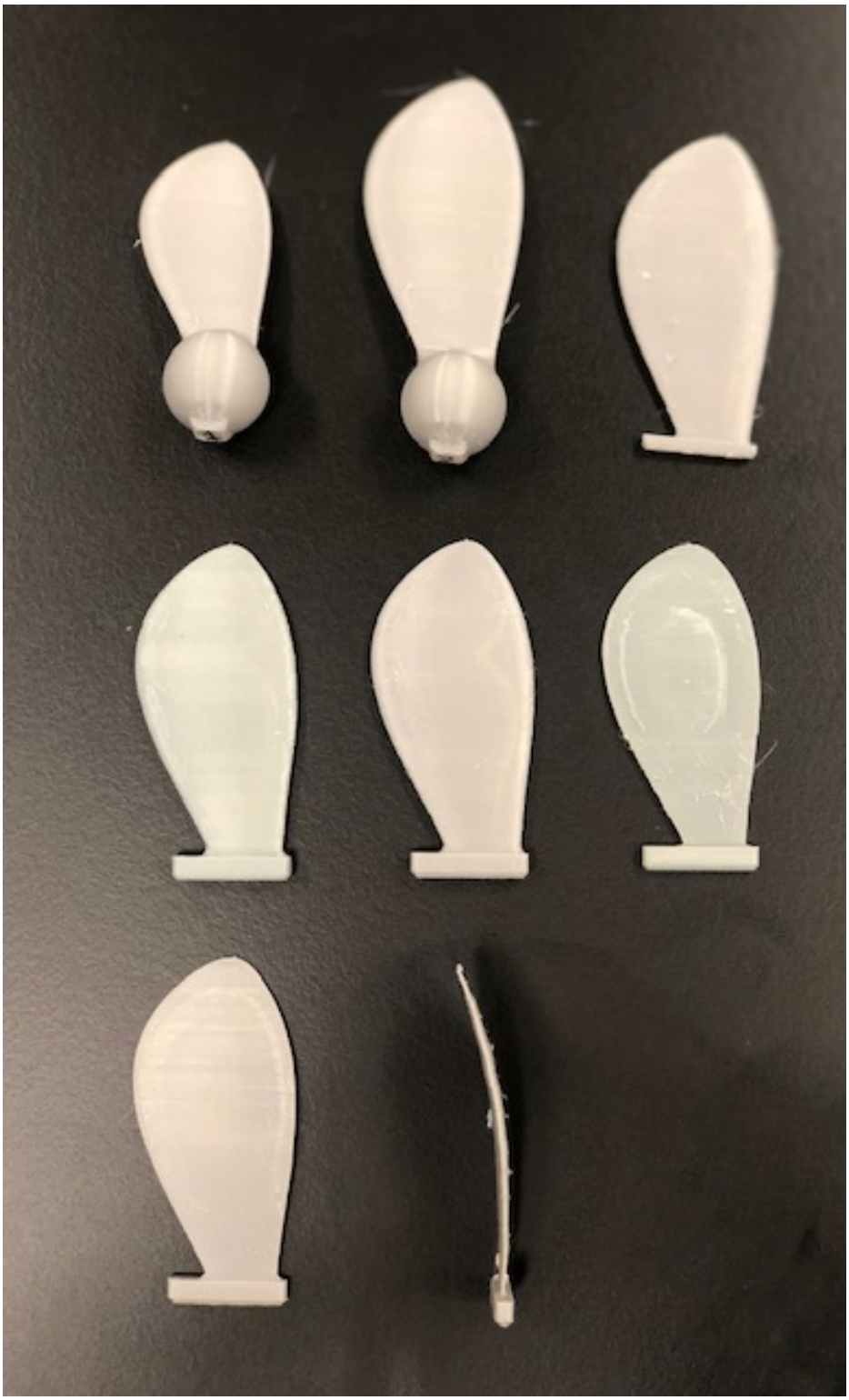

Figure 6.5: Evolution of Physically-demonstrated Autorotating Aircraft Gen: 1 - 7. The bottom two objects are of the same generation, demonstrating dihedral angle as a function of compression designed into the toolpath for FFF warping.

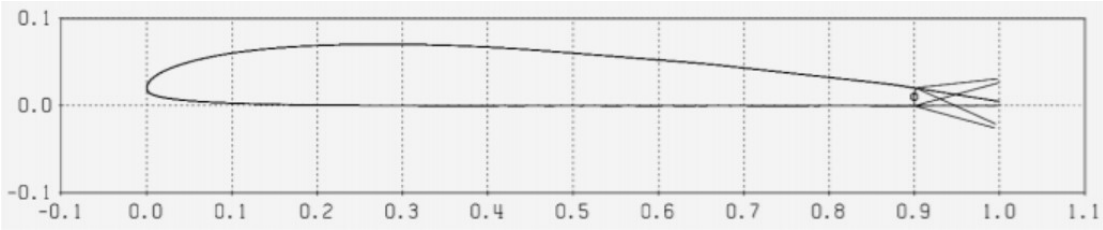

Figure 6.6: Cross-section of Bio-inspired AG38 Airfoil with flap modulation [Jameson et al., 2007]

Simulation

The simulation of aircraft ISD consisted of two parts. The first part is developed from the behavior of the ISA to determine the initial ejection velocity and angle of the aircraft and the second models its trajectory based on the initial velocity conditions. Simulations were implemented in the MATLAB Simulink® environment. For both simulations the solver used was ode45 with variable step size. The max step size permitted was 0.01 seconds and the relative tolerance between steps was 0.001.

Ejection Modeling

The simulation for the deployment of the actuator used energy based methods. The in-situ actuator was modeled as a beam and its stored energy could be calculated using beam-energy methods based on the deflection. This value was then multiplied by a constant, experimentally determined, to get the stored spring energy [Besnea et al., 2018]. Additional experiments were used to calculate the percent energy loss during the swing to the impact point. The force and velocity loss due to breaking the target off off the PRUSA poly-carbonate-based build surface were also experimentally determined. Using work energy relations the force of impact could be calculated. From the impact energy and ejection able the initial conditions for the ejection could be calculated.

The first step in the simulations uses the actuator geometry and the pull-back distance to calculated the strain energy, U, using beam energy methods, as seen in equation 6.38. Equation 6.36 gives the bending inertia, I_b, of the spring-component of the actuator as a beam. Equation 6.37 provides the force of the pull based on how far back the pull is, Δ, and where the puling location is, S_p. E is the Modulus of Elasticity of the printed material.

$$I_b = (width^3 \times height)/12 \tag{6.36}$$

$$P = 3EI_b\Delta/S_p^3 \tag{6.37}$$

$$U = \frac{p^2\ S_p^3}{6EI_b} \tag{6.38}$$

In order to determine the velocity of the paddle at the point of impact with the target, the rotational inertial, I_r of the spring was found using equation 6.39. In order to do this the spring section was modeled as a rod and the paddle section was modeled as a rectangular prism with parallel axis theorem was applied. Where L_s is the length of the spring section, m_s is the mass of the spring section, L_p is the length of the paddle section, W_p is the width of the paddle section, and m_p is the mass of the paddle section.

$$I_r = \frac{1}{3}m_s L_s^3 + \frac{1}{12}m_p(W_p^2 + L_p^2) + m_P(L_s + 0.5L_p)^2 \tag{6.39}$$

With these values conservation of energy can be used to find the angular velocity, ω, of the actuator at the point of impact 6.40. It was experimentally determined using high speed video that a multiplicative coefficient of 0.76 was needed to get an accurate value of the energy at the equilibrium point. This constant was assumed to hold at the impact point as well.

$$U_{\text{pull back}} = U_{\text{impact}} + 1/2I_r\omega^2 \tag{6.40}$$

The energy at the impact point was found using a similar method to the pull back energy with the displacement instead being measured to the object impact location.

The paddle velocity at the point of impact can be found by multiplying the

angular velocity by the position of the target object. Experimentally it was found that 80% of the energy was transferred into the target, thus equation 6.41 can be used to find the targets kinetic energy, T, the instant after impact.

$$T = 0.8 \times \frac{1}{2} m_{target} V_{impact}^2 \tag{6.41}$$

In order to model the velocity loss for the target breaking off of the build plate a break-off time and the force of adhesion were needed. In order to determine the break-off time a high speed camera was used and it was found that the target broke off the build plate in approximately $1/200^{th}$ of a second. The force of adhesion was found to be 1.254 times the contact surface area of the target. The velocity loss due to breaking off the build plate could then be found as in equation 6.42.

$$V_{loss} = \frac{F_{adhesion} \times 0.005}{m_{target}} \tag{6.42}$$

This velocity loss from the surface detachment was then added to the velocity calculated from impact to get the final ejection velocity. The angle of ejection was user supplied to get the vertical and horizontal components.

Trajectory Modeling

As mentioned in the subsection heading, implementation of the simulation used ode45 as a solver with variable step size. The max step size permitted was 0.01 seconds and the relative tolerance between steps was 0.001.

With the initial velocity conditions from the ejection equations and a user defined initial orientation of the object's body frame, a 6 degree of freedom (DOF) flight simulation based on Newton's and Euler's (Eq. 6.45) equations of motions was used to find the both the path and orientation of the object after ejection.

$$\overrightarrow{F} = d\overrightarrow{P}/dt = m\,d\overrightarrow{V}/dt \tag{6.43}$$

$$I_x\dot{\omega}_x = M_x - (I_z - I_y)\omega_y\omega_z I_y\dot{\omega}_y = M_y - (I_x - I_y)\omega_x\omega_z I_z\dot{\omega}_z = M_z - (I_y - I_x)\omega_y\omega_x \tag{6.44}$$

$$\overrightarrow{M} = \mathbf{I}\dot{\overrightarrow{\omega}} + (\overrightarrow{\omega} + \mathbf{I}\overrightarrow{\omega}) \tag{6.45}$$

Where F is the force, P is momentum, t is time, m is mass, I is inertia, ω is angular velocity, and M is the moments. For calculating the initial rotational rate the impact moment was used in equation 6.46. During the printing process two regions on the maple leaf were in connect with the bed, one being the contact line and another being the point at where the wing segment was thickest. Using high speed video we were able to verify that the initial instant of rotation was about the second contact point and as such the radius between the pod and the second contact point was used for the impact radius. Note that the time of $1/200^{th}$ still holds here.

$$\omega_{Z,0} = 0.005(R_{impact} \times F_{impact})/I_{ZZ} \tag{6.46}$$

Where R_{impact} is the radius in the x-axis from the impact point to the center-of-mass. Initial rotation is assumed to only be about the Z-axis. A termination condition based on z-position was used. Mass and inertia values are found from the CAD model of the object and inputted into the simulation by the user.

The object evolution as controlled by the 6-DOF simulation, at a given simulation instant, using the calculated values for force and moment (as described later in this section) starts with the calculation of the acceleration in the body frame. Since the mass is constant, Eq. 6.43 can be expressed as Eq. 6.47.

$$\overrightarrow{a}_b = \overrightarrow{F}/m + \overrightarrow{V}_b \times \overrightarrow{\omega}_b \tag{6.47}$$

In Eq. 6.47, a is the acceleration. Velocity in the body frame is then found by integrating acceleration in the body frame as shown in Eq. 6.48

$$\overrightarrow{V}_b = \int \overrightarrow{a}_b dt \tag{6.48}$$

The angular accelerations are found using Euler's equations of motions, implemented as Eq. 6.49

$$\dot{\overrightarrow{\omega}} = (\overrightarrow{M} - \overrightarrow{\omega} \times \mathbf{I}\overrightarrow{\omega})\mathbf{I}^{-1} \tag{6.49}$$

This was then be integrated to get angular velocity as shown in Eq. 6.50

$$\overrightarrow{\omega} = \int \dot{\overrightarrow{\omega}} dt \tag{6.50}$$

The next variable to be calculated was the rotation matrix, also known as the direction cosine matrix (DCM). The naming convention used through this section is that $\mathbf{R}_{a,b}$ is the DCM to rotate from frame b to frame a. The first step in find the DCM is to find the rate of change of the Euler angles, Eq. 6.51

$$\begin{aligned}
\dot{\phi} &= \omega_x + (\omega_y sin(\phi) + \omega_z cos(\phi)) sin(\theta)/cos(\theta) \\
\dot{\theta} &= \omega_y cos(\phi) - \omega_z sin(\phi) \\
\dot{\psi} &= (\omega_y sin(\psi) + \omega_z cos(\phi))/cos(\theta)
\end{aligned} \tag{6.51}$$

Where ϕ is the roll, θ is the pitch, and ψ is the yaw. These are then integrated to get the Euler angles Eq. 6.52

$$\begin{aligned}\phi &= \int \dot{\phi} dt \\ \theta &= \int \dot{\theta} dt \\ \psi &= \int \dot{\psi} dt\end{aligned} \tag{6.52}$$

With the Euler angles we then get the DCM using the standard ZYX convection in the inertial body frame; Eq. 6.53

$$\mathbf{R}_{b,i}\begin{bmatrix} c(\theta)c(\psi) & -c(\phi)s(\psi)+s(\phi)s(\theta)c(\psi) & s(\phi)s(\psi)+c(\phi)s(\theta)c(\psi) \\ c(\theta)s(\psi) & c(\phi)c(\psi)+s(\phi)s(\theta)s(\psi) & -s(\phi)c(\psi)+c(\phi)s(\theta)s(\psi) \\ -s(\theta) & s(\phi)c(\theta) & c(\phi)c(\theta) \end{bmatrix} \tag{6.53}$$

Using the rotation matrix, the velocity in the inertial frame is then calculated as in Eq. 6.54

$$\overrightarrow{V}_{inertial} = \mathbf{R}^{T}_{body,inertial}\overrightarrow{V}_{body} \tag{6.54}$$

.

Finally the inertial velocity is integrated to get the objects position in the inertial frame, Eq. 6.55

$$\overrightarrow{X}_{inertial} = \int \overrightarrow{V}_{inertial} dt \tag{6.55}$$

where X is the object position.

Additionally the forces and moments need to be calculated for the simulation. Historically, multiple methods have been used to model lift for both auto-rotating and mechanically rotated wings including, blade element theory [Rijs and Smulders, 1990, Holden et al., 2015], actuator disk theory as per Ref. [Azuma and Yasuda, 1989, Rao et al., 2014], and wing vortex theory as demon-

strated in Ref. [Lee and Choi, 2018]. Blade element theory subdivides a propeller into smaller parts and then finds the forces on each part as per Ref. [Leishman, 2008]. These values are then integrated over the whole blade over one revolution to give forces and moments [Soe Thura Win and Kyi Hla Win, 2020]. Actuator disk theory, also called momentum theory, models a propeller as a thin, ideal disk and gives a relationship between power, thrust, area, and air density. Previous work involving this method found the terminal velocity is proportional to the root of the seed weight divided by the effective disk area, such as in Ref. [Azuma and Yasuda, 1989].

Since a high fidelity simulation was not required, a simple blade-element-theory-based method was used. The aircraft was sub-divided into three sections of the seed. The first section was from the seed pod to the center of gravity; this section would rotate backwards with respect to the forward-flight incidence angle and was thus assumed to generate no lift nor drag. The second section is defined as the region from the CG to the CP; i.e. this is the section rotating with the leading edge forward but in the wash of the first section. The section was assumed to generate lift and drag with at a constant reduced percentage to approximate the aerodynamic efficiency in wash. Ref. [Chinwicharnam and Thipyopas, 2016] talks about the aerodynamic efficiency of pusher and tractor configurations with respect to the aerodynamic downstream effects from the propulsion system. Ref. [Lee and Choi, 2018] claims 12% of lift being generated by the seed pod while noting that wake effects can cause error obtaining this figure. The literature converges on a conclusion that if this lifting region is small, it could also be assumed to be zero, as per Ref. [Soe Thura Win and Kyi Hla Win, 2020]. The final segment was the rest of the wing, rotating forward and not in the wash. This section was assumed to be generating full lift and drag. For the two lift and drag gener-

ating sections, the equations for lift eq. 6.57 and drag eq. 6.58 took velocity as the vector sum of the rotational velocity at the center of pressure, of the section. Equation 6.56 provides the net velocity of the aircraft in the inertial frame.

$$\overrightarrow{V}_{eff} = \omega \times R_{CPCG,y} + \mathbf{R}_{body,inertial}\overrightarrow{V}_{Inertial} \tag{6.56}$$

$$F_{Lift,z} = 1/2\rho C_{L,z} A_{ref,x} V_{x,eff}^2 \tag{6.57}$$

$$\begin{aligned} F_{Drag,x} &= -1/2\rho C_{D,x} A_{ref,x} V_{x,eff}^2 sign(V_{x,eff}) \\ F_{Drag,y} &= -1/2\rho C_{D,y} A_{ref,y} V_{y,eff}^2 sign(V_{y,eff}) \\ F_{Drag,z} &= -1/2\rho C_{D,z} A_{ref,z} V_{z,eff}^2 sign(V_{z,eff}) \end{aligned} \tag{6.58}$$

Where R_{CPCG} is the radius of the center of pressure relative to the center of gravity (with the CG taken as the origin), ρ is the air density, C_L is the coefficient of lift, A_{ref} is the reference area for the respective equation, and C_D is the coefficient of drag.

For lift it was assumed that only the body x component of the velocity contributed to lift and that lift was only in the body z axis.

All reference areas, center of pressure location, viscosity, and atmospheric density were assumed constant and inputted by the user based on appropriate modeling techniques. Calculation of Cl and Cd are based on interpolation of a lookup table, with respect to angle of attack, for the appropriate Reynolds number, calculated using Eq. 6.59

$$R_e = \rho ||\overrightarrow{V}_{eff}||_2 L/\mu \tag{6.59}$$

where L is the characteristic length and μ is the viscosity of the air. At-

mospheric values were taken as International Standard Atmosphere (ISA) values giving a density of 1.225 kg/m^3 and viscosity of 1.789×10^{-5} kg/m/s.

Finally gravity needs to be added to the lift and drag forces to get total force on the object, Eq. 6.60.

$$\overrightarrow{F}_{body,total} = \overrightarrow{F}_{lift} + \overrightarrow{F}_{drag} + \mathbf{R}_{body,inertial}(-9.81m\hat{z}) \tag{6.60}$$

The location of the center of pressure in the object body frame was used to calculate the moments from the aerodynamic forces, Eq. 6.61.

$$\overrightarrow{M} = \overrightarrow{R}_{CPCG} \times (\overrightarrow{F}_{Drag} + \overrightarrow{F}_{Lift}) \tag{6.61}$$

Fig. 6.7 simulates the trajectory of the aircraft under rotation, generating lift. The blue quivers demonstrate the orientation of the aircraft, span-tip-axis encompassing the positive arrow. The yellow trajectory demonstrates the aircraft not under any rotation, falling under a ballistic trajectory. The black marks signify 2hz sampling rates to visualize time as a function of distance. Both the rotating and ballistic aircraft were provided the same ISA conditions (except for orientation to provide rotation and lift-generation) and were subjected to the aerodynamic modeling presented above. The results provide insight as to the predicted RPM, and that our design will generate lift under rotation. The rotating aircraft exhibits a longer trajectory, and demonstrates an improvement with respect to the iterations presented in the prototyping section. The aircraft now had a theoretical expected result, and could be fabricated and subjected to ISD for comparison of results to those observed by the CV sensing.

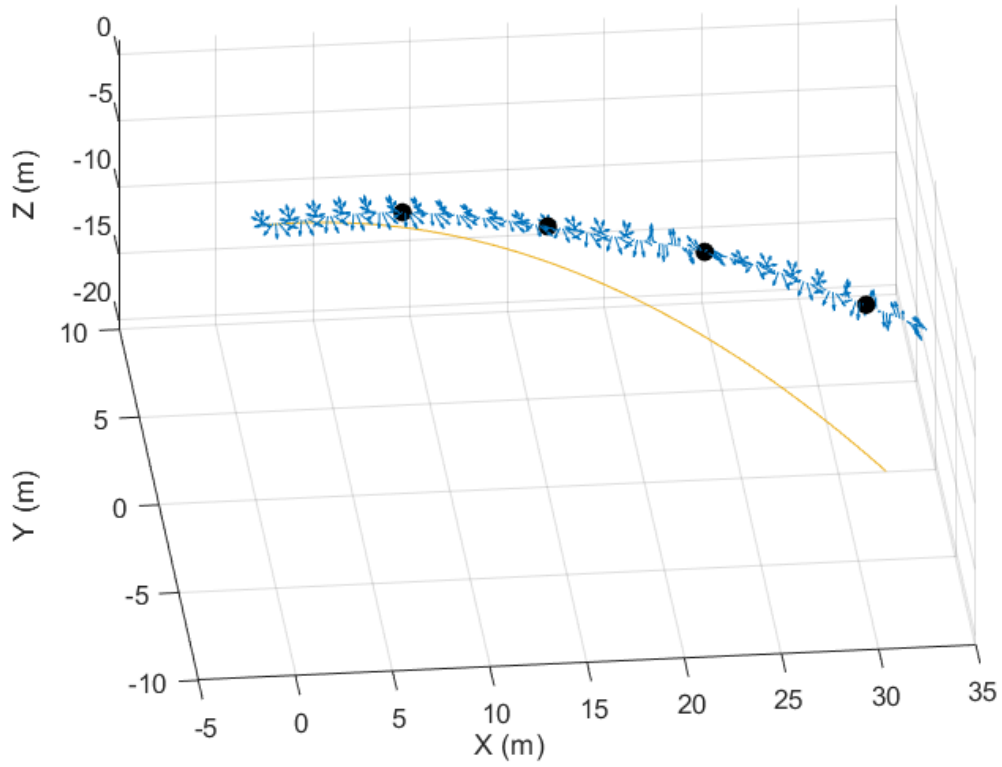

Figure 6.7: Simulated trajectory and RPM of aircraft generating lift under rotation of 600 RPM (blue) and 0 RPM (yellow) in the aerodynamic, lift-generating models. The blue quivers represent the position and orientation of the aircraft, the black dots are 2hz tick marks, and the orange line is a ballistic trajectory with the same initial conditions.

Programming ISD of Aircraft

As previously defined, the gCode file format was used as the machine code manipulator. The gCode file format is a standard open source file format used by the vast majority of consumer-grade 3D printers. By using a prolific, open source file format the processing scripts and methodologies we used for the object ejection could be easily moved to other FDM/FFF printing platforms. In our implementation PrusaSlicer and Simplify3D® were used for gCode generation.

When designing or choosing an object for ejection, consideration needs to be taken so that the process of deflecting the ISA doesn't impact the target object. The simplest way to ensure this is to have the target object be equal to or shorter than the interface tab on the actuator. It would also be possible for an object taller than the actuator to be deployed if the gantry motion for deployment does not interfere with the object to be deployed. While this would not be possible with the Prusa i3 we used, there may be other machines more suited to that application

Once a 3D model for a desired aircraft has been made, it needs to be prepared for printing. As for the printing and programming of ISA process, the first step in the process is to take the 3D model and convert it to a gCode file, with the object centered at the origin. Once the appropriate gCode file had been generated a custom MATLAB® script was used to modify the file for autonomous ejection through ISD.

The next step was to modify the file to have an ejection base. Not used in ATCAM, the ejection base was designed to provide a secure attachment point of an aircraft to the printer while allowing to a quick detachment when the part was ejected through ISD. This allows for objects with phenotype variations within a certain design scope to be deployable through ISD The user can define whether

Algorithm 3: Aircraft Preparation Workflow

Input: Aircraft model to be deployed
Output:gCode file to deploy Aircraft
Use slicing program to get gCode file of aircraft located at coordinate system origin
if *Rotate aircraft for deployment* **then**
| Rotate aircraft for determined AOA
| Default to +10 deg if not specified
| Add rotation code to gCode file
else
| Aircraft preoriented for ISD
end
if *Add ejection base to aircraft* **then**
| Translate aircraft z-cordinates up
| Add ejection base to gCode file
else
| Replace bottom of aircraft with ejection base gCode
end
Translate coordinates in gCode File
if *Add actuator* **then**
| **if** *Default actuator orientation doesn't fit on print bed* **then**
| | Translate and rotate actuator as appropriate
| **end**
| Add ejection actuator to gCode file
end
Add ejection pull to gCode file
if *Add repeats* **then**
| Add desired number of copies of the aircraft without the actuator to end of gCode file
end

they want the base added to the bottom of the object or to replace the bottom of the object. If the base is added to the bottom of the object the z-coordinates in the ejection object gCode were offset up and the gCode for the base was inserted into the file. The file manipulation was done in such a way as to preserve the print settings for the original object. If the base is to replace the bottom of the object the corresponding number of layers to match the bases height are removed and replace with the gCode for the base.

Once the base has been added the combined object is then translated to the appropriate location for printing and deployment. This is achieved by offsetting the X and Y coordinates in the gCode file. If the user desires, a new actuator can also be added to the gCode. Using pre-generated code, the actuator is spliced in layer-by-layer.

The paddle location and orientation were chosen such that the object was as close to the actuator as possible, while allowing the print head to push an existing actuator out of the way to allow for printing another object if the actuator was already present.

Code was added to deflect the actuator, causing the object to be ejected. The result of the script is a gCode file that prints the object, and paddle if desired, and then ejects the object.

Finally, if the user desires they can add additional ejections. This is done by adding additional object and ejection code, without the actuator, to the end of the file before printer shutdown as many times as the user desires.

Algorithm 4: Aircraft Fabrication and Deployment workflow

Input:gCode file to deploy aircraft
Output:deployed aircraft(s)
Upload gCode file to printer and start print
if *Multiple aircraft to be printed* **then**
  Set up appropriate receptacle
end
Printer will print actuator and first aircraft simultaneously
Printer will deflect actuator to specified angle and release
Printer will eject aircraft
while *Multiple aircraft left to be printed* **do**
  Subsequent aircraft will be printed. Print head will move paddle-end of actuator as necessary
  Printer will eject aircraft
end

Testing Methods and Results

In order to characterize the performance of the actuator and the accuracy of the simulation we preformed a series of tests were performed analyzing the ejection trajectories.

Full Trajectory Tests

The first type of testing was done using a pair of high speed cameras to record the ejection and resulting trajectory. The first camera was located directly over the build platform to observe the impact and the second was located further back and side-facing to the printer to observe the trajectory of the ejected object.

From the camera located above the build platform we could determine the angular velocity of the actuator before and after impact with the target object as well as the initial velocity of the target object to determine how energy was transferred during the collision. With a given actuator part of the test was repeated for every deployment for the first 10 deployments and then every five deployments

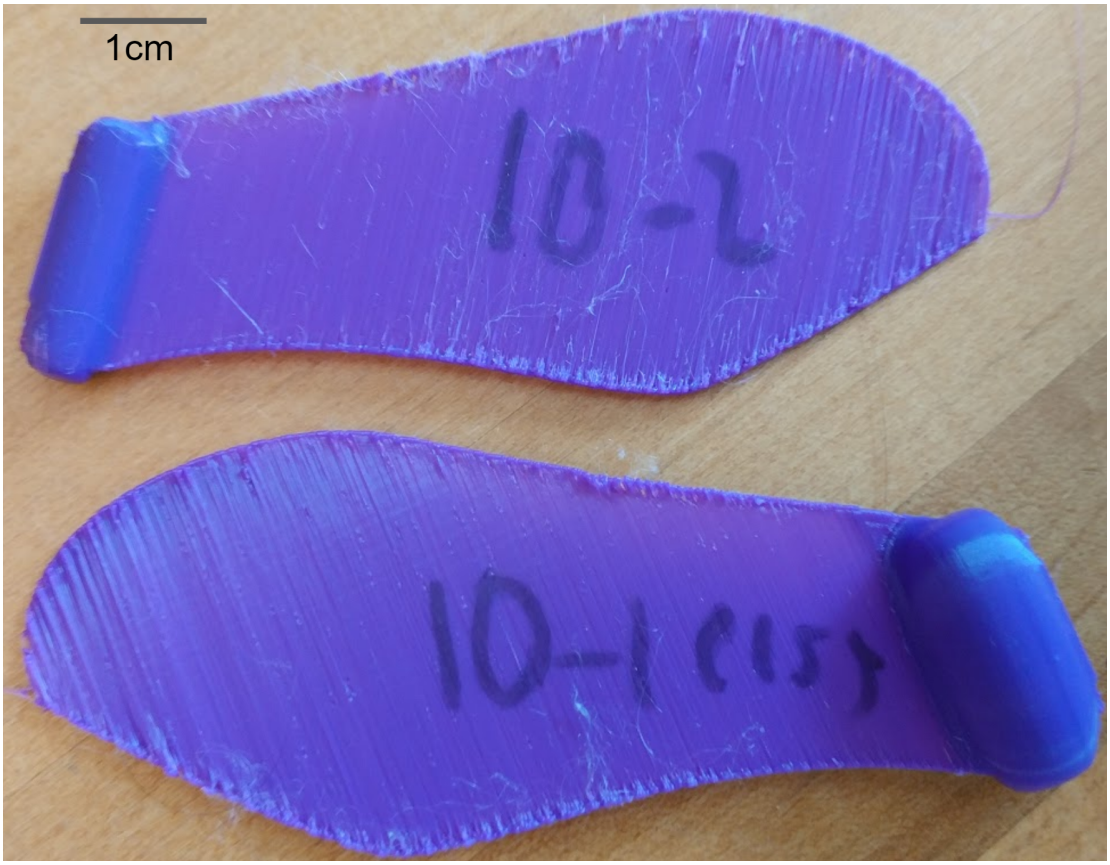

Figure 6.8: Example of printed seed.

until 60 total deployments had occurred in order to characterize any changes in the impact energy transfer over an actuators lifetime.

With the side facing camera the trajectory of the ejected object could be observed and compared to estimated values.

Actuator Impact Tests

For the second type of testing a load cell was secured to the build platform (with a pre-printed ISA) in the location where the target object would normally be printed. A custom toolpath was then used to repeatedly deploy the actuator, with 30 second pauses in between actuation's, to characterize the force of impact over the lifespan of an individual actuator. When the actuator deployed it impacted

the load cell causing an output signal, processed by an op amp, that was then read in by a Raspberry Pi micro controller. The Raspberry Pi then saved the value to a text file and waited for the next data point. The data was timestamped, which could then be compared against the known delay between deployments, to reduce possible errors in the data collection.

Through physical testing, the frequency of the data sampling rate was converged to 10hz, taken as the minimum threshold to capture the data correctly without generating redundant noise. The selection of 10hz was also a hardware limitation, serving as the blend of data fidelity and polling rate of analog-to-digital conversion.

Deployment Sensing

A third test configuration had the ejected object travel a short distance before impacting a target plate attached to a load cell. This test configuration, as seen in Fig. 6.13, ejects the dynamic coupon from ATCAM to produce simple ballistic motion. Additionally, a disk and cube were also subjected to ISD for control purposes. Various milestones of different generations were also subjected to ISD to allow

Similarly to the impact test, when a deployed object impacted the load cell causing an output signal, processed by an op amp, that was then read in by a Raspberry Pi micro controller. The Raspberry Pi then saved the value to a text file and waited for the next data point. The plate attached to the load cell was made from laser cut acrylic and was used to ensure a sufficiently large area such the the ejected object would reliably impact. Using a known mass we were able to statically load the plate in different locations to verify that different locations on the plate would not change the load cell readings.

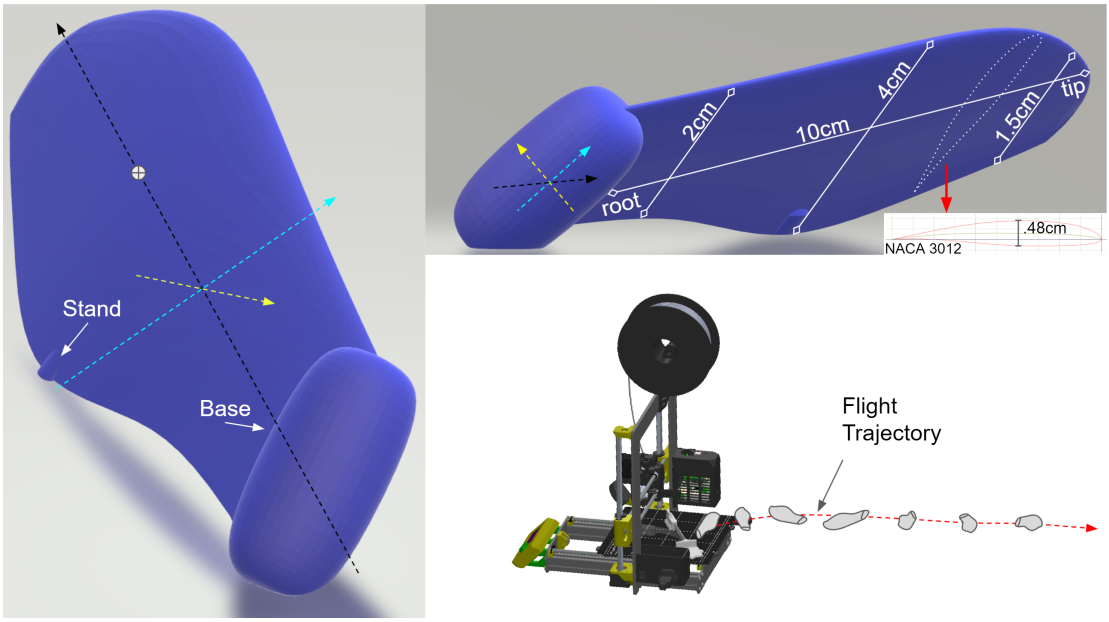

Figure 6.9: Top and Left: Final Aircraft (Seed 12) specifications and features. Bottom: Printer Configuration for ISD of Aircraft

Computer Vision for Localization and Trajectory Tracking

A second micro controller was used to capture and process video recordings. Unlike in the first experiment, where video data was processed manually, we used an open source computer vision system (OpenCV for Python) to record the trajectory and velocity of the ejected object. For these trials plastic filaments were chosen that had high contrast against a white background and the camera was located such that the pixels per cm would be constant along the expected trajectory. An example of the masking that allowed for an aircraft to be identified by its color is provided in Figure 6.11.

As seen in this figure, the centroid was assumed to be the center of mass with respect to density distribution of the aircraft. This assumption was only made for the sake of a robust tracking process for the computer vision platform. The centroid of each deployed aircraft was tracked over the deployment trajectory. The distance of each object was observed by the CV system and is overlaid for

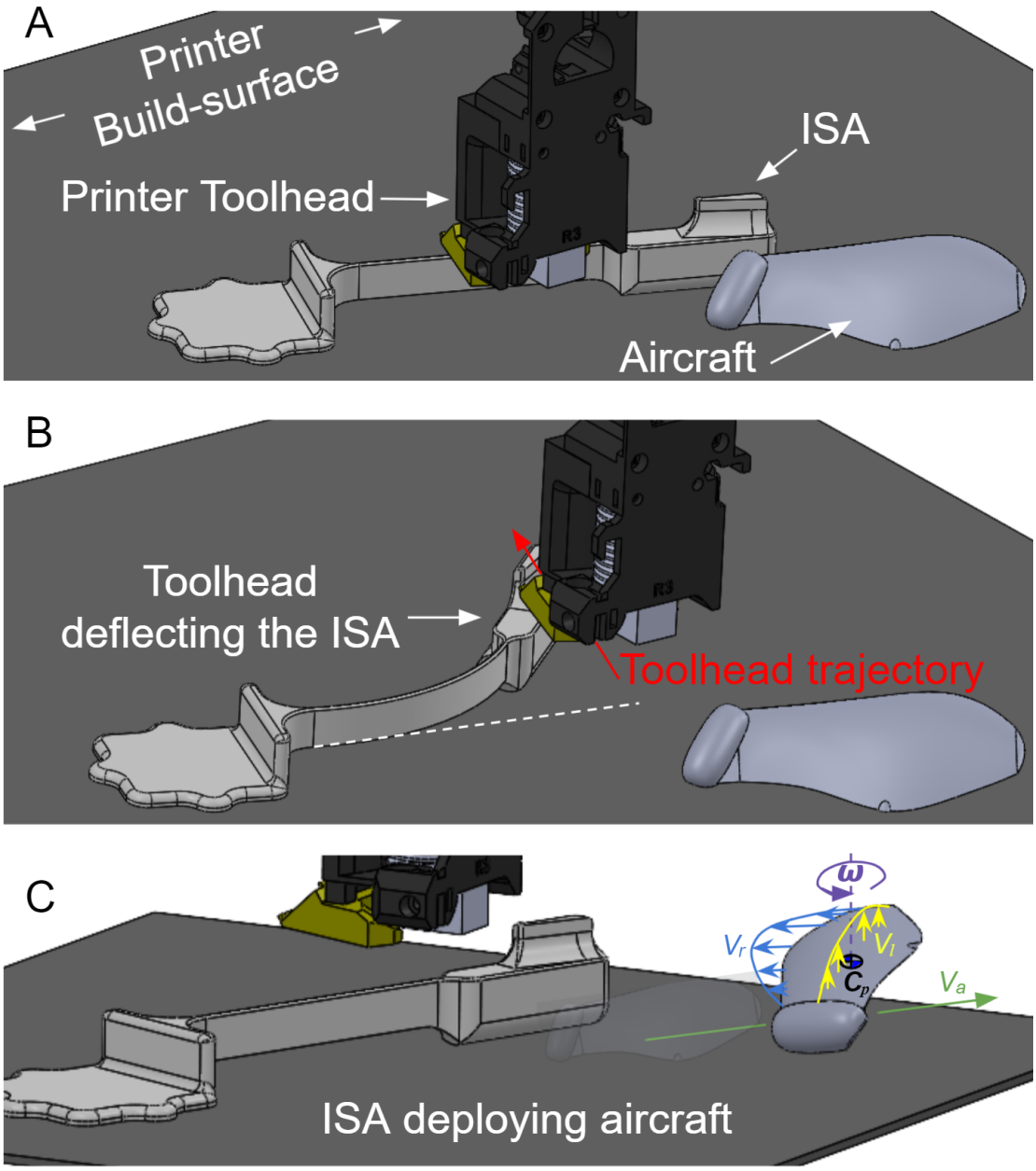

Figure 6.10: ISD method and visualized as-printed configuration and deployment of aircraft

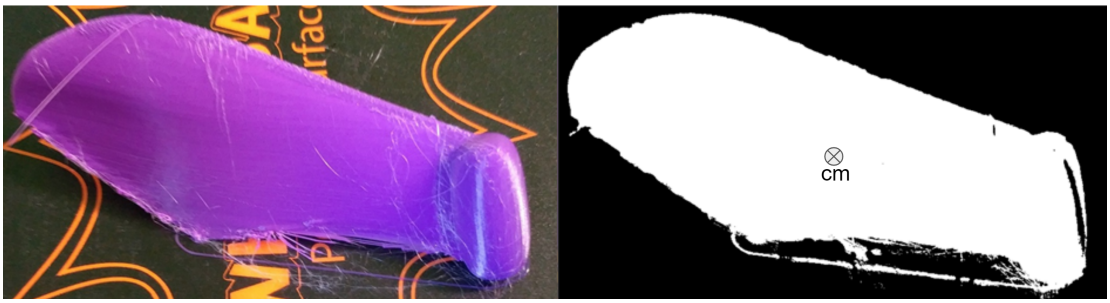

Figure 6.11: ISD method and visualized as-printed configuration and deployment of aircraft

comparative purposes in Figure 6.14.

The deployment configuration of a test article is demonstrated in Fig. 6.10.

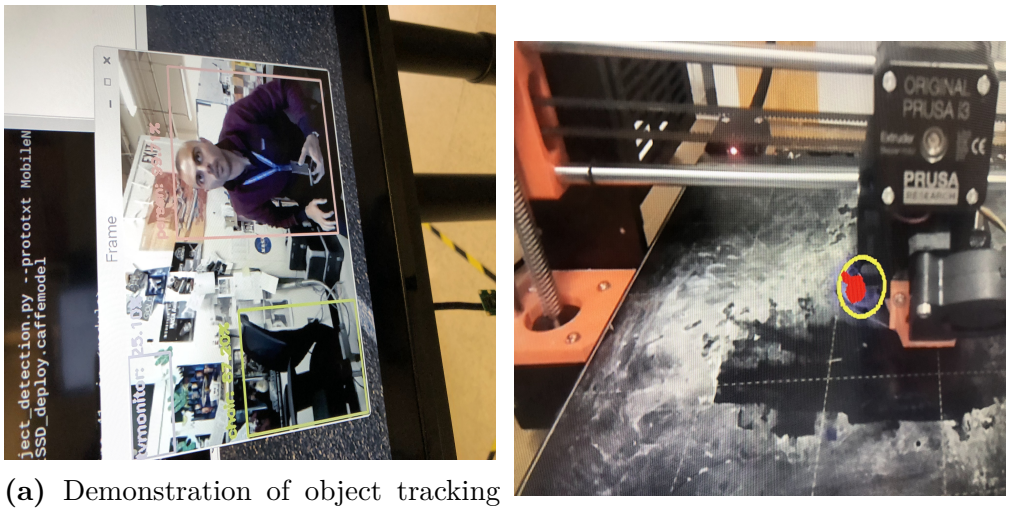

(a) Demonstration of object tracking with OpenCV. The bounding boxes of various colors signify the objects detected and paired with a known classification and their respective confidence.

(b) Demonstration of altered strategy to track Am parts, following a specific color and the trajectory of its centroid.

Figure 6.12: Implementations of automated tracking methods utilizing computer vision

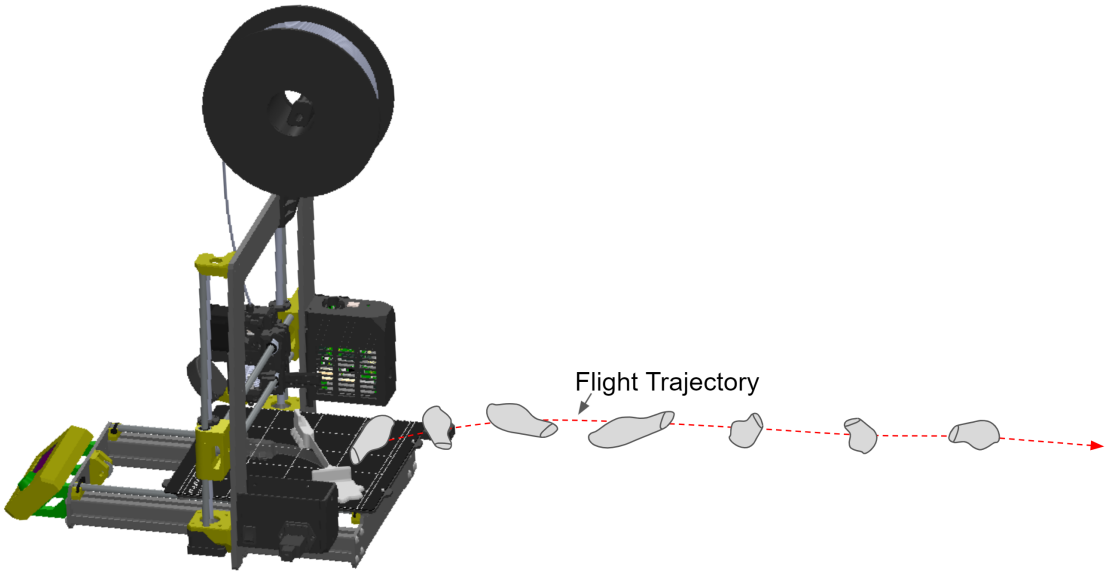

Figure 6.13: Printer Configuration for ISD of Aircraft

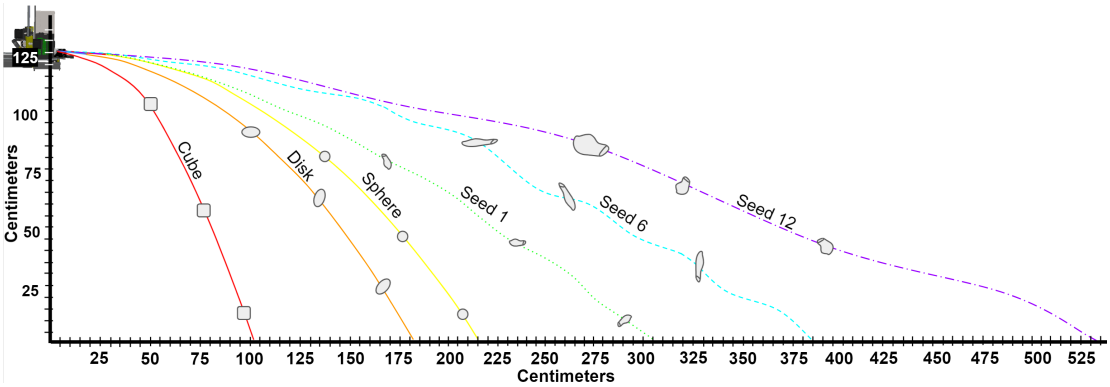

Figure 6.14: Comparison of ISD object mean trajectories with respect to distance traveled, as observed by CV system.

6.3 Discussion

As demonstrated above, the CV system successfully tracked the trajectory of the ISD objects and aircraft. The sphere, disk, and cube were used as a baseline and demonstrated poor distances through the ISD process. This implies that they have extremely low lift-to-weight ratios, a common indicator of aerodynamic efficiency. The first generation of seed was able to be deployed, although extremely infrequently. It flew a distance of 305 centimeters. Its trajectory demonstrated that the induced drag was likely enabling it to travel a further distance compared to the sphere, which acts as a baseline given its theoretical geometric drag coefficient.

The trajectory of seed 6 was an improvement over seed 1, reaching 385 centimeters. This implies improved aerodynamics and a potentially improved coefficient of lift due to the oscillation that was observed during its flight. The low frequency of the oscillations demonstrates that the RPM of the lifting surface is low, and consequently it is likely providing just enough lift to maintain stability and travel further than seed 1 given that they both had the same mass and input ISD force. Seed 12 was the final configuration and displayed a favorable distance of approx-

imately 530 centimeters from a height of 124 centimeters. This provides a rough glide ratio of 4.3, which is in-line with the average estimate of an autorotating helicopter (glide ratio of 4). The trajectory demonstrates sufficient RPM and an aircraft which is clearly rotating at a higher frequency than seed 6 and demonstrating a longer range with the same amount of input energy, implying improved aerodynamic efficiency.

When the CV results are compared to that from the simulation provided earlier in this chapter for Seed 12 in Fig. 6.7, the physical and simulated results are surprisingly similar. The RPM of the physical seed is a little lower, at approximately 450RPM as opposed to the theoretical 600RPM from the simulation. The distance traveled is also comparatively similar. The simulation allowed for the object to fall 20 meters just to observe stability of the aircraft during its flight; however, if the fall height of the aircraft is limited to 1.25 meters as it was in the physical experiment the theoretical distance would be roughly 7 meters. As provided by Fig. 6.14, the aircraft flew 5.3 meters. This reduction in efficiency is expected, as the simulation does not account for inertial error in the manufacturing process of both the aircraft and the ISA. Additionally, the simulation does not account for errors that accumulate from the ISD process, nor does it account for the fatigue that ATCAM detected within ISA's over deployment cycles.

Another interesting result was that although the RPM of the physical aircraft was approximately 25 percent less than the theoretical value, the velocity of the physical aircraft was over 30 percent less than the theoretical result. This might be a function of induced drag not accounted for and a theoretically optimistic C_d. The stability of the aircraft was validated as a function of the velocity of the aircraft. The rule derived by Ref. [Jameson et al., 2007] and Ref. [Jameson et al., 2012] defines the stability of a samara seed aircraft as the angular velocity > 1.2 the

aircraft velocity. The reduction in the aircraft velocity likely assisted the stability of the aircraft, which can be observed by the stable trajectory demonstrated in Fig. 6.14. By successfully providing the user with the trajectory and velocity of the ISD aircraft, designs which have varied theoretical performance as per the simulation can now be physically characterized and validated. This result provides our final deliverables regarding an autonomous system which fabricates and deploys an aircraft off of its build surface, a system and one which senses and characterizes performance improvement of an object it has automatically manufactured and deployed.

6.4 Future Work

The implications of the work presented in this chapter provide significant promise for further development and testing schemes to automatically correlate object phenotypes to variations in object performance. Although the work I have presented lays the foundation by pairing numerous systems I automated to work in conjunction for this process, robust full-cycle automation requires this final step. The next logical step of continuing the pursuit of this objective is to allow ATCAM to converge to a predetermined, locally optimal solution. Varying the number of iterations ATCAM requires to reach this solution is analogous to a "step-size" for a simulation, as increasing the number of steps would theoretically increase the fidelity of the solution as well in exchange for a longer period of time and increased resources. This analogy holds for the maximum theoretical number of steps as well (such as the capabilities of the solver with respect to the sensitivity of a mesh), as ATCAM's theoretical iterations are limited as a function of the capabilities of the manufacturing platform ATCAM is leveraged on.

There are a finite number of tests ATCAM can run, depending on the sensi-

tivity of the manufacturing process and volume of the manufacturing platform. I bounded these constraints considerably to provide some control over the process and narrow the maximum number of solutions I would be provided with (Seed 1 through Seed 12 are good examples of the step size with respect to phenotype variation). This theoretical threshold should be explored further to increase the confidence in ATCAM's results to reach design optimality. Regardless of these considerations, the framework provided in this document is applicable to any manufacturing platform, as the core of the work conducted here is just to integrate more dimensions of physical sensing into the manufacturing process and leverage the implicit capabilities of manufacturing platforms (such as for ISA's to conduct ISD) and obtain dynamic coupons. Varying the concept of a dynamic coupon to different manufacturing platforms and processes is an exciting prospect, and I look forward to observing how this concept further will be developed further through the publications generated by the work.

Chapter 7

Summary of Deliverables and Applications

This document has demonstrated the validity of a model which represents an actual multi-physics system, implemented through the integration of fabrication and testing on the same platform. The model was developed with assumptions that allowed for the linearization of the equations of motion which govern the transfer of energy. By tracing this energy from intentionally-discrete models, we calculated potential energy embedded into a fabricated spring via the nozzle that manufactured it. This potential energy gets translated into kinetic energy through a simplified harmonic oscillator, providing momentum that is conserved in contact with a sphere. The launching of this sphere allowed for us to observe the physics associated with flight, allowing for observed accelerations to be compared to simulated values. The premise of this idea was developed into the concept of dynamic coupons, which were presented in Chapter 5.

The errors of the simulated acceleration of the system was found to be within single-digit percentage of observed values. The error is low, as we tuned and parameterized the model with respect to observed values. The utility of this

model is that the system may now be digitally optimized, as we have successfully characterized the system. Further errors can be associated to manufacturing and material-specific phenomena, provided the concurrent acceptance of the assumptions stated in this document. The work in this dissertation provides the basis to design and size components with the understanding that expected kinetic energy transferred by the system can be predicted through simulation. This entails the capability to characterize designs through sensed performance of objects and implied manufacturability.

The technology takes a digital design and modifies it for the desired actuation of a component to be fabricated within the build volume. The manufacturing process-specific toolpathing software generates a code which is modified for autonomous cyber-physical interfacing. When the software is executed, the additive manufacturing process takes place and additional dimensions of physical interfacing cause fabricated objects to dynamically interact. We visualize the framework through a referenced demonstration as an example of the kinematic interaction between two manufactured objects on the same build-platform. Examples of additional parameters of information contained in this demonstration are the range of velocities and spring constants the manufactured objects will exhibit through build-plate interactions. The unique aspects of this technology are highlighted in green in the flowchart visualized in Figure 7.1, demonstrate the process through the referenced example.

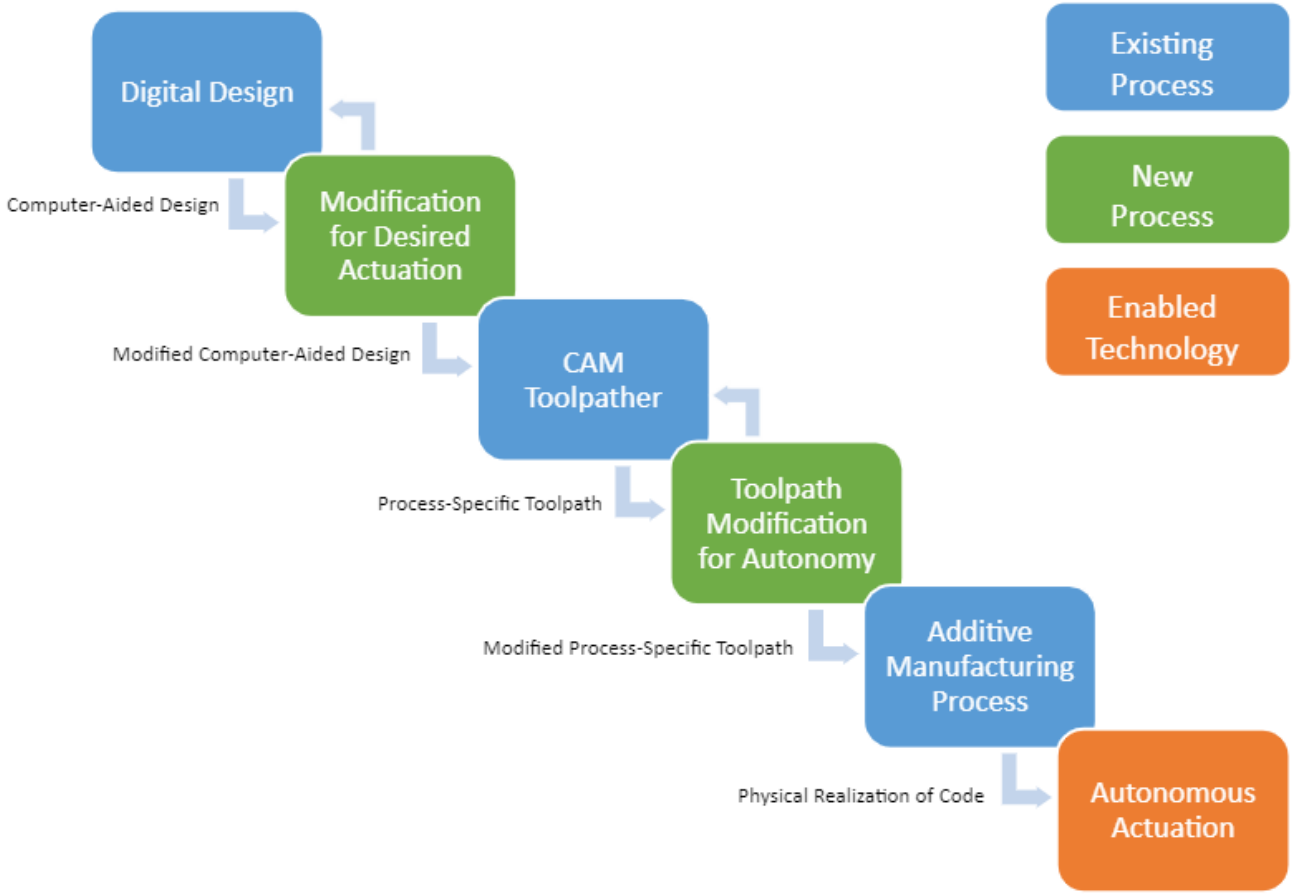

Figure 7.1: Subsystems For Autonomous Actuation

7.1 Unique features to Date

The work is enabled by the combination of new algorithms, enabling the autonomous cyber-physical interaction of 3D-printed parts on the build-tray for automated high-volume testing of additively manufactured components. The first algorithm allows for the physical interaction of a 3D-Printed object with its environment, with the second algorithm allowing for the autonomy of such interactions. The combined algorithms allow for the high-volume production and autonomous actuation and testing of additively manufactured parts through physical interfacing of printed components with one-another and the machine that manufactured them. These digital modifications allow for the automated embedding and physical validation of additional dimensions of information through the manufacturing process.

7.2 Overview of Deliverables

The first of two building blocks required for the autonomous actuation of an additively fabricated component on the manufacturing platform is the 'Modification of the Design for Desired Actuation'. This process describes the creation of a secondary object (the ISA) to interface with and store elastic energy from the additive manufacturing process. This ISA would be capable of then autonomously transferring the potential energy into the primary object (the sphere) with the desired designed dynamics through conservation of momentum. The input and output of this block is a 3D-model (in our example, a surface-tesselation-language (.stl) file).

The second building block required takes the output of the manufacturing platform's toolpathing software and modifies the toolpath with a post-script that

integrates the numerics required for autonomy. This 'Toolpath Modification for Autonomy' takes digital information that has been generated by manufacturing process-specific toolpathing software and modifies it for autonomous interfacing with the manufacturing hardware to translate energy through the manufactured object (the ISA). The input and output of this block is a modified toolpath (in our example, a Gantry Code (.gcode)).

7.3 Applications of Deliverables

Users of this work are being provided with a platform and test-bed for digitally embedding additional dimensions of information into currently-existing systems through ISD. By demonstrating advances in ISD from ISLS to ISA, we were able to demonstrate a method for quick, portable, repeatable, and high-volume deployment. Industry may leverage the technology with a multitude of processes for creating novel interactions that may have commercial applications. A novelty of this innovation lies in the ability to conduct significantly more experiments than otherwise possible utilizing current systems without any physical modifications. The ability to digitally transfer this capability is very powerful and requires minimal investment to adopt from a commercial perspective.

Industrial applications may benefit heavily from the ability to autonomously and repeatably deploy a high volume of experiments on additive manufacturing platforms, even through our demonstrated example. The repeatable ability for an object to 'fly off of the machine that made it' essentially enables automated clearing of the processed build volume. The increased throughput through the automation of clearing a machine without the need for additional robotic manipulators may be economically appealing. This is especially relevant as industry continues to adopt a larger percentage of additive manufacturing as part of its

workflow.

Given the current status of the work, I have developed tools which allow for the serial automation of the following processes:

- Modification of a digital 3D model enabling its deployment (Chapter 3)
- Automated fabrication and deployment of an AM object (Chapters 3 and 4)
- Automated modification of an AM object's phenotype (Chapter 4)
- Automated manufacturing and deployment of AM objects with modified phenotypes (Chapter 4)
- The concept and implementation of dynamic coupons (Chapter 5)
- Automated characterization and performance sensing of AM objects (Chapter 5)
- Automated characterization of AM feedstock (Chapter 5)
- A strategy to decide whether performance of the modified AM object has improved (Chapter 5 and 6)
- An autonomous system which fabricates and deploys an aircraft off of its build surface (Chapter 6)

7.4 Papers and Academic Contributions

The papers generated from this work were distributed as follows:

- Printing and Programming of In-Situ Actuators (Chapters 3 and 4)

- Automating Sequential Additive Manufacturing by Retrofitting In-Situ Deployment (Chapters 3 and 4)
- ATCAM: Automated Testing and Characterization of Additive Manufacturing (Chapter 5)
- An Object Which Flies off of the Additive Platform (Chapter 6)
- On the Additive Fabrication of Aerostructures for Micro Aerial Vehicles (Chapter 6)

The current deliverables from this work have been submitted to the National Aeronautics and Space Administration. At the time of this writing, this work has been issued a non-utility provisional patent-pending status with the United States Patent and Trademark Office under the title "Augmented Manufacturing by Embedding Autonomous Interactions Between Manufactured Components and Manufacturing Machines" Docket No. ARC-18452-1.

Appendix A

Appendix

A.0.1 Variables

Defining Variables:

Modulus of Elasticity of Printer Material:

E

Density of Ball Print:

ρ_b

Density of Paddle Print:

ρ_p

Height of Paddle:

H_p

Height of Spring:

H_s

Length of Paddle:

L_p

Length of Spring:

L_s

Width of Paddle:

W_p

Width of Spring:

W_s

Velocity of Ball:

V_b

Kinetic Energy:

Ke

Origin of Ball:

O_b

Origin of Paddle:

O_p

Location of Nozzle Pull:

Loc_n

Displacement of Spring:

D_s

Mass of Ball:

M_b

Mass of Paddle:

M_p

Mass of Spring:

M_s

Moment of Inertia of Spring Cross Section:

I_{s_cs}

Moment of Inertia of Paddle Center:

I_{p_c}

Moment of Inertia of Spring End:

I_s

Moment of Inertia of Assembly:

$$I_a$$

Transferred Energy:

$$E_t]$$

Angular Frequency:

$$\omega$$

Impact Velocity:

$$V_{Imp}$$

Kinetic Energy of Ball:

$$Ke_b$$

Velocity of Ball:

$$v_b$$

Volume of Ball:

$$V_b$$

Force:

$$F$$

Strain Energy:

$$U$$

A.0.2 Equations

A.1 Supplementary Equations

Eq1:

$$M_b = V_b * \rho$$

Eq2:

$$M_p = W_p * L_p * H_p * \rho_p$$

Eq3:

$$M_s = W_s * L_s * H_s * \rho_b$$

Eq4:

$$I_{s_{cs}} = \frac{(W_s^3 * H_s)}{12}$$

Eq5:

$$F = \frac{3EI_{s_{cs}}D_s}{Loc_n^3}$$

Eq6:

$$I_s = \frac{M_s L_s^3}{3}$$

Eq7:

$$I_{p_c} = \frac{M_p(W_p^2 + L_p^2)}{12}$$

Eq8:

$$I_a = I_s + I_c + M_p(L_s + .5L_p)^2$$

Eq9:

$$\omega = \sqrt{\frac{2U}{I_a}}$$

Eq10:

$$V_{imp} = \omega O_b$$

Eq11:

$$(KE)_{ball} = \frac{1}{2} V_{imp}^2 M_p E_t$$

Eq12:

$$V_b = \sqrt{2\frac{(KE)_b}{M_b}}$$

Bibliography

[Abraham, 1970] Abraham, F. F. (1970). Functional dependence of drag coefficient of a sphere on reynolds number. *The Physics of Fluids*, 13(8):2194–2195.

[Ahmed et al.,] Ahmed, M., Islam, M. R., Vanhoose, J., Hewavitharana, L., Stanich, A., and Hossain, M. Comparisons of bending stiffness of 3d printed samples of different materials. In *ASME 2016 International Mechanical Engineering Congress and Exposition*. American Society of Mechanical Engineers Digital Collection.

[Ahn et al., 2002] Ahn, S.-H., Montero, M., Odell, D., Roundy, S., and Wright, P. K. (2002). Anisotropic material properties of fused deposition modeling abs. *Rapid prototyping journal*, 8(4):248–257.

[Albus et al., 1983] Albus, J. S., Barbera, T., Bloom, H., Fitzgerald, M. L., Kent, E., and McLean, C. R. (1983). Hierarchical control for robots in an automated factory.

[Allen, 2018] Allen, E. (2018). Approximate ballistics formulas for spherical pellets in free flight. *Defence technology*, 14(1):1–11.

[Anderegg et al., 2019] Anderegg, D. A., Bryant, H. A., Ruffin, D. C., Skrip Jr, S. M., Fallon, J. J., Gilmer, E. L., and Bortner, M. J. (2019). In-situ monitoring of polymer flow temperature and pressure in extrusion based additive manufacturing. *Additive Manufacturing*, 26:76–83.

[Anderson and Pandy, 1993] Anderson, F. C. and Pandy, M. G. (1993). Storage and utilization of elastic strain energy during jumping. *Journal of biomechanics*, 26(12):1413–1427.

[Anderson et al., 2018] Anderson, I. E., White, E. M., and Dehoff, R. (2018). Feedstock powder processing research needs for additive manufacturing development. *Current Opinion in Solid State and Materials Science*, 22(1):8–15.

[Arakawa, 2017] Arakawa, K. (2017). An analytical model of dynamic sliding friction during impact. *Scientific reports*, 7:40102.

[Arias-Montano et al., 2012a] Arias-Montano, A., Coello, C. A. C., and Mezura-Montes, E. (2012a). Multi-objective airfoil shape optimization using a multiple-surrogate approach. In *2012 IEEE Congress on Evolutionary Computation*, pages 1–8. IEEE.

[Arias-Montano et al., 2012b] Arias-Montano, A., Coello, C. A. C., and Mezura-Montes, E. (2012b). Multiobjective evolutionary algorithms in aeronautical and aerospace engineering. *IEEE Transactions on Evolutionary Computation*, 16(5):662–694.

[Armero and Romero, 2001] Armero, F. and Romero, I. (2001). On the formulation of high-frequency dissipative time-stepping algorithms for nonlinear dynamics. part i: low-order methods for two model problems and nonlinear elastodynamics. *Computer Methods in Applied Mechanics and Engineering*, 190(20-21):2603–2649.

[Aroca et al., 2017] Aroca, R. V., Ventura, C. E., De Mello, I., and Pazelli, T. F. (2017). Sequential additive manufacturing: automatic manipulation of 3d printed parts. *Rapid Prototyping Journal*.

[Attaran, 2017] Attaran, M. (2017). The rise of 3-d printing: The advantages of additive manufacturing over traditional manufacturing. *Business Horizons*, 60(5):677–688.

[Azuma and Yasuda, 1989] Azuma, A. and Yasuda, K. (1989). Flight performance of rotary seeds. *Journal of Theoretical Biology*, 138(1):23 – 53.

[Babichev et al., 2002] Babichev, S. A., Ries, J., and Lvovsky, A. I. (2002). Quantum scissors: teleportation of single-mode optical states by means of a nonlocal single photon. Preprint at `https://arxiv.org/abs/quant-ph/0208066`.

[Babu et al., 2015] Babu, S. S., Love, L., Dehoff, R., Peter, W., Watkins, T. R., and Pannala, S. (2015). Additive manufacturing of materials: Opportunities and challenges. *MRS Bulletin*, 40(12):1154–1161.

[Baker et al., 2019] Baker, A. B., Bates, S. R., Llewellyn-Jones, T. M., Valori, L. P., Dicker, M. P., and Trask, R. S. (2019). 4d printing with robust thermoplastic polyurethane hydrogel-elastomer trilayers. *Materials & Design*, 163:107544.

[Bankupalli et al., 2020] Bankupalli, N., Rao, D. S., and Krishna, T. V. (2020). Role of butadiene content on tribological properties of polymeric components fabricated by fdm. *Materials Today: Proceedings*.

[Barclift and Williams, 2012] Barclift, M. W. and Williams, C. B. (2012). Examining variability in the mechanical properties of parts manufactured via polyjet direct 3d printing. In *International Solid Freeform Fabrication Symposium*, pages 6–8. University of Texas at Austin Austin, Texas.

[Barrett et al., 2015] Barrett, R., Freeman, I., and Ning, A. (2015). Effect of airfoil and composite layer thicknesses on an aerostructural blade optimization for wind turbines. In *2015 IEEE Conference on Technologies for Sustainability (SusTech)*, pages 195–202. IEEE.

[Barros et al., 2011] Barros, R. C., Basgalupp, M. P., De Carvalho, A. C., and Freitas, A. A. (2011). A survey of evolutionary algorithms for decision-tree induction. *IEEE Transactions on Systems, Man, and Cybernetics, Part C (Applications and Reviews)*, 42(3):291–312.

[Baumers et al., 2016] Baumers, M., Dickens, P., Tuck, C., and Hague, R. (2016). The cost of additive manufacturing: machine productivity, economies of scale and technology-push. *Technological forecasting and social change*, 102:193–201.

[Behringer, 2014] Behringer, R. (2014). *Manipulating the mouse embryo: a laboratory manual*. Cold Spring Harbor Laboratory Press, New York.

[Bender, 1987] Bender, D. (1987). Lyapunov-like equations and reachability/observabiliy gramians for descriptor systems. *IEEE Transactions on Automatic Control*, 32(4):343–348.

[Berman, 2012] Berman, B. (2012). 3-d printing: The new industrial revolution. *Business horizons*, 55(2):155–162.

[Besnea et al., 2018] Besnea, D., Rizescu, C., Rizescu, D., Comeaga, D., Ciobanu, R., and Moraru, E. (2018). Study of deflection behavior of 3d printed leaf springs. In *IOP Conference Series: Materials Science and Engineering*, volume 444, page 042008. IOP Publishing.

[Bhushan and Caspers, 2017] Bhushan, B. and Caspers, M. (2017). An overview of additive manufacturing (3d printing) for microfabrication. *Microsystem Technologies*, 23(4):1117–1124.

[Bikas et al., 2019] Bikas, H., Lianos, A., and Stavropoulos, P. (2019). A design framework for additive manufacturing. *The International Journal of Advanced Manufacturing Technology*, 103(9-12):3769–3783.

[Bikas et al., 2016] Bikas, H., Stavropoulos, P., and Chryssolouris, G. (2016). Additive manufacturing methods and modelling approaches: a critical review. *The International Journal of Advanced Manufacturing Technology*, 83(1-4):389–405.

[Bodaghi et al., 2018] Bodaghi, M., Damanpack, A., and Liao, W. (2018). Triple shape memory polymers by 4d printing. *Smart Materials and Structures*, 27(6):065010.

[Bonaventura and Della Rocca, 2018] Bonaventura, L. and Della Rocca, A. (2018). Convergence analysis of a cell centered finite volume diffusion operator on non-orthogonal polyhedral meshes. *arXiv preprint arXiv:1806.09180*.

[Bone et al., 2020] Bone, J. M., Childs, C. M., Menon, A., Poczos, B., Feinberg, A. W., LeDuc, P. R., and Washburn, N. R. (2020). Hierarchical machine learning for high-fidelity 3d printed biopolymers. *ACS Biomaterials Science & Engineering*.

[Bongard, 2011] Bongard, J. (2011). The 'what','how'and the 'why'of evolutionary robotics. In *New Horizons in Evolutionary Robotics*, pages 29–35. Springer.

[Borenstein and Moraglio, 2014] Borenstein, Y. and Moraglio, A. (2014). *Theory and principled methods for the design of metaheuristics*. Springer.

[Bourell et al., 2014] Bourell, D. L., Rosen, D. W., and Leu, M. C. (2014). The roadmap for additive manufacturing and its impact. *3D Printing and Additive Manufacturing*, 1(1):6–9.

[Bowyer, 2020] Bowyer, A. (2020). *RepRap*. University of Bath. open source 3D printer hardware and software standards.

[Brans, 2013] Brans, K. (2013). 3d printing, a maturing technology. *IFAC Proceedings Volumes*, 46(7):468–472.

[Bredeche et al., 2012] Bredeche, N., Montanier, J.-M., Liu, W., and Winfield, A. F. (2012). Environment-driven distributed evolutionary adaptation in a population of autonomous robotic agents. *Mathematical and Computer Modelling of Dynamical Systems*, 18(1):101–129.

[Brest et al., 2006] Brest, J., Greiner, S., Boskovic, B., Mernik, M., and Zumer, V. (2006). Self-adapting control parameters in differential evolution: A comparative study on numerical benchmark problems. *IEEE transactions on evolutionary computation*, 10(6):646–657.

[Brockmeier, 2000] Brockmeier, O. (2000). *Automated loading and unloading of the Stratasys FDM 1600 Rapid Prototyping System*. PhD thesis, Virginia Tech.

[Brown, 2020] Brown, K. (2020). *White Knight 3D printer*. NAK3D Designs. open source 3D printer.

[Brown et al., 1975] Brown, R. L., Durbin, J., and Evans, J. M. (1975). Techniques for testing the constancy of regression relationships over time. *Journal of the Royal Statistical Society: Series B (Methodological)*, 37(2):149–163.

[Brus and Barvíř, 2015] Brus, J. and Barvíř, R. (2015). Coping with integrating low-cost 3d printing and surface models: A case study on prusa i3. In *Surface Models for Geosciences*, pages 45–59. Springer.

[Calà et al., 2018] Calà, A. L. A., Luder, A., Boschi, F., Tavola, G., and Taisch, M. (2018). Migration towards digital manufacturing automation—an assessment approach. In *2018 IEEE Industrial Cyber-Physical Systems (ICPS)*, pages 714–719. IEEE.

[Cantú-Paz, 2001] Cantú-Paz, E. (2001). Migration policies, selection pressure, and parallel evolutionary algorithms. *Journal of heuristics*, 7(4):311–334.

[Cardona et al., 2016] Cardona, C., Curdes, A., and Isaacs, A. (2016). Effects of filament diameter tolerances in fused filament fabrication. *IU Journal of Undergraduate Research*, 2(1):44–47.

[Cavus, 2016] Cavus, N. (2016). Aircraft design optimization with artificial intelligence. In *54th AIAA Aerospace Sciences Meeting*, page 2001.

[Centin and Signoroni, 2018] Centin, M. and Signoroni, A. (2018). Advancing mesh completion for digital modeling and manufacturing. *Computer Aided Geometric Design*, 62:73–90.

[Chadha et al., 2018] Chadha, C., Crowe, K. A., Carmen, C. L., and Patterson, A. E. (2018). Exploring an am-enabled combination-of-functions approach for modular product design. *Designs*, 2(4):37.

[Chen, 2010] Chen, L. (2010). An integral approach for large deflection cantilever beams. *International Journal of Non-Linear Mechanics*, 45(3):301–305.

[Cheng et al., 2006] Cheng, Q.-l., Ke, Y.-l., and Dong, H.-y. (2006). Numerical simulation study on milling force for aerospace aluminum alloy. *ACTA AERONAUTICA ET ASTRONAUTICA SINICA-SERIES A AND B-*, 27(4):724.

[Chinwicharnam and Thipyopas, 2016] Chinwicharnam, K. and Thipyopas, C. (2016). Comparison of wing–propeller interaction in tractor and pusher configuration. *International Journal of Micro Air Vehicles*, 8(1):3–20.

[Choong et al., 2017] Choong, Y. Y. C., Maleksaeedi, S., Eng, H., Wei, J., and Su, P.-C. (2017). 4d printing of high performance shape memory polymer using stereolithography. *Materials & Design*, 126:219–225.

[Chua et al., 2017] Chua, C. K., Wong, C. H., and Yeong, W. Y. (2017). *Standards, quality control, and measurement sciences in 3D printing and additive manufacturing*. Academic Press.

[Chugh et al., 2016] Chugh, T., Jin, Y., Miettinen, K., Hakanen, J., and Sindhya, K. (2016). A surrogate-assisted reference vector guided evolutionary algorithm for computationally expensive many-objective optimization. *IEEE Transactions on Evolutionary Computation*, 22(1):129–142.

[Chung and Yoo, 2002] Chung, J. and Yoo, H. H. (2002). Dynamic analysis of a rotating cantilever beam by using the finite element method. *Journal of Sound and vibration*, 249(1):147–164.

[Coccia et al., 2015] Coccia, G., Di Nicola, G., and Sotte, M. (2015). Design, manufacture, and test of a prototype for a parabolic trough collector for industrial process heat. *Renewable energy*, 74:727–736.

[Conev et al., 2020] Conev, A., Litsa, E. E., Perez, M. R., Diba, M., Mikos, A. G., and Kavraki, L. E. (2020). Machine learning-guided three-dimensional printing of tissue engineering scaffolds. *Tissue Engineering Part A*.

[Coogan and Kazmer, 2017] Coogan, T. J. and Kazmer, D. O. (2017). Bond and part strength in fused deposition modeling. *Rapid Prototyping Journal*.

[Costabile et al., 2017] Costabile, G., Fera, M., Fruggiero, F., Lambiase, A., and Pham, D. (2017). Cost models of additive manufacturing: A literature review. *International Journal of Industrial Engineering Computations*, 8(2):263–283.

[Cotteleer and Joyce, 2014] Cotteleer, M. and Joyce, J. (2014). 3d opportunity: Additive manufacturing paths to performance, innovation, and growth. *Deloitte Review*, 14:5–19.

[Cross, 1999] Cross, R. (1999). Impact of a ball with a bat or racket. *American Journal of Physics*, 67(8):692–702.

[Crowell et al., 2018] Crowell, A. M., Cramer, S. A., Lopez, J. P., Rashka, E. K., Reuss, R. C., Wordsworth, V. K., and Lewin, G. C. (2018). Development of a quality assurance tool for additive manufacturing. In *2018 Systems and Information Engineering Design Symposium (SIEDS)*, pages 76–81. IEEE.

[Crump et al., 1996] Crump, S. S., Comb, J. W., Priedeman Jr, W. R., and Zinniel, R. L. (1996). Process of support removal for fused deposition modeling. US Patent 5,503,785.

[Ćwikła et al., 2017] Ćwikła, G., Grabowik, C., Kalinowski, K., Paprocka, I., and Ociepka, P. (2017). The influence of printing parameters on selected mechanical properties of fdm/fff 3d-printed parts. In *IOP Conf. Ser. Mater. Sci. Eng*, volume 227.

[da Rocha et al., 2010] da Rocha, P. A. S., e Souza, R. D. d. S., and de Lima Tostes, M. E. (2010). Prototype cnc machine design. In *2010 9th IEEE/IAS International Conference on Industry Applications-INDUSCON 2010*, pages 1–5. IEEE.

[Dai et al., 2020] Dai, S., Deng, Z. C., Yu, Y. J., Zhang, K., Wang, S. H., and Ye, J. (2020). Orthotropic elastic behaviors and yield strength of fused deposition modeling materials: Theory and experiments. *Polymer Testing*, 87:106520.

[Daryadel et al., 2019] Daryadel, S., Behroozfar, A., and Minary-Jolandan, M. (2019). Toward control of microstructure in microscale additive manufacturing of copper using localized electrodeposition. *Advanced Engineering Materials*, 21(1):1800946.

[Davis et al., 2012] Davis, L. D., De Jong, K., Vose, M. D., and Whitley, L. D. (2012). *Evolutionary algorithms*, volume 111. Springer Science & Business Media.

[Deb, 2014] Deb, K. (2014). Multi-objective optimization. In *Search methodologies*, pages 403–449. Springer.

[Deb et al., 2002] Deb, K., Anand, A., and Joshi, D. (2002). A computationally efficient evolutionary algorithm for real-parameter optimization. *Evolutionary computation*, 10(4):371–395.

[Deb and Jain, 2013] Deb, K. and Jain, H. (2013). An evolutionary many-objective optimization algorithm using reference-point-based nondominated sorting approach, part i: solving problems with box constraints. *IEEE Transactions on Evolutionary Computation*, 18(4):577–601.

[del Mar Espinosa et al., 2019] del Mar Espinosa, M., Domínguez, M., Romero, L., Domínguez, I. A., Jiménez, M., et al. (2019). Additive manufacturing technologies: An overview about 3d printing methods and future prospects. *Complexity*, 2019:1–30.

[Delic et al., 2019] Delic, M., Eyers, D. R., and Mikulic, J. (2019). Additive manufacturing: empirical evidence for supply chain integration and performance from the automotive industry. *Supply Chain Management: An International Journal*.

[Delli and Chang, 2018] Delli, U. and Chang, S. (2018). Automated process monitoring in 3d printing using supervised machine learning. *Procedia Manufacturing*, 26:865–870.

[Demoly et al., 2011] Demoly, F., Troussier, N., Eynard, B., Falgarone, H., Fricero, B., and Gomes, S. (2011). Proactive assembly oriented design approach based on the deployment of functional requirements. *Journal of computing and information science in engineering*, 11(1).

[Dickey, 2016] Dickey, M. D. (2016). Hydrogel composites: Shaped after print. *Nature materials*, 15(4):379.

[Dilberoglu et al., 2017] Dilberoglu, U. M., Gharehpapagh, B., Yaman, U., and Dolen, M. (2017). The role of additive manufacturing in the era of industry 4.0. *Procedia Manufacturing*, 11:545–554.

[Dirac, 1953] Dirac, P. (1953). The lorentz transformation and absolute time. *Physica*, 19(1-–12):888–896.

[Dizon et al., 2018] Dizon, J. R. C., Espera Jr, A. H., Chen, Q., and Advincula, R. C. (2018). Mechanical characterization of 3d-printed polymers. *Additive Manufacturing*, 20:44–67.

[Dodgson, 1987] Dodgson, M. (1987). Small firms, advanced manufacturing technology and flexibility. *Journal of General Management*, 12(3):58–75.

[Dudek, 2013] Dudek, P. (2013). Fdm 3d printing technology in manufacturing composite elements. *Archives of Metallurgy and Materials*, 58(4):1415–1418.

[Dumas et al., 2014] Dumas, J., Hergel, J., and Lefebvre, S. (2014). Bridging the gap: automated steady scaffoldings for 3d printing. *ACM Transactions on Graphics (TOG)*, 33(4):98.

[Eiben et al., 1999] Eiben, Á. E., Hinterding, R., and Michalewicz, Z. (1999). Parameter control in evolutionary algorithms. *IEEE Transactions on evolutionary computation*, 3(2):124–141.

[Eiben and Smith, 2015] Eiben, A. E. and Smith, J. (2015). From evolutionary computation to the evolution of things. *Nature*, 521(7553):476.

[Elbadawi et al., 2020] Elbadawi, M., Castro, B. M., Gavins, F. K., Ong, J. J., Gaisford, S., Pérez, G., Basit, A. W., Cabalar, P., and Goyanes, A. (2020). M3diseen: A novel machine learning approach for predicting the 3d printability of medicines. *International Journal of Pharmaceutics*, 590:119837.

[Endres et al., 1998] Endres, H., Feiten, W., and Lawitzky, G. (1998). Field test of a navigation system: Autonomous cleaning in supermarkets. In *Proceedings. 1998 IEEE International Conference on Robotics and Automation (Cat. No. 98CH36146)*, volume 2, pages 1779–1781. IEEE.

[Espalin et al., 2014] Espalin, D., Muse, D. W., MacDonald, E., and Wicker, R. B. (2014). 3d printing multifunctionality: structures with electronics. *The International Journal of Advanced Manufacturing Technology*, 72(5-8):963–978.

[Esslinger and Gadow, 2020] Esslinger, S. and Gadow, R. (2020). Additive manufacturing of bioceramic scaffolds by combination of fdm and slip casting. *Journal of the European Ceramic Society*, 40(11):3707–3713.

[Evans, 2012] Evans, B. (2012). A world of 3d printers. In *Practical 3D Printers*, pages 1–26. Springer.

[Everton et al., 2016] Everton, S. K., Hirsch, M., Stravroulakis, P., Leach, R. K., and Clare, A. T. (2016). Review of in-situ process monitoring and in-situ metrology for metal additive manufacturing. *Materials & Design*, 95:431–445.

[Fang et al., 2015] Fang, W., Yang, S., and Yao, X. (2015). A survey on problem models and solution approaches to rescheduling in railway networks. *IEEE Transactions on Intelligent Transportation Systems*, 16(6):2997–3016.

[Felton et al., 2014] Felton, S., Tolley, M., Demaine, E., Rus, D., and Wood, R. (2014). A method for building self-folding machines. *Science*, 345(6197):644–646.

[Fernandez-Vicente et al., 2015] Fernandez-Vicente, M., Canyada, M., and Conejero, A. (2015). Identifying limitations for design for manufacturing with desktop fff 3d printers. *International Journal of Rapid Manufacturing*, 5(1):116–128.

[Feynman and Vernon Jr., 1963] Feynman, R. and Vernon Jr., F. (1963). The theory of a general quantum system interacting with a linear dissipative system. *Annals of Physics*, 24:118–173.

[Figueredo and Wolf, 2009] Figueredo, A. J. and Wolf, P. S. A. (2009). Assortative pairing and life history strategy – a cross-cultural study. *Human Nature*, 20:317–330.

[Filipic et al., 1999] Filipic, B., Urbancic, T., and Krizman, V. (1999). A combined machine learning and genetic algorithm approach to controller design. *Engineering Applications of Artificial Intelligence*, 12(4):401–409.

[Floreano, 2015] Floreano, D. (2015). Science, technology and the future of small autonomous drones. *Nature*, 521(7553):460–466.

[Forster, 2015] Forster, A. M. (2015). Materials testing standards for additive manufacturing of polymer materials: state of the art and standards applicability. *N/A*.

[Frangopol and Maute, 2003] Frangopol, D. M. and Maute, K. (2003). Life-cycle reliability-based optimization of civil and aerospace structures. *Computers & structures*, 81(7):397–410.

[Fregene and Bolden, 2010] Fregene, K. and Bolden, C. L. (2010). Dynamics and control of a biomimetic single-wing nano air vehicle. In *Proceedings of the 2010 American Control Conference*, pages 51–56. IEEE.

[Froes and Boyer, 2019] Froes, F. H. and Boyer, R. (2019). *Additive Manufacturing for the Aerospace Industry*. Elsevier.

[Galantucci et al., 2019] Galantucci, L. M., Guerra, M. G., Dassisti, M., and Lavecchia, F. (2019). Additive manufacturing: New trends in the 4th industrial revolution. In *International Conference on the Industry 4.0 model for Advanced Manufacturing*, pages 153–169. Springer.

[Garanger et al., 2018] Garanger, K., Khamvilai, T., and Feron, E. (2018). 3d printing of a leaf spring: A demonstration of closed-loop control in additive manufacturing. In *2018 IEEE Conference on Control Technology and Applications (CCTA)*, pages 465–470. IEEE.

[Garcia et al., 2018] Garcia, C. A., Lanas, D., Edison, A. M., Altamirano, S., and Garcia, M. V. (2018). An approach of cyber-physical production systems architecture for robot control. In *IECON 2018-44th Annual Conference of the IEEE Industrial Electronics Society*, pages 2847–2852. IEEE.

[Garcia et al., 2012] Garcia, C. R., Correa, J., Espalin, D., Barton, J. H., Rumpf, R. C., Wicker, R., and Gonzalez, V. (2012). 3d printing of anisotropic metamaterials. *Progress In Electromagnetics Research*, 34:75–82.

[Gaynor and Guest, 2016] Gaynor, A. T. and Guest, J. K. (2016). Topology optimization considering overhang constraints: Eliminating sacrificial support material in additive manufacturing through design. *Structural and Multidisciplinary Optimization*, 54(5):1157–1172.

[Ge et al., 2016] Ge, Q., Sakhaei, A. H., Lee, H., Dunn, C. K., Fang, N. X., and Dunn, M. L. (2016). Multimaterial 4d printing with tailorable shape memory polymers. *Scientific reports*, 6:31110.

[Gilmer et al., 2018] Gilmer, E. L., Miller, D., Chatham, C. A., Zawaski, C., Fallon, J. J., Pekkanen, A., Long, T. E., Williams, C. B., and Bortner, M. J.

(2018). Model analysis of feedstock behavior in fused filament fabrication: Enabling rapid materials screening. *Polymer*, 152:51 – 61. SI: Advanced Polymers for 3D Printing/Additive Manufacturing.

[Gladman et al., 2016] Gladman, A. S., Matsumoto, E. A., Nuzzo, R. G., Mahadevan, L., and Lewis, J. A. (2016). Biomimetic 4d printing. *Nature materials*, 15(4):413.

[Goh et al., 2020] Goh, G., Sing, S., and Yeong, W. (2020). A review on machine learning in 3d printing: applications, potential, and challenges. *Artificial Intelligence Review*, pages 1–32.

[Gomis-Bellmunt and Flavio Campanile, 2010] Gomis-Bellmunt, O. and Flavio Campanile, L. (2010). *Design Rules for Actuators in Active Mechanical Systems*. Springer.

[Götzelmann et al., 2017] Götzelmann, T., Branz, L., Heidenreich, C., and Otto, M. (2017). A personal computer-based approach for 3d printing accessible to blind people. In *Proceedings of the 10th International Conference on PErvasive Technologies Related to Assistive Environments*, pages 1–4.

[Grau et al., 2017] Grau, A., Indri, M., Bello, L. L., and Sauter, T. (2017). Industrial robotics in factory automation: From the early stage to the internet of things. In *IECON 2017-43rd Annual Conference of the IEEE Industrial Electronics Society*, pages 6159–6164. IEEE.

[Greenhalgh and Hiley, 2003] Greenhalgh, E. and Hiley, M. (2003). The assessment of novel materials and processes for the impact tolerant design of stiffened composite aerospace structures. *Composites part A: applied science and manufacturing*, 34(2):151–161.

[Griffey, 2014] Griffey, J. (2014). The types of 3-d printing. *Library Technology Reports*, 50(5):8–12.

[Grimmelsmann et al., 2018] Grimmelsmann, N., Kreuziger, M., Korger, M., Meissner, H., and Ehrmann, A. (2018). Adhesion of 3d printed material on textile substrates. *Rapid Prototyping Journal*, 24(1):166–170.

[Günther et al., 2014] Günther, D., Heymel, B., Günther, J. F., and Ederer, I. (2014). Continuous 3d-printing for additive manufacturing. *Rapid Prototyping Journal*, 20(4):320–327.

[Hadley and McCarthy, 2011] Hadley, J. R. and McCarthy, D. J. (2011). Producibility and confidence indices during defense acquisition. In *NDIA Ground Vehicle Systems Engineering and Technology Symposium*.

[Haidegger and Paniti, 2019] Haidegger, G. and Paniti, I. (2019). Issues in manufacturing automation & robotics within the past 4 decades and vision for the next.

[Hamel et al., 2019] Hamel, C. M., Roach, D. J., Long, K. N., Demoly, F., Dunn, M. L., and Qi, H. J. (2019). Machine-learning based design of active composite structures for 4d printing. *Smart Materials and Structures*, 28(6):065005.

[Hametner et al., 2011] Hametner, R., Kormann, B., Vogel-Heuser, B., Winkler, D., and Zoitl, A. (2011). Test case generation approach for industrial automation systems. In *The 5th International Conference on Automation, Robotics and Applications*, pages 57–62. IEEE.

[Hao et al., 2014] Hao, Z., AghaKouchak, A., Nakhjiri, N., and Farahmand, A. (2014). Global integrated drought monitoring and prediction system (GIDMaPS) data sets. *figshare* `https://doi.org/10.6084/m9.figshare.853801`.

[Harris et al., 2002] Harris, C. E., Starnes, J. H., and Shuart, M. J. (2002). Design and manufacturing of aerospace composite structures, state-of-the-art assessment. *Journal of aircraft*, 39(4):545–560.

[Harvey et al., 2005] Harvey, I., Paolo, E. D., Wood, R., Quinn, M., and Tuci, E. (2005). Evolutionary robotics: A new scientific tool for studying cognition. *Artificial life*, 11(1-2):79–98.

[Hassan et al., 2018] Hassan, M. K., Paltrinieri, A., Dreassi, A., Miani, S., and Sclip, A. (2018). The determinants of co-movement dynamics between sukuk and conventional bonds. *The Quarterly Review of Economics and Finance*, 68:73–84.

[Hassen and Kirka, 2018] Hassen, A. A. and Kirka, M. M. (2018). Additive manufacturing: The rise of a technology and the need for quality control and inspection techniques. *Materials Evaluation*, 76(4):438–453.

[Heer and Bieller, 2018] Heer, C. and Bieller, S. (2018). World robotics - industrial robot report 2018. *IFR 2018 World Robotics Report*, (1):1–3.

[Heikkinen et al., 2020] Heikkinen, T., Stolt, R., and Elgh, F. (2020). Incorporating design for additive manufacturing in multidisciplinary design automation–challenges identified. *Computer-Aided Design and Applications*, 17(5):936–947.

[Hicks et al., 2019] Hicks, A. C., Lyons, M. P., and Pedrone, M. C. (2019). Removing a printed item from a printer. US Patent App. 15/726,511.

[Hilton et al., 2015] Hilton, E., Linsey, J., and Goodman, J. (2015). Understanding the prototyping strategies of experienced designers. In *2015 IEEE Frontiers in Education Conference (FIE)*, pages 1–8. IEEE.

[Hocking, 2013] Hocking, R. R. (2013). *Methods and applications of linear models: regression and the analysis of variance*. John Wiley & Sons.

[Hoffman, 1999] Hoffman, D. (1999). Cost benefits analysis of test automation. *STAR West*, 99.

[Holden et al., 2015] Holden, J. R., Caley, T. M., and Turner, M. G. (2015). Maple seed performance as a wind turbine. *53rd AIAA Aerospace Sciences Meeting*.

[Holshouser et al., 2013] Holshouser, C., Newell, C., Palas, S., Love, L. J., Kunc, V., Lind, R. F., Lloyd, P. D., Rowe, J. C., Blue, C. A., Duty, C. E., Peter, W. H., and Dehoff, R. R. (2013). Out of bounds additive manufacturing. *Advanced Materials and Processes*, 171(3).

[Honarvar, 2020] Honarvar, F. (2020). A review of ultrasonic testing applications in additive manufacturing: Defect evaluation, material characterization, and process control. *Ultrasonics*, page 106227.

[Hosmer et al., 1997] Hosmer, D. W., Hosmer, T., Le Cessie, S., and Lemeshow, S. (1997). A comparison of goodness-of-fit tests for the logistic regression model. *Statistics in medicine*, 16(9):965–980.

[Hu et al., 2017] Hu, G., Damanpack, A., Bodaghi, M., and Liao, W. (2017). Increasing dimension of structures by 4d printing shape memory polymers via fused deposition modeling. *Smart Materials and Structures*, 26(12):125023.

[Huang et al., 2015] Huang, Y., Leu, M. C., Mazumder, J., and Donmez, A. (2015). Additive manufacturing: current state, future potential, gaps and needs, and recommendations. *Journal of Manufacturing Science and Engineering*, 137(1):014001.

[Huber et al., 1997] Huber, J. E., Fleck, N. A., and Ashby, M. F. (1997). The selection of mechanical actuators based on performance indices. volume 453. The Royal Society.

[Hueber et al., 2016] Hueber, C., Horejsi, K., and Schledjewski, R. (2016). Review of cost estimation: methods and models for aerospace composite manufacturing. *Advanced Manufacturing: Polymer & Composites Science*, 2(1):1–13.

[Hurst, 2016] Hurst, E. J. (2016). 3d printing in healthcare: emerging applications. *Journal of Hospital Librarianship*, 16(3):255–267.

[Hylton et al., 2012] Hylton, T., Martin, C., Tun, R., and Castelli, V. (2012). The darpa nano air vehicle program. In *50th AIAA Aerospace Sciences Meeting Including the New Horizons Forum and Aerospace Exposition*, page 583.

[Ibrahim et al., 2018] Ibrahim, Y., Melenka, G. W., and Kempers, R. (2018). Additive manufacturing of continuous wire polymer composites. *Manufacturing letters*, 16:49–51.

[Indri and Lazzero, 2015] Indri, M. and Lazzero, I. (2015). The robolab experience: aims, challenges and results of a joint academia-industry lab of industrial robotics. In *2015 IEEE 20th Conference on Emerging Technologies & Factory Automation (ETFA)*, pages 1–8. IEEE.

[Inoma et al., 2020] Inoma, A. O., Ibhadode, O. O., and Ibhadode, A. A. (2020). The perception and deployment of 3d printing in the nigerian educational sector for science and engineering programs. *Scientific African*, page e00641.

[Iqbal et al., 2015] Iqbal, M. Z., Arcuri, A., and Briand, L. (2015). Environment modeling and simulation for automated testing of soft real-time embedded software. *Software & Systems Modeling*, 14(1):483–524.

[Isenhour et al., 1989] Isenhour, T., Eckert, S., and Marshall, J. (1989). Intelligent robots-the next step in laboratory automation. *Analytical Chemistry*, 61(13):805A–814A.

[Ishengoma and Mtaho, 2014] Ishengoma, F. R. and Mtaho, A. B. (2014). 3d printing: developing countries perspectives. *arXiv preprint arXiv:1410.5349*.

[Jakovljevic et al., 2019] Jakovljevic, Z., Lesi, V., Mitrovic, S., and Pajic, M. (2019). Distributing sequential control for manufacturing automation systems. *IEEE Transactions on Control Systems Technology*.

[Jameson et al., 2012] Jameson, S., Fregene, K., Chang, M., Allen, N., Youngren, H., and Scroggins, J. (2012). Lockheed martin's samarai nano air vehicle: challenges, research, and realization. In *50th AIAA Aerospace Sciences Meeting Including the New Horizons Forum and Aerospace Exposition*, page 584.

[Jameson et al., 2007] Jameson, S., Satterfield, B., Bolden, C., Allen, N., Palmdale, C., Youngren, H., and Portland, M. (2007). Samarai nano air vehicle–a revolution in flight. In *AUVSI Unmanned Systems North America Conference Proceedings*.

[Jansen et al., 2010] Jansen, P. W., Perez, R. E., and RA Martins, J. R. (2010). Aerostructural optimization of nonplanar lifting surfaces. *Journal of Aircraft*, 47(5):1490–1503.

[Jarque and Bera, 1987] Jarque, C. M. and Bera, A. K. (1987). A test for normality of observations and regression residuals. *International Statistical Review/Revue Internationale de Statistique*, pages 163–172.

[Javaid and Haleem, 2019] Javaid, M. and Haleem, A. (2019). Current status and applications of additive manufacturing in dentistry: A literature-based review. *Journal of oral biology and craniofacial research*.

[Jenkins, 2018] Jenkins, H. (2018). Manufacturing automation. In *Robotics and Automation Handbook*, pages 543–561. CRC Press.

[Jiang et al., 2018a] Jiang, J., Stringer, J., Xu, X., and Zheng, P. (2018a). A benchmarking part for evaluating and comparing support structures of additive manufacturing. In *3rd International Conference on Progress in Additive Manufacturing (Pro-AM 2018)*, pages 196–202.

[Jiang et al., 2018b] Jiang, J., Xu, X., and Stringer, J. (2018b). Support structures for additive manufacturing: a review. *Journal of Manufacturing and Materials Processing*, 2(4):64.

[Jiménez et al., 2019] Jiménez, M., Romero, L., Domínguez, I. A., Espinosa, M. d. M., and Domínguez, M. (2019). Additive manufacturing technologies: An overview about 3d printing methods and future prospects. *Complexity*, 2019.

[Jin et al., 2017] Jin, Y., Du, J., Ma, Z., Liu, A., and He, Y. (2017). An optimization approach for path planning of high-quality and uniform additive manufacturing. *The International Journal of Advanced Manufacturing Technology*, 92(1-4):651–662.

[Jin et al., 2013] Jin, Y. A., He, Y., and Fu, J. Z. (2013). An adaptive tool path generation for fused deposition modeling. In *Advanced Materials Research*, volume 819, pages 7–12. Trans Tech Publ.

[Jin et al., 2014] Jin, Y.-a., He, Y., Fu, J.-z., Gan, W.-f., and Lin, Z.-w. (2014). Optimization of tool-path generation for material extrusion-based additive manufacturing technology. *Additive manufacturing*, 1:32–47.

[Johnson and Mall, 1985a] Johnson, W. and Mall, S. (1985a). A fracture mechanics approach for designing adhesively bonded joints. In *Delamination and debonding of materials*. ASTM International.

[Johnson and Mall, 1985b] Johnson, W. S. and Mall, S. (1985b). A fracture mechanics approach for designing adhesively bonded joints. In *Delamination and debonding of materials*. ASTM International.

[Jones et al., 2011] Jones, R., Haufe, P., Sells, E., Iravani, P., Olliver, V., Palmer, C., and Bowyer, A. (2011). Reprap – the replicating rapid prototyper. *Robotica*, 29(1):177–191.

[Joshi and Sheikh, 2015] Joshi, S. C. and Sheikh, A. A. (2015). 3d printing in aerospace and its long-term sustainability. *Virtual and Physical Prototyping*, 10(4):175–185.

[Kakanuru and Pochiraju, 2020] Kakanuru, P. and Pochiraju, K. (2020). Moisture ingress and degradation of additively manufactured pla, abs and pla/sic composite parts. *Additive Manufacturing*, 36:101529.

[Kalles and Papagelis, 2010] Kalles, D. and Papagelis, A. (2010). Lossless fitness inheritance in genetic algorithms for decision trees. *Soft Computing*, 14(9):973–993.

[Kane et al., 1987] Kane, T., Ryan, R., and Banerjeer, A. (1987). Dynamics of a cantilever beam attached to a moving base. *Journal of Guidance, Control, and Dynamics*, 10(2):139–151.

[Kannan and Manoj, 2015] Kannan, K. S. and Manoj, K. (2015). Outlier detection in multivariate data. *Applied Mathematical Sciences*, 9(47):2317–2324.

[Karafotias et al., 2014] Karafotias, G., Hoogendoorn, M., and Eiben, Á. E. (2014). Parameter control in evolutionary algorithms: Trends and challenges. *IEEE Transactions on Evolutionary Computation*, 19(2):167–187.

[Kassapoglou, 2013] Kassapoglou, C. (2013). *Design and analysis of composite structures: with applications to aerospace structures*. John Wiley & Sons.

[Katakura et al., 2019] Katakura, S., Kuroki, Y., and Watanabe, K. (2019). A 3d printer head as a robotic manipulator. In *Proceedings of the 32nd Annual ACM Symposium on User Interface Software and Technology*, pages 535–548.

[Katakura and Watanabe, 2018] Katakura, S. and Watanabe, K. (2018). Printmotion: Actuating printed objects using actuators equipped in a 3d printer. In *The 31st Annual ACM Symposium on User Interface Software and Technology Adjunct Proceedings*, pages 137–139.

[Kaufman et al., 2020] Kaufman, D., McKay, N., Routson, C., Erb, M., Davis, B., Heiri, O., Jaccard, S., Tierney, J., Dätwyler, C., Axford, Y., Brussel, T., Cartapanis, O., Chase, B., Dawson, A., de Vernal, A., Engels, S., Jonkers, L., Marsicek, J., Moffa-Sánchez, P., Morrill, C., Orsi, A., Rehfeld, K., Saunders, K., Sommer, P. S., Thomas, E., Tonello, M., Tóth, M., Vachula, R., Andreev, A., Bertrand, S., Biskaborn, B., Bringué, M., Brooks, S., Caniupán, M., Chevalier,

M., Cwynar, L., Emile-Geay, J., Fegyveresi, J., Feurdean, A., Finsinger, W., Fortin, M.-C., Foster, L., Fox, M., Gajewski, K., Grosjean, M., Hausmann, S., Heinrichs, M., Holmes, N., Ilyashuk, B., Ilyashuk, E., Juggins, S., Khider, D., Koinig, K., Langdon, P., Larocque-Tobler, I., Li, J., Lotter, A., Luoto, T., Mackay, A., Magyari, E., Malevich, S., Mark, B., Massaferro, J., Montade, V., Nazarova, L., Novenko, E., Pařil, P., Pearson, E., Peros, M., Pienitz, R., Płóciennik, M., Porinchu, D., Potito, A., Rees, A., Reinemann, S., Roberts, S., Rolland, N., Salonen, S., Self, A., Seppä, H., Shala, S., St-Jacques, J.-M., Stenni, B., Syrykh, L., Tarrats, P., Taylor, K., van den Bos, V., Velle, G., Wahl, E., Walker, I., Wilmshurst, J., Zhang, E., and Zhilich, S. (2020). A global database of holocene paleotemperature records. *Scientific Data*, 7(1):115.

[Keennon et al., 2012] Keennon, M., Klingebiel, K., and Won, H. (2012). Development of the nano hummingbird: A tailless flapping wing micro air vehicle. In *50th AIAA aerospace sciences meeting including the new horizons forum and aerospace exposition*, page 588.

[Kehoe et al., 2015] Kehoe, B., Patil, S., Abbeel, P., and Goldberg, K. (2015). A survey of research on cloud robotics and automation. *IEEE Transactions on automation science and engineering*, 12(2):398–409.

[Kennedy et al., 2019] Kennedy, S. K., Dalley, A. M., and Kotyk, G. J. (2019). Additive manufacturing: Assessing metal powder quality through characterizing feedstock and contaminants. *Journal of materials engineering and performance*, 28(2):728–740.

[Kessentini et al., 2019] Kessentini, A., Mohammed Sayeed Ahmed, G., and Madiouli, J. (2019). Design optimization and fe analysis of 3d printed carbon peek based mono leaf spring. *Micromachines*, 10(5):279.

[Khoo et al., 2015] Khoo, Z. X., Teoh, J. E. M., Liu, Y., Chua, C. K., Yang, S., An, J., Leong, K. F., and Yeong, W. Y. (2015). 3d printing of smart materials: A review on recent progresses in 4d printing. *Virtual and Physical Prototyping*, 10(3):103–122.

[Kim et al., 2016] Kim, E., Shin, Y.-J., and Ahn, S.-H. (2016). The effects of moisture and temperature on the mechanical properties of additive manufacturing components: fused deposition modeling. *Rapid Prototyping Journal*, 22(6):887–894.

[Kim et al., 2018] Kim, H., Lin, Y., and Tseng, T.-L. B. (2018). A review on quality control in additive manufacturing. *Rapid Prototyping Journal*.

[Kimberlin, 2003] Kimberlin, R. D. (2003). *Flight testing of fixed-wing aircraft*. American Institute of Aeronautics and Astronautics.

[Koester et al., 2016] Koester, L., Taheri, H., Bond, L. J., Barnard, D., and Gray, J. (2016). Additive manufacturing metrology: State of the art and needs assessment. In *AIP conference Proceedings*, volume 1706, page 130001. AIP Publishing LLC.

[Kokkinis et al., 2015] Kokkinis, D., Schaffner, M., and Studart, A. R. (2015). Multimaterial magnetically assisted 3d printing of composite materials. *Nature communications*, 6:8643.

[Kuang et al., 2019] Kuang, X., Roach, D. J., Wu, J., Hamel, C. M., Ding, Z., Wang, T., Dunn, M. L., and Qi, H. J. (2019). Advances in 4d printing: Materials and applications. *Advanced Functional Materials*, 29(2):1805290.

[Kuznetsov et al., 2018] Kuznetsov, V. E., Solonin, A. N., Urzhumtsev, O. D., Schilling, R., and Tavitov, A. G. (2018). Strength of pla components fabricated with fused deposition technology using a desktop 3d printer as a function of geometrical parameters of the process. *Polymers*, 10(3):313.

[Kwas et al., 2014] Kwas, A., MacDonald, E., Kief, C. J., Wicker, R., Soto, C., Bañuelos, L., Aarestad, J., Zufelt, B., Stegeman, J. D., and Tolbert, C. (2014). Printing multi-functionality: additive manufacturing for cubesats. In *AIAA SPACE 2014 Conference and Exposition*, page 4193.

[Laplume et al., 2016] Laplume, A., Anzalone, G. C., and Pearce, J. M. (2016). Open-source, self-replicating 3-d printer factory for small-business manufacturing. *The International Journal of Advanced Manufacturing Technology*, 85(1-4):633–642.

[LaTorre et al., 2008] LaTorre, A., Peña, J., Robles, V., and De Miguel, P. (2008). Supercomputer scheduling with combined evolutionary techniques. In *Metaheuristics for Scheduling in Distributed Computing Environments*, pages 95–120. Springer.

[Leach, 2014] Leach, N. (2014). 3d printing in space. *Architectural Design*, 84(6):108–113.

[Lee, 1995] Lee, H. (1995). Divergence and flutter of a cantilever rod with an intermediate spring support. *International journal of solids and structures*, 32(10):1371–1382.

[Lee and Choi, 2018] Lee, I. and Choi, H. (2018). Scaling law for the lift force of autorotating falling seeds at terminal velocity. *Journal of Fluid Mechanics*, 835:406–420.

[Lee and Huang, 2013] Lee, J. and Huang, A. (2013). Fatigue analysis of fdm materials. *Rapid prototyping journal*, 19(4):291–299.

[Leishman, 2008] Leishman, J. G. (2008). *Principles of helicopter aerodynamics*. Cambridge University Press.

[Leite et al., 2018] Leite, M., Fernandes, J., Deus, A. M., Reis, L., and Vaz, M. F. (2018). Study of the influence of 3d printing parameters on the mechanical properties of pla.

[Lensgraf and Mettu, 2016] Lensgraf, S. and Mettu, R. R. (2016). Beyond layers: A 3d-aware toolpath algorithm for fused filament fabrication. In *2016 IEEE International Conference on Robotics and Automation (ICRA)*, pages 3625–3631. IEEE.

[Li et al., 2019] Li, N., Huang, S., Zhang, G., Qin, R., Liu, W., Xiong, H., Shi, G., and Blackburn, J. (2019). Progress in additive manufacturing on new materials: A review. *Journal of Materials Science & Technology*, 35(2):242–269.

[Li et al., 2017] Li, X., Lian, Q., Li, D., Xin, H., and Jia, S. (2017). Development of a robotic arm based hydrogel additive manufacturing system for in-situ printing. *Applied Sciences*, 7(1):73.

[Ligon et al., 2017] Ligon, S. C., Liska, R., Stampfl, J., Gurr, M., and Mulhaupt, R. (2017). Polymers for 3d printing and customized additive manufacturing. *Chemical reviews*, 117(15):10212–10290.

[Liu et al., 2014] Liu, L., Shamir, A., Wang, C. C., and Whiting, E. (2014). 3d printing oriented design: geometry and optimization. In *SIGGRAPH ASIA Courses*, pages 1–1.

[Liu, 1995] Liu, X.-W. (1995). Five-axis nc cylindrical milling of sculptured surfaces. *Computer-Aided Design*, 27(12):887–894.

[Llewellyn-Jones et al., 2016] Llewellyn-Jones, T., Allen, R., and Trask, R. (2016). Curved layer fused filament fabrication using automated toolpath generation. *3D Printing and Additive Manufacturing*, 3(4):236–243.

[Lötstedt, 1981] Lötstedt, P. (1981). Coulomb friction in two-dimensional rigid body systems. *ZAMM-Journal of Applied Mathematics and Mechanics/Zeitschrift für Angewandte Mathematik und Mechanik*, 61(12):605–615.

[Lu and Wong, 2018] Lu, Q. Y. and Wong, C. H. (2018). Additive manufacturing process monitoring and control by non-destructive testing techniques: challenges and in-process monitoring. *Virtual and physical prototyping*, 13(2):39–48.

[Luo et al., 2017] Luo, J., Liu, Q., Yang, Y., Li, X., Chen, M.-r., and Cao, W. (2017). An artificial bee colony algorithm for multi-objective optimisation. *Applied Soft Computing*, 50:235–251.

[Ly and Kim, 2017] Ly, S. T. and Kim, J. Y. (2017). 4d printing–fused deposition modeling printing with thermal-responsive shape memory polymers. *International Journal of Precision Engineering and Manufacturing-Green Technology*, 4(3):267–272.

[MacCurdy et al., 2016] MacCurdy, R., Katzschmann, R., Kim, Y., and Rus, D. (2016). Printable hydraulics: A method for fabricating robots by 3d co-printing solids and liquids. In *2016 IEEE International Conference on Robotics and Automation (ICRA)*, pages 3878–3885. IEEE.

[Macdonald et al., 2014] Macdonald, E., Salas, R., Espalin, D., Perez, M., Aguilera, E., Muse, D., and Wicker, R. B. (2014). 3d printing for the rapid prototyping of structural electronics. *IEEE access*, 2:234–242.

[Mandache, 2019] Mandache, C. (2019). Overview of non-destructive evaluation techniques for metal-based additive manufacturing. *Materials Science and Technology*, 35(9):1007–1015.

[Mao et al., 2016] Mao, K., Harman, M., and Jia, Y. (2016). Sapienz: Multi-objective automated testing for android applications. In *Proceedings of the 25th International Symposium on Software Testing and Analysis*, pages 94–105. ACM.

[Mao et al., 2017] Mao, K., Harman, M., and Jia, Y. (2017). Crowd intelligence enhances automated mobile testing. In *Proceedings of the 32nd IEEE/ACM International Conference on Automated Software Engineering*, pages 16–26. IEEE Press.

[Mardiyansah and Yamin, 2019] Mardiyansah, I. and Yamin, M. (2019). Redesign prusa i3 3d printer using software solidworks 2016. *International Journal of Design and Manufacturing Technology (IJDMT) Volume*, 10:1–11.

[Mazhari et al., 2021] Mazhari, A. A., Ticknor, R., Swei, S., Krzesniak, S., and Teodorescu, M. (2021). Automated Testing and Characterization of Additive Manufacturing (ATCAM). *Journal of Materials Engineering and Performance*.

[Mazhari et al., 2020a] Mazhari, A. A., Zhang, A., Ticknor, R., Swei, S., Hyde, E., and Teodorescu, M. (2020a). Printing and Programming of In-Situ Actuators. In *2020 IEEE/ASME International Conference on Advanced Intelligent Mechatronics (AIM)*, pages 445–450, Boston, MA, USA. IEEE.

[Mazhari et al., 2020b] Mazhari, A. A., Zhang, A., Ticknor, R., Swei, S., Hyde, E., and Teodorescu, M. (2020b). Printing and programming of in-situ actuators. In *2020 IEEE/ASME International Conference on Advanced Intelligent Mechatronics (AIM)*, pages 445–450. IEEE.

[Mazzanti et al., 2019] Mazzanti, V., Malagutti, L., and Mollica, F. (2019). Fdm 3d printing of polymers containing natural fillers: A review of their mechanical properties. *Polymers*, 11(7):1094.

[Medina and Lawrence, 2008] Medina, E. A. and Lawrence, D. A. (2008). Reachability and observability of linear impulsive systems. *Automatica*, 44(5):1304–1309.

[Mehrabi et al., 2000] Mehrabi, M. G., Ulsoy, A. G., and Koren, Y. (2000). Reconfigurable manufacturing systems: Key to future manufacturing. *Journal of Intelligent manufacturing*, 11(4):403–419.

[Meisel et al., 2013] Meisel, N., Gaynor, A., Williams, C., and Guest, J. (2013). Multiple-material topology optimization of compliant mechanisms created via polyjet 3d printing. In *24th Annual international solid freeform fabrication symposium an additive manufacturing conference*, page 28.

[Meisel et al., 2015] Meisel, N. A., Elliott, A. M., and Williams, C. B. (2015). A procedure for creating actuated joints via embedding shape memory alloys in polyjet 3d printing. *Journal of intelligent material systems and structures*, 26(12):1498–1512.

[Meng et al., 2019] Meng, L., Zhang, W., Quan, D., Shi, G., Tang, L., Hou, Y., Breitkopf, P., Zhu, J., and Gao, T. (2019). From topology optimization design to additive manufacturing: Today's success and tomorrow's roadmap. *Archives of Computational Methods in Engineering*, pages 1–26.

[Miller et al., 2016] Miller, D., Fitzner, I., Fuller, S., and Revzen, S. (2016). Focused modularity: Rapid iteration of design and fabrication of a meter-scale hexapedal robot. In *ASSISTIVE ROBOTICS: Proceedings of the 18th International Conference on CLAWAR 2015*, pages 430–438. World Scientific.

[Minh and Tuyet, 2020] Minh, P. S. and Tuyet, T. T. (2020). Influence of 3d-printing parameters on flexural strength of pla plastic products. *International Journal of Mechanical Engineering*, 7(3):1–4.

[Moilanen and Vadén, 2013] Moilanen, J. and Vadén, T. (2013). 3d printing community and emerging practices of peer production. *First Monday*, 18(8).

[Momeni et al., 2017] Momeni, F., Liu, X., Ni, J., et al. (2017). A review of 4d printing. *Materials & design*, 122:42–79.

[Montero et al., 2001] Montero, M., Roundy, S., Odell, D., Ahn, S.-H., and Wright, P. K. (2001). Material characterization of fused deposition modeling (fdm) abs by designed experiments. *Society of Manufacturing Engineers*, 10(13552540210441166).

[Morel et al., 2019] Morel, G., Pereira, C. E., and Nof, S. (2019). Historical survey and emerging challenges of manufacturing automation modeling and control: A systems architecting perspective. *Annual reviews in control*, 47:21–34.

[Morris et al., 1993] Morris, M., Donovan, J., Kegelman, J., Schwab, S., Levy, R., and Crites, R. (1993). Aerodynamic applications of pressure sensitive paint. *AIAA journal*, 31(3):419–425.

[Mubarik et al., 2020] Mubarik, M. H., Weller, D. D., Bleier, N., Tomei, M., Aghassi-Hagmann, J., Tahoori, M. B., and Kumar, R. (2020). Printed machine learning classifiers. In *2020 53rd Annual IEEE/ACM International Symposium on Microarchitecture (MICRO)*, pages 73–87. IEEE.

[Muñiz-Lerma et al., 2018] Muñiz-Lerma, J. A., Nommeots-Nomm, A., Waters, K. E., and Brochu, M. (2018). A comprehensive approach to powder feedstock characterization for powder bed fusion additive manufacturing: A case study on alsi7mg. *Materials*, 11(12):2386.

[Murr, 2016] Murr, L. E. (2016). Frontiers of 3d printing/additive manufacturing: from human organs to aircraft fabrication. *Journal of Materials Science & Technology*, 32(10):987–995.

[Myers and Myers, 1990] Myers, R. H. and Myers, R. H. (1990). *Classical and modern regression with applications*, volume 2. Duxbury press Belmont, CA.

[n.a., 2020] n.a. (2020). *Cincinnati SAAM*. The Cincinnati Shaper Company. commercial 3D printer.

[n.a, 2020] n.a (2020). *Figure 4 3D Printer*. 3D Systems. commercial 3D printer.

[n.a., 2020a] n.a. (2020a). *Form Cell 3D Printer Farm*. Formlabs. commercial 3D printer.

[n.a., 2020b] n.a. (2020b). *Stratasys Continuous Build 3D Printer*. Stratasys.

[n.a., 2020c] n.a. (2020c). *Teirtime X5 3D Printer*. Beijing Tiertime Technology Co. Ltd. commercial 3D printer.

[Nabhani, 2001] Nabhani, F. (2001). Machining of aerospace titanium alloys. *Robotics and Computer-Integrated Manufacturing*, 17(1-2):99–106.

[Nadgorny and Ameli, 2018] Nadgorny, M. and Ameli, A. (2018). Functional polymers and nanocomposites for 3d printing of smart structures and devices. *ACS applied materials & interfaces*, 10(21):17489–17507.

[Najmon et al., 2019] Najmon, J. C., Raeisi, S., and Tovar, A. (2019). Review of additive manufacturing technologies and applications in the aerospace industry. In *Additive manufacturing for the aerospace industry*, pages 7–31. Elsevier.

[Nandi et al., 2017] Nandi, C., Caspi, A., Grossman, D., and Tatlock, Z. (2017). Programming language tools and techniques for 3d printing. In *2nd Summit on Advances in Programming Languages (SNAPL 2017)*. Schloss Dagstuhl-Leibniz-Zentrum fuer Informatik.

[Nasirov, 2019] Nasirov, A. (2019). *Multiscale Modeling of Fused Filament Fabricated Specimens*. PhD thesis, Tennessee Technological University.

[Nazir et al., 2020] Nazir, A., Azhar, A., Nazir, U., Liu, Y.-F., Qureshi, W. S., Chen, J.-E., and Alanazi, E. (2020). The rise of 3d printing entangled with smart computer aided design during covid-19 era. *Journal of Manufacturing Systems*.

[Nelaturi et al., 2019] Nelaturi, S., Behandish, M., Mirzendehdel, A. M., and de Kleer, J. (2019). Automatic support removal for additive manufacturing post processing. *Computer-Aided Design*, 115:135–146.

[Ngo et al., 2018] Ngo, T. D., Kashani, A., Imbalzano, G., Nguyen, K. T., and Hui, D. (2018). Additive manufacturing (3d printing): A review of materials, methods, applications and challenges. *Composites Part B: Engineering*, 143:172–196.

[Niaki et al., 2019] Niaki, M. K., Torabi, S. A., and Nonino, F. (2019). Why manufacturers adopt additive manufacturing technologies: The role of sustainability. *Journal of cleaner production*, 222:381–392.

[Nof and Silva, 2018] Nof, S. Y. and Silva, J. R. (2018). Perspectives on manufacturing automation under the digital and cyber convergence. *Polytechnica*, 1(1-2):36–47.

[NORBERG, 1973] NORBERG, R. A. (1973). Autorotation, self-stability, and structure of single-winged fruits and seeds (samaras) with comparative remarks on animal flight. *Biological Reviews*, 48(4):561–596.

[Nycz et al., 2018] Nycz, A., Noakes, M., and Cader, M. (2018). Additive manufacturing–a new challenge for automation and robotics. In *Conference on Automation*, pages 3–13. Springer.

[Ochoa et al., 2018] Ochoa, C. A., Meuche, K. S., and Atkins, E. M. (2018). Multicopter operations for autonomous assembly applications in manufacturing environments. In *2018 Modeling and Simulation Technologies Conference*, page 3888.

[O'Connell, 2020] O'Connell, J. (2020). Belt 3d printer: All you need to know.

[Olivas et al., 2010] Olivas, R., Salas, R., Muse, D., MacDonald, E., Wicker, R., Newton, M., and Church, K. (2010). Structural electronics through additive manufacturing and micro-dispensing. In *International Symposium on Microelectronics*, volume 2010, pages 000940–000946. International Microelectronics Assembly and Packaging Society.

[Ou et al., 2010] Ou, Q., Chen, X., Gutschmidt, S., Wood, A., and Leigh, N. (2010). A two-mass cantilever beam model for vibration energy harvesting applications. In *2010 IEEE International Conference on Automation Science and Engineering*, pages 301–306. IEEE.

[Owens et al., 2018] Owens, W., Cinque, D., Heim, A., Park, D., Tang, D., and Mulroney, R. (2018). A method for in-flight adjustment of wing dihedral with folding wings and tail.

[Pan et al., 2016] Pan, A. Q., Huang, Z. F., Guo, R. J., and Liu, J. (2016). Effect of fdm process on adhesive strength of polylactic acid (pla) filament. In *Key Engineering Materials*, volume 667, pages 181–186. Trans Tech Publ.

[Parasuraman et al., 1993] Parasuraman, R., Molloy, R., and Singh, I. L. (1993). Performance consequences of automation-induced'complacency'. *The International Journal of Aviation Psychology*, 3(1):1–23.

[Parasuraman and Riley, 1997] Parasuraman, R. and Riley, V. (1997). Humans and automation: Use, misuse, disuse, abuse. *Human factors*, 39(2):230–253.

[Park et al., 2016] Park, S., Kim, J., Lee, H., Jang, D., and Jun, S. (2016). Methodology of technological evolution for three-dimensional printing. *Industrial Management & Data Systems*.

[Pax et al., 2012] Pax, C., Smith, Z., Mayer, A., and Pettis, N. (2012). *Automated 3D build processes*. US Patent US8282380B2.

[Pei, 2014] Pei, E. (2014). 4d printing: dawn of an emerging technology cycle. *Assembly Automation*, 34(4):310–314.

[Petricca et al., 2011] Petricca, L., Ohlckers, P., and Grinde, C. (2011). Micro- and nano-air vehicles: State of the art. *International journal of aerospace engineering*, 2011.

[Phillips and Costello, 1972] Phillips, J. W. and Costello, G. A. (1972). Large deflections of impacted helical springs. *the Journal of the Acoustical Society of America*, 51(3B):967–973.

[Pietrantuono and Russo, 2018] Pietrantuono, R. and Russo, S. (2018). Robotics software engineering and certification: Issues and challenges. In *2018 IEEE International Symposium on Software Reliability Engineering Workshops (ISSREW)*, pages 308–312. IEEE.

[Pines and Bohorquez, 2006] Pines, D. J. and Bohorquez, F. (2006). Challenges facing future micro-air-vehicle development. *Journal of aircraft*, 43(2):290–305.

[Poole and O'Farrell, 1971] Poole, M. A. and O'Farrell, P. N. (1971). The assumptions of the linear regression model. *Transactions of the Institute of British Geographers*, pages 145–158.

[Popescu and Amza, 2017] Popescu, D. and Amza, C. (2017). Additive manufacturing automation for industry 4.0. *Res. & Sci. Today*, 13:50.

[Popescu et al., 2018] Popescu, D., Zapciu, A., Amza, C., Baciu, F., and Marinescu, R. (2018). Fdm process parameters influence over the mechanical properties of polymer specimens: A review. *Polymer Testing*, 69:157–166.

[Pradel et al., 2018] Pradel, P., Zhu, Z., Bibb, R., and Moultrie, J. (2018). Investigation of design for additive manufacturing in professional design practice. *Journal of Engineering Design*, 29(4-5):165–200.

[Preacher et al., 2006] Preacher, K. J., Curran, P. J., and Bauer, D. J. (2006). Computational tools for probing interactions in multiple linear regression, multilevel modeling, and latent curve analysis. *Journal of Educational and Behavioral Statistics*, 31(4):437–448.

[Prendergast and Burdick, 2019] Prendergast, M. E. and Burdick, J. A. (2019). Recent advances in enabling technologies in 3d printing for precision medicine. *Advanced Materials*, page 1902516.

[Prestes et al., 2016] Prestes, E., Marques, L., Neuland, R., Mantelli, M., Maffei, R., Dogru, S., Prado, J., Macedo, J., and Madhavan, R. (2016). 2016 humanitarian robotics and automation technology challenge. *Robotics & Automation Magazine, IEEE*, 23(3).

[Prusa, 2020] Prusa, J. (2020). *Prusa i3 Mk3 3D printer*. Prusa Research a.s. commercial 3D printer.

[Qi et al., 2019] Qi, X., Chen, G., Li, Y., Cheng, X., and Li, C. (2019). Applying neural-network-based machine learning to additive manufacturing: current applications, challenges, and future perspectives. *Engineering*, 5(4):721–729.

[Qiu-zhong and Hao-yu, 2011] Qiu-zhong, Z. and Hao-yu, Z. (2011). Digital product definition method based on 3d annotation technology [j]. *Journal of Machine Design*, 1.

[Quaid and Hollis, 1996] Quaid, A. E. and Hollis, R. L. (1996). Cooperative 2-dof robots for precision assembly. In *Proceedings of IEEE International Conference on Robotics and Automation*, volume 3, pages 2188–2193. IEEE.

[Rajkumar and Shanmugam, 2018] Rajkumar, A. R. and Shanmugam, K. (2018). Additive manufacturing-enabled shape transformations via fff 4d printing. *Journal of Materials Research*, 33(24):4362–4376.

[Rajpurohit, 2018] Rajpurohit, S. R. (2018). Flexural strength of fused filament fabricated (fff) pla parts on an open-source 3d printer. *Advances in Manufacturing*, 6(4):430–441.

[Ramola et al., 2019] Ramola, M., Yadav, V., and Jain, R. (2019). On the adoption of additive manufacturing in healthcare: a literature review. *Journal of Manufacturing Technology Management*.

[Rao et al., 2014] Rao, M., Hoysall, D. C., and Gopalan, J. (2014). Mahogany seed–a step forward in deciphering autorotation. *Current Science*, 106(8):1101.

[Raza and Khosravi, 2015] Raza, M. Q. and Khosravi, A. (2015). A review on artificial intelligence based load demand forecasting techniques for smart grid and buildings. *Renewable and Sustainable Energy Reviews*, 50:1352–1372.

[Regina et al., 2018] Regina, F., Lavecchia, F., and Galantucci, L. M. (2018). Preliminary study for a full colour low cost open source 3d printer, based on the combination of fused deposition modelling (fdm) or fused filament fabrication (fff) and inkjet printing. *International Journal on Interactive Design and Manufacturing (IJIDeM)*, 12(3):979–993.

[Regulski et al., 2019] Regulski, K., Wilk-Kołodziejczyk, D., Szymczak, T., Gumienny, G., Pirowski, Z., Jaśkowiec, K., and Kluska-Nawarecka, S. (2019). Data mining methods for prediction of multi-component al-si alloy properties based on cooling curves. *Journal of Materials Engineering and Performance*, 28(12):7431–7444.

[Rijs and Smulders, 1990] Rijs, R. and Smulders, P. (1990). Blade element theory for performance analysis of slow running wind turbines. *Wind Engineering*, 14(2):62–79.

[Roberts et al., 2015] Roberts, L., Bruck, H. A., and Gupta, S. K. (2015). Autonomous loitering control for a flapping wing miniature aerial vehicle with independent wing control. In *ASME 2014 International Design Engineering Technical Conferences and Computers and Information in Engineering Conference*. American Society of Mechanical Engineers Digital Collection.

[Rodríguez-Panes et al., 2018] Rodríguez-Panes, A., Claver, J., and Camacho, A. M. (2018). The influence of manufacturing parameters on the mechanical behaviour of pla and abs pieces manufactured by fdm: A comparative analysis. *Materials*, 11(8):1333.

[Ronkkonen et al., 2005] Ronkkonen, J., Kukkonen, S., and Price, K. V. (2005). Real-parameter optimization with differential evolution. In *2005 IEEE Congress on Evolutionary Computation*, volume 1, pages 506–513. IEEE.

[Rosemurgy et al., 2016] Rosemurgy, W. J., Beck, R. F., and Maki, K. J. (2016). A velocity decomposition formulation for 2d steady incompressible lifting problems. *European Journal of Mechanics-B/Fluids*, 58:70–84.

[Rosen, 2007] Rosen, D. W. (2007). Computer-aided design for additive manufacturing of cellular structures. *Computer-Aided Design and Applications*, 4(5):585–594.

[Royakkers and van Est, 2015] Royakkers, L. and van Est, R. (2015). A literature review on new robotics: automation from love to war. *International journal of social robotics*, 7(5):549–570.

[Ruemler et al., 2017] Ruemler, S. P., Zimmerman, K. E., Hartman, N. W., Hedberg, T., and Barnard Feeny, A. (2017). Promoting model-based definition to establish a complete product definition. *Journal of manufacturing science and engineering*, 139(5).

[Russell and Hall, 2008] Russell, R. and Hall, D. (2008). Manufacturing the future: Federal priorities for manufacturing r&d.

[Rylands et al., 2016] Rylands, B., Böhme, T., Gorkin, R., Fan, J., and Birtchnell, T. (2016). The adoption process and impact of additive manufacturing on manufacturing systems. *Journal of Manufacturing Technology Management*.

[Sabbapathy, 2013] Sabbapathy, L. (2013). Hummingbird's-eye view for the us military. *Leonardo Times, 17 (3) 2013*.

[Samozino et al., 2008] Samozino, P., Morin, J.-B., Hintzy, F., and Belli, A. (2008). A simple method for measuring force, velocity and power output during squat jump. *Journal of biomechanics*, 41(14):2940–2945.

[Sanatgar et al., 2017] Sanatgar, R. H., Campagne, C., and Nierstrasz, V. (2017). Investigation of the adhesion properties of direct 3d printing of polymers and nanocomposites on textiles: Effect of fdm printing process parameters. *Applied Surface Science*, 403:551–563.

[Sass, 2007] Sass, L. (2007). Synthesis of design production with integrated digital fabrication. *Automation in construction*, 16(3):298–310.

[Sa'ude et al., 2018] Sa'ude, N., Ibrahim, M., Ibrahim, M., Wahab, M., Haq, R., Marwah, O., and Khirotdin, R. (2018). Additive manufacturing of copper-abs filament by fused deposition modeling (fdm). *Journal of Mechanical Engineering*, pages 23–32.

[Schmidt and Lipson, 2009] Schmidt, M. and Lipson, H. (2009). Distilling free-form natural laws from experimental data. *science*, 324(5923):81–85.

[Schurmann, 2020] Schurmann, S. (2020). *Black Belt 3D printer*. Blackbelt 3D. commercial 3D printer.

[Scott, 2017] Scott, C. (2017). *Stratasys Unveils Continuous Build 3D Demonstrator, Extends Partnership with Desktop Metal - 3DPrint.com: The Voice of 3D Printing / Additive Manufacturing*.

[Secretan et al., 2011] Secretan, J., Beato, N., D'Ambrosio, D. B., Rodriguez, A., Campbell, A., Folsom-Kovarik, J. T., and Stanley, K. O. (2011). Picbreeder: A case study in collaborative evolutionary exploration of design space. *Evolutionary Computation*, 19(3):373–403.

[Seifi et al., 2016] Seifi, M., Salem, A., Beuth, J., Harrysson, O., and Lewandowski, J. J. (2016). Overview of materials qualification needs for metal additive manufacturing. *Jom*, 68(3):747–764.

[Sells et al., 2010] Sells, E., Bailard, S., Smith, Z., Bowyer, A., and Olliver, V. (2010). Reprap: the replicating rapid prototyper: maximizing customizability by breeding the means of production. In *Handbook of Research in Mass Customization and Personalization: (In 2 Volumes)*, pages 568–580. World Scientific.

[Seo et al., 2010] Seo, J. H., Seol, D. M., Lee, J. H., and Rhee, S. H. (2010). Flexible cfd meshing strategy for prediction of ship resistance and propulsion performance. *International Journal of Naval Architecture and Ocean Engineering*, 2(3):139–145.

[Serpell and Smith, 2010] Serpell, M. and Smith, J. E. (2010). Self-adaptation of mutation operator and probability for permutation representations in genetic algorithms. *Evolutionary Computation*, 18(3):491–514.

[Serrano et al., 2019] Serrano, E., Vitorino, L., and Almeida, H. A. (2019). Impact of additive technologies in the health sector for 2030. In *2019 IEEE 6th Portuguese Meeting on Bioengineering (ENBENG)*, pages 1–4. IEEE.

[Shaikh et al., 2016] Shaikh, S., Kumar, N., Jain, P. K., and Tandon, P. (2016). Hilbert curve based toolpath for fdm process. In *CAD/CAM, Robotics and Factories of the Future*, pages 751–759. Springer.

[Shakor et al., 2019] Shakor, P., Nejadi, S., Paul, G., and Malek, S. (2019). Review of emerging additive manufacturing technologies in 3d printing of cementitious materials in the construction industry. *Frontiers in Built Environment*, 4:85.

[Shanmugam et al., 2019] Shanmugam, S., Naik, A., Sujan, T., and Desai, S. (2019). Developing robust 3d printed parts for automotive application using design for additive manufacturing and optimization techniques. In *INCOSE International Symposium*, volume 29, pages 394–407. Wiley Online Library.

[Shanyi, 2007] Shanyi, D. (2007). 12 advanced composite materials and aerospace engineering.

[Shen and Furrer, 2000] Shen, G. and Furrer, D. (2000). Manufacturing of aerospace forgings. *Journal of Materials Processing Technology*, 98(2):189–195.

[Shevchik et al., 2018] Shevchik, S. A., Kenel, C., Leinenbach, C., and Wasmer, K. (2018). Acoustic emission for in situ quality monitoring in additive manufacturing using spectral convolutional neural networks. *Additive Manufacturing*, 21:598–604.

[Shokrieh and Rezaei, 2003] Shokrieh, M. M. and Rezaei, D. (2003). Analysis and optimization of a composite leaf spring. *Composite structures*, 60(3):317–325.

[Sierra et al., 2020] Sierra, J., Villa, D. S., Velasquez, A. M., and Villaneda, W. (2020). Relation between mechanical properties and 3d printer configurations parameters using pla at open source prusa i3. *International Journal of Integrated Engineering*, 12(8):97–108.

[Silva et al., 2019] Silva, J. M., Javales, R., and Silva, J. R. (2019). A new requirements engineering approach for manufacturing based on petri nets. *IFAC-PapersOnLine*, 52(10):97–102.

[Silva et al., 2020] Silva, J. R., Silva, J. M., and Vaquero, T. S. (2020). Formal knowledge engineering for planning: Pre and post-design analysis. In *Knowledge Engineering Tools and Techniques for AI Planning*, pages 47–65. Springer.

[Silverbrook, 2010] Silverbrook, K. (2010). Three dimensional (3d) printer system with placement and curing mechanisms. US Patent 7,766,641.

[Singh, 2011] Singh, R. (2011). Process capability study of polyjet printing for plastic components. *Journal of mechanical science and technology*, 25(4):1011–1015.

[Slaughter et al., 2017] Slaughter, A., Yampolskiy, M., Matthews, M., King, W. E., Guss, G., and Elovici, Y. (2017). How to ensure bad quality in metal additive manufacturing: In-situ infrared thermography from the security perspective. In *Proceedings of the 12th International Conference on Availability, Reliability and Security*, pages 1–10.

[Smith et al., 2018] Smith, T., Failla, J. A., Lindahl, J. M., Kim, P., Hassen, A. A., Duty, C. E., Joshi, P., Stevens, C., and Kunc, V. (2018). Structural health monitoring of 3d printed structures. Technical report, Oak Ridge National Lab.(ORNL), Oak Ridge, TN (United States).

[Smyth, 2017] Smyth, A. (2017). Investigation of aircraft wingtip collisions on the ground.

[Sobachkin and Dumnov, 2013] Sobachkin, A. and Dumnov, G. (2013). Numerical basis of cad-embedded cfd. Dassault Systemes SolidWorks.

[Soe Thura Win and Kyi Hla Win, 2020] Soe Thura Win, L. and Kyi Hla Win, Shane, e. a. (2020). *AIM2020*, page 1625–1631. IEEE.

[Sohankar et al., 1998] Sohankar, A., Norberg, C., and Davidson, L. (1998). Low-reynolds-number flow around a square cylinder at incidence: study of blockage, onset of vortex shedding and outlet boundary condition. *International journal for numerical methods in fluids*, 26(1):39–56.

[Spoerk et al., 2018] Spoerk, M., Gonzalez-Gutierrez, J., Sapkota, J., Schuschnigg, S., and Holzer, C. (2018). Effect of the printing bed temperature on the adhesion of parts produced by fused filament fabrication. *Plastics, Rubber and Composites*, 47(1):17–24.

[Stansbury and Idacavage, 2016] Stansbury, J. W. and Idacavage, M. J. (2016). 3d printing with polymers: Challenges among expanding options and opportunities. *Dental Materials*, 32(1):54–64.

[Steenhuis and Pretorius, 2015] Steenhuis, H. and Pretorius, L. (2015). Additive manufacturing or 3d printing and its adoption. In *International Association for Management of Technology 2015 Conference Proceedings. University of Pretoria, Pretoria, South Africa*, pages 2468–2479.

[Steenhuis et al., 2020] Steenhuis, H.-J., Fang, X., Ulusemre, T., et al. (2020). Global diffusion of innovation during the fourth industrial revolution: The case of additive manufacturing or 3d printing. *International Journal of Innovation and Technology Management (IJITM)*, 17(01):1–34.

[Steuben et al., 2016] Steuben, J. C., Iliopoulos, A. P., and Michopoulos, J. G. (2016). Implicit slicing for functionally tailored additive manufacturing. *Computer-Aided Design*, 77:107–119.

[Stevens, 1984] Stevens, J. P. (1984). Outliers and influential data points in regression analysis. *Psychological bulletin*, 95(2):334.

[Stewart and Trinkle, 1996] Stewart, D. E. and Trinkle, J. C. (1996). An implicit time-stepping scheme for rigid body dynamics with inelastic collisions and coulomb friction. *International Journal for Numerical Methods in Engineering*, 39(15):2673–2691.

[Stiltner et al., 2011] Stiltner, L. J., Elliott, A. M., and Williams, C. B. (2011). A method for creating actuated joints via fiber embedding in a polyjet 3d printing process. In *International Solid Freeform Fabrication Symposium*, volume 22, pages 583–592.

[Straub, 2016] Straub, J. (2016). Automated testing and quality assurance of 3d printing/3d printed hardware: Assessment for quality assurance and cybersecurity purposes. In *2016 IEEE AUTOTESTCON*, pages 1–5. IEEE.

[Straub, 2017] Straub, J. (2017). Physical security and cyber security issues and human error prevention for 3d printed objects: detecting the use of an incorrect printing material. In *Dimensional Optical Metrology and Inspection for Practical Applications VI*, volume 10220, page 102200K. International Society for Optics and Photonics.

[Sturm et al., 2019] Sturm, L. D., Albakri, M. I., Tarazaga, P. A., and Williams, C. B. (2019). In situ monitoring of material jetting additive manufacturing process via impedance based measurements. *Additive Manufacturing*, 28:456–463.

[Su et al., 2020] Su, J.-W., Li, D., Xie, Y., Zhou, T., Gao, W., Deng, H., Xin, M., and Lin, J. (2020). A machine learning workflow for 4d printing: understand and predict morphing behaviors of printed active structures. *Smart Materials and Structures*, 30(1):015028.

[Tellaeche et al., 2015] Tellaeche, A., Maurtua, I., and Ibarguren, A. (2015). Human robot interaction in industrial robotics. examples from research centers to industry. In *2015 IEEE 20th Conference on Emerging Technologies & Factory Automation (ETFA)*, pages 1–6. IEEE.

[Thomas and Gilbert, 2014] Thomas, D. S. and Gilbert, S. W. (2014). Costs and cost effectiveness of additive manufacturing. *NIST special publication*, 1176:12.

[Thompson et al., 2016] Thompson, M. K., Moroni, G., Vaneker, T., Fadel, G., Campbell, R. I., Gibson, I., Bernard, A., Schulz, J., Graf, P., Ahuja, B., et al. (2016). Design for additive manufacturing: Trends, opportunities, considerations, and constraints. *CIRP annals*, 65(2):737–760.

[Thrimurthulu et al., 2004] Thrimurthulu, K., Pandey, P. M., and Reddy, N. V. (2004). Optimum part deposition orientation in fused deposition modeling. *International Journal of Machine Tools and Manufacture*, 44(6):585–594.

[Thummalapenta et al., 2012] Thummalapenta, S., Sinha, S., Singhania, N., and Chandra, S. (2012). Automating test automation. In *Proceedings of the 34th International Conference on Software Engineering*, pages 881–891. IEEE Press.

[Tibbits, 2014] Tibbits, S. (2014). 4d printing: multi-material shape change. *Architectural Design*, 84(1):116–121.

[Tofail et al., 2018] Tofail, S. A., Koumoulos, E. P., Bandyopadhyay, A., Bose, S., O'Donoghue, L., and Charitidis, C. (2018). Additive manufacturing: scientific and technological challenges, market uptake and opportunities. *Materials today*, 21(1):22–37.

[Torrado and Roberson, 2016] Torrado, A. R. and Roberson, D. A. (2016). Failure analysis and anisotropy evaluation of 3d-printed tensile test specimens of different geometries and print raster patterns. *Journal of Failure Analysis and Prevention*, 16(1):154–164.

[Torrado et al., 2015] Torrado, A. R., Shemelya, C. M., English, J. D., Lin, Y., Wicker, R. B., and Roberson, D. A. (2015). Characterizing the effect of additives to abs on the mechanical property anisotropy of specimens fabricated by material extrusion 3d printing. *Additive Manufacturing*, 6:16–29.

[Totaro and Gürdal, 2009] Totaro, G. and Gürdal, Z. (2009). Optimal design of composite lattice shell structures for aerospace applications. *Aerospace Science and Technology*, 13(4-5):157–164.

[Townsend et al., 2016] Townsend, A., Senin, N., Blunt, L., Leach, R., and Taylor, J. (2016). Surface texture metrology for metal additive manufacturing: a review. *Precision Engineering*, 46:34–47.

[Trapp et al., 2017] Trapp, J., Rubenchik, A. M., Guss, G., and Matthews, M. J. (2017). In situ absorptivity measurements of metallic powders during laser powder-bed fusion additive manufacturing. *Applied Materials Today*, 9:341–349.

[Travieso-Rodriguez et al., 2019] Travieso-Rodriguez, J. A., Jerez-Mesa, R., Llumà, J., Traver-Ramos, O., Gomez-Gras, G., and Roa Rovira, J. J. (2019). Mechanical properties of 3d-printing polylactic acid parts subjected to bending stress and fatigue testing. *Materials*, 12(23):3859.

[Tumer and Stone, 2003a] Tumer, I. Y. and Stone, R. B. (2003a). Mapping function to failure mode during component development. *Research in Engineering Design*, 14(1):25–33.

[Tumer and Stone, 2003b] Tumer, I. Y. and Stone, R. B. (2003b). Mapping function to failure mode during component development. *Research in Engineering Design*, 14(1):25–33.

[Tut et al., 2010] Tut, V., Tulcan, A., Cosma, C., and Serban, I. (2010). Application of cad/cam/fea, reverse engineering and rapid prototyping in manufacturing industry. *International Journal of Mechanics*, 4(4):79–86.

[Tymrak et al., 2014] Tymrak, B., Kreiger, M., and Pearce, J. M. (2014). Mechanical properties of components fabricated with open-source 3-d printers under realistic environmental conditions. *Materials & Design*, 58:242–246.

[Ulrich et al., 2010] Ulrich, E. R., Pines, D. J., and Humbert, J. S. (2010). From falling to flying: the path to powered flight of a robotic samara nano air vehicle. *Bioinspiration & biomimetics*, 5(4):045009.

[Urhal et al., 2019] Urhal, P., Weightman, A., Diver, C., and Bartolo, P. (2019). Robot assisted additive manufacturing: A review. *Robotics and Computer-Integrated Manufacturing*, 59:335–345.

[Van Veldhuizen et al., 2003] Van Veldhuizen, D. A., Zydallis, J. B., and Lamont, G. B. (2003). Considerations in engineering parallel multiobjective evolutionary algorithms. *IEEE Transactions on Evolutionary Computation*, 7(2):144–173.

[Vanek et al., 2014] Vanek, J., Galicia, J. A. G., and Benes, B. (2014). Clever support: Efficient support structure generation for digital fabrication. In *Computer graphics forum*, volume 33, pages 117–125. Wiley Online Library.

[Vargas et al., 2014] Vargas, P. A., Di Paolo, E. A., Harvey, I., and Husbands, P. (2014). *The horizons of evolutionary robotics*. MIT press.

[Vogel-Heuser et al., 2015] Vogel-Heuser, B., Fay, A., Schaefer, I., and Tichy, M. (2015). Evolution of software in automated production systems: Challenges and research directions. *Journal of Systems and Software*, 110:54–84.

[Vogelesang and Vlot, 2000] Vogelesang, L. B. and Vlot, A. (2000). Development of fibre metal laminates for advanced aerospace structures. *Journal of Materials Processing Technology*, 103(1):1–5.

[Volpato et al., 2014] Volpato, N., Aguiomar Foggiatto, J., and Coradini Schwarz, D. (2014). The influence of support base on fdm accuracy in z. *Rapid prototyping journal*, 20(3):182–191.

[Wang et al., 2000] Wang, J., Deng, Y., and Xu, G. (2000). Reachability analysis of real-time systems using time petri nets. *IEEE Transactions on Systems, Man, and Cybernetics, Part B (Cybernetics)*, 30(5):725–736.

[Wang et al., 2002] Wang, J., Periaux, J., and Sefrioui, M. (2002). Parallel evolutionary algorithms for optimization problems in aerospace engineering. *Journal of Computational and Applied Mathematics*, 149(1):155–169.

[Wang et al., 2017] Wang, T., Kwok, T.-H., and Zhou, C. (2017). In-situ droplet inspection and control system for liquid metal jet 3d printing process. *Procedia Manufacturing*, 10:968–981.

[Watson and Taminger, 2018] Watson, J. and Taminger, K. (2018). A decision-support model for selecting additive manufacturing versus subtractive manufacturing based on energy consumption. *Journal of Cleaner Production*, 176:1316–1322.

[Watson et al., 2002] Watson, R. A., Ficici, S. G., and Pollack, J. B. (2002). Embodied evolution: Distributing an evolutionary algorithm in a population of robots. *Robotics and Autonomous Systems*, 39(1):1–18.

[Wegst and Ashby, 2004] Wegst, U. and Ashby, M. (2004). The mechanical efficiency of natural materials. *Philosophical Magazine*, 84(21):2167–2186.

[Wehner et al., 2016] Wehner, M., Truby, R. L., Fitzgerald, D. J., Mosadegh, B., Whitesides, G. M., Lewis, J. A., and Wood, R. J. (2016). An integrated design and fabrication strategy for entirely soft, autonomous robots. *Nature*, 536(7617):451.

[Whitten et al., 2020] Whitten, D., Dietrich, J., Donar, M., Echempati, R., and Donar, C. (2020). Automated 3d printer bed clearing mechanism. Technical report, SAE Technical Paper.

[Wiberg, 2019] Wiberg, A. (2019). *Towards Design Automation for Additive Manufacturing: A Multidisciplinary Optimization approach*, volume 1854. Linköping University Electronic Press.

[Wielandt, 1982] Wielandt, E. (1982). The leaf-spring seismometer: Design and performance. *Bulletin of the Seismological Society of America*, 72(6A):2349–2367.

[Williams and Starke Jr, 2003] Williams, J. C. and Starke Jr, E. A. (2003). Progress in structural materials for aerospace systems. *Acta Materialia*, 51(19):5775–5799.

[Williams et al., 2013] Williams, M. N., Grajales, C. A. G., and Kurkiewicz, D. (2013). Assumptions of multiple regression: Correcting two misconceptions. *Practical Assessment, Research, and Evaluation*, 18(1):11.

[Wimpenny et al., 2017] Wimpenny, D. I., Pandey, P. M., and Kumar, L. J. (2017). *Advances in 3D printing & additive manufacturing technologies*. Springer.

[Winkler and Biffl, 2012] Winkler, D. and Biffl, S. (2012). Improving quality assurance in automation systems development projects. *Quality Assurance and Management*, pages 20–40.

[Wissink et al., 2010] Wissink, A., Potsdam, M., Sankaran, V., Sitaraman, J., Yang, Z., and Mavriplis, D. (2010). A coupled unstructured-adaptive cartesian cfd approach for hover prediction. In *American Helicopter Society 66th Annual Forum*, pages 1300–1317. AHS International Alexandria, VA.

[Witt, 2015] Witt, D. (2015). Plastics take center stage in 3-d printing surge: The overnight sensation of additive manufacturing is developing over the long term. *Plastics Engineering*, 71(9):36–39.

[Wittbrodt and Pearce, 2015] Wittbrodt, B. and Pearce, J. M. (2015). The effects of pla color on material properties of 3-d printed components. *Additive Manufacturing*, 8:110–116.

[Wohlers, 2019] Wohlers, T. T. (2019). *Wohlers report 2019: 3D printing and additive manufacturing state of the industry*. Wohlers Associates.

[Wollschlaeger et al., 2017] Wollschlaeger, M., Sauter, T., and Jasperneite, J. (2017). The future of industrial communication: Automation networks in the era of the internet of things and industry 4.0. *IEEE industrial electronics magazine*, 11(1):17–27.

[Wong, 2012] Wong, K. V. (2012). A review of additive manufacturing. *ISRN Mechanical Engineering*, 2012.

[Woo, 2017] Woo, S. (2017). Reliability design of mechanical system for mechanical civil engineer.

[Wood, 2015] Wood, B. M. (2015). 5 multifunctionality in additive manufacturing. *Design and Manufacture of Plastic Components for Multifunctionality: Structural Composites, Injection Molding, and 3D Printing*, 171.

[Wood et al., 2012] Wood, R. J., Finio, B., Karpelson, M., Ma, K., Pérez-Arancibia, N. O., Sreetharan, P. S., Tanaka, H., and Whitney, J. P. (2012). Progress on pico air vehicles. *The International Journal of Robotics Research*, 31(11):1292–1302.

[Woodson et al., 2019] Woodson, T., Alcantara, J. T., and do Nascimento, M. S. (2019). Is 3d printing an inclusive innovation?: An examination of 3d printing in brazil. *Technovation*, 80:54–62.

[Wu et al., 2015] Wu, D., Chatzigeorgiou, D., Youcef-Toumi, K., and Ben-Mansour, R. (2015). Node localization in robotic sensor networks for pipeline inspection. *IEEE Transactions on Industrial Informatics*, 12(2):809–819.

[Wu, 2020] Wu, N. (2020). *Creality*. Creality company. commercial 3D printer.

[Xiaomao et al., 2011] Xiaomao, H., Chunsheng, Y., and Yongjun, H. (2011). Tool path planning based on endpoint build-in optimization in rapid prototyping. *Proceedings of the Institution of Mechanical Engineers, Part C: Journal of Mechanical Engineering Science*, 225(12):2919–2926.

[Xu and He, 2004] Xu, X. and He, Q. (2004). Striving for a total integration of cad, capp, cam and cnc. *Robotics and Computer-Integrated Manufacturing*, 20(2):101–109.

[Yang et al., 2018] Yang, G.-Z., Bellingham, J., Dupont, P. E., Fischer, P., Floridi, L., Full, R., Jacobstein, N., Kumar, V., McNutt, M., Merrifield, R., et al. (2018). The grand challenges of science robotics. *Science Robotics*, 3(14):eaar7650.

[Yao, 1999] Yao, X. (1999). Evolving artificial neural networks. *Proceedings of the IEEE*, 87(9):1423–1447.

[Youngren et al., 2009] Youngren, H., Jameson, S., and Satterfield, B. (2009). Design of the samarai monowing rotorcraft nano air vehicle. In *Proceedings of the American Helicopter Society AHS 65th Annual Forum and Technology Display*.

[Zadeh et al., 2019] Zadeh, H. N., Huber, T., Dixon, F., Fee, C., and Clucas, D. (2019). Fabrication of cellulose hydrogel objects through 3d printed sacrificial molds. In *International Conference of Progress in Digital and Physical Manufacturing*, pages 265–270. Springer.

[Zhang and Zhao, 2007] Zhang, H. and Zhao, G. (2007). Adaptive hexahedral mesh generation based on local domain curvature and thickness using a modified grid-based method. *Finite Elements in Analysis and Design*, 43(9):691–704.

[Zhong and Nof, 2020] Zhong, H. and Nof, S. Y. (2020). Evolving dloc theory and emerging applications. In *Dynamic Lines of Collaboration*, pages 97–107. Springer.

[Zhou et al., 2015] Zhou, Y., Huang, W. M., Kang, S. F., Wu, X. L., Lu, H. B., Fu, J., and Cui, H. (2015). From 3d to 4d printing: approaches and typical applications. *Journal of Mechanical Science and Technology*, 29(10):4281–4288.

[Zou et al., 2016a] Zou, R., Xia, Y., Liu, S., Hu, P., Hou, W., Hu, Q., and Shan, C. (2016a). Isotropic and anisotropic elasticity and yielding of 3d printed material. *Composites Part B: Engineering*, 99:506–513.

[Zou et al., 2016b] Zou, R., Xia, Y., Liu, S., Hu, P., Hou, W., Hu, Q., and Shan, C. (2016b). Isotropic and anisotropic elasticity and yielding of 3d printed material. *Composites Part B: Engineering*, 99:506 – 513.